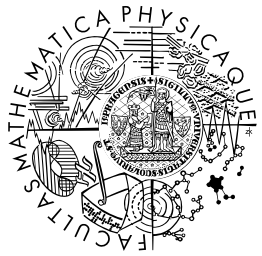

FACULTY
OF MATHEMATICS
AND PHYSICS
Charles University

DOCTORAL THESIS

Markéta Pešková

Proton structure studies using hard exclusive processes at COMPASS experiment

Department of Low Temperature Physics

Supervisor of the doctoral thesis:	Mgr. Jan Matoušek, Ph.D.
Study programme:	Subnuclear Physics
Study branch:	Physics

Prague 2024

ABSTRACT

The exclusive processes, such as *Hard Exclusive Meson Production* (HEMP) and *Deeply Virtual Compton Scattering* (DVCS) are an excellent tool for studying *Generalised Parton Distributions* (GPD). GPDs provide a novel and relatively unexplored view into the structure of nucleon and expand the knowledge given from parameterising *Parton Distribution Functions* (PDF) and parton densities to a more complex, three-dimensional picture. While the golden channel of GPD parametrisation is DVCS, the exclusive meson production gives access to complementary GPDs, provides information of flavour dependence of GPDs, and in case of exclusive π^0 production in particular, also represents the main background process of DVCS, hence it is essential to constrain it. The theoretical formalism of GPD and HEMP description is outlined in the first part of the thesis. The measurement of exclusive processes represents an important part of COMPASS-II programme. The dedicated GPD programme commenced with a 4-weeks-long pilot run in 2012, followed by the main data taking in 2016–2017, using 160 GeV/c muon beams and a liquid hydrogen target, equipped with a recoil proton detector. The COMPASS spectrometre and its configuration for the GPD programme is described in the second section. The exclusive processes require a perfect performance of the electromagnetic calorimeters. The third part explains in detail the principle of operation of the two COMPASS electromagnetic calorimetres used in this analysis and describes their calibration. In the fourth section, we present the procedure of inspecting the data quality, the steps of the analysis, and the selection of the events. The fifth part describes the procedure of extraction of the differential cross-section of the exclusive π^0 production as a function of the four-momentum transfer $|t|$ and the azimuthal angle ϕ. The results and systematic effects are discussed.

KEYWORDS

Generalised Parton Distributions, GPD, Hard exclusive meson production, HEMP, Exclusive π^0 production, COMPASS

ABSTRAKT

Exkluzivní procesy, jako je hluboký virtuální Comptonův rozptyl (DVCS) nebo tvrdá exkluzívní produkce mesonů (HEMP), jsou jedinečným nástrojem ke studiu 3D struktury nukleonu pomocí zobecněných partonových distribucí (GPD). GPD představují perspektivní a málo prozkoumaný směr studia struktury a vnitřní dynamiky nukleonu, který může značně rozšířit úroveň znalostí získanou prostřednictvím partonových distribučních funkcí (PDF). Přestože nejčistším experimentálním kanálem pro studium GPD je DVCS, exkluzivní produkce mesonů jednak poskytuje přístup ke komplementárním GPD, na které DVCS citlivé není, jednak pomůže rozlišit GPD specifické pro kvarky různých vůní podle kvarkového složení daného mesonu. Exkluzívní produkce π^0 navíc představuje hlavní zdroj pozadí pro DVCS proces, což z něj činí proces hodný zájmu. Formalismus GPD je shrnutý v první, teoretické části této práce. Experiment COMPASS se věnoval studiu exkluzívních procesů v druhé fázi svého experimentálního programu, COMPASS-II. GPD program započal 4-týdenním pilotním během v roce 2012, a pokračoval hlavní částí měření v letech 2016 a 2017. Byl použit mionový svazek obou polarit s energií 160 GeV/c a terč z kapalného vodíku uložený v detektoru odraženého protonu. Popis měřícího aparátu experimentu COMPASS a jeho specifika pro GPD program jsou popsány v druhé části práce. Jelikož meson π^0 se rozpadá na dva fotony, je k jeho detekci potřeba dobře vyladěných kalorimetrů s dobrým rozlišením. Ve třetí sekci je popsán princip fungování použitých kalorimetrů a jejich kalibrace. Čtvrtá část popisuje vzorek dat, proceduru jejich sběru a selekce a kontroly jejich kvality. Konečně pátá část obsahuje postup extrakce diferenciálního účinného průřezu exkluzívní produkce mesonu π^0 a diskuzi výsledků a výpočet systematické chyby.

KLÍČOVÁ SLOVA

Generalizované Partonové Distribuce, GPD, Tvrdá exkluzívní produkce mesonů, HEMP, Tvrdá exkluzívní produkce π^0, COMPASS

PEŠKOVÁ, Markéta. *Proton structure studies using hard exclusive processes at COMPASS experiment*. Prague, 2024, 186 p. Doctoral thesis. Charles University, Faculty of Mathematics and Physics, Department of Low Temperature Physics. Advised by Mgr. Jan Matoušek, Ph.D.

DECLARATION

I declare that I carried out this doctoral thesis independently, and only with the cited sources, literature and other professional sources. It has not been used to obtain another or the same degree.

I understand that my work relates to the rights and obligations under the Act No. 121/2000 Sb., the Copyright Act, as amended, in particular the fact that the Charles University has the right to conclude a license agreement on the use of this work as a school work pursuant to Section 60 subsection 1 of the Copyright Act.

Prague ....

Author's signature

ACKNOWLEDGEMENT

I would like to express my sincere gratitude to my supervisor, Jan Matoušek, for his assistance with my analysis, for his practical guidance, programming support, and insightful corrections. I extend my deepest appreciation and gratitute to Petr Pacner for his invaluable help with the programming aspects of this analysis, that have been essential to this work. His guidance in improving my programming practices along with his practical advice, has been incredibly helpful.

I am very grateful to my husband, Michael Pešek, for his unwavering support and valuable advice regarding my work. His assistance in fostering my understanding of physics has been truly beneficial.

My gratitude extends to David Bělohrad, for his advice and support, and Martin Zemko, Vincent Andrieux, and Antonín Květoň for being there to answer my numerous programming-related questions.

Special thanks go to Karolína Lavičková for her excellent collaboration on the analysis. I am also grateful to Nicole d'Hose for guiding me through the theoretical aspects of the analysis, providing constructive feedback, and helping me interpret the results. Finally, I would like to extend my thanks to Bakur Parsamyan for his valuable advice and precise remarks as well as to the entire 2016/17 analysis group for their collaboration, guidance, feedback, and support.

Contents

List of Figures

Introduction

Nucleons represent the building blocks of all matter. The pioneering scattering experiments conducted at the *Stanford Linear Accelerator Center* (SLAC) laboratories in the late 1960s conclusively demonstrated that nucleons, despite not being elementary particles, possess an intricate internal structure. Using both elastic and inelastic electron-proton scattering, the presence of point-like constituents within nucleons was established. The Parton Model, introduced shortly after by Richard Feynman, described these point-like constituents as partons, fermions with spin 1/2, later identified with the quarks in Gell-Mann's Quark Model. Further experimental investigations brought an evidence for an additional constituent of the nucleon – a boson with spin 1, named the gluon. This discovery prompted the formulation of a novel non-abelian gauge theory of strong interaction, known as *Quantum Chromodynamics* (QCD), which elucidates the dynamics within composite particles. Gluons serve as gauge bosons that mediate the strong interaction that binds the quarks together. The QCD has stood the test of time and remains the preeminent framework for understanding strong interactions. It not only provides a comprehensive description of high-energy particle collisions with significant momentum transfer, calculable within perturbative QCD, but also offers insights into the structure and dynamics of nucleons and hadrons at lower energies.

In the high-energy regime, the QCD formalism allows to calculate interactions by means of perturbative expansion due to the asymptotic freedom given from the running coupling constant α_S. In the soft regime the confinement of the strongly coupled particles does not allow a perturbative solution. Thus, the intrinsic structure of composite particles can only be parametrised by phenomenological models utilising experimental data, or recently calculated by Lattice QCD simulations. Nevertheless, until the 1980s, it was commonly believed that the structure and functioning of nucleons were well understood.

Contrary to this assumption, fundamental properties such as the origin of nucleon mass and spin turned out to be more elusive than previously thought. In 1974, Ellis and Jaffe described the measured spin of a proton $1/2\hbar$ as a sum of spins of valence quarks [1]. However, a surprising revelation emerged in 1988 from the EMC experiment at CERN, contradicting this belief. The EMC measured that the quark contribution to the proton spin is only one third [2]. Subsequently, extensive

efforts were undertaken to address this discrepancy, known as the 'proton spin crisis'. Successive polarised *Deep Inelastic Scattering* (DIS) experiments conducted at various facilities including SMC and COMPASS at CERN, HERMES at DESY, experiments at the SLAC laboratory and at JLab, and the polarised proton-proton experiment RHIC at BNL, have confirmed the findings from the EMC. The hope of the community that the remaining part of proton spin could be attributed to the gluon contribution, was subsequently thwarted [3]. This leaves only one last possible candidate to cover the remaining fraction of the proton spin, the orbital angular momenta of partons. However, this contributions remains unknown to this day, which leaves the 'proton spin crisis' unresolved.

New approaches have been explored; one of the possible concepts that drew interest in the late 1990s were the GPD. They represent a three-dimensional view of the nucleon structure by correlating the longitudinal momentum fraction of a parton with its position in the transverse plane. This renders GPDs sensitive to the total angular momentum of partons within the nucleon, making them a promising avenue for resolving the 'proton spin crisis' [4]. Additionally, the study of GPDs is motivated by their interpretation in the impact parameter space [5], which allows to study the nucleon transverse extension depending on the momentum. This is sometimes referred to as nucleon tomography.

GPDs are not directly experimentally accessible. Two most important reactions used to study GPDs are DVCS, $\gamma^* \mathrm{p} \to \gamma \mathrm{p}'$, and HEMP, $\gamma^* \mathrm{p} \to \mathrm{M}\mathrm{p}'$, where $\mathrm{M} = \pi, \rho, \omega$, etc. GPDs enter into the cross sections of these processes through Compton Form Factors. To this day, only the unpolarised GPD H is constrained relatively well by the unpolarised PDFs and data from unpolarised cross sections of DVCS and HEMP. Nevertheless, additional precise data spanning a broader range of kinematics is required. The most recent measurements of the exclusive processes from COMPASS and JLab are promising to bring new input for phenomenologists [6, 7, 8, 9]. The parametrisation of GPD E, which associates the longitudinally polarised nucleon with an unpolarised parton, poses a considerably greater challenge. The first attempts to constrain GPD E have been made by JLab, HERMES, and COMPASS [10, 11, 12, 13]. The reason behind the difficulties in accessing the GPD E is that only a limited number of observables is sensitive to it, such as Pauli form factors of proton and neutron, and azimuthal asymmetries from the DVCS and HEMP processes measured on transversely polarised targets

or the DVCS cross section measured on an unpolarised target.

The benefit of studying the meson production stems in the possibility to separate flavour-dependent GPDs due to different quarkonic content of mesons. Both vector and pseudoscalar mesons provide access to different GPDs, and it is essential to parametrise as many experimentally measurable GPDs as possible in order to constrain less explored or inaccessible GPDs. Another asset of exclusive meson production are the different sensitivities to GPDs. While DVCS process is sensitive to the chiral-even GPDs, the meson production gives access to chiral-odd GPDs. The primary subject of this thesis is the measurement of the differential cross section of exclusive $\gamma^* \mathrm{p} \to \pi^0 \mathrm{p}'$ production as a function of four-momentum transfer between the target and recoil proton, t, and the azimuthal angle between the scattering plane and hadron production plane, ϕ. The exclusive π^0 production is in particular sensitive to the GPD $\bar{E}_T$, known as Boer-Mulders GPD.

In the following Section $[\![\hookrightarrow 1.]\!]$, we will briefly describe the theoretical background of the GPD model and the framework applied for the exclusive π^0 production. The layout of the COMPASS spectrometer and the principle of event reconstruction will be given in Section $[\![\hookrightarrow 2.]\!]$. In Section $[\![\hookrightarrow 3.]\!]$ we will discuss the calibrations performed on the electromagnetic calorimeters and the issues that arose during the process. The luminosity determination, selection criteria for the π^0 candidates in the experimental data, and simulations used to estimate the background will be described in Section $[\![\hookrightarrow 4.]\!]$. Section $[\![\hookrightarrow 5.]\!]$ will be dedicated to the exclusive π^0 cross section extraction and the evaluation of the systematics. In the conclusion we will present a summary and a discussion of the results.[1]

[1] In the whole text we use an assumption of $c = 1$ for brevity.

1 Theoretical Formalism

In the following section, we will give an introduction to the theoretical background of this work. We will briefly describe the formalism of a scattering experiment, the elastic and the deep inelastic scattering, and the parton model arising from these measurements. Then, we will discuss the generalisation of the parton distribution functions from Wigner's distributions to generalised parton distributions and their comparison with other types of parton distribution functions. Subsequently, we will present the experimental accessibility of generalised parton distributions. Next, we will introduce the theoretical framework for the description of HEMP and the primary topic of this thesis, the exclusive π^0 production. Finally, we will give a short overview of the experimental efforts to measure the exclusive π^0 production. The theoretical summary of this complex topic follows mostly the comprehensive description given by Markus Diehl [14, 15, 16, 17] and Cédric Mezrag [18]. I also draw inspiration from the PhD theses of my colleagues Matthias Gorzellik [19], Brian Ventura [20], and Antoine Vidon [21].

1.1 Formalism of Scattering Experiments

Scattering experiments have played a crucial role in probing the structure of matter since the famous Rutherford's experiment, who discovered the atomic nucleus and put an upper limit on its size more than a hundred years ago. Elastic scattering experiments continued to provide new findings on the size and shape of the nucleus and brought evidence of its structure consisting of protons and neutrons. While this method provided a wealth of information on the radius or shape of nucleons, it took another fifty years to discover the existence and character of the inner structure of nucleons, which has been suspected since the first measurement of the magnetic moment of the proton by O. Stern [22]. Given the substantial discrepancy between the experimental findings and the theoretical prediction for the magnetic moment of a spin-1/2 Dirac particle, the idea of the proton as a point-like particle became indefensible.

1.1.1 Elastic Scattering

M. N. Rosenbluth was the first to bring the idea that an electron elastically scattered off a proton is influenced by reduced charges and reduced magnetic moments. Even though he attributed it to a hypothesis of the proton being composed from a neutron core and a positively charged meson cloud [23], which was proven not to be the case, R. Hofstadter carried on with the concept. He explained the experimental results [24] of elastic scattering of electrons off protons and α particles with the Mott cross section modified with a phenomenological form factor $F(q)$. He related the form factor to the charge distribution $\rho(r)$ of the proton by a Fourier transformation [25]

$$\begin{aligned}\frac{\mathrm{d}\sigma}{\mathrm{d}\Omega} &= \left(\frac{\alpha^2(\hbar c)^2}{4E^2\sin^4\left(\frac{\theta}{2}\right)}\right)\left(1-\beta^2\sin^2\left(\frac{\theta}{2}\right)\right)|F(q)|^2 \\ &:= \left(\frac{\mathrm{d}\sigma}{\mathrm{d}\Omega}\right)_{\text{Rutherford}}\left(1-\beta^2\sin^2\left(\frac{\theta}{2}\right)\right)|F(q)|^2 \\ &:= \left(\frac{\mathrm{d}\sigma}{\mathrm{d}\Omega}\right)^*_{\text{Mott}}|F(q)|^2 = \left(\frac{\mathrm{d}\sigma}{\mathrm{d}\Omega}\right)^*_{\text{Mott}}\left|\int_V \rho(\vec{r})e^{i\vec{q}\vec{r}}\,\mathrm{d}^3\vec{r}\right|,\end{aligned} \tag{1.1}$$

where V denotes a volume, the energy of the beam electron is represented by E, α is the electromagnetic coupling constant, β represents the velocity of the electron in units of c, $\hbar$ is the Planck constant, the momentum transfer between the incident and outgoing electron is denoted by $q = |\vec{q}|$, and θ is the polar scattering angle of the electron. The asterisk represents the fact, that the recoil of the target particle is not considered. The lowest-order diagram of the elastic scattering is shown in the left part of Fig 2.1. Hofstadter assumed an exponential distribution of the charge ρ, which was quite well reproduced by the data. However, it was shown that a single form factor cannot encompass the full complexity of the charge and magnetic distribution within a proton.

It can be shown from the first principles, that the elastic ep cross section can be separated into a leptonic and hadronic part. A complete description of the hadronic part, satisfying the Lorentz invariance, is given by two real functions [26].

Hence, the elastic ep cross section in modern notation [27] reads

$$\begin{aligned}\frac{\mathrm{d}\sigma}{\mathrm{d}\Omega} &= \left(\frac{\mathrm{d}\sigma}{\mathrm{d}\Omega}\right)^{*}_{\mathrm{Mott}} \frac{E'}{E}\left(G_E^2\left(Q^2\right) + \frac{\tau}{\epsilon}G_M^2\left(Q^2\right)\right)/(1+\tau) \\ &:= \left(\frac{\mathrm{d}\sigma}{\mathrm{d}\Omega}\right)_{\mathrm{Mott}}\left(G_E^2\left(Q^2\right) + \frac{\tau}{\epsilon}G_M^2\left(Q^2\right)\right)/(1+\tau),\end{aligned} \tag{1.2}$$

where $Q^2 = -q^2$ is the four-momentum transfer to the proton from the electron, and $\tau = \frac{Q^2}{4M^2}$, where M is the proton mass. The G_E and G_M, given in units of elementary charge e and $\mu_N = e\hbar/2M$, are the electric and magnetic Sachs form factors, respectively. The values of the two form factors can be extracted from the cross section by keeping the Q^2 constant and varying the beam energy E, a method called Rosenbluth separation [23]. Another representation is possible in terms of the Dirac and Pauli form factors, F_1 and F_2. Their relation to the Sachs form factors is given by

$$\begin{aligned}F_1\left(Q^2\right) &= \frac{G_E\left(Q^2\right) + \tau G_M\left(Q^2\right)}{1+\tau}, \\ F_2\left(Q^2\right) &= \frac{G_M\left(Q^2\right) - G_E\left(Q^2\right)}{1+\tau}.\end{aligned} \tag{1.3}$$

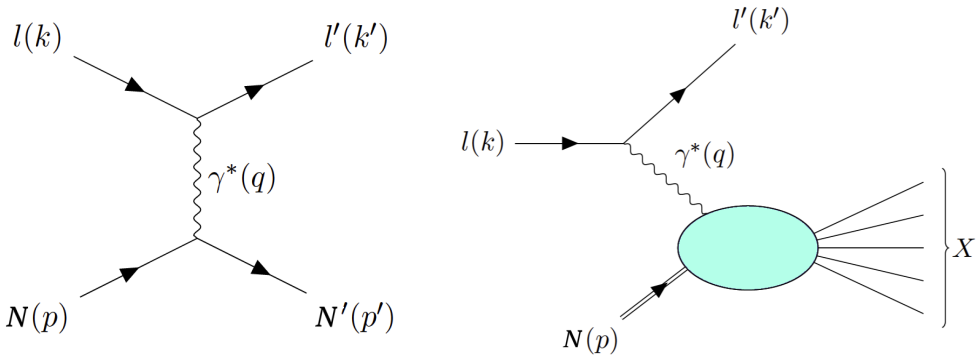

Fig. 1.1: Leading-order diagrams of elastic scattering (left) and deep inelastic scattering (right) with an exchange of a virtual photon.

1.1.2 Deep Inelastic Scattering

The DIS has become a standard tool for the investigation of the structure and inner dynamics of hadrons. The lowest-order diagram of the DIS process is illustrated

in the right part of the Fig 2.1. The left part of the figure describes the interaction of a lepton with a target nucleon, elastically scattering and leaving it intact. In the case of DIS, a constituent quark is struck with an exchanged virtual photon γ^*, which forces the active quark out from the nucleon and one or more hadrons X are created in the final state:

$$\mathrm{l}(k) + \mathrm{N}(p) \to \mathrm{l}(k') + \mathrm{X} \tag{1.4}$$

Here we denote k and k' as the momenta of the incident and scattered lepton, and p as the momentum of the target nucleon. In the following, we will neglect the lepton mass $m \ll M$, where M denotes the nucleon mass, unless stated otherwise. In DIS, the following set of relativistic invariant variables is commonly used:

$$Q^2 = -q^2 = -(k - k')^2 = 2EE'(1 - \cos\theta), \tag{1.5}$$

$$x_B = \frac{Q^2}{2p \cdot q}, \tag{1.6}$$

$$y = \frac{q \cdot p}{p \cdot k} = \frac{E - E'}{E}, \tag{1.7}$$

$$\nu = E - E', \tag{1.8}$$

$$W^2 = (p + q)^2, \tag{1.9}$$

where $Q^2 = -q^2$ denotes the virtual photon mass squared, as previously mentioned in the ⟦↩1.1.1.⟧, E, E' stand for the energy of the incident and scattered lepton, respectively, in the laboratory frame, and θ denotes the scattering polar angle of the lepton. x_B is the Bjorken variable describing the longitudinal momentum fraction of a nucleon carried by the active quark, y represents the relative lepton energy loss, and finally, W denotes the invariant mass of the hadronic final state. The DIS processes are characterized by $W^2 \gg M^2$.

In DIS, a high virtuality is assumed, $M^2 \ll Q^2 \to \infty$ and $M \ll \nu \to \infty$, approaching infinity in the so-called Bjorken limit. There are three types of DIS processes. If none of the outgoing hadrons X are detected, it is called an inclusive DIS process. If a single outgoing hadron is selected from the hadronic system, it denotes a semi-inclusive DIS process. Finally, the case of an exclusive DIS process concerns the measurement with all final state particles detected.

At the leading order of perturbation theory, the DIS cross section reads [28]:

$$\mathrm{d}\sigma = \frac{1}{4k\cdot p}\frac{e_{em}^4}{Q^4}L_{\mu\nu}W^{\mu\nu}2\pi\frac{\mathrm{d}^3k'}{(2\pi)^3 2E'}, \tag{1.10}$$

where $L_{\mu\nu}$ is the leptonic tensor $L_{\mu\nu} = L_{\mu\nu}^{(\mathrm{S})}(k,k') + iL_{\mu\nu}^{(\mathrm{A})}(k,s_L;k')$, and $W_{\mu\nu}$ is the hadronic tensor $W_{\mu\nu} = W_{\mu\nu}^{(\mathrm{S})}(q,p) + iW_{\mu\nu}^{(\mathrm{A})}(q,p;S;)$.

Introducing dimensionless structure functions F_1, F_2 and g_1, g_2

$$\begin{aligned} F_1\left(x,Q^2\right) &\equiv MW_1\left(\nu,Q^2\right), \\ F_2\left(x,Q^2\right) &\equiv \nu W_2\left(\nu,Q^2\right), \\ g_1\left(x,Q^2\right) &\equiv M^2\nu G_1\left(\nu,Q^2\right), \\ g_2\left(x,Q^2\right) &\equiv M\nu^2 G_2\left(\nu,Q^2\right), \end{aligned} \tag{1.11}$$

the DIS cross section reads

$$\frac{\mathrm{d}^3\sigma}{\mathrm{d}x_B\ \mathrm{d}y\ \mathrm{d}\phi} = \frac{4\alpha_{em}^2}{Q^2}\left[\frac{y}{2}F_1\left(x_B,Q^2\right) + \frac{1}{2x_B y}\left(1-y-\frac{y^2\gamma^2}{4}\right)F_2\left(x_B,Q^2\right)\right], \tag{1.12}$$

where $\gamma = (2x_B M)/Q \to 0$ in the Bjorken limit ($v,\ Q^2 \to \infty$). The structure functions F_1 and F_2 were constrained by numerous experiments, covering a wide range in x_B and Q^2 for both proton and neutron targets. The results from different experiments on the proton structure function F_2^{p} as a function of Q^2 and varying values of x_B are shown on the left side of Fig. 1.2.

The polarised part of the DIS cross section is parametrised by the functions g_1 and g_2. For the longitudinally polarised lepton beam ($\leftarrow$) and the nucleon spin polarised longitudinally with respect to the beam axis ($\Rightarrow$), the cross section reads as follows [28]

$$\frac{\mathrm{d}^3\sigma^{\leftrightarrows}}{\mathrm{d}x_{Bj}\ \mathrm{d}y\ \mathrm{d}\phi} - \frac{\mathrm{d}^3\sigma^{\leftrightarrows}}{\mathrm{d}x_{Bj}\ \mathrm{d}y\ \mathrm{d}\phi} = \frac{4\alpha^2}{Q^2}\left[\left(2-y-\frac{y^2\gamma^2}{2}\right)g_1\left(x_{Bj},Q^2\right) - y\gamma^2 g_2\left(x_{Bj},Q^2\right)\right] \tag{1.13}$$

And for the nucleon target polarised transversely with respect to the beam direction, the cross section reads

$$\frac{\mathrm{d}^3\sigma^{\leftarrow\Uparrow}}{\mathrm{d}x_{Bj}\ \mathrm{d}y\ \mathrm{d}\phi} - \frac{\mathrm{d}^3\sigma^{\leftarrow\Downarrow}}{\mathrm{d}x_{Bj}\ \mathrm{d}y\ \mathrm{d}\phi} = \frac{4\alpha^2}{Q^2}\left[\gamma\sqrt{1-y-\frac{y^2\gamma^2}{4}}\left(\frac{y}{2}g_1\left(x,Q^2\right) + 2g_2\left(x,Q^2\right)\right)\right] \tag{1.14}$$

1.1.3 Parton Distribution Functions

The Parton Model was developed by Richard Feynman in 1960s [30] as an interpretation of the results from the SLAC experiment of electron-proton scattering at the energy of 20 GeV. While the results of elastic scattering cross section showed a strong Q^2 dependence of the F_2 structure function, in DIS the results exhibited only a very weak dependence. This was the first hint of existence of point-like particles present inside a proton, as the Fourier transformation of a constant function is a δ-function. The point-like partons were soon after identified with quarks (and anti-quarks) from the quark model [31, 32] and with gluons.

The scattering in the quark-parton model is assumed as being off point-like partons that appear free in the frame of high momentum proton. The cross section is then given as an incoherent sum of the individual cross sections of point-like quarks

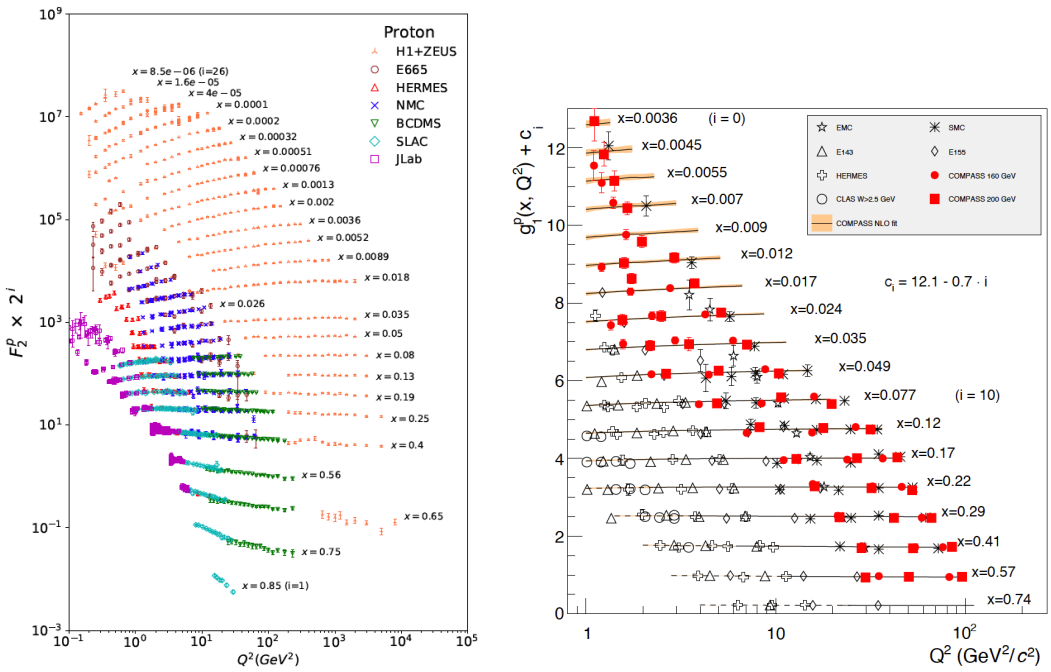

Fig. 1.2: Evolution of F_2 (left) and g_1 (right) as a function of x_B and Q^2. Figures are taken from [29].

$$
\begin{aligned}
F_1\left(x_B, Q^2\right) &= \frac{1}{2}\sum_f e_f^2\left(q_f\left(x_B\right) + \bar{q}_f\left(x_B\right)\right), \\
F_2\left(x_B, Q^2\right) &= x_B\sum_f e_f^2\left(q_f\left(x_B\right) + \bar{q}_f\left(x_B\right)\right),
\end{aligned}
\tag{1.15}
$$

where e_f is the electrical charge of quark f in units of elementary charge and the $q_f\left(x_B\right)$ are the number density PDFs for quark f. The second moment of the number densities in x_B variable for flavours $\mathrm{u}, \mathrm{d}, \mathrm{s}$, and c (and their respective anti-quarks) is shown in the top band of Fig. 1.3. From the 1.15 one can directly derive the Callan-Gross relation, valid for parton with spin 1/2 [33]:

$$
2x_B F_1^{DIS}(x_B) = F_2^{DIS}(x_B), \tag{1.16}
$$

For longitudinally polarised nucleon, the helicity distribution $\Delta q_f(x_B)$, represents the difference of the probabilities that the helicity $\rightarrow$ of the struck quark f with a longitudinal momentum fraction x_B is parallel or anti-parallel to the spin of the nucleon $\Rightarrow$

$$
\Delta q_f\left(x_B\right) = q_f^{\rightrightarrows}\left(x_B\right) - q_f^{\leftrightarrows}\left(x_B\right) \tag{1.17}
$$

The second moment of the helicity in x_B for flavours $\mathrm{u}, \mathrm{d}, \mathrm{s}$, and c (and their respective anti-quarks) is shown in the bottom band of Fig. 1.3. Thus, in the analogy to the Eq. 1.17, the number density distribution $q_f(x_B)$ in a longitudinally polarised nucleon reads

$$
q_f\left(x_B\right) = q_f^{\rightrightarrows}\left(x_B\right) + q_f^{\leftrightarrows}\left(x_B\right) \tag{1.18}
$$

And similarly to Eq. 1.15, the polarised structure function is given [33]

$$
g_1\left(x_B\right) = \frac{1}{2}\sum_f e_f^2\left(\Delta q_f\left(x_B\right) + \Delta\bar{q}_f\left(x_B\right)\right), \tag{1.19}
$$

In spin physics, a significant quantity of interest is the first moment of g_1 in x_B. In the leading order, it is expressed as [34]

$$
\int_0^1 g_1\left(x_B, Q^2\right) = \frac{1}{12}\left(a_3 + \frac{1}{3}a_8\right) + \frac{1}{9}a_0 \tag{1.20}
$$

where the quantity a_3 denotes the isovector charge, a_8 is the octet charge, and the flavour singlet charge is represented by a_0. In terms of flavour composition, these quantities read as follows

$$
\begin{aligned}
a_3 &= \Delta u - \Delta d + \Delta \bar{u} - \Delta \bar{d}, \\
a_8 &= \Delta u + \Delta d - 2\Delta s + \Delta \bar{u} + \Delta \bar{d} - 2\Delta \bar{s}, \\
a_0 &= \Delta\Sigma = \sum_f \Delta q_f + \Delta \bar{q}_f,
\end{aligned}
\tag{1.21}
$$

where the following notation is used

$$
\Delta q_f = \int_0^1 \Delta q_f \left(x_B\right) dx_B \tag{1.22}
$$

The isovector charge a_3 equals to the weak coupling constant $|\frac{g_A}{g_V}|$. The octet a_8 is known from hyperon decay and assumptions of $\mathrm{SU}(3)_f$ symmetry [34]. The quantity a_0 denotes the total contribution of quarks and anti-quarks to the spin of the nucleon. For higher orders in QCD-modified quark-parton model, the $\Delta\Sigma$ becomes Q^2-dependent and the Eq. 1.20 is modified by corrections in a higher order of the coupling constant α_s. In the $\overline{MS}$ renormalisation scheme the singlet axial charge $a_0\left(Q^2\right)$ remains identical to the $\Delta\Sigma$ [35], while in the off-shell scheme the gluon polarisation can also contribute to the a_0 [36]

$$
a_0\left(Q^2\right) = \Delta\Sigma_{\mathrm{off}} - 3\frac{\alpha_s\left(Q^2\right)}{2\pi}\Delta g\left(Q^2\right) \tag{1.23}
$$

The EMC experiment was the first to measure the g_1 of proton in 1988 [2]. Using Eqs. 1.20, 1.21 together with the known values of a_3 and a_8, they constrained the a_0 to be compatible with zero, pointing it to a sizeable negative contribution of strange quarks $\Delta s + \Delta \bar{s}$. That finding lead to the conclusion that in fact only a small part of the proton spin originates from the quark contribution. While later experimental efforts brought a slightly larger value of a_0 at the order of 0.3 [38], the principal conclusion of the pioneering EMC measurement remains unchanged.

The findings of EMC experiment set off the proton spin crisis. The naive model of nucleon spin consisting from the contributions of valence quarks, introduced by Ellis and Jaffe [1] had to be revised. Jaffe-Manohar sum rule describes the decomposition of the nucleon spin as [39]

$$
\frac{1}{2} = \frac{1}{2}\Delta\Sigma + \Delta G + L_q + L_g, \tag{1.24}
$$

where the quantity ΔG denotes the total contribution of gluon spins to the nucleon spin, and J_q and J_g are the total angular momenta of quarks and gluons,

respectively. It has been shown by various experiments that neither the combination of $\Delta\Sigma + \Delta G$ would be sufficient to complete the nucleon spin. The RHIC experiment measured the $\Delta G = 0.2^{+0.06}_{-0.07}$ [3], pointing then to a non-zero proton spin component created by the angular orbital momenta of partons.

The third distribution $\Delta_{\mathrm{T}} q_f\left(x_B\right)$, transversity distribution, is defined for transversely polarised parton and nucleon and represents the difference of the number density of quarks with spin parallel to the spin of the nucleon from the number density of quarks with spin anti-parallel

$$\Delta_{\mathrm{T}} q_f = q_f^{\uparrow\Uparrow}\left(x_B\right) - q_f^{\downarrow\Uparrow}\left(x_B\right). \tag{1.25}$$

Transversity distribution is a leading-twist quantity, such as helicity and number density PDF, thus it might be expected to be of the same order as the helicity. However, within the framework of QCD-improved quark-parton model, it is suppressed in low x_B range in the Q^2 evolution with respect to helicity. The transversity is connected with the helicity and the number density by the Soffer's inequality [28]

$$\left|\Delta_{\mathrm{T}} q_f\left(x_B\right)\right| \leq \frac{1}{2}\left|q_f\left(x_B\right) + \Delta q_f\left(x_B\right)\right|. \tag{1.26}$$

The transversity distribution was introduced by Ralston and Soper in 1979 [40], however, it attracted more interest of theorists in 1990s, leading to the emergence of initial proposals for its measurement. Nonetheless, very little data remains available to date (e.g. [41]). The main reason is that the transversity is a chiral-odd quantity (the active quark undergoes a spin-flip in the measured process), which makes it inaccessible in fully inclusive DIS due to the conservation of helicity (i.e. chirality) in QCD. To access transversity, two main processes are commonly used: the *Semi-Inclusive DIS* (SIDIS), with one hadron in initial and one in final state, and the Drell-Yan process, with two hadrons in the initial state. Recent measurements were conducted at COMPASS experiment, JLab or RHIC. The extraction of the $x_B \Delta_{\mathrm{T}} q_f$ for $f = u_v, d_v$ is shown in Fig. 1.4.

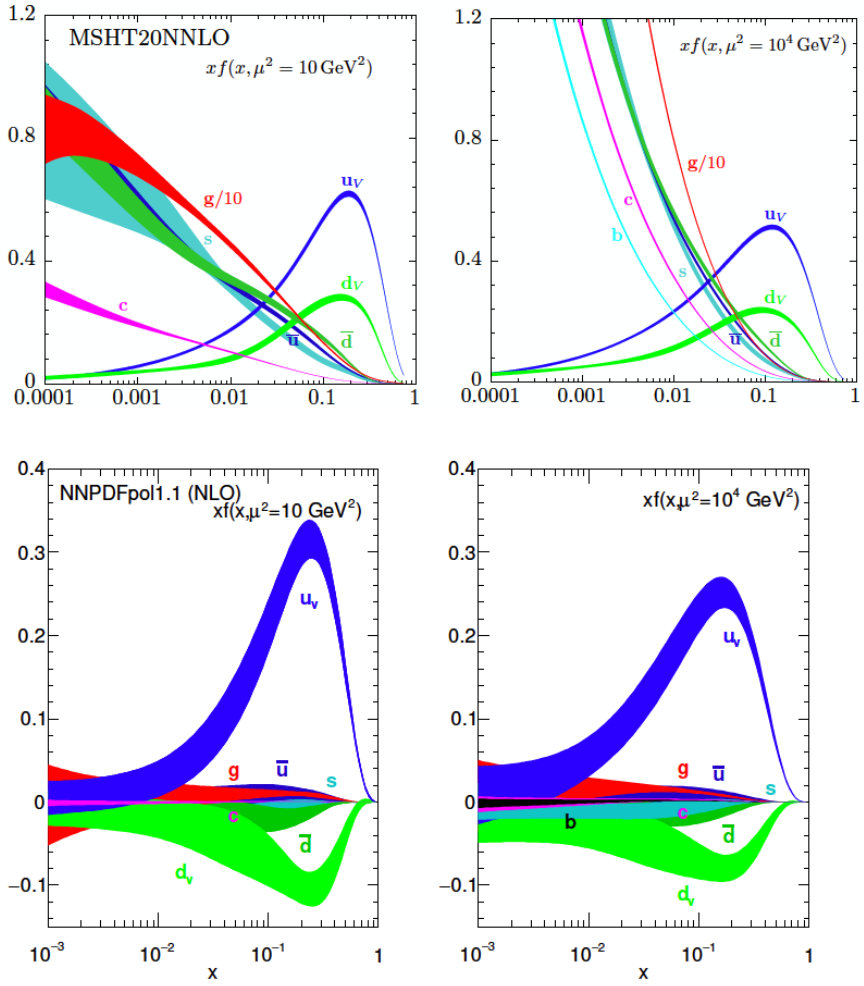

Fig. 1.3: The bands represent x times the unpolarised parton distributions $f(x)$ (where $f = u_v, d_v, \bar{u}, \bar{d}, s \simeq \bar{s}, c = \bar{c}, b = \bar{b}, g$) obtained from the global NNLO MSHT20 analysis (top) at scales $\mu^2 = 10$ GeV^2 (left) and $\mu^2 = 10^4$ GeV^2 (right) with $\alpha_s(M_Z^2) = 0.118$. The polarised PDFs are obtained from NLO NNPDFpol1.1 (bottom). Figures are taken from [29].

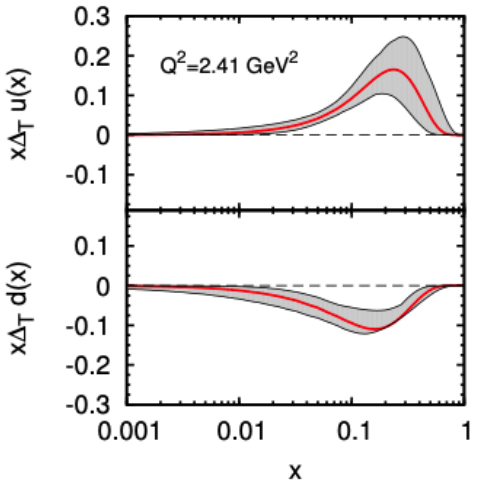

Fig. 1.4: The transversity distribution function $x_B \Delta_T q_f(x_B)$ for $f = u, d$ extraction in red lines, with uncertainty bands in shaded areas [41] from the combined SIDIS and e^+e^- data from COMPASS, HERMES, and Belle at $Q^2 = 2.41$ GeV^2.

1.2 Generalised Approaches

Parton distribution functions and form factors, introduced in the previous section, provided a wealth of information on the one-dimensional image of hadrons in terms of longitudinal momentum and polarisation carried by the quarks, anti-quarks and gluons, and their spatial distribution, respectively. However, in order to have a more comprehensive understanding of hadron structure, a combination of both approaches is necessary. Separately, PDFs and form factors fail to capture the hadron structure in the full complexity. One example is the impact of total angular momenta of partons and their contribution to the total spin of a hadron. Resolving the spin puzzle mentioned in the previous section requires a solution that encompasses these aspects. In recent years, it has been demonstrated that the approach of GPDs may provide the right answer [14].

Due to the uncertainty principle, it's impossible to simultaneously determine the spatial position and momentum along the same direction. Nonetheless, there is a method to describe both information encompassed in one distribution. The most general description is represented by the parton correlation function. It will be demonstrated that specific projections can link various other distributions, offering

different perspectives on the study of hadron properties. We will examine different types of parton distributions and their interrelationships, starting from the most general and descending back to PDFs and form factors.

1.2.1 Parton Correlation Function

Although all parton distributions discussed below are defined in a covariant way, it is convenient to use an infinite momentum frame in the positive z direction. In this frame, the light-cone coordinates are commonly used to represent a given four-vector v as

$$v^{\pm} = \frac{1}{\sqrt{2}}\left(v^0 \pm v^3\right) \quad \boldsymbol{v} = \left(v^1, v^2\right), \tag{1.27}$$

for a longitudinal part of the vector $v^{\pm}$, and the transverse component $\boldsymbol{v}$.

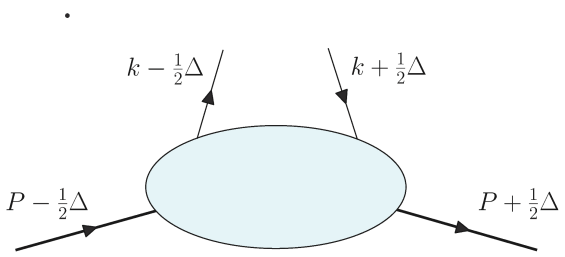

Fig. 1.5: A scheme of a general quark field operator in a form of a handbag diagram, with proton momenta assigned to the bold lines and active quark momenta to the upwards and downwards pointing lines. The blue blob marks the inner structure of the proton.

A two-parton correlation function for quarks in momentum space is defined as the matrix element of a bi-linear quark field operator between proton states

$$\begin{aligned} H(k, P, \Delta) &= (2\pi)^{-4} \int \mathrm{d}^4 z e^{izk} \\ &\times \left\langle p\left(P + \frac{1}{2}\Delta\right)\right| \bar{q}\left(-\frac{1}{2}z\right) \mathcal{L}\Gamma q\left(\frac{1}{2}z\right) \left|p\left(P - \frac{1}{2}\Delta\right)\right\rangle . \end{aligned} \tag{1.28}$$

where $\langle p|$ is the proton state with momentum $P = (p - p')/2$, $\Delta = p - p'$ is the momentum transfer to the proton, q ($\bar{q}$) represents the active quark (anti-quark) with momentum k and position z, and Γ denotes a Dirac matrix with a particular spin state and $\mathcal{L}$ marks a Wilson line to preserve the gauge-invariance

of the operator. The schematics of the bilinear quark field operator in a form of a handbag diagram is shown in Fig. 1.5.

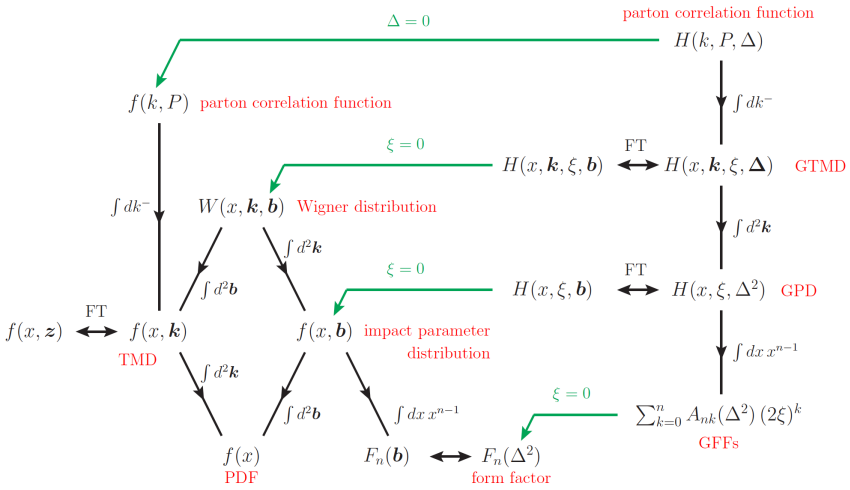

Fig. 1.6: Diagram illustrates relations between different projections of the general quark correlation function $H\,(k, P, \Delta)$. The double arrows marked with "FT" denote the Fourier transformation between $\boldsymbol{\Delta}$ and $\boldsymbol{b}$ or between $\boldsymbol{k}$ and $\boldsymbol{z}$. Fractions of plus-momentum, commonly called longitudinal momentum fraction, are defined as $x = k^+/P^+$ and $2\xi = -\Delta^+/P^+$. The invariant momentum transfer can be expressed in terms of longitudinal and transverse variables as $\Delta^2 = -\left(a\xi^2 m^2 + \boldsymbol{\Delta}^2\right)/\left(1-\xi^2\right)$. Figure taken from Ref. [15].

The parton correlation function is not an physical pbservable by itself. As illustrated in Fig. 1.6, one can perform three different operations, which reduce the general parton correlation function defined in Eq. 1.28 into measurable observables. The first represents the forward limit of $\Delta = 0$, where is no momentum transfer to the hadron. Such reduction of the function $H\,(k, P, \Delta)$ appears in the inclusive processes evaluated via the optical theorem, such as PDFs or transverse momentum dependent PDFs (TMD) (as can be seen in Fig. 1.6), where a probabilistic interpretation is possible. It is a convention to choose a frame where $\boldsymbol{P} = 0$. Conversely, in the case of non-forward kinematics $\Delta \neq 0$ the function appears in the amplitude of the exclusive processes with target proton momentum $P - \Delta/2$ and final state proton momentum $P + \Delta/2$.

The second operation is the integration of the general correlation function over $\boldsymbol{k}$, k^-, or k^+. It typically leads to physical observables. After integrating over k^- the quark and anti-quark fields are evaluated in a positive momentum direction at $z^+ = 0$. This allows for a convenient interpretation where the partons are regarded as quasi-free just before the interaction with the physical probe [15]. The matrix element in Fig. 1.5 with parton states of positive momenta $k^+ + \Delta^+/2$ and $k^+ - \Delta^+/2$ is described as an emission and reabsorption of a quark, anti-quark, or (for $\Delta^+ \neq 0$ only) emission or absorption of a quark-antiquark pair (see Fig. 1.11). Another feature of the integration over k^- is that the partons in this framework have no longer a definite virtuality, i.e. they are not on their mass shell. It is in fact convenient for studying the proton structure as on-shell partons are at odds with the phenomenon of confinement, i.e. unphysical. Distributions originating after integration over $\boldsymbol{k}$ are called "collinear", as they become insensitive to the transverse momentum of partons. It is the case for PDFs or GPDs. When one also integrates over the k^+, the resulting distributions become fully independent from the parton momentum and the product of fields in the matrix element 1.28 becomes a local current. The matrix element is then described by one or several form factors, dependent on the invariant momentum transfer $\Delta^2 = t$.

The third operation is given by Fourier transformation of the transverse component. The transverse momentum transfer $\boldsymbol{\Delta}$ can be transformed to the average transverse spatial position of partons $\boldsymbol{b} = \sum_i k_i^+ \boldsymbol{b}_i / \sum_i k_i^+$, which represents the radial distance from the centre of plus-momentum of the spectator partons. Similarly, the average transverse momentum $\boldsymbol{k}$ is the Fourier conjugate of $\boldsymbol{z}$, the position difference, where "average" and "difference" refer to the initial and final state 1.5.

1.2.2 Wigner Distributions

The most general and comprehensive physical observable describing the partonic structure of hadrons are the *Generalised Transverse Momentum Dependent parton distributions* (GTMD), introduced by Lorcé and Pasquini [42]. GTMD is a 5-dimensional object (2 position and 3 momentum coordinates) defined in the infinite plus-momentum frame of the hadron, illustrated in Fig. 1.7.

It is convenient to redefine the parameters of the GTMD distribution as

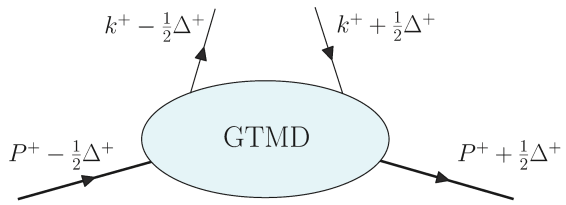

Fig. 1.7: A handbag diagram of a generalised transverse momentum dependent parton distribution, with proton plus-momenta assigned to the bold lines and active quark plus-momenta to the upwards and downwards pointing lines. The blue blob denotes the GTMD distribution.

$$x = \frac{k^+}{P^+}, \quad \xi = -\frac{\Delta^+}{2p^+} = x_B \frac{1 + \frac{\Delta^2}{2Q^2}}{2 - x_B + x_B \frac{\Delta^2}{Q^2}} \approx \frac{x_B}{2 - x_B}, \tag{1.29}$$

where ξ is the skewness parameter, corresponding to the longitudinal momentum transfer to the active quark. It is related to the Bjorken variable x_B for large Q^2. Also, an on-shell condition applies to the hadron requiring $P\Delta = 0$ and $4P^2 + \Delta^2 = 4M^2$, where M denotes the hadron mass. These conditions allow to define GTMDs as a function of $(x, \boldsymbol{k}, \xi, \boldsymbol{\Delta})$, or $(x, \boldsymbol{k}, \xi, \boldsymbol{b})$ via Fourier transformation. GTMDs have been studied in theoretical context and it is unclear, whether they can be accessed in any physical process. There are 16 independent complex GTMD distributions that encode partonic structure of hadrons correlating transverse spatial positions, and both longitudinal and transverse momenta of partons. They relate to two sets of 8 real-valued distributions that decouple the transverse spatial position of partons $\boldsymbol{b}$ (or $\boldsymbol{\Delta}$ in Fourier transformation) from the transverse parton momentum $\boldsymbol{k}$.

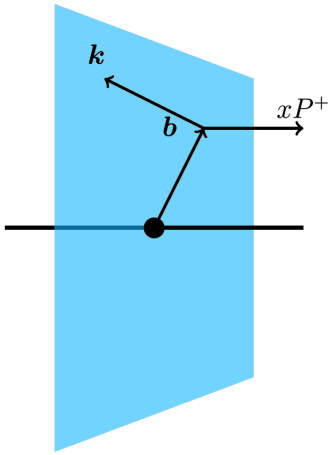

Fig. 1.8: An illustration of a transverse plane representation of a Wigner distribution variables, the transverse spatial position $\boldsymbol{b}$, the transverse momentum $\boldsymbol{k}$, and the longitudinal momentum xP^+.

GTMDs have a direct connection to the Wigner distributions (in the limit of

$\xi \to 0$) of the parton-hadron system, which represent a quantum-mechanical analogue of classical phase-space distributions [43]. The Wigner distribution $W(p,q)$, describing the dependency on the transverse position, the transverse and the longitudinal momentum of a parton as illustrated in Fig. 1.8, distribution is defined as

$$W(q,p) = \int_{-\infty}^{+\infty} \mathrm{d}z e^{ipz} \psi^*(q-z)\psi(q+z) \tag{1.30}$$

where p denotes the generalised momentum, q stands for the generalised position, and $\psi(q)$ is the wave function in the position space. Wigner distribution in the quantum-mechanical case does not have a probabilistic interpretation as it is off-diagonal, i.e. encompasses information on the interference, and is therefore not positive-definite on the quantum scale [42], while in the classical case it becomes positive-definite and reduces to the phase-space probability density. Nevertheless, it is still possible to calculate the expectation value of an operator $\mathcal{O}(q,p)$ formulated by the following convolution with the Wigner distribution

$$\langle \mathcal{O} \rangle = \int \mathrm{d}^3q \; \mathrm{d}^3p \; \mathcal{O} \; W(q,p) \tag{1.31}$$

Moreover, after an integration over one of the variable one can obtain a probability density of the other variable

$$\int \mathrm{d}^3p \; W(q,p) = \rho(q) \quad , \quad \int \mathrm{d}^3q \; W(q,p) = \rho(p), \tag{1.32}$$

which comes from the property of Wigner distribution of being equivalently defined in the momentum space as in the position space through the Fourier transformation.

The formalism can be extended within the relativistic framework using quantum field theory. For the following gauge invariant quark field $\Psi(x)$

$$\Psi(x) = \exp\left(-ig\int_0^\infty \mathrm{d}\lambda n \cdot A(\lambda n + x)\right)\psi(x), \tag{1.33}$$

where n is a constant four-vector, g is the coupling constant, and $\psi(x)$ is a free quark field, the Wigner operator for a quark field of flavour f is defined

$$\mathcal{W}_\Gamma^f(q,p) = \int \mathrm{d}^4z e^{ipz} \, \bar{\Psi}^f(q-z)\Gamma\mathcal{L}\,\Psi^f(q+z), \tag{1.34}$$

where q is the space-time position of the quark and p denotes its momentum, Γ and $\mathcal{L}$ were defined in Eq. 1.28. The Wigner distribution of quarks within a hadron

(from here on only a proton is considered) is obtained from the Wigner operator as follows

$$\mathcal{W}_{\Gamma}^{f}(q,p) = \int \frac{\mathrm{d}^4\Delta}{(2\pi)^4} . \langle P'|\mathcal{W}_{\Gamma}^{f}(q,z)|P\rangle \tag{1.35}$$

The Wigner distribution can be understood as an autocorrelation function of the wave function $\Psi(x)$ and contain a full correlations between the quark transverse spatial position and three-momentum. Wigner distributions have been intensively studied by theorists in the past decade due to their property that it is possible to calculate the expectation value of any single-particle physical observable from its phase-space average with the Wigner distribution as a weighting factor [43]. Among such observables is the quark orbital angular momentum L_q, which makes the Wigner distributions particularly attractive. The L_q can be calculated from the Wigner distribution of unpolarised quarks within a longitudinally polarised proton.

1.2.3 Generalised Parton Distributions

The concept of GPDs was introduced by Müller et al. [45], Ji [46], and Radyushkin [47] in 1990s. As illustrated in Fig. 1.6 and elaborated in the previous ⟦↩1.2.1.⟧, GPDs represent three-dimensional projections of GTMDs. Particularly, there give access to the longitudinal momentum of a parton and its transverse spatial position. It implicates that after integration they can be reduced either to form factors or PDFs (indicated in the Fig. 1.6). They depend on the parton longitudinal momentum fraction x and longitudinal momentum transfer ξ as defined in Eq. 1.29, and the Mandelstahm invariant $t = (p - p') = \Delta^2$, the momentum transfer to the proton. While t is directly experimentally accessible, the longitudinal momentum fraction x appears convoluted with the function representing the hard scattering amplitude [15]. A weak Q^2 dependence appears through the evolution equations, either DGLAP or ERBL, depending on the kinematic domain described by the relation of x and ξ, more details will be given in the following.

The physics sensitive to GPDs is encompassed within exclusive processes, in which invariant momentum transfer t is much smaller than the hard scale, often given by the photon virtuality Q^2. The most common processes used to access GPD parametrisation are DVCS, $\gamma^*\mathrm{p} \to \gamma\mathrm{p}$ and the HEMP, $\gamma^*\mathrm{p} \to \mathrm{Mp}$. Using

the concept of QCD factorisation, the inner structure of the probed proton can be separated from the hard scattering kernel describing the probe.

1.2.3.1 Factorisation

The factorisation is the key component of studying the proton structure as it enables to disentangle the information on the physical probe, i.e. the hard scattering amplitude of the probe off an active parton, from the soft part, which describes the spectator partons distribution within the proton. The hard part is calculable within perturbative QCD, while the soft part is nonperturbative and is described by means of parton distributions. The separation of the perturbative and nonperturbative part happens at the level of scattering amplitudes. The factorisation formula is defined as the following convolution [15]

$$\mathcal{A}\left(\xi, \Delta^2, Q^2\right) = \sum_f \int_{-1}^{1} \mathrm{d}x C_f(x, \xi; \log(Q/\mu)) A_f\left(x, \xi, \Delta^2; \mu\right), \tag{1.36}$$

where C_f represents the hard scattering part, A_f denotes the soft part of the helicity amplitude, which contains the GPDs, and μ corresponds to the factorisation scale. The sum runs over all parton flavours f. An example graph of an exclusive process and its schematic factorisation is shown in Fig. 1.15. Separation is performed in form of a cut-off in terms of the factorisation scale μ. The hard scattering kernel is characterised by a condition $\boldsymbol{k} > \mu$, and the soft part is described by momenta $\boldsymbol{k} < \mu$. At the leading order in α_S the hard-scattering kernels for exclusive processes are a linear combination of $1/\left(\xi - x - i\epsilon\right)$ and $1/\left(\xi + x - i\epsilon\right)$ terms. It leads to a non-trivial convolution for $\mathrm{Re}\mathcal{A}$, while the $\mathrm{Im}\mathcal{A}$ involves $A\left(x, \xi, \Delta^2\right)$ at the points of poles, where $x = \pm\xi$ [15]. In higher order of α_S logarithms of Q/μ appear in the hard-scattering kernel C_f. The dependence on the factorisation scale μ cancels between C_f and A_f up to the chosen order in α_S, such as in case of PDFs. The separate dependence of GPDs on x and ξ cannot be directly determined from the scattering amplitude. It can only be extracted from the evolution of A_f, combined with the dependence of C_f on Q/μ, through the relation of x and ξ, see Fig. 1.10 for illustration. More details on the relation of x and ξ in the next ⟦↪1.2.3.2.⟧.

Both hard and the soft parts are expanded by means of operator product expansion to distinguish dominant and sub-dominant contributions. The amplitude

of a process is then expanded in a series of non-singular local operators (for more details, see [48]). While the hard scattering amplitude is perturbatively expanded in orders of α_S, the soft part is decomposed in orders of a so-called "twist". Twist refers to a classification scheme for operators based on their scaling behaviour with respect to Q^2. Simply put, the twist of an operator determines how fast it decreases with increasing momentum transfer to the hadron system. A leading twist (twist-2) corresponds to the dominant term with a high momentum transfer, while higher twists represent more complicated operators of $\mathcal{O}\left(1/Q^2\right)^n$, with n as the increasing order. Mathematically, the twist is defined as the dimension of the local operator minus spin (the spin being the dimension of their representation in the Lorentz group). The diagram of the HEMP process in Fig. 1.15 shows the leading twist term.

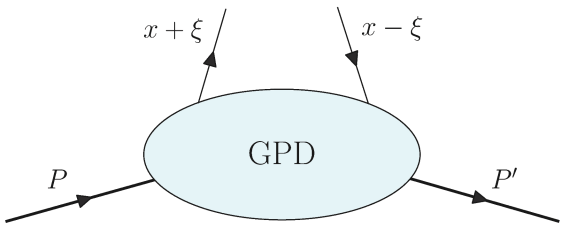

Fig. 1.9: A schematic diagram illustrating the kinematics of an exclusive process described by the GPDs in the handbag model.

The most important consequence of the factorisation of a scattering amplitude is the universality of the parton distributions, i.e. independence on the experimental process. It implies that it is possible to measure a certain quantity through one experimental channel and utilise its knowledge to parameterise a another one, not yet known or not easily accessible, by a different channel. The factorisation theorem is proven in case of DVCS for both longitudinally and transverse polarisation of the virtual photon. However, same does not apply for HEMP, where the factorisation is proven only for the longitudinal part of the cross section [51][52]. In the case of the transversely polarised γ^*, the collinear factorisation leads to infrared singularities [53]. Currently there is no QCD framework available to deal with the infrared sensitive contributions, which means that the theoretical predictions for the transverse part of the HEMP cross section can only be parameterised from phenomenological approaches. This makes the predictions model dependent.

One of the models was proposed by Goloskokov and Kroll GK [54] (see Subsection 1.3.1), where the regularisation of the infrared singularities was performed by means of using the parton transverse momenta $\boldsymbol{k}$ and the so-called Sudakov term.

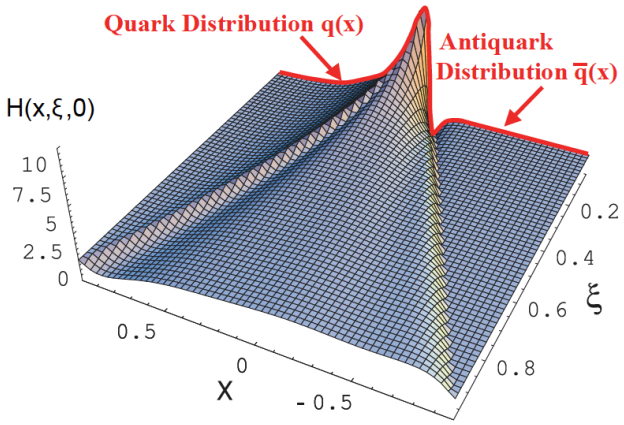

Fig. 1.10: The model calculation of the scale evolution of the GPD $H^u\,(x,\xi,t=0)$ [49]. The red line at $\xi=0$ corresponds to the unpolarised number density PDF q^u for $x>0$ and $\bar{q}^u$ for $x<0$. Figure taken from Ref. [50].

1.2.3.2 Definition and properties of GPDs

The GPD diagram 1.9 describes the soft part of the scattering amplitude, where the active quark of longitudinal momentum fraction $x+\xi$ is selected from the proton of momentum p, and after the interaction with the virtual photon, described by the hard scattering kernel, it is reabsorbed with a different momentum fraction $x-\xi$ into a different transverse position within the proton with altered momentum p'. Within the light-cone gauge the Wilson line reduces to unity and the parton correlator 1.28 can be rewritten to the GPD form factor $A\,(x,\xi,t)$ from the Eq. 1.36 as

$$A^f_\Gamma(x,\xi,t=-\Delta^2)=\frac{1}{2}\int\frac{\mathrm{d}z^-}{2\pi}e^{ixP^+z^-}\langle p',\Lambda'|\bar{\psi}i\left(-\frac{z}{2}\right)\Gamma\psi\left(\frac{z}{2}\right)|p,\Lambda\rangle|_{z^+=\boldsymbol{z}=0} \quad (1.37)$$

Different helicity contributions from Γ lead to eight GPDs at twist-2, four parton helicity-conserving (chiral even) GPDs, H^f, $\tilde{H}^f$, E^f, and $\tilde{E}^f$, and four corresponding parton helicity-flip (chiral-odd or "transversity") GPDs: H^f_T, $\tilde{H}^f_T$,

E_T^f, and $\tilde{E}_T^f$. The Figs. 1.12, 1.13 illustrate the definition of all the chiral even and chiral odd GPDs in terms of parton and proton helicities. The chiral even GPDs correlate the unpolarised or longitudinally polarised parton with the transverse momentum transfer t to the nucleon. H and E is sometimes referred to as "unpolarised" (with respect to the spin of the partons, not the target proton), and $\tilde{H}$ and $\tilde{E}$ as "polarised" GPDs, as the first group involves the sum over the parton helicities, and the latter involves a difference between the helicities. The chiral odd GPDs on the other hand correlate the transversely polarised partons with t. The DVCS process does not allow the parton helicity flip, and hence is only sensitive to chiral even GPDs. Conversely, the HEMP process does allow the helicity flip, which gives access to transversity GPDs.

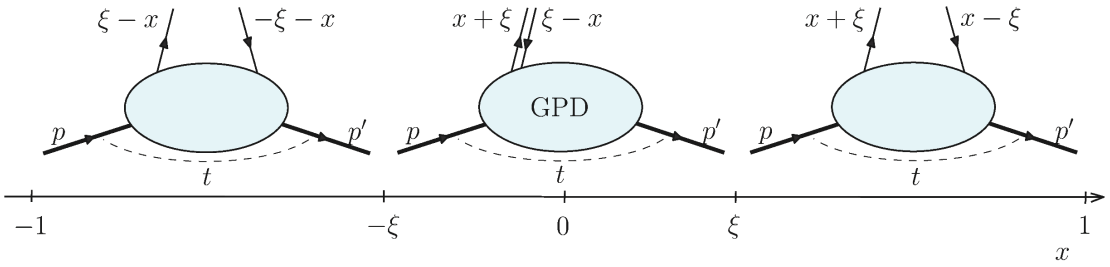

Fig. 1.11: Three different regions of $x \pm \xi$ momentum of a parton.

The variable x and ξ both acquire values in the interval $[-1, 1]$, where positive x describes the distribution of quarks and the negative x corresponds to antiquarks. By comparing the relation between x and ξ, one gets three different domains describing different processes, as is illustrated in Fig. 1.11

- $-1 \leq x \leq \xi \leq 0$: Both momentum fractions $x - \xi$ and $x + \xi$ are negative. In this case GPDs describe the emission and re-absorption of an anti-quark. In this region, the evolution acts in a similar way as the DGLAP evolution of PDFs (the acronym stands for Dokshitzer, Gribov, Lipatov, Altarelli, Parisi). For more details on the GPD evolution, see e.g. [14, 18].

- $x \in [-\xi, \xi]$: This domain corresponds to a situation, where a $q\bar{q}$ pair is emitted from the proton. In this region, the GPDs evolve under a different set of equations, named ERBL (Efremov-Radyushkin-Brodsky-Lepage) for meson production, and the domain is called accordingly, the ERBL domain.

This region is of particular interest, as it does not have an equivalent in PDF evolution and it allows to study the mesonic structure of a proton.

- $0 \leq \xi \leq x \leq 1$: Both momentum fractions $x + \xi$ and $x - \xi$ are positive, which corresponds to emission and reabsorbing of a quark. Such as the first domain, this region is also governed by the DGLAP evolution equations.

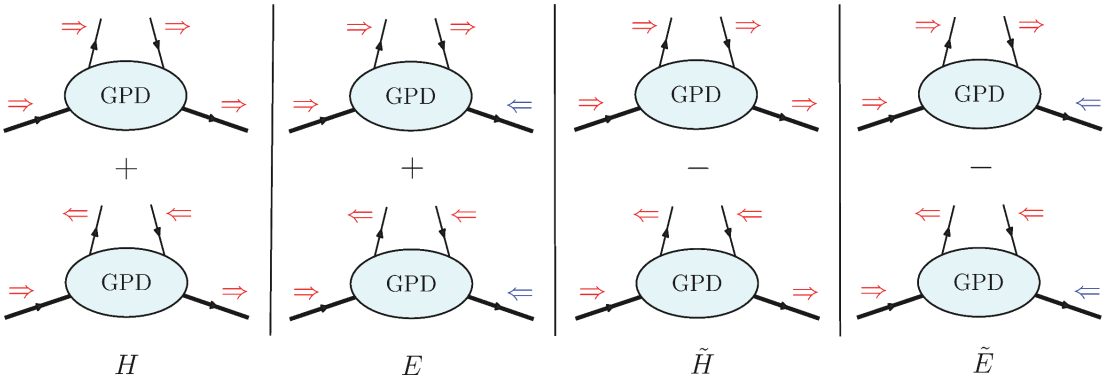

Fig. 1.12: Schematic description of chiral even GPDs with respect to the helicity states of the target and the parton. The arrows indicate the helicity states, and red arrows mark conserved helicity, while the blue ones indicate the helicity flip. The chiral even GPDs H and E describe an unpolarised parton, while $\tilde{H}$ and $\tilde{E}$ a longitudinally polarised one.

Helicity representation and symmetry properties

To investigate the spin structure of the GPDs it is convenient to represent them in a form of helicity amplitudes. The Eq. 1.37 can be rewritten in terms of the helicities of the proton and the partons as [16]

$$\begin{aligned} A^q_{\Lambda'\lambda',\Lambda\lambda} &= \int \frac{\mathrm{d}z^-}{2\pi} e^{ixP^+z^-} \left\langle p', \Lambda' \right| \mathcal{O}^q_{\lambda'\lambda}(z) \left| p, \Lambda \right\rangle \Big|_{z^+=z_\perp=0}, \\ A^g_{\Lambda'\lambda',\Lambda\lambda} &= \frac{1}{P^+} \int \frac{\mathrm{d}z^-}{2\pi} e^{ixP^+z^-} \left\langle p', \Lambda' \right| \mathcal{O}^g_{\lambda'\lambda}(z) \left| p, \Lambda \right\rangle \Big|_{z^+=z_\perp=0}. \end{aligned} \tag{1.38}$$

where the operator $\mathcal{O}^f_{\lambda'\lambda}$ represents the abbreviation of the quark (gluon) fields and the corresponding Dirac matrix for a particular helicity state (for precise definition,

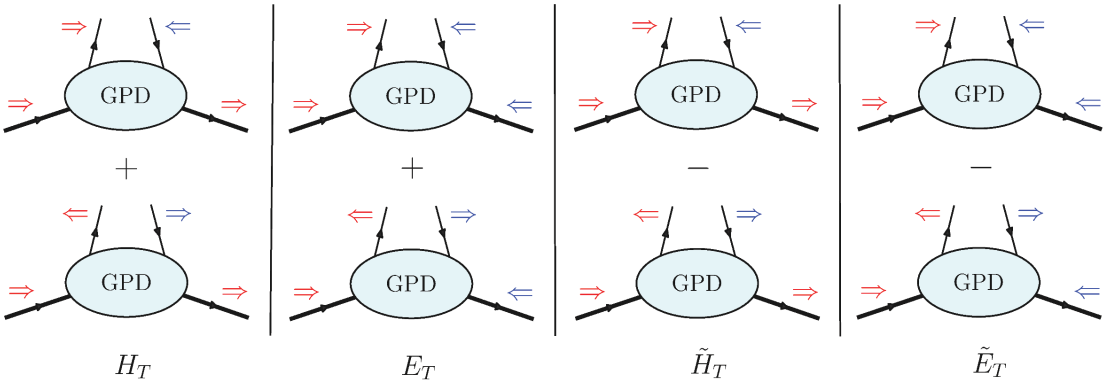

Fig. 1.13: Schematic description of chiral odd GPDs with respect to the helicity states of the target and the parton. The arrows indicate the helicity states, and red arrows mark conserved helicity, while the blue ones indicate the helicity flip. Note that in contrast to the chiral even GPDs, there is a helicity flip of the parton present as well. The chiral odd GPDs concern only transversely polarised parton, while polarisation states of the proton can differ.

see [16]). Λ (Λ') denote the helicity state of the target (recoiled) proton, and λ (λ') the helicity of the emitted (reabsorbed) parton. Explicitly, the amplitudes for the chiral even GPDs can be expressed as a linear combination of GPDs

$$\begin{aligned}
A^f_{++,++} &= \sqrt{1-\xi^2}\left(\frac{H^f+\tilde{H}^f}{2} - \frac{\xi^2}{1-\xi^2}\frac{E^f+\tilde{E}^f}{2}\right)\\
A^f_{-+,-+} &= \sqrt{1-\xi^2}\left(\frac{H^f-\tilde{H}^f}{2} - \frac{\xi^2}{1-\xi^2}\frac{E^f-\tilde{E}^f}{2}\right)\\
A^f_{++,-+} &= -\epsilon\frac{\sqrt{t_0-t}}{2M}\frac{E^f-\xi\tilde{E}^f}{2}\\
A^f_{-+,++} &= \epsilon\frac{\sqrt{t_0-t}}{2M}\frac{E^f+\xi\tilde{E}^f}{2},
\end{aligned} \tag{1.39}$$

where the helicities $+\frac{1}{2}$ and $-\frac{1}{2}$ are abbreviated by $+$ and $-$ signs. The quantity $-t_0 = \frac{4\xi^2M^2}{1-\xi^2}$ represents the minimal value of the momentum transfer to the proton, and $\epsilon = \mathrm{sgn}\,(D^1)$, where D^1 is the x-component of $D^\alpha = P^+\Delta^\alpha - \Delta^+P^\alpha$. The Eqs. 1.39 read exactly the same for $f = q, g$.

The amplitudes for chiral odd GPDs for quarks are formulated as follows

$$\begin{aligned}
A^q_{++,+-} &= \epsilon\frac{\sqrt{t_0-t}}{2M}\left(\tilde{H}^q_{\mathrm{T}} + (1-\xi)\frac{E^q_{\mathrm{T}}+\tilde{E}^q_{\mathrm{T}}}{2}\right),\\
A^q_{-+,--} &= \epsilon\frac{\sqrt{t_0-t}}{2M}\left(\tilde{H}^q_{\mathrm{T}} + (1+\xi)\frac{E^q_{\mathrm{T}}-\tilde{E}^q_{\mathrm{T}}}{2}\right),\\
A^q_{++,--} &= \sqrt{1-\xi^2}\left(H^q_{\mathrm{T}} + \frac{t_0-t}{4M^2}\tilde{H}^q_{\mathrm{T}} - \frac{\xi^2}{1-\xi^2}E^q_{\mathrm{T}} + \frac{\xi^2}{1-\xi^2}\tilde{E}^q_{\mathrm{T}}\right),\\
A^q_{-+,+-} &= -\sqrt{1-\xi^2}\,\frac{t_0-t}{4M^2}\tilde{H}^q_{\mathrm{T}}.
\end{aligned} \tag{1.40}$$

For gluons, the Eqs. 1.40 receive a multiplying factor $\epsilon\sqrt{1-\xi^2}\sqrt{t_0-t}/2M$. The inversion of the Eqs. 1.39 and 1.40 allows to extract the particular GPDs. The essential asset of GPDs, giving the possibility to access the orbital angular momenta of partons, is that the mismatch between the initial and final state helicity has to be compensated by the orbital angular momentum to ensure its conservation, in cases when $t > t_0$. In the collinear limit $t = t_0$, the matrix elements where the helicity is not conserved vanish as

$$\left(\frac{\sqrt{t_0-t}}{2M}\right)^{|\Lambda'-\lambda'-\Lambda+\lambda|}$$

The helicity amplitudes satisfy the following relation

$$A_{-\Lambda'-\lambda',-\Lambda-\lambda} = (-1)^{\Lambda'-\lambda'-\Lambda+\lambda}\left(A_{\Lambda'\lambda',\Lambda\lambda}\right)^*, \tag{1.41}$$

as a consequence of parity invariance.

GPDs themselves satisfy also the time reversal invariance. For $F \in \{H, E, \tilde{H}, \tilde{E}, H_{\mathrm{T}}, E_{\mathrm{T}}, \tilde{H}_{\mathrm{T}}\}$ the following relation holds

$$F^f(x,\xi,t) = F^f(x,-\xi,t), \tag{1.42}$$

and for $\tilde{E}^f_{\mathrm{T}}$ the following applies

$$\tilde{E}^f_{\mathrm{T}}(x,\xi,t) = -\tilde{E}^f_{\mathrm{T}}(x,-\xi,t). \tag{1.43}$$

This implies, that all GPDs except the $\tilde{E}_{\mathrm{T}}$ are even in ξ. The time reversal change of sign in ξ reflects the fact that under the time reversal, the initial and final states are interchanged. The same behaviour applies in the case of complex conjugates of F and $\tilde{E}_{\mathrm{T}}$. Taking both of these constrains leads to the requirement of all 8 GPDs to be real valued [16].

Forward limit

In the forward limit the momentum transfer vanishes $\xi = t = 0$ and $x \to x_B$. The forward limit in general case was already discussed in ⟦↩1.2.1.⟧. In case of GPDs, some of them reduce in the forward limit to PDFs

$$\begin{aligned} H^q(x_B,0,0) &= q(x_B), & H^g(x_B,0,0) &= x_B g(x_B), \\ \tilde{H}^q(x_B,0,0) &= \Delta q(x_B), & \tilde{H}^g(x_B,0,0) &= x_B \Delta g(x_B), \\ H_{\mathrm{T}}^q(x_B,0,0) &= \Delta_{\mathrm{T}} q(x_B), & H_{\mathrm{T}}^g(x_B,0,0) &= x_B \Delta_{\mathrm{T}} g(x_B). \end{aligned} \tag{1.44}$$

There are no such counterparts for GPDs E, $\tilde{E}$, E_{T}, or $\tilde{E}_{\mathrm{T}}$ as in DIS the nucleon spin flip (illustrated in Figs. 1.12 and 1.13) is not allowed.

Sum rules and polynomiality

The polynomiality is a non-trivial property of GPDs and concerns Mellin moments of GPDs as a polynomial functions of ξ. For GPD H^q the Mellin moment reads

$$\int_{-1}^{1} \mathrm{d}x x^{n-1} H^q(x,\xi,t) = h_0^{(n)}(t)\xi^0 + h_2^{(n)}(t)\xi^2 + \ldots + h_n^{(n)}(t)\xi^n. \tag{1.45}$$

The polynomiality of GPDs is a consequence of the Lorentz invariance of GPDs. It allows to decompose a given Mellin moment of a particular GPD into a set of form factors. In particular, the first moments of GPDs $H, E, \tilde{H}$ and $\tilde{E}$ give the Dirac form factor F_1, the Pauli form factor F_2, axial g_A, and pseudo-scalar form factor h_A, respectively

$$\begin{aligned} \sum_q e_q \int_{-1}^{1} dx H^q(x,\xi,t) &= F_1(t), \\ \sum_q e_q \int_{-1}^{1} dx E^q(x,\xi,t) &= F_2(t), \\ \sum_q e_q \int_{-1}^{1} dx \tilde{H}^q(x,\xi,t) &= g_A(t), \\ \sum_q e_q \int_{-1}^{1} dx \tilde{E}^q(x,\xi,t) &= h_A(t). \end{aligned} \tag{1.46}$$

The second Mellin moment of the sum of GPD H and E is interesting in particular, as it gives access to the total angular momentum of a quark and gluon

as [56]

$$\begin{aligned} J^q &= \frac{1}{2}\lim_{t\to 0}\int_{-1}^{1} \mathrm{d}x\; x\left[H^q(x,\xi,t)+E^q(x,\xi,t)\right], \\ J^g &= \frac{1}{2}\lim_{t\to 0}\int_{-1}^{1} \mathrm{d}x\left[H^g(x,\xi,t)+E^g(x,\xi,t)\right] \end{aligned} \tag{1.47}$$

These relations are also known as the "Ji's sum rule".

Positivity bounds

The positivity bounds are a set of boundary conditions to restrict the values of GPDs to obey the unitarity of the S-matrix. Positivity bounds emerge from the positivity of the norm on a Hilbert space of states [57]. There is a hierarchy of inequalities relating GPDs to PDFs, and it can be extended beyond the forward limit $t = 0$ into the DGLAP region, in particular a region, where $|\xi| < |x|$. The positivity of the norm emerges from the Cauchy-Schwartz inequality. For a GPD formally written as a following scalar product

$$H(x,\xi)|_{x\geq\xi} = \langle \Phi_1 \mid \Phi_2 \rangle\,, \tag{1.48}$$

then the Cauchy-Schwartz inequality reads

$$|H(x,\xi)|_{x\geq\xi} \leq \| \, |\Phi_1\rangle \, \| \times \| \, |\Phi_2\rangle \, \|. \tag{1.49}$$

And the positivity bound for quarks is then defined as

$$|H^q\,(x,\xi,t)| \leq \sqrt{q\,(x_1)\,q\,(x_2)}, \tag{1.50}$$

where the $x_1 = \frac{x+\xi}{1+\xi}$ and $x_2 = \frac{x-\xi}{1-\xi}$, and for gluons as

$$|H^g\,(x,\xi,t)| \leq \sqrt{(1-\xi^2)\,x_1 x_2\; g\,(x_1)\,g\,(x_2)}. \tag{1.51}$$

Other inequality binding the GPD H^q and E^q is defined as [59]

$$\left[H^q(x,\xi,t) - \frac{\xi^2}{1-\xi^2}E^q(x,\xi,t)\right]^2 + \left[\frac{\sqrt{t_0-t}}{2M_N\sqrt{1-\xi^2}}E^q(x,\xi,t)\right]^2 \leq \frac{q\,(x_1)\,q\,(x_2)}{1-\xi^2}. \tag{1.52}$$

Or a weaker but simpler inequality expressed as

$$\left|H^q(x,\xi,t) - \frac{\xi^2}{1-\xi^2}E^q(x,\xi,t)\right| \leq \sqrt{\frac{q\,(x_1)\,q\,(x_2)}{1-\xi^2}}. \tag{1.53}$$

From the Eq. 1.52 following relation can be derived

$$|E^q(x,\xi,t)| \leq \frac{2M}{\sqrt{t_0 - t}} \sqrt{q\left(x_1\right) q\left(x_2\right)}. \tag{1.54}$$

And similarly for $\tilde{H}^q$ and $\tilde{E}^q$ one has

$$\begin{aligned} \left|\tilde{H}^q(x,\xi,t)\right| &\leq \sqrt{\frac{-t}{t_0 - t} \frac{q\left(x_1\right) q\left(x_2\right)}{1-\xi^2}}, \\ \left|\tilde{E}^q(x,\xi,t)\right| &\leq \frac{2M}{\xi\sqrt{t_0 - t}} \sqrt{q\left(x_1\right) q\left(x_2\right)}. \end{aligned} \tag{1.55}$$

Impact parameter dependent parton distributions

In the forward limit of $\xi = 0$, using the Fourier transformation a very intuitive picture of a proton arises. The GPD H^f in this special case represents densities of partons with a given fraction of the proton longitudinal momentum, x, correlated with their position in the transverse plane with respect to the longitudinal momentum, $\boldsymbol{b}^2$

$$q\left(x, \boldsymbol{b}^2\right) = \int \frac{\mathrm{d}^2\boldsymbol{\Delta}}{4\pi^2} e^{-i\boldsymbol{b}\cdot\boldsymbol{\Delta}} H^f\left(x, 0, t = -\boldsymbol{\Delta}^2\right), \tag{1.56}$$

with respect to the centre of the momentum of the nucleon in the transverse plane $\boldsymbol{R} = \sum_i x_i \boldsymbol{r}$ [60]. The transverse parton position $\boldsymbol{b}$ is often referred to as the impact parameter. The relation 1.56 is commonly known as the nucleon tomography [5][60]. It allows to perform a two-dimensional scan of the inner structure of the nucleon as a function of x for a particular parton flavour, as is illustrated in Fig. 1.14.

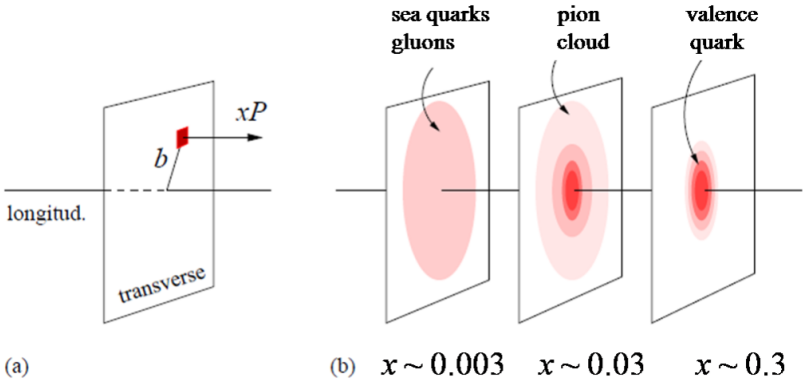

Fig. 1.14: The nucleon tomography: (a) The Fourier transformation of the GPD $H^f(x,0,t)$ to the impact parameter parton distribution $q^f(x,\boldsymbol{b})$ for a fixed longitudinal momentum x describes the distribution of the transverse spatial distance of partons with the particular x from the centre of momentum $\boldsymbol{R}$ in the transverse plane with respect to the longitudinal momentum of the nucleon P. (b) The spatial distribution of partons in the transverse plane for different fixed longitudinal momentum fractions x. Taken from Ref. [61].

1.3 Hard Exclusive Meson Production

The most commonly used process to parameterise GPDs is the DVCS, where a virtual photon is scattered and a real photon is irradiated $\gamma^* p \to \gamma p'$. For more details and results from DVCS measurement from COMPASS experiment, see Ref. [6]. The scattering amplitude of HEMP process contains an additional distribution amplitude to describe the final state meson. These are not present in the DVCS, which makes the HEMP process more difficult to extract the GPDs from the scattering amplitude. The asset of using the HEMP process to parameterise the GPDs complementary to the DVCS is the sensitivity to different GPDs. While DVCS involves the chiral even GPDs $H, E, \tilde{H}$ and $\tilde{E}$, the meson production is most sensitive to the chiral odd GPDs, in particular to a special combination $\bar{E}_T = 2\tilde{H}_T + E_T$, which is sometimes referred to as an GPD equivalent of the TMD Boer-Mulders function, and to the GPD H_T. Parameterising the chiral odd GPDs can give access to proton properties, which cannot be gained through the

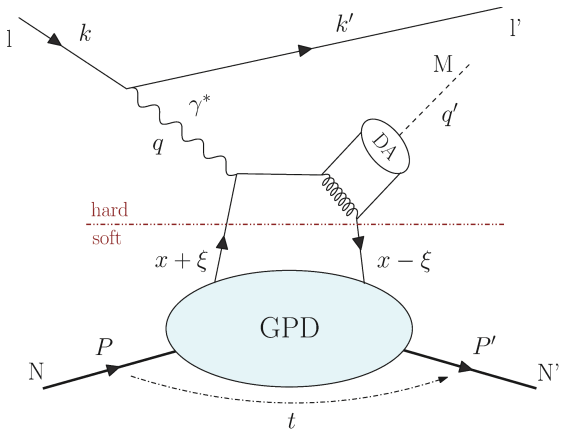

Fig. 1.15: A schematic diagram of a hard exclusive meson production lN → l′N′M in a handbag model. The incoming (scattered) lepton is denoted l (l'), the target (recoil) nucleon N (N'), and the final-state meson M. The red dash-dotted line illustrates the factorisation between the hard scattering kernel and the soft part described by GPDs.

chiral even GPDs. For example, the first moment of the $\bar{E}_{\mathrm{T}}$ can be interpreted as the proton's transverse anomalous magnetic moment [62]. And as has been already outlined above, the H_{T} in the forward limit is reduced to the $\Delta_{\mathrm{T}}q$ PDF, which is related to the tensor charge of the proton [63]. In addition, the vector meson production also involves chiral even GPDs H and E, and the pseudo-scalar meson production contains GPDs $\tilde{H}$ and $\tilde{E}$ in their scattering amplitude. Another asset of using HEMP process with respect to DVCS is a possibility to separate GPDs of different flavours due to the various quark contents of the probed mesons. The exclusive π^0 production also represents the main source of background for the DVCS process, which highlights the importance of this channel in the process of parameterising the full set of GPDs.

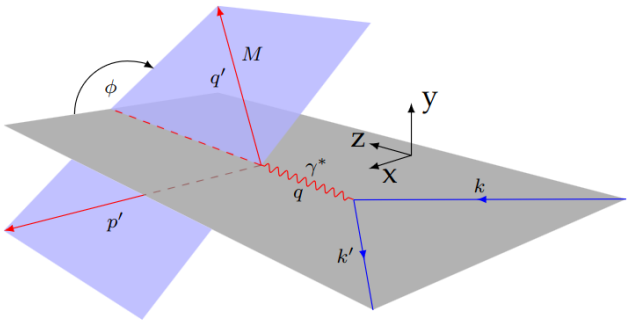

Fig. 1.16: The laboratory frame of the exclusive meson production and the definition of the angles: ϕ denoting the angle between the leptonic scattering plane and hadron production plane, and ϕ_S representing the angle of the target polarisation. Adapted from Ref. [61].

The HEMP process can be described in terms of a handbag model as illustrated in Fig. 1.15. As has been discussed in the ⟦↩1.2.3.1.⟧, the factorisation between the hard scattering process of a virtual photon off the active parton and the soft part of the amplitude described by the GPDs has been proven for the case of longitudinally polarised virtual photons γ^*_{L}, which is not the case of the transversely polarised virtual photons γ^*_{T}.

The amplitudes for the exclusive meson production can be written in terms of helicity amplitudes $\mathcal{A}_{\lambda'\Lambda',\lambda\Lambda}$ as has been already described in ⟦↩1.2.3.2.⟧

$$\begin{aligned}\mathcal{A}_{\lambda'\Lambda',\lambda_{\gamma^*}\Lambda}(x,\xi,t) = \sum_{\lambda_q\lambda_{q'}} \int_{-1}^{1} \mathrm{d}x C_{\lambda'\lambda_{q'},\lambda_{\gamma^*}\lambda_q}(x,\xi,\log(Q/\mu)) \\ \times A_{\Lambda'\lambda_{q'},\Lambda\lambda_q}(x,\xi,t,\mu),\end{aligned} \tag{1.57}$$

where the sum runs over the unknown spins of the spectacle partons λ_q (λ'_q) before (or after) the reaction. The quantity $C_{0\lambda_{q'},\lambda_{\gamma^*}\lambda_q}$ describes the hard reaction $\gamma^* q$, and the $A_{\Lambda'\lambda_{q'},\Lambda\lambda_q}$ represents soft part of the amplitude containing the GPDs as defined in Eq. 1.39 and 1.40. The dependence of the factorisation scale μ cancels out between the C and A up to a desired order. When the helicity amplitude is expanded in the corresponding combination of GPDs, the Eq. 1.57 can be broken down to a set of equations with similar form but containing GPDs instead the helicity amplitude. Thus, a new quantity, a *Meson Production Form Factor* (MPFF),

can be defined as

$$\mathcal{F} = \sum_{\lambda_q \lambda_{q'}} \int_{-1}^{1} \mathrm{d}x C_{0\lambda_{q'},\lambda_{\gamma^*}\lambda_q}\left(x, \xi, \log(Q/\mu)\right) F(x, \xi, t, \mu), \tag{1.58}$$

where F represents a particular GPD. The MPFFs are analogous to the Compton form factors, that appear in the DVCS amplitude, and involve a combination of relevant Feynman diagrams of the particular order with a covariant meson spin wave function [64]. The cross section for the exclusive meson production in general can be expressed in terms of polarised photo-absoption cross sections or interference terms $\sigma^{\Lambda\Lambda}_{\lambda_{\gamma^*}\lambda_{\gamma^*}}$, also called structure functions, which are proportional to a bi-linear combination of helicity amplitudes [17]

$$\sigma^{\Lambda\Lambda}_{\lambda_{\gamma^*}\lambda_{\gamma^*}} \propto \sum_{\Lambda'} \left(\mathcal{A}_{\lambda'\Lambda',\lambda_{\gamma^*}\Lambda}\right)^* \mathcal{A}_{\lambda'\Lambda',\lambda_{\gamma^*}\Lambda}. \tag{1.59}$$

Using the relation 1.41 and $\sigma^{ji}_{nm} = (\sigma^{ji}_{mn})^*$, and following the derivation used in [65], one gets the master formula for the exclusive meson production

$$\begin{aligned}
&\left[\frac{\alpha_{\mathrm{em}}}{8\pi^3}\frac{y^2}{1-\varepsilon}\frac{1-x_B}{x_B}\frac{1}{Q^2}\right]^{-1}\frac{\mathrm{d}^4\sigma}{\mathrm{d}x_B dQ^2 \mathrm{d}\phi \mathrm{d}\phi_S} \\
&= \frac{1}{2}\left(\sigma^{++}_{++} + \sigma^{--}_{++}\right) + \varepsilon\sigma^{++}_{00} - \varepsilon\cos(2\phi)\,\mathrm{Re}\,\sigma^{++}_{+-} - \sqrt{\varepsilon(1+\varepsilon)}\cos\phi\,\mathrm{Re}\left(\sigma^{++}_{+0} + \sigma^{--}_{+0}\right) \\
&\quad - P_\ell\sqrt{\varepsilon(1-\varepsilon)}\sin\phi\,\mathrm{Im}\left(\sigma^{++}_{+0} + \sigma^{--}_{+0}\right) \\
&\quad - S_{\mathrm{L}}\left[\varepsilon\sin(2\phi)\,\mathrm{Im}\,\sigma^{++}_{+-} + \sqrt{\varepsilon(1+\varepsilon)}\sin\phi\,\mathrm{Im}\left(\sigma^{++}_{+0} - \sigma^{--}_{+0}\right)\right] \\
&\quad + S_{\mathrm{L}}P_\ell\left[\sqrt{1-\varepsilon^2}\frac{1}{2}\left(\sigma^{++}_{++} - \sigma^{--}_{++}\right) - \sqrt{\varepsilon(1-\varepsilon)}\cos\phi\,\mathrm{Re}\left(\sigma^{++}_{+0} - \sigma^{--}_{+0}\right)\right] \\
&\quad - S_{\mathrm{T}}\left[\sin\left(\phi-\phi_S\right)\mathrm{Im}\left(\sigma^{+-}_{++} + \varepsilon\sigma^{+-}_{00}\right) + \frac{\varepsilon}{2}\sin\left(\phi+\phi_S\right)\mathrm{Im}\,\sigma^{+-}_{+-}\right. \\
&\quad + \frac{\varepsilon}{2}\sin\left(3\phi-\phi_S\right)\mathrm{Im}\,\sigma^{-+}_{+-} + \sqrt{\varepsilon(1+\varepsilon)}\sin\phi_S\,\mathrm{Im}\,\sigma^{+-}_{+0} \\
&\quad \left. + \sqrt{\varepsilon(1+\varepsilon)}\sin\left(2\phi-\phi_S\right)\mathrm{Im}\,\sigma^{-+}_{+0}\right] + S_{\mathrm{T}}P_\ell\left[\sqrt{1-\varepsilon^2}\cos\left(\phi-\phi_S\right)\mathrm{Re}\,\sigma^{+-}_{++}\right. \\
&\quad \left. - \sqrt{\varepsilon(1-\varepsilon)}\cos\phi_S\,\mathrm{Re}\,\sigma^{+-}_{+0} - \sqrt{\varepsilon(1-\varepsilon)}\cos\left(2\phi-\phi_S\right)\mathrm{Re}\,\sigma^{-+}_{+0}\right],
\end{aligned} \tag{1.60}$$

where the ε denotes the virtual photon polarisation parameter, which can be in the Bjorken limit approximated as

$$\varepsilon = \frac{1 - y - \frac{1}{4}y^2\gamma^2}{1 - y + \frac{1}{2}y^2 + \frac{1}{4}y^2\gamma^2}. \tag{1.61}$$

1.3.1 Exclusive π^0 Cross Section

In the case of the exclusive π^0 production, when considering the valence quarks only, the MPFFs appearing when applying the helicity amplitudes expansion from Eqs. 1.39 and 1.40 [55] with Eq. 1.57 with only the following flavours contribute

$$\mathcal{F}^{\pi^0} = \frac{1}{\sqrt{2}}\left(e_u\mathcal{F}^u - e_d\mathcal{F}^d\right) = \frac{1}{\sqrt{2}}\left(\frac{2}{3}\mathcal{F}^u + \frac{1}{3}\mathcal{F}^d\right). \tag{1.62}$$

The cross section of the exclusive π^0 induced by a polarised muon beam in a reaction $\mu p \to \mu' p' \pi^0$ has been studied at COMPASS experiment in 2012 pilot run [66] and in the main data taking in 2016/17. The reduced cross section $\gamma^* p \to \pi^0 p'$ for an unpolarised target, used in the COMPASS measurement (more details in the [[↪2.]]) can be obtained from Eq. 1.60 by isolating the virtual photon flux $\Gamma\left(Q^2, \nu, E_\mu\right)$ using Hand's convention [67]

$$\Gamma\left(Q^2, \nu, E_\mu\right) = \frac{\alpha_{em}\left(1 - x_B\right)}{2\pi Q^2 y E_\mu}\left[y^2\left(1 - \frac{2m_\mu^2}{Q^2}\right) + \frac{2}{1 + Q^2/\nu^2}\left(1 - y - \frac{Q^2}{4E_\mu^2}\right)\right], \tag{1.63}$$

and omitting the terms of Eq. 1.60 depending on the target polarisation as

$$\begin{aligned}\frac{1}{\Gamma}\frac{\mathrm{d}^4\sigma}{\mathrm{d}Q^2\ \mathrm{d}\nu \mathrm{d}t\ \mathrm{d}\phi} = \frac{1}{2\pi}\Bigg[&\frac{1}{2}\left(\sigma_{++}^{++} + \sigma_{++}^{--}\right) + \varepsilon\sigma_{00}^{++} - \varepsilon\cos(2\phi)\,\mathrm{Re}\,\sigma_{+-}^{++} \\ &- \sqrt{\varepsilon(1+\varepsilon)}\cos\phi\,\mathrm{Re}\left(\sigma_{+0}^{++} + \sigma_{+0}^{--}\right) \\ &- P_l\sqrt{\varepsilon(1-\varepsilon)}\sin\phi\,\mathrm{Im}\left(\sigma_{+0}^{++} + \sigma_{+0}^{--}\right)\Bigg].\end{aligned} \tag{1.64}$$

The last term of the Eq. 1.64, representing the interference term of amplitudes of longitudinally and transversely polarised virtual photons, is strongly suppressed by the factor $\varepsilon\left(1 - \varepsilon\right)$, as the virtual photon polarisation parameter ε is close to one in COMPASS kinematics (for more details, [[↪4.]]). As the Eq. 1.64 is dependent on the lepton helicity, when the cross section is averaged over the μ^+ and μ^- contributions, the last term cancels out and the averaged $\gamma^* p \to \pi^0 p'$ cross section reads

$$\frac{\mathrm{d}\sigma^{\gamma^* p}}{\mathrm{d}t\mathrm{d}\phi} = \frac{1}{2\pi}\left[\frac{\mathrm{d}\sigma_\mathrm{T}}{\mathrm{d}t} + \epsilon\frac{\mathrm{d}\sigma_\mathrm{L}}{\mathrm{d}t} + \epsilon\cos(2\phi)\frac{\mathrm{d}\sigma_\mathrm{TT}}{\mathrm{d}t} + \sqrt{2\epsilon(1+\epsilon)}\cos(\phi)\frac{\mathrm{d}\sigma_\mathrm{LT}}{\mathrm{d}t}\right], \tag{1.65}$$

where we relabeled the amplitudes to an abbreviated a common notation $\sigma_T, \sigma_L, \sigma_{TT}$, and σ_{LT}, used in e.g. [17, 68]

$$
\begin{aligned}
\sigma_{\mathrm{T}} &= \frac{1}{2}\left(\sigma_{++}^{++} + \sigma_{++}^{--}\right), \\
\sigma_{\mathrm{L}} &= \sigma_{00}^{++}, \\
\sigma_{\mathrm{TT}} &= -\operatorname{Re}\sigma_{+-}^{++}, \\
\sigma_{\mathrm{LT}} &= -\frac{1}{\sqrt{2}}\operatorname{Re}\left(\sigma_{+0}^{++} + \sigma_{+0}^{--}\right),
\end{aligned}
$$

and integrated over Q^2 and ν. The subscript T(L) marks the contribution from transversely (longitudinally) polarised γ^*, the subscripts TT and LT signify the interference terms between transversely-transversely and longitudinally-transversely polarised photons.

There are six independent helicity amplitudes $\mathcal{A}_{\lambda'\Lambda',\lambda\Lambda}$, which constitute the structure functions from the exclusive π^0 cross section [69], $\mathcal{A}_{0+0+}$ and $\mathcal{A}_{0-0+}$ for longitudinally polarised virtual photon, and $\mathcal{A}_{0-++}, \mathcal{A}_{0--+}, \mathcal{A}_{0+++}$ and $\mathcal{A}_{0+-+}$ for the transversely polarised γ^*. Here, the helicity of the virtual photon can achieve values $\lambda = -1, 0, 1$, the π^0 helicity is $\lambda' = 0$, and Λ (Λ') mark the target (recoil) proton helicities, which are naturally denoted "+" for $1/2$ and "−" for $-1/2$. The structure functions can be written in terms of the aforementioned amplitudes, neglecting the smallest amplitudes, as follows [69]

$$
\begin{aligned}
\frac{\mathrm{d}\sigma_{\mathrm{L}}}{\mathrm{d}t} &= \frac{1}{k}\left[\left|\mathcal{A}_{0+0+}\right|^2 + \left|\mathcal{A}_{0-0+}\right|^2\right], \\
\frac{\mathrm{d}\sigma_{\mathrm{T}}}{\mathrm{d}t} &= \frac{1}{2k}\left[\left|\mathcal{A}_{0-++}\right|^2 + \left|\mathcal{A}_{0--+}\right|^2 + \left|\mathcal{A}_{0+++}\right|^2 + \left|\mathcal{A}_{0+-+}\right|^2\right] \\
&\simeq \frac{1}{2k}\left[\left|\mathcal{A}_{0-++}\right|^2 + 2\left|\mathcal{A}_{0+++}^{N}\right|^2\right], \\
\frac{\mathrm{d}\sigma_{\mathrm{TT}}}{\mathrm{d}t} &= -\frac{1}{k}\operatorname{Re}\left[\mathcal{A}_{0-++}^{*}\mathcal{A}_{0--+} + \mathcal{A}_{0+++}^{*}\mathcal{A}_{0+-+}\right] \\
&\simeq -\frac{1}{k}\left|\mathcal{A}_{0+++}^{N}\right|^2, \\
\frac{\mathrm{d}\sigma_{\mathrm{LT}}}{\mathrm{d}t} &= -\frac{1}{\sqrt{2}k}\operatorname{Re}\left[\mathcal{A}_{0-0+}^{*}\left(\mathcal{A}_{0-++} - \mathcal{A}_{0--+}\right) + 2\mathcal{A}_{0+0+}^{*}\mathcal{A}_{0+-+}\right] \\
&\simeq -\frac{1}{\sqrt{2}k}\operatorname{Re}\left(\mathcal{A}_{0-++}^{*}\mathcal{A}_{0-0+}\right),
\end{aligned}
\tag{1.66}
$$

where the quantity k is the phase space factor

$$\begin{aligned} k =& 16\pi \left(W^2 - M^2\right) \sqrt{\Lambda\left(W^2, -Q^2, M^2\right)} \\ =& 16\pi Q^2 \left(\frac{1}{x_B} - 1\right) \\ & \times \sqrt{\left(W^2 - M^2\right)^2 + Q^4 + 2W^2Q^2 + 2Q^2M^2} \\ =& Q^4 k', \end{aligned} \tag{1.67}$$

and the $\mathcal{A}^N_{0\Lambda'\lambda\Lambda}$ denotes the so-called natural amplitude [69] $A^N_{0\Lambda'\lambda\Lambda} = \frac{1}{2}[A_{0\Lambda'\lambda\Lambda} + A_{0\Lambda'-\lambda\Lambda}]$ (with respect to the unnatural amplitude, which is a difference of these amplitudes), which does not change sign upon the change of helicity of the virtual photon.

In the notation of [54], the helicity amplitudes for the π^0 production in terms of MPFFs, as defined in Eq. 1.58, can be written as

$$\begin{aligned} \mathcal{A}_{0+0+} &= \sqrt{1-\xi^2}\frac{e_0}{Q}\left[\tilde{\mathcal{H}} - \frac{\xi^2}{1-\xi^2}\tilde{\mathcal{E}}\right], \\ \mathcal{A}_{0-0+} &= -\frac{e_0}{Q}\frac{\sqrt{-t'}}{2M}\xi\tilde{\mathcal{E}}, \\ \mathcal{A}_{0-++} &= e_0\frac{\mu_\pi}{Q^2}\sqrt{1-\xi^2}\mathcal{H}_{\mathrm{T}}, \\ \mathcal{A}^N_{0+++} &= -e_0\frac{\mu_\pi}{Q^2}\frac{\sqrt{-t'}}{4M}\bar{\mathcal{E}}_{\mathrm{T}}, \end{aligned} \tag{1.68}$$

where $t' = t - t_0$, and $\mu_\pi = m^2_{uppi}/\left(m_u + m_d\right)$. Finally, combining the Eqs 1.66 and 1.68 leads to the dependence of the structure function on the MPFFs

$$\begin{aligned} \frac{\mathrm{d}\sigma_{\mathrm{L}}}{\mathrm{d}t} &= \frac{4\pi\alpha}{k'}\frac{1}{Q^6}\left\{\left(1-\xi^2\right)|\tilde{\mathcal{H}}|^2 - 2\xi^2\,\mathrm{Re}\left[\tilde{\mathcal{H}}^*\tilde{\mathcal{E}}\right] - \frac{t'}{4M^2}\,\xi^2|\tilde{\mathcal{E}}|^2\right\} \\ \frac{\mathrm{d}\sigma_{\mathrm{T}}}{\mathrm{d}t} &= \frac{4\pi\alpha}{2k'}\frac{\mu_\pi^2}{Q^8}\left[\left(1-\xi^2\right)|\mathcal{H}_{\mathrm{T}}|^2 - \frac{t'}{8M^2}\left|\bar{\mathcal{E}}_{\mathrm{T}}\right|^2\right], \\ \frac{\mathrm{d}\sigma_{\mathrm{TT}}}{\mathrm{d}t} &= \frac{4\pi\alpha}{k'}\frac{\mu_\pi^2}{Q^8}\frac{t'}{16M^2}\left|\bar{\mathcal{E}}_{\mathrm{T}}\right|^2, \\ \frac{\mathrm{d}\sigma_{\mathrm{LT}}}{\mathrm{d}t} &= \frac{4\pi\alpha}{\sqrt{2}k'}\frac{\mu_\pi}{Q^7}\xi\sqrt{1-\xi^2}\frac{\sqrt{-t'}}{2M}\,\mathrm{Re}\left[\mathcal{H}^*_{\mathrm{T}}\;\tilde{\mathcal{E}}\right]. \end{aligned} \tag{1.69}$$

1.4 Available Experimental Data

The availability of the experimental data on the exclusive π^0 production is rather scarce. This channel was studied in several experiment at Jefferson Laboratory (JLab) and COMPASS. The complementary channel of exclusive π^+ production was probed at HERMES experiment at DESY in 1997 and 2002-2005, as well as at JLab.

The HERMES collaboration measured the production of exclusive π^+ first in 1997 using a longitudinally polarised hydrogen gaseous target with a positron beam of $E = 27.6$ GeV [70]. The target was not equipped with any recoil proton detector, thus a missing mass method was used to reconstruct the exclusive event. This measurement brought the first results of an azimuthal single-spin asymmetry in exclusive π^+ electroproduction. Between 2002 and 2005 HERMES conducted a similar measurement with a transversely polarised target [71]. The result of this measurement lead to the first estimation of some of the GPDs. Another focus of the measurement was the extraction of the exclusive π^+ electroproduction cross section using the combined statistics from 1996 to 2005 [72]. The differential γ^*p cross section as a function of Q^2, x_B, and $-t' = t_0 - t$ from the HERMES exclusive measurements is shown in Fig. 1.17.

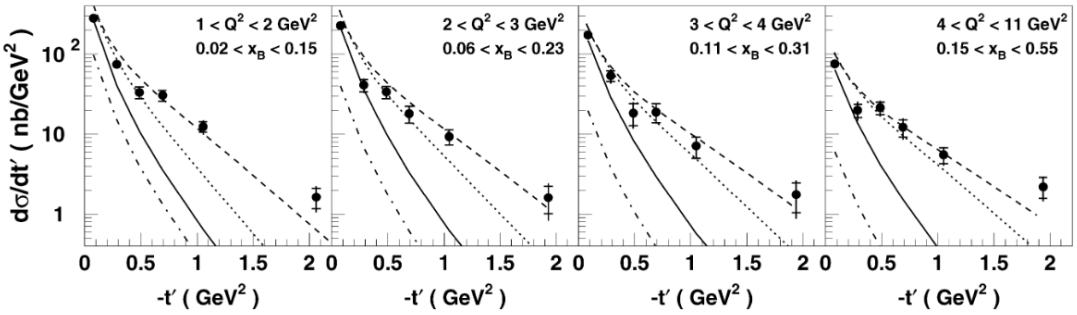

Fig. 1.17: The results of the differential γ^*p cross section of exclusive π^+ electroproduction as a function of Q^2, x_B, and $-t'$. The black dots represent the data from the period 1996 to 2005, and the lines denote different theoretical models [72].

The HERMES results helped to constrain the theoretical models. The first attempt to describe the π^+ production was performed by Goloskokov and Kroll [68]. They concluded that the dominant part of the cross section in small $-t'$, coming

from the γ_L^*, originates from the pion pole. This channel consists of an exchange of a virtual π^+ between the virtual photon and the nucleon. The associated amplitude, having a $(t - m_\pi)$ term in the denominator of the propagator, enhances the longitudinal response.

From the experimental point of view, the exclusive π^0 production has the advantage with respect to the charged pions in the absence of the pion pole in the amplitude. On the other hand, the detection is more complicated due to the decay of the neutral pion into two photons. Also the total cross section of this channel is expected to be much smaller than its charged counterparts. The first measurement of the exclusive π^0 production beam-spin asymmetries was performed at CLAS experiment at JLab Hall B [7]. They used a polarised electron beam of $E = 5.77$ GeV and a liquid hydrogen target in the kinematic domain of valence quarks sector. The experimental setup contained a detection system for the scattered electron, identification of photons from the π^0 decay, and a time-of-flight detector for capturing the recoil proton. Apart from the beam-spin asymmetries, the exclusive π^0 electroproduction cross section was extracted [8, 69]. The main asset of the CLAS measurement was a very high luminosity, which allowed for examining the cross section as a function of ϕ in bins of t', Q^2 and x_B, and also performing comprehensive studies in variety of kinematic bins. The structure functions from the exclusive π^0 cross section $\mathrm{d}\sigma_\mathrm{U}/\mathrm{d}t = \mathrm{d}\sigma_\mathrm{T}/\mathrm{d}t + \varepsilon \mathrm{d}\sigma_\mathrm{L}/\mathrm{d}t$, $\mathrm{d}\sigma_\mathrm{TT}/\mathrm{d}t$, and $\mathrm{d}\sigma_\mathrm{LT}/\mathrm{d}t$ are shown in Fig. 1.18. The results were found to be compatible with the GK model [54], which incorporated the modifications coming from the investigation of the π^+ channel [68]. A different approach was brought by *Goldstein and Liuti* (GL) [73, 74]. Their model predicts a different behaviour at small $-t$. The data however do not exclude either of the models.

The most recent experimental effort of the CLAS collaboration was measuring the beam spin asymmetry related to the structure function $\sigma_{\mathrm{LT}'}/\sigma_0$, where $\sigma_0 = \sigma_\mathrm{T} + \varepsilon\sigma_\mathrm{L}$, on the CLAS12 spectrometer with longitudinally polarised electron beam of $E = 10.6$ GeV and unpolarised liquid hydrogen target with complete simultaneous detection of the final state particles. Their results of the $\mathrm{d}\sigma_{\mathrm{LT}'}/\mathrm{d}t$ extraction fitted with GK model and Regge-based JML model is shown in Fig. 1.19.

A similar experimental programme to CLAS with a different kinematic coverage was conducted at JLab Hall A [75]. They measured exclusive processes at small

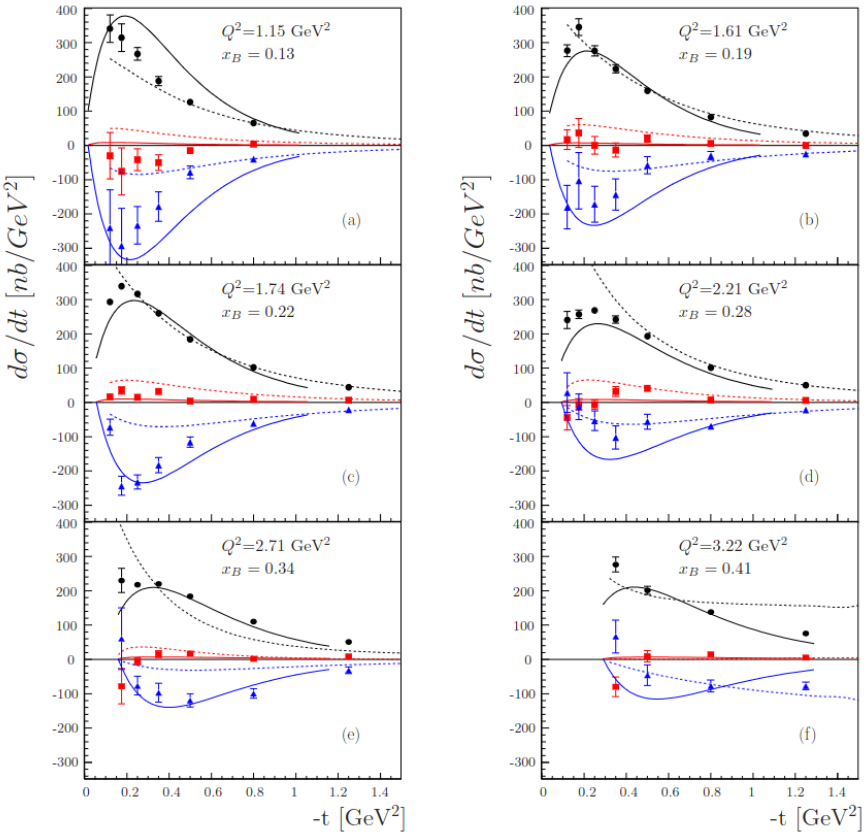

Fig. 1.18: A selection from the results of the exclusive π^0 production, the extracted structure functions from the differential cross section as a function of t at CLAS [69]. Black circles mark $d\sigma_U/dt = d\sigma_T/dt + \varepsilon d\sigma_L/dt$, the blue triangles $d\sigma_{TT}/dt$, and the red squares represent $d\sigma_{LT}/dt$. The curves represent the theoretical predictions from the GK model [54] (solid), and the GL model [73][74] (dashed). Note that the unpolarised structure function is strongly positive, the $d\sigma_{TT}/dt$ is negative, and the $d\sigma_{LT}/dt$ is compatible with zero.

$-t'$ ranging from 0.01 to 0.206 GeV^2 using 5.75 GeV electron beam impinging on a liquid hydrogen target. The kinematics was selected to $x_B = 0.37$ and two values of $Q^2 = 1.9$ and $Q^2 = 2.3$ GeV^2. The detection of the final state was not complete, thus the missing mass technique was used.

However the main contribution of the Hall A GPD programme was a later measurement with varying beam energies, which allowed for the separation of the

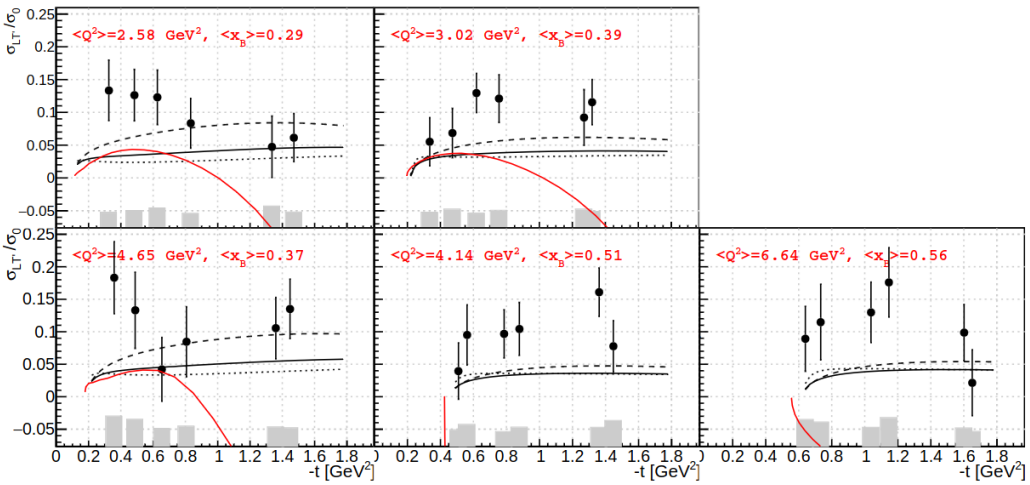

Fig. 1.19: Structure function $\mathrm{d}\sigma_{\mathrm{LT}'}/\mathrm{d}t$, extracted from the beam spin asymmetries, as a function of $-t$. The grey bands represent the systematic error, the black lines mark the GK model: the solid lines show the default parametrisation, the dashed lines show the effect of $\bar{E}_{\mathrm{T}}$ multiplied by a factor of 0.5, and the dotted lines show the effect of H_{T} multiplied by the same factor. The red curves represent the Regge-based JML model [9].

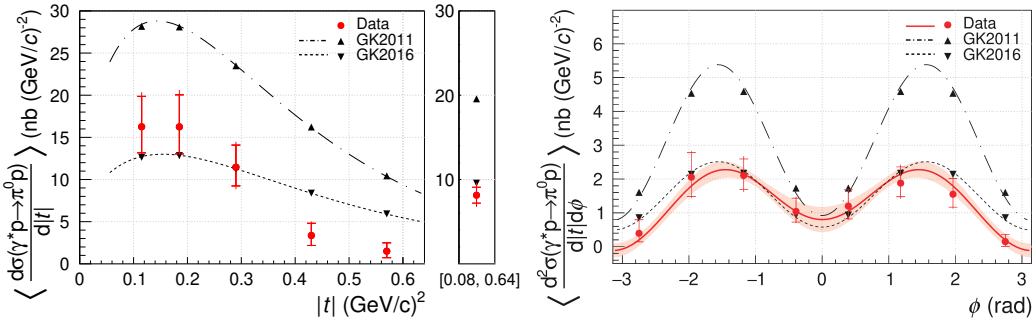

Fig. 1.20: The results of the exclusive π^0 production cross section as a function of $|t|$ (left) and ϕ (right), averaged over the beam polarities [66]. The inner error bars represent the statistical errors and the outer error bars denote the quadratic sum of statistical and systematic uncertainties. The data are compared to two versions of the GK model predictions [54, 84].

σ_L and σ_T structure functions using the Rosenbluth separation [76]. The results from this measurement are shown in Fig. 1.21.

The JLab Hall C measured the electroproduction of the exclusive π^0 [78] and exclusive π^+ [79] as well. Their measurement was however taken close to the $\Delta\,(1232)$ resonance, hence the physics of these measurements does not target GPDs.

Another facility, which investigated the exclusive meson production, is the COMPASS experiment. Studies with longitudinally and transversely polarised targets were performed on the beam spin asymmetries for channels of exclusive ρ^0 [80, 83] and the exclusive ω [81, 82]. The dedicated GPD programme to measure the DVCS and HEMP processes on an unpolarised hydrogen target took place in 2012 and in years 2016 and 2017. The 2012 measurement was a 4-weeks-long pilot run using longitudinally polarised muon beam of both polarities and $E = 160$ GeV. Among other channels of meson production, the exclusive π^0 production cross section was studied in bins of Q^2, ν, $|t|$, and ϕ in the kinematic domain of intermediate $\langle x_B \rangle = 0.093$ [66], which is the first investigation of this exclusive channel in this kinematic domain. The results of the differential exclusive π^0 cross section as a function of $|t|$ (on the left) and ϕ (on the right), averaged over the beam polarities, are shown in Fig. 1.20. The results from the 2016 data is presented in this work. The description of the experimental setup used for the COMPASS GPD programme is outlined in the following [[↪2.]], and the extraction of the differential cross section of the exclusive π^0 production as a function of $|t|$ and ϕ from the 2016 data, together with a detailed comparison with the 2012 results is elaborated in [[↪5.]].

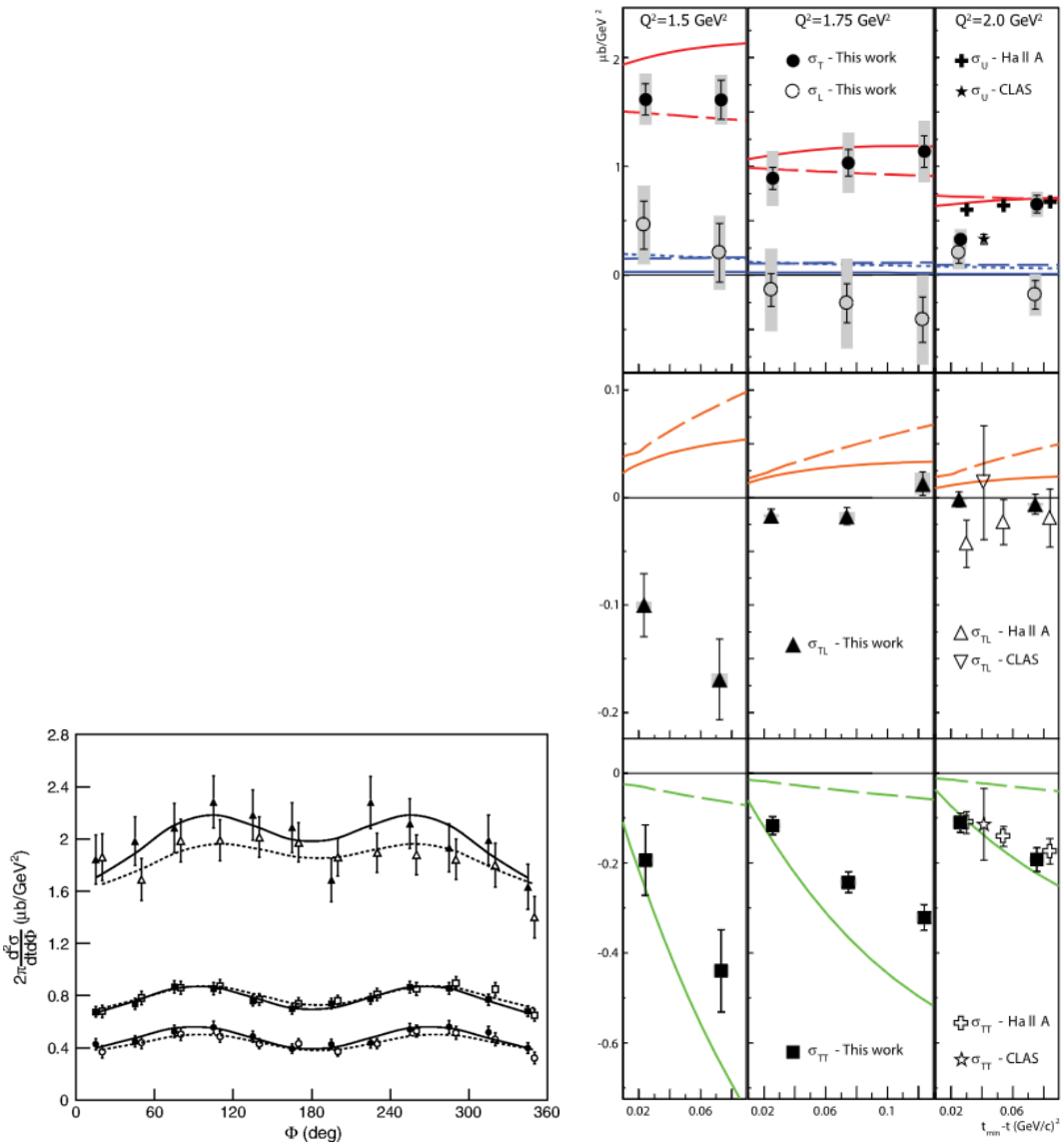

Fig. 1.21: The results of the structure functions from the exclusive π^0 production cross section using the Rosenbluth separation [76] as a function of $-t'$ from JLab Hall A for $Q^2 = 1.5$ GeV^2 (left column), $Q^2 = 1.75$ GeV^2 (centre), and $Q^2 = 2$ GeV^2 (right column). The full circles mark the $\mathrm{d}\sigma_\mathrm{T}/\mathrm{d}t$, the open circles represent the $\mathrm{d}\sigma_\mathrm{L}/\mathrm{d}t$, the triangles show the $\mathrm{d}\sigma_\mathrm{LT}/\mathrm{d}t$, and the squares are $\mathrm{d}\sigma_\mathrm{TT}/\mathrm{d}t$. The full lines represent the predictions from the GK model [54], and the long-dashed lines are predictions from the GL model [73, 74], and the short-dashed lines show the VGG model [77].

2 COMPASS Experimental Setup

Common Muon and Proton Apparatus for Structure and Spectroscopy (COMPASS) is a fixed target experiment located at the M2 beamline of the CERN *Super Proton Synchrotron* (SPS) accelerator utilising a secondary or tertiary beams from the T6 production target [85][61]. It accommodates both hadron and lepton beams, specifically longitudinally polarised muons with natural polarisation of cca 80%. The apparatus allows for measuring with beam energies ranging from about 60 to 280 GeV for muons and 20 to 350 GeV for hadrons [86]. The intensities reach up to 10^8/s hadrons and 4×10^7/s muons. The setup supports measurements with unpolarised and longitudinally or transversely polarised targets.

The main focus of the experiment is the spin structure of the nucleon, hadron spectroscopy, and studies of chiral dynamics. COMPASS commenced in 1996 by joining two competing collaborations, CHEOPS and HMC, which shared similar requirements for the experimental setup although had a different focus. The second phase of the experimental programme, COMPASS-II, commenced in 2010 focusing on studying the spin structure of the nucleon using of SIDIS and Drell-Yan processes, in order to extract TMDs and fragmentation functions, and DVCS and HEMP for parameterising GPDs.

In the following section we will give a brief description of the apparatus and the specific setup used for the GPD programme, which took place in a four-weeks-long pilot run in 2012 and the main two-year measurement in 2016/17.

2.1 Beamline

The muon beam used in the GPD programme is produced as a tertiary beam from the primary 450 GeV protons extracted from SPS impinging on a beryllium production target T6, located about 1 km upstream from the COMPASS experimental hall. The muon beam of a chosen polarity is obtained from the decay of the secondary beam produced on T6. The secondary beam from the T6 consists mainly of pions and an 3.6% admixture of kaons, which also decay into muons with branching ratio of 0.6355. The parity violation and the helicity conservation of the weak decay allow for the muon beam to be naturally polarised.

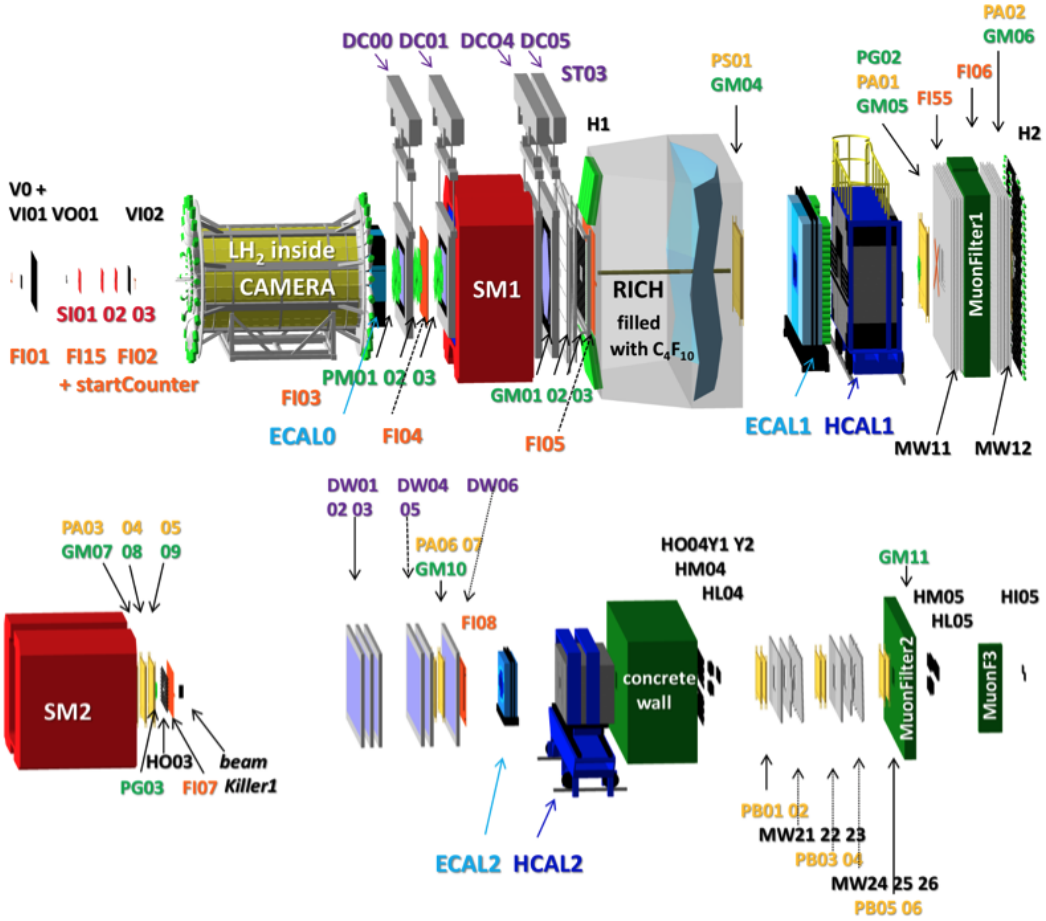

Fig. 2.1: A schematic view of the COMPASS spectrometer setup for the 2016/17 measurement [87].

In the laboratory frame the polarisation of the can be determined as [85]

$$P_{\mu^{\mp}} = \pm \frac{m_{\pi,\mathrm{K}}^2 + \left(1 - 2\frac{E_{\pi,\mathrm{K}}}{E_{\mu}}\right) m_{\mu}^2}{m_{\pi,\mathrm{K}}^2 - m_{\mu}^2}.$$

The factor of merit has been optimised for a polarisation $P_{\mu^{\mp}} = (80 \pm 5)\,\%$. While this value could be improved, it would be at the expense of smaller muon fluxes. The muon beam momentum of 160 GeV has been selected to have the best figure of merit of polarisation, muon flux and high enough Q^2. After passing through the decay tunnel, the muon beam is injected into a 800 m long tunnel for focusing and shaping before it arrives in the COMPASS experimental hall.

The SPS delivers the beam in bunches called spills over a time period of 4.8 s. The cycle of spills, called supercycle, is distributed between several experiments. As the yield of the μ^+ beam from the T6 target is 2.7× larger than of μ^-, different target thickness is used to produce the respective beams, in order to produce the yields of muon fluxes as close as possible to minimise pile-up and over-occupancy of detectors. A 100 mm long Be target is used for the μ^+ production with resulting flux of about $7.6 \cdot 10^7$ muons per spill, and a 500 mm target for the μ^- with the corresponding flux of $6.3 \cdot 10^7$ per spill. This corresponds to approximately $1.4 \cdot 10^7$/s in average.

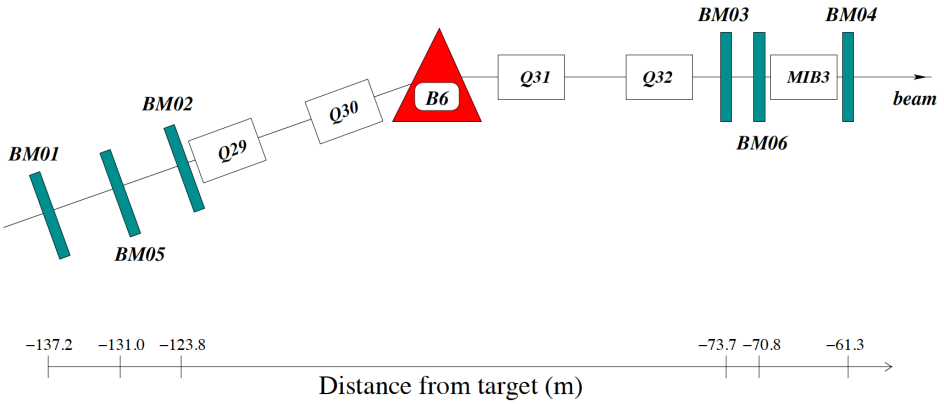

Fig. 2.2: The Beam Momentum Station [85].

In order to distinguish the exclusive π^0 production from the greatly prevalent DIS processes, a precise measurement of the beam momentum is required. The beam optics in the M2 beamline allows for a momentum spread of 5% from the nominal 160 GeV. The measurement of the momentum of each individual muon is performed by *Beam Momentum Station* (BMS) 100 m upstream of the target. The schematic sketch of the BMS is shown in Fig. 2.2. BMS consists of three dipole magnets (denoted B6) surrounded by six tracking detectors.

Four of those (BM01–BM04) are hodoscope planes performing the momentum measurement by determining the track curvature in the magnetic field, and the two remaining are scintillating fiber hodoscopes (BM05–BM06) inserted in between each hodoscope pair to provide an additional redundancy. The BMS reconstructs the beam momentum with an uncertainty of 1%, with an efficiency of $\approx 93\%$.

2.2 Unpolarised Liquid Hydrogen Target

For the GPD an unpolarised liquid hydrogen (ℓH) was used. The scheme of the target is shown in Fig. 2.3. The 2.5 m long and 40 mm wide target was inserted into the time-of-flight system for detecting the recoiled proton, described in ⟦↪2.3.⟧. This target configuration was installed for the first time in 2012 for the pilot run. The target consists of kapton layers, surrounded by super-insulation aluminum foils. It is inserted into a vacuum cryostat made from carbon fiber, cooling the liquid hydrogen to the temperature of 18 K at a pressure of 1020 mbar.

There are two main features of the ℓH target:

- Low material budget: Since in exclusive reactions a particular interest focuses in small momentum transfers to the proton target, the absorption of the recoiled proton in the target material has to be reduced to minimum. By lightening the target material it was possible to measure a recoiled proton with momentum down to 270 MeV, corresponding to a minimum momentum transfer $|t| = 0.07$ GeV^2.

- Homogeneous ℓH density: In order to measure cross sections of exclusive processes a precise luminosity determination is required. For that purpose the target density has to be homogeneous with minimal gas phase. This allows for a precision of the luminosity determination within a few percent.

2.2.1 Target Position

In order to correctly evaluate the luminosity, the precise target position and effective volume has to determined. In the following, we will briefly describe the principle of the target position measurement, details can be found in Ref. [21] for real data (RD) and in Ref. [90] for the MC.

The first step is dividing the target to 27 transverse slices with centres estimated by the peak of number of vertices. The vertex resolution is improved by a requirement of at least 3 charged tracks associated with the vertex (one incoming muon and two outgoing charged particles). The kinematics of the data sample is set to select events with $Q^2 > 0.1$ GeV^2 to provide a large statistics. The method used for the tomography of the target is similar to a Hough Circle

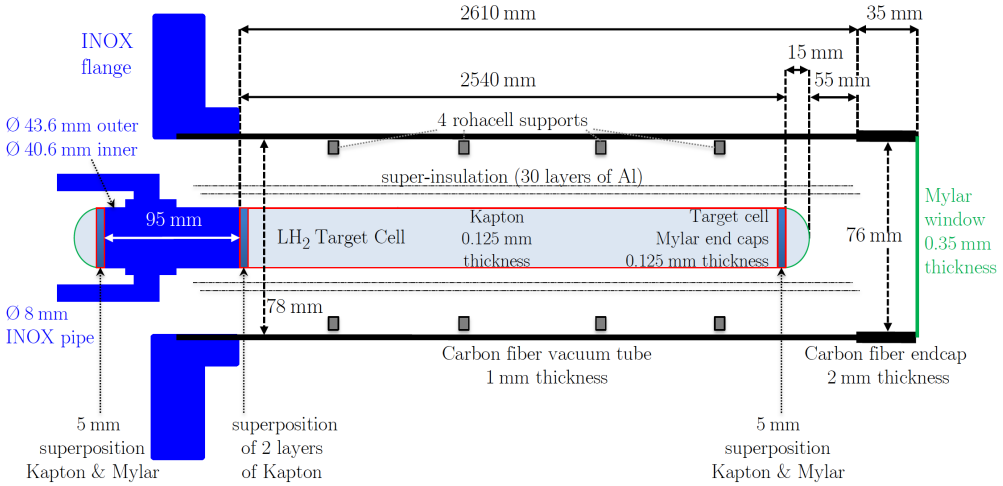

Fig. 2.3: A schematic view of the ℓH target used for the GPD programme [88, 89].

Transform[1], determining the circle parameters (x, y, R) from the gradient of the vertex distribution in the target.

The density of the vertices is of course the highest along the beam trajectory and also in the kapton cell material, which is more dense than the liquid hydrogen. The position of the kapton cell with the diameter of 4 cm is determined from each of the vertical slices. The target has a slight tilt along the z-axis (to contain the gas bubble on upstream part of the target and prevent its spreading), which in combination with a slight bending of the kapton tube creates an approximate banana-shape of the target [21]. The illustration of the target tomography in the transversal and longitudinal direction is given in Fig. 2.4. The upper band shows the vertex distribution in the transverse plane in the upstream (left side) and downstream (right side) of the target and the bottom part demonstrates the longitudinal profile. The target radius cut $R = 1.9$ cm has been introduced (in pink circle) to exclude the vertices originating in the kapton cell material. Also, it is apparent that due to the impossibility to fill the target cell fully with the liquid hydrogen, a gaseous bubble appeared in the upper-upstream part of the target. Vertices from this part had to removed from the analysis ($y < 1.2$ cm).

[1]The Hough Transform detects straight lines, circles, or ellipses based on the polar transformation of the coordinates. It is used for the purpose of tomography or shape recognition.

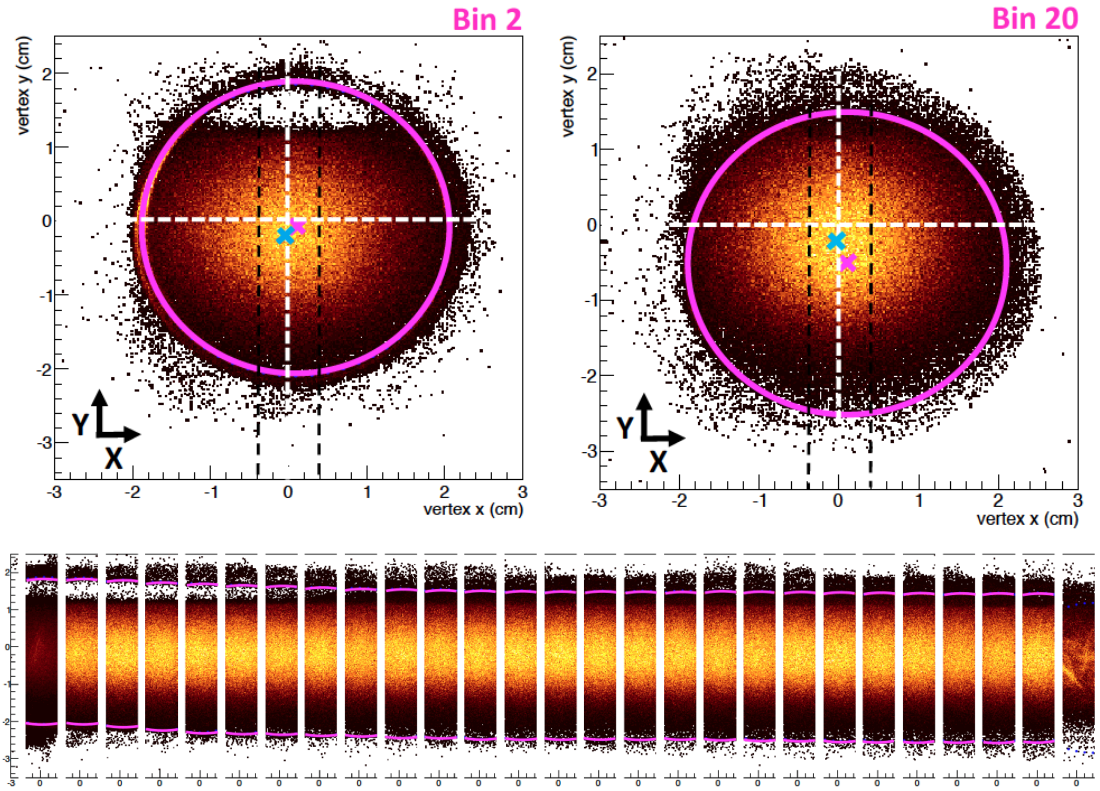

Fig. 2.4: The upper band shows the two transversal slices (upstream (left) and downstream (right) part) of the target with 2D distributions of interaction vertices. The pink circle marks the boundary of the kapton cell of the target, and the crosses represent the target (pink) and the beam (blue) centre. The bottom row illustrates the longitudinal distribution of the vertices. The pink lines mark the kapton cell. One can notice the apparent lack of interaction vertices in the upper-upstream part of the target cell, due to the presence of gaseous hydrogen. From Ref. [21].

The banana-shape of the target was not implemented in the MC simulation for 2016. The target has been simulated as a tilted cylinder. The overlap with the real target amounts to 99.5%. The remaining 0.5% difference is treated with a simultaneous cut applied to real data and MC, $-318.5 < z_{\text{vtx}} < -78.5$ cm, to only leave the overlapping part. More details on the investigation of the matter can be found in Ref. [90].

2.3 CAMERA Detector

The recoiled proton time-of-flight detector, called *COMPASS Apparatus for Measurement of Exclusive ReActions* (CAMERA), is placed around the hydrogen target, as illustrated in Fig. 2.5. It consists of two concentric barrels (ring A and ring B) of radii 24 cm and 110 cm, respectively. Both rings are composed of 24 scintillators, covering 15° in the radial direction around the target. In order to improve the azimuthal resolution, the ring B is rotated by 7.5° with respect to ring A.

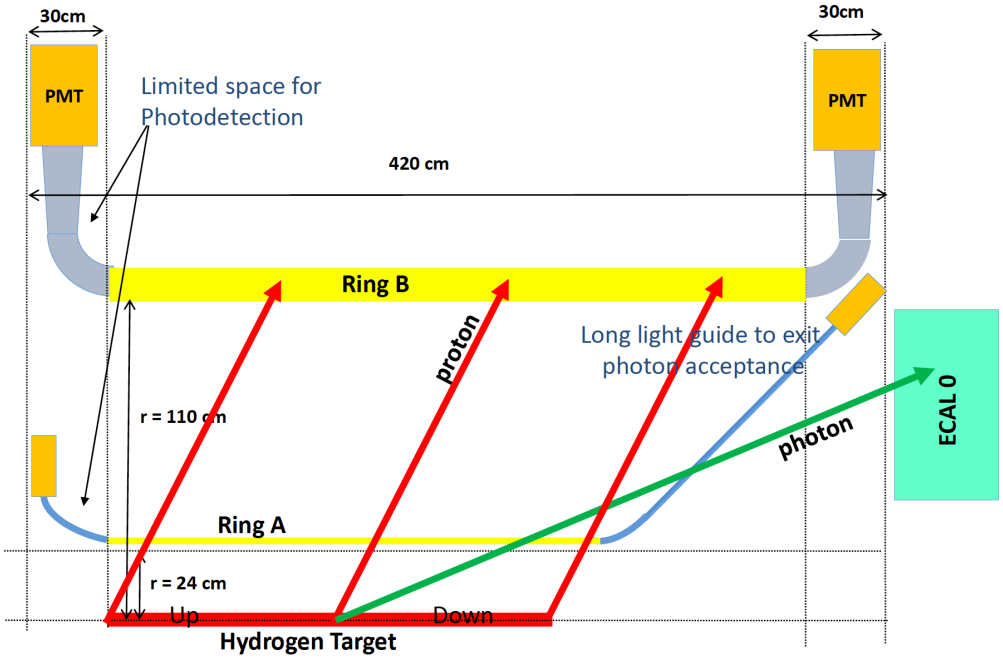

Fig. 2.5: A scheme illustrating dimensions of CAMERA detector and the hydrogen target, with the arrows indicating the outgoing particles: protons originating from different parts of the target, and photon arriving in ECAL0, located behind the target area [103].

The longitudinal (z) position of the hit is determined from the time difference of the signals in the two *Photo-Multiplier Tube* (PMT), connected to each scintillator slab by a long light-guide to minimise the budget material in proximity of the target.

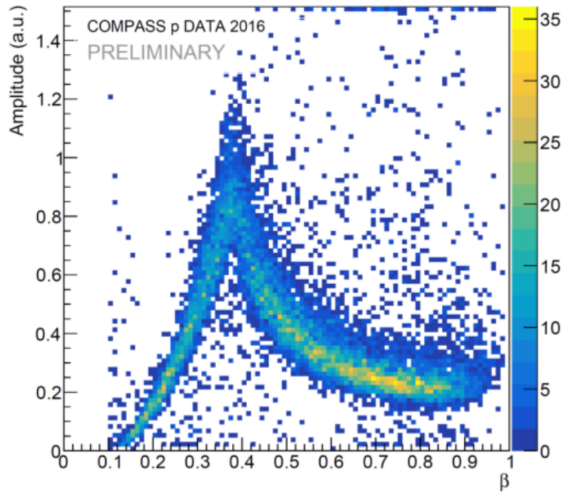

Fig. 2.6: The energy loss of the recoiled proton in the ring B of CAMERA as a function of the proton velocity.

The *Time Of Flight* (TOF) and *Distance Of Flight* (DOF) of the recoiled proton are reconstructed from the coincident hits in both rings. The proton velocity is then derived from TOF and DOF. The minimal velocity of the recoiled proton is $\beta \approx 0.2$ (corresponding to proton momentum of 270 MeV). The recoiled proton is stopped in ring B, up to $\beta \approx 0.4$. The Fig. 2.6 illustrates the characteristic signal of the proton's energy loss obtained from ring B as a function of its velocity. Protons faster then $\beta \approx 0.4$ (corresponding to momentum 460 MeV) cross both rings and leave the CAMERA volume.

The thickness of both slabs is optimised to introduce a minimal material budget and provide high enough light yield in the scintillators. The length of scintillator slabs in ring A is 275 cm and their thickness is 0.4 cm. In case of ring B the length is 360 cm and the thickness is 5 cm. The scintillating material emits light at 430 nm. The time resolution of the detector is approximately 350 ps.

The detection of a charged particle in CAMERA relies on four time stamps, $t^{\text{up}}_{A_i}$, $t^{\text{down}}_{A_i}$, $t^{\text{up}}_{B_j}$, and $t^{\text{down}}_{B_j}$, two for each scintillator slab $A_i, B_j, (i,j) \in [0,23]^2$, corresponding to each upstream and downstream PMTs. From these measured values, the TOF and DOF can be reconstructed. First, the z-position of the hit in ring A and B has to be calculated using the effective light speed through the

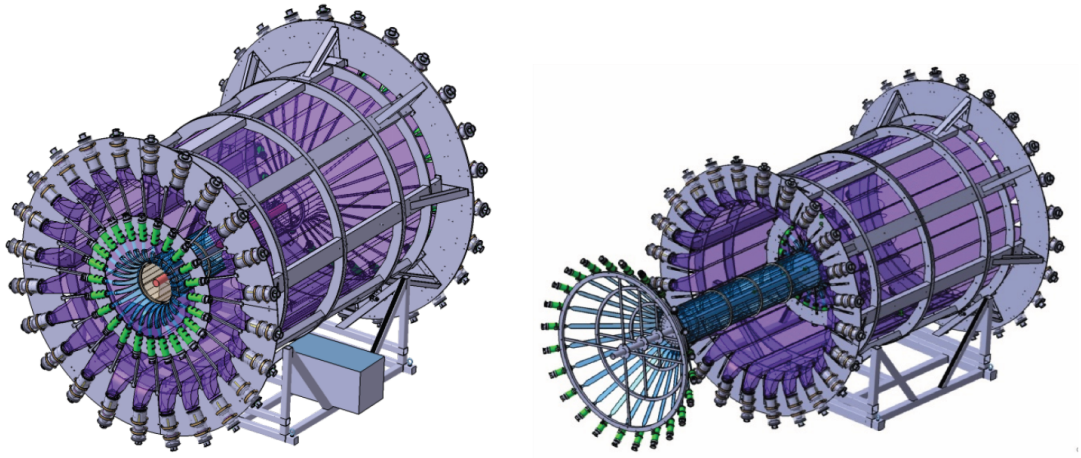

Fig. 2.7: A schematic 3D view of the CAMERA detector. Taken from [21]. Upstream view shown in the left figure, the downstream view on the right.

scintillator material v_{A_i}, v_{B_j} and the CAMERA calibration constants C_{A_i}, C_{B_j}

$$z_{A_i} = \frac{1}{2} v_{A_i} \left(t_{A_i}^{\text{up}} - t_{A_i}^{\text{down}} \right) + C_{A_i}, \quad z_{B_j} = \frac{1}{2} v_{B_j} \left(t_{B_j}^{\text{up}} - t_{B_j}^{\text{down}} \right) + C_{B_j}. \tag{2.1}$$

The DOF D of the particle between the rings is then given as

$$D_{i,j} = \sqrt{\left(R_{B_j} - R_{A_i} \right)^2 + \left(z_{B_j} - z_{A_i} \right)^2}, \tag{2.2}$$

where the R_{A_i} and R_{B_j} denote the radii of the inner and outer scintillator slab, respectively, from the target centre. The TOF T of the particle between the rings can be derived as

$$T = \frac{\left(t_{B_j}^{\text{up}} + t_{B_j}^{\text{down}} \right)}{2} - \frac{\left(t_{A_i}^{\text{up}} + t_{A_i}^{\text{down}} \right)}{2} + C_{i,j}, \tag{2.3}$$

adjusted to an additional calibration constant $C_{i,j}$, which will be elaborated in the following Section [[↪2.3.1.]]. From these quantities, the particle velocity β and its momentum p can be determined (still assuming $c = 1$)

$$\beta = \frac{D}{T} \tag{2.4}$$

$$p = M\beta\gamma = M \frac{\beta}{\sqrt{1 - \beta^2}}. \tag{2.5}$$

It should be noted, that the raw momentum reconstructed from CAMERA does not take into account the energy losses within the target and the material of the CAMERA scintillators. An additional correction was introduced using the Bethe-Bloch formula. The details on the energy loss correction are given in Ref. [92].

2.3.1 CAMERA Calibration

In the following subsection, the calibration methods used for the 2016 measurements are briefly outlined. For more detailed information, see Ref. [21, 20].

The CAMERA calibration is performed in four steps: the calibration of the azimuthal position of each scintillator slab; the calibration of the radial distance from the target; the calibration of the longitudinal z-position of a hit; and the calibration of the TOF. For these calibration procedures, four different types of particles are used:

- Recoiled protons from the exclusive ρ^0 muoproduction.
- Recoiled protons from the elastic pion-proton scattering: The advantage of the pions is a very high rate of elastically scattered protons from the target. The elastic process allows for an easy prediction of the proton trajectory from measurement of the incident and scattered pion only. The predicted trajectory is then compared with the measured hits from the CAMERA.
- Cosmic muons without the presence of the beam or magnetic field.
- δ-rays from the target.

Azimuthal φ Calibration

Each of the 24 scintillator slabs has a nominal central azimuthal position, corrected by a calibration coefficient,

$$\forall i \in [0, 23] \begin{cases} \varphi_{A_i}^{\text{nom}} &= 120 - \frac{360}{24} i + \varphi_{A_i}^{\text{calib}} \\ \varphi_{B_i}^{\text{nom}} &= 120 - \frac{360}{24} i + 7.5 \varphi_{B_i}^{\text{calib}} \end{cases}$$

The calibrated azimuthal positions are obtained from the exclusive ρ^0 data. They are computed from the correlation of the signal received from each sector with the expected position from the spectrometer prediction $\varphi_{[A,B]}^{\text{spec}}$ [20].

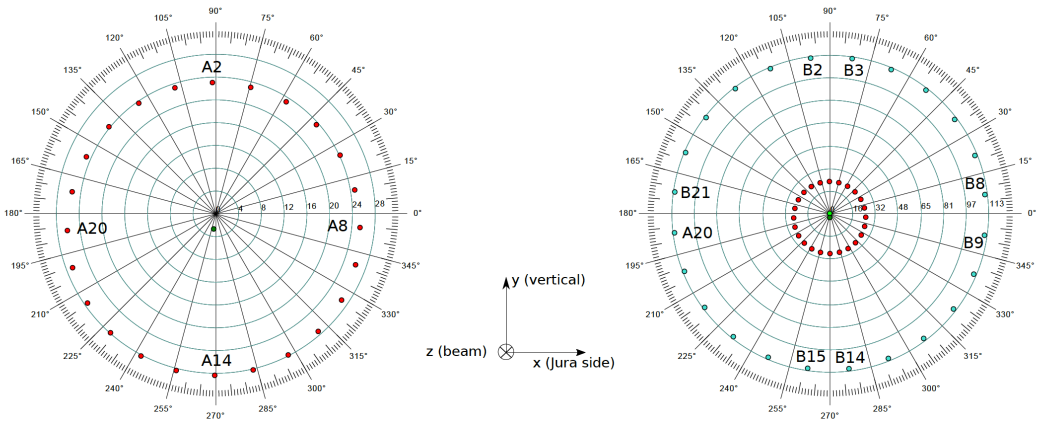

Fig. 2.8: To the left, the radial positions of the ring A slabs are displayed in red, the effective centre in green. To the right, the radial positions of ring B slabs are shown in turquoise and the effective centre in light green. The black lines in both figures denote the nominal positions of the scintillator centres (every 15°) [20].

Radial Calibration

The nominal radii of the slabs in A and B ring are 25 and 110 cm, respectively. The data from a geometrical survey suggests that the radii are slightly larger, $r_A^{\text{nom}} = 25.7$ cm and $r_B^{\text{nom}} = 111.6$ cm, and the axes of both rings are deviated from the z axis. The azimuthal calibration of CAMERA provides an estimation of the alignment of the rings based on the deviation from the nominal azimuthal position of each slab.

From the fit $F(\varphi) = p_0 + p_1 \sin(p_2 \cdot \varphi + p_3)$ of the azimuthal deviations, the effective center of a particular ring can be obtained in polar coordinates with respect to the origin, as shown in Fig. 2.8. The measured deviation of ring A is $\delta x = -0.373$ cm and $\delta y = -2.66$ cm, and deviation for ring B $\delta x = -0.405$ cm and $\delta y = 0.279$ cm. Given the default size of the ring B, it was decided to neglect the deviation for this ring in the data analysis and ring B was considered as concentric around the z-axis [20].

Longitudinal Calibration

The position of a hit in a CAMERA scintillator along the z-axis is reconstructed from the difference of the two time stamps from the upstream and downstream PMTs, as defined in Eq. 2.1. In order to obtain the calibration parameters v_{A/B_i} and C_{A/B_i}, the estimation of the longitudinal position of a hit in ring B z_{B_i} is required. This quantity is extracted from the information from the spectrometer combined with the kinematic fit (the method of kinematic fit is described in [[↪4.]]) as follows:

$$z_{B_i}^{\text{spec}} = \frac{R_{B_i} - r_{\text{vtx}}}{\tan\left(\theta_{p'}^{\text{spec}}\right)} + z_{\text{vtx}}, \tag{2.6}$$

where $r_{\text{vtx}} = \sqrt{x_{\text{vtx}}^2 + y_{\text{vtx}}^2} \cdot \cos\left(\varphi^{\text{spec}} - \varphi_{\text{vtx}}\right)$ (in which the $\varphi_{\text{vtx}} = \arctan y_{\text{vtx}}/x_{\text{vtx}}$), and $\theta_{p'}^{\text{spec}}$ is the polar angle of recoiled proton obtained from the spectrometer information. From the Eq. 2.1 and 2.6 one can extract the calibration parameters v_{B_i} and C_{B_i}. For the prediction of the longitudinal position in ring A $z_{A_i}^{\text{pred}}$, an interpolation between the vertex position and the calibrated ring B position is performed using:

$$z_{A_i}^{\text{pred}} = \frac{R_{A_i} - r_{\text{vtx}}}{R_{B_i} - r_{\text{vtx}}} \cdot \left(z_{B_i} - z_{\text{vtx}}\right) + z_{\text{vtx}}. \tag{2.7}$$

Time-of-flight and Momentum Calibration

To obtain the real TOF and DOF, the calibration constants $C_{i,j}$ have to be determined to correlate the time response of the two rings. If we rewrite the Eq. 2.3 to a more condensed form:

$$T = T_{i,j}^{\text{raw}} + C_{i,j}, \tag{2.8}$$

we can express the calibration constants as

$$C_{i,j} = \frac{D_{i,j}}{\beta c} - \frac{t_{B_j}^{\text{up}} + t_{B_j}^{dn}}{2} + \frac{t_{A_i}^{\text{up}} + t_{A_i}^{dn}}{2} = \frac{D_{i,j}}{\beta} - T_{i,j}^{\text{raw}} \tag{2.9}$$

The recoiled proton velocity β, however, depends not only on the initial proton momentum that for an exclusive process can be obtained from conservation laws, but also on the unknown energy loss of the low-momentum particle in the target. In order to determine the proton velocity, two possible tests can be performed. One uses the cosmic muons and its advantage lies in being independent on any other measured physics process using the standard muon beam [21].

The second method utilises the strong correlation between the uncalibrated TOF $T^{\text{raw}}_{i,j}$ and the DOF $D_{i,j}$ [20], illustrated in Fig. 2.9. It is assumed that the correlation is caused by the δ-rays from the target traversing through the inner to the outer CAMERA ring. The proton velocity in Eq. 2.9 is replaced by the velocity of the δ-electrons β_δ. And with the known velocity, one can obtain the calibration constants $C_{i,j}$ from the Eq. 2.9 [20].

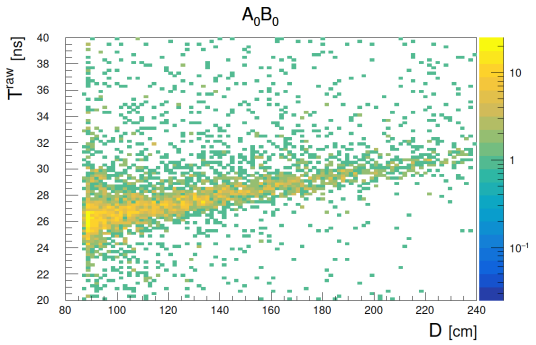

Fig. 2.9: The uncalibrated time-of-flight distribution T^{raw} as a function of distance-of-flight D for the scintillator pair (A0, B0). The linear fit is applied to extract the mean velocity of δ particles [20].

CAMERA in Monte Carlo Simulations

Simulation of the response of all detectors to the passing particles was done using the TGEANT framework [89], which is based on GEANT4 [112]. The interaction of each particle with the CAMERA scintillator material is defined by the position, time and the deposited energy $(x_{\text{MC}}, y_{\text{MC}}, z_{\text{MC}}, T_{\text{MC}}, \text{d}E_{\text{MC}})$. Light from these 'hits' is propagated to the upstream and downstream PMTs. The time stamps are then obtained from Eq. 2.1 as

$$\begin{aligned} t^{\text{up}}_{[A,B]_i} &= T^{\text{MC}}_{[A,B]_i} + \frac{z_{\text{MC}} - C_{[A,B]_i}}{v_{[A,B]_i}} \\ t^{\text{down}}_{[A,B]_i} &= T^{\text{MC}}_{[A,B]_i} - \frac{z_{\text{MC}} - C_{[A,B]_i}}{v_{[A,B]_i}}, \end{aligned} \tag{2.10}$$

where the constants $C_{[A,B]_i}$ and $v_{[A,B]_i}$ are obtained from the calibration of the real data (RD). Hits within 10 ns range in each PMT are merged together and saved as one hit, to emulate the PMT dead time. Using the MC time stamps, MC tracks

in CAMERA are reconstructed in the same fashion as in RD, with the exception of the TOF calibration, which is set to 0 for MC.

In order to reproduce the experimental resolution, a Gaussian smearing of the longitudinal position has been included, in a form of a standard deviation of the longitudinal hit position Eq. 2.1

$$\sigma\left(z_{[A,B]}\right) = \frac{\sqrt{\sigma^2\left(t^{\mathrm{up}}_{[A,B]_i}\right) + \sigma^2\left(t^{\mathrm{down}}_{[A,B]_i}\right)}}{2} \cdot v_{[A,B]_i} \tag{2.11}$$

The longitudinal resolution $\sigma(z_{[A,B]_i})$ is extracted from the distribution $\Delta z^{\mathrm{data}}_{[A,B]} = z_{[A,B]} - z^{\mathrm{spec}}_{[A,B]}$ from the RD. Assuming that the upstream and downstream PMTs have the same resolution, the Eq. 2.12 leads to

$$\sigma\left(t_{[A,B]_i}\right) = \frac{\sqrt{2}}{v_{[A,B]_i}} \cdot \sigma\left(z_{[A,B]}\right) \tag{2.12}$$

The distributions $\Delta z^{\mathrm{data}}_{[A,B]} = z_{[A,B]}$ are a convolution of the resolutions of the spectrometer and of the CAMERA. The spectrometer resolution is well reproduced by the TGEANT MC simulation. The pure CAMERA resolution is then extracted from

$$\sigma^2\left(z_{[A,B]}\right) = \sigma^2\left(z_{[A,B]}\right)^{\mathrm{data}} - \sigma^2\left(z_{[A,B]}\right)^{\mathrm{MC}}, \tag{2.13}$$

with the assumption that the convolution of CAMERA and spectrometer resolutions is a simple convolution with a Gaussian distribution. The obtained smearing values are following

$$\begin{aligned} \sigma\left(z_A\right) &= 3.54 \text{ cm} \\ \sigma\left(z_B\right) &= 2.47 \text{ cm} \end{aligned} \tag{2.14}$$

2.4 The Spectrometer

The COMPASS spectrometer consists of two stages, the *Large Angle Spectrometre* (LAS) and the *Small Angle Spectrometre* (SAS) equipped with bending dipole magnets, SM1, and SM2, respectively. It has a variety of tracking detectors, electromagnetic and hadronic calorimeters, and a muon identification. For particle identification. For particle identification, there are two muon detectors and a *Ring Imaging Cherenkov detector* (RICH) detector. The angular acceptance of the spectrometer reaches up to 180 mrad.

2.4.1 Tracking Detectors

The 60 m long spectrometer is equipped with various tracking detectors of various types, depending on the transverse size of the detector active area and the distance with respect to the target area. The trackers are divided into three groups: *Very Small Area Trackers* (VSAT), *Small Area Trackers* (SAT), and *Large Area Trackers* (LAT). VSATs are positioned close to the beam axis, and possess a very high rate stability and a high spatial and time resolution, as they are required to distinguish secondary particles from the beam halo. Among the VSAT belong the *Scintilating Fibers* (SciFi), *silicon microstrip trackers* (SILICON), *Pixel Gas Electron Multiplier* (Pixel-GEM) detectors, and central regions of the *Pixel Micro-Mesh Gaseous Structures* (Pixel-MicroMegas). With the increasing radial distances from the beam axis, the resolution plays decreasingly important role, while the requirement on the geometric coverage increases. SAT, which are located at distances of about 2,5 cm to 40 cm from the beam axis, compromise between a good resolution and a large coverage. Among these detectors belong the *Gas Electron Multiplier* (GEM) and the outer parts of the Pixel-MicroMegas. LAT have a large spatial coverage allowing for a large acceptance. Among the LAT belong *Multi-Wire Proportional Chamber* (MWPC), *Drift Chamber* (DC) and one Straw detector. The active area and the spatial and time resolution of all the VSAT, SAT, and LAT trackers are summarised in Table 2.1. Large number of the tracking planes along the spectrometer allows for a high reconstruction efficiency, not particularly sensitive to the performance (or lack there of) of any individual detector. Details on the principle of operation of each tracker type can be found in [85].

2.4.2 Particle Identification

In order to determine a particle species associated with the measured momenta and charged tracks, the spectrometer is geared with the RICH detector, 2 muon walls, 3 electromagnetic and 2 hadron calorimeters. Neither hadron calorimeters nor RICH were not used in the presented measurement of exclusive π^0 production, thus they will not be discussed here.

Group	Type	A [cm^2]	δ_x[μm]	δ_t[ns]
VSAT	SciFi	$3.9^2 - 12.3^2$	$130 - 210$	0.4
	SILICON	5×7	$8 - 11$	2.5
	Pixel-GEM	10×10	95	9.9
VSAT SAT	Pixel-MicroMegas	pixels on 5×5 strips on 40×40	90	9
SAT	GEM	31×31	70	12
LAT	MWPC	$178 \times 90 - 120$	1600	N/A
	DC	180×127	$190 - 500$	N/A
	Straw	280×323	190	N/A

Tab. 2.1: An summary of the tracking detector technologies used in COMPASS spectrometer. A denotes the active area of each detector, δ_x and δ_t represent the spatial and time resolution, respectively [85].

Muon walls

The muon detection takes advantage of its long life-time and small cross section of its interaction with matter. The muon detectors, called *Muon Wall* (MW), 1 and 2, utilise heavy absorbers to distinguish scarcely-interacting muons from other charged particles. The MW1 is placed in LAS and consists of two tracking planes surrounding a 60 m thick iron absorber, Muon Filter 1. The MW2 is located in SAS and uses tracking stations behind a 2.4 m concrete absorber, Muon Filter 2. The tracking systems of MW1 and MW2 work on a principle of gaseous wire detectors in drift tubes.

Electromagnetic Calorimeters

Each stage of the spectrometer is equipped with three electromagnetic calorimeters (ECAL0, ECAL1, and ECAL2). The ECAL0, placed 3 m downstream from the target, was introduced for the first time for the 2012 GPD pilot run. It allows detection of photons large polar angles, as the Fig. 2.10 illustrates. For the 2016/17 data-taking, the aperture of the detector was enlarged, allowing to improve the coverage in the high x_B region. The photons at medium polar angles are captured by ECAL1, which is located at a distance of 13 m from the target centre. The

photons at small polar angles are detected in ECAL2, located in SAS. The ECAL2 was not used in the exclusive π^0 measurement, due to the low occupancy of photons from high-energetic exclusive π^0 mesons at very small polar angles.

The construction of the COMPASS electromagnetic calorimeters is mostly based on lead glass or shashlik modules of different sizes and radiation lengths, as is depicted in Fig. 2.11. The lead glass functions as the absorption and the detection material at the same time. The incoming photon is converted into an electromagnetic shower. The resulting Cherenkov radiation from electrons and positrons is detected by photomultiplier tubes. The shashlik modules alternate lead layers with scintillating material. In the lead occurs the photon conversion into e^+e^- pairs, which then produce light in the scintillating layer. The radiation is collected by 16 wavelength-shifting optical fibers and transferred in photomultipliers or micro-pixel avalanche photodiodes. The amount of light collected in a given module is proportional to the amount of energy deposited in the module. To obtain the energy, various module, time and energy-dependent calibrations ⟦↪3.⟧ need to be taken into account.

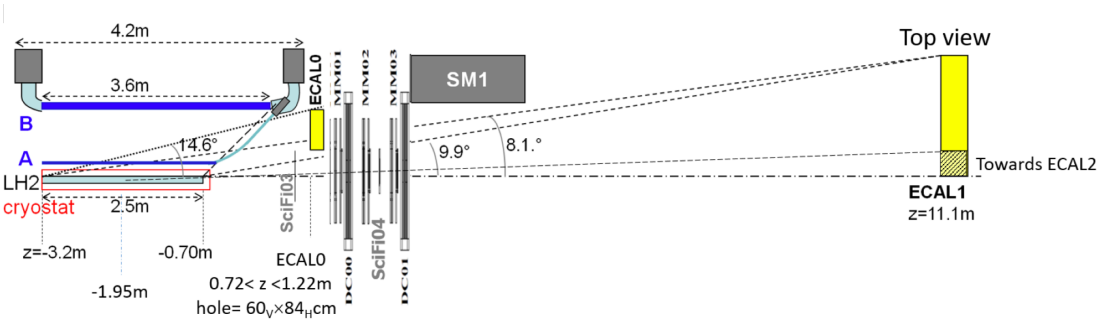

Fig. 2.10: The scheme demonstrates the angular acceptance of the two calorimeters used in the exclusive π^0 production, ECAL0 and ECAL1. Taken from Ref. [20].

ECAL	Active area	Module size	Channels	Energy res. $\frac{\Delta E}{E}$
ECAL0	102×102 cm^2	39.6×39.6 mm^2	1746	$0,07\sqrt{\frac{\text{GeV}}{E}} \oplus 0,02$
ECAL1	$4 \times 2,9$ m^2	$(38)^2 - (140)^2$ mm^2	1476	$0,06\sqrt{\frac{\text{GeV}}{E}} \oplus 0,02$
ECAL2	$2,4 \times 1,8$ m^2	38×38 mm^2	3072	$0,06\sqrt{\frac{\text{GeV}}{E}} \oplus 0,02$

Tab. 2.2: Properties of the electromagnetic calorimeters at COMPASS.

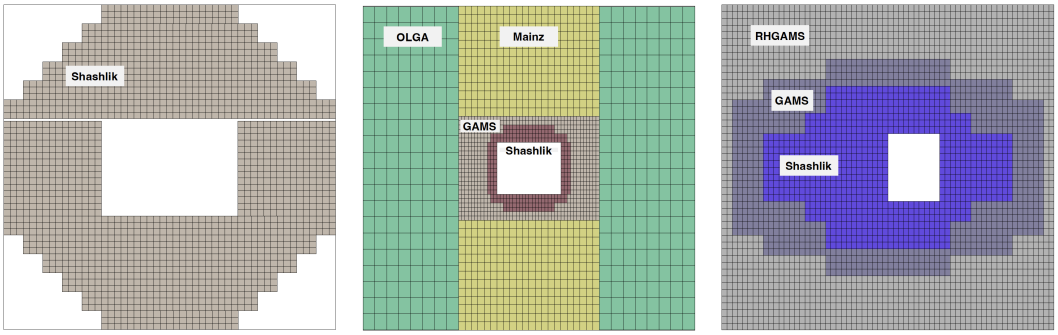

Fig. 2.11: 2D $X - Y$ projections of the COMPASS electromagnetic calorimeters: The ECAL0 (left) is exclusively made of shashlik modules. The ECAL1 (centre) is composed from shashlik modules around the beam hole, surrounded by lead glass modules, called GAMS[3], and the outer part are covered by larger lead glass modules called Mainz and Olga. The ECAL2 (right) consists of shashlik modules in the centre, GAMS, and RHGAMS. Figures are generated by the PHAST software for COMPASS physics analysis [98].

2.5 The Trigger System

Due to the high intensity of the beam typically used in the COMPASS experimental programme, a trigger system [93] is necessary to filter interesting physics events. The trigger system works on a principle of a first level trigger. The scheme of the layout of triggers throughout the spectrometer is shown in Fig. 2.12. The information is transferred to the read-out and front-end electronics via the trigger control system. The latency between the initial muon interaction and the trigger decision is in the order of 1 µs. No higher level trigger was employed for the measurements. In this analysis, two main types of trigger were used: the muon trigger, registering scattered muons, and the random trigger. The scattered muon detection is based on coincidences between several pairs of scintillating hodoscopes segmented in vertical or horizontal direction. The coincidence logic is described by coincidence matrices.

2.5.1 The Muon Trigger

The muon trigger serves for detection of the scattered muon, while rejecting halo muons by the veto system. It has been originally implemented for DIS measurements allowing for a wide coverage in Q^2 and x_B. The muon trigger uses two different methods of scattered muon detection: based on the energy loss, and the track origin. Both principles are illustrated in Fig. 2.13.

- The energy loss trigger uses the deflection of the muon track in the dipole field of the spectrometer magnets SM1 and SM2 to determine the energy loss. It works on a principle of coincidences of vertically oriented slabs in two hodoscope stations in the *Ladder Trigger* (LT) system, H4L and H5L. Both stations are placed behind the muon filters close to the rear end of the spectrometer, covering small muon scattering angles (or $Q^2 < 0.5$ GeV^2)

- The target pointing triggers use coincidences in hodoscope stations with horizontally oriented slabs, i.e. sensitive along the non-bending direction in the dipole magnetic field ($Z - Y$). The measured points of a track are extrapolated to the target area, $Z = 0$, where the intersection with the target volume is tested. There are three target-pointing trigger systems: MT with

stations H4M and H5M, the *Outer Trigger* (OT), with hodoscopes H3O and H4O, and the *LAS Trigger* (LAST), equipped with hodoscopes H1 and H2. This method is used for large scattering angles ($Q^2 > 0.5$ GeV^2).

As was already mentioned above, in order to distinguish between the scattered muon and the beam halo, a veto is implemented upstream of the target area. It consists of two stations, which can detect particles distant from the beam axis and tag them in an anti-coincidence with the rest of the trigger system. The downside of using a veto is the dead time it introduces for the measurement. The knowledge of the veto dead time is essential to precisely determine the effective beam flux.

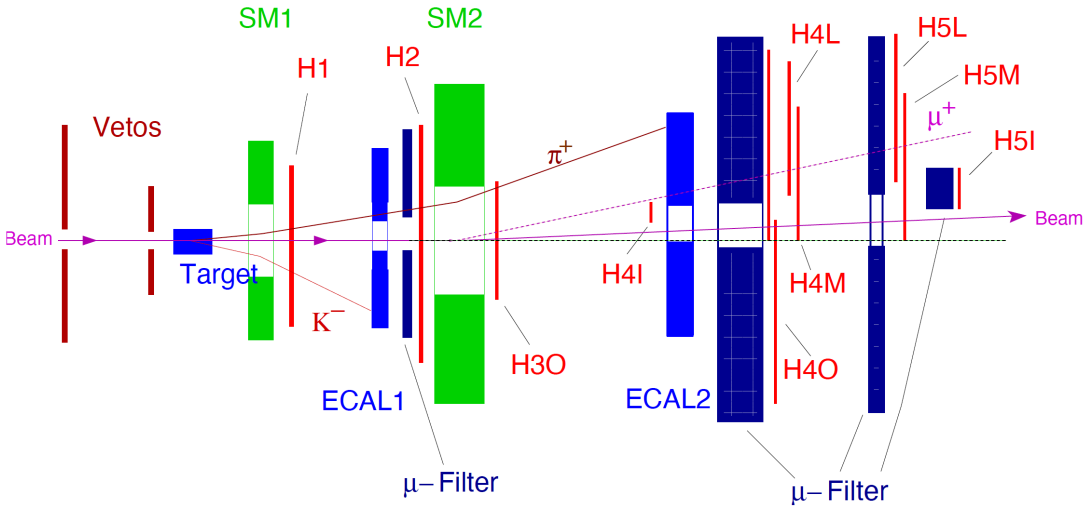

Fig. 2.12: Scheme of the trigger layout within the COMPASS spectrometer [94].

2.5.2 The Random Trigger

The *Random Trigger* (RT) is generated by β^+ decay of a $^{22}_{11}$Na source. The positron annihilates with an electron, creating two 511 keV photons, which are detected in coincidence by two scintillators surrounding the source. It is located in a separate facility far from the spectrometer to avoid any correlation with the beam or any activity in the target. The random trigger is a key ingredient for the calculation of the beam flux.

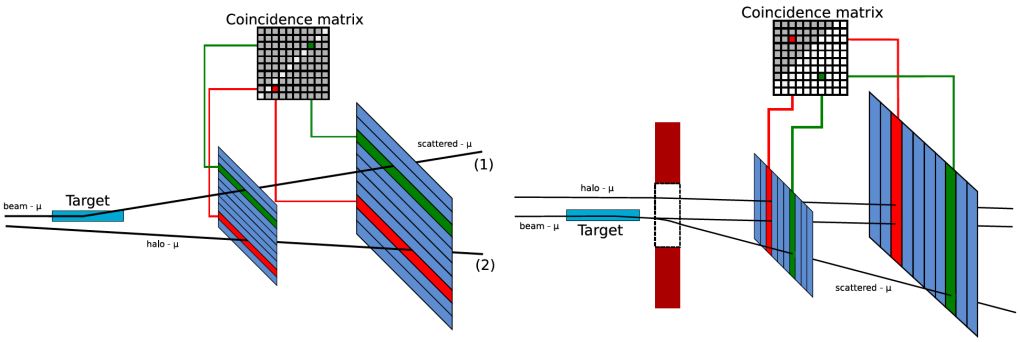

Fig. 2.13: The principle of target pointing (left) and energy loss (right) coincidence matrices [94].

2.6 Data Acquisition System and Data Reconstruction

The *Data AcQuisition* (DAQ) gathers information contains and process approximately 300000 channels. The scheme of the DAQ flow is shown in Fig. 2.14. The first layer of the data acquisition consists of the front-end electronics. Its purpose is digitising the raw analog signals from the detectors and pre-amplification of pulses, when necessary. There are three types of front-ends, depending on the detector: Combination of a discriminator with a *Time-to-Digital Converter* (TDC) converters for recording time stamps. Analog-to-digital (ADC) converters for sampling and digitising analog pulses. Combination of a discriminator and a scaler to record hit rates.

The front-ends are synchronised with the DAQ by the *Trigger Control System* (TCS). The second stage of the DAQ is the read-out. There are different types of the read-out boards: *COMPASS Accumulate, Transfer and Control Hardware* (CATCH) modules, *GEM and Silicon Control and Acquisition* (GeSiCA), Hot GeSiCA (HGeSiCa gathering information from calorimeters) modules, and the *Generic Advanced Numerical Device for Analog and Logic Functions* (GANDALF) modules, which read out signals from the CAMERA PMTs. When a signal is sent by the TCS, the read-out boards are activated to collect data and append them to the TCS metadata (spill and event number) to comprise the basic data structure used by the rest of the DAQ, at a global frequency of 10 kHz. The event-by-

event data blocks from the read-out modules are then transmitted directly to the multiplexers, or via optical Slink or *Trigger Implementation for GANDALF Electronic Readout* (TIGER) modules. Slink and TIGER modules reduce the number of inputs and combine them to a larger data unit. The *Field Programmable Gate Array* (FPGA) multiplexers further process up to 15 links and reduce them to one output, which is then transferred to the event-building switch. The TIGER module, in particular, is used to process data from the GANDALF front-ends. The TIGER module is capable of processing up to 18 GANDALF front-ends (only 12 were used to gather data from all the 96 channels from CAMERA PMTs). The output from TIGER is then transmitted to multiplexers through optical Slink fibre.

The typical event size is 45 kB. The data in chunks of a size of 1 GB are sent to four read-out computers (PCCORE) via spill-buffer cards, which provide further processing. The data are temporarily stored in PCCORE machines (capacity of 32 TB), about 1% of the data is used for online monitoring. The final step is the transfer to the permanent CERN storage repository, *CERN Advanced STORage manager* (CASTOR). The current DAQ is in use since 2014. Except of the more efficient hardware solution to the data acquisition, the new DAQ brought an improved stability and excellent up-time performance, which reached 99% during the data-taking of 2017.

The collected raw data from the detectors have to be processed by a reconstruction software in order to extract the topology and kinematics of each physical event. The reconstruction is performed offline by the *COMPASS Reconstruction AnaLysis software* (CORAL). CORAL is a C++ based modular framework, used for real data and simulations, calibrations, and computation of detector efficiencies. The first stage of the real data reconstruction is decoding, using the DAQ data decoding library, while the Monte Carlo data are subjected to digitisation of the hits in detectors to mimic ADC/TDC responses. It concerns the fact that a particle crossing a detector typically fires more than one channel creating a hit cluster. In MC a clusterisation procedure is employed to merge neighbouring hits or detector channels together, as mentioned MC simulation of CAMERA ⟦↩2.3.⟧. After decoding of the data and clusterisation of the simulations, both can be treated in the same manner, leading to the reconstruction of tracks, and calorimeter and RICH information. The procedure of charged track reconstruction

utilises the Kalman algorithm [97]. The tracks are combined into a fit of the vertex within the target area. The Kalman algorithm determines whether a particular hit belongs to a certain track and interaction vertex. Reconstructed tracks, vertices, calorimeter clusters, and information on the particle identification, together with the respective uncertainties, are then saved into reconstructed data file in mini Data Summary Trees (mDST) format. From this point the data are ready for physics analysis using the *PHysics Analysis Software* (PHAST) [98]. PHAST is a ROOT [99] based framework containing functions to access and analyse information from the mDSTs.

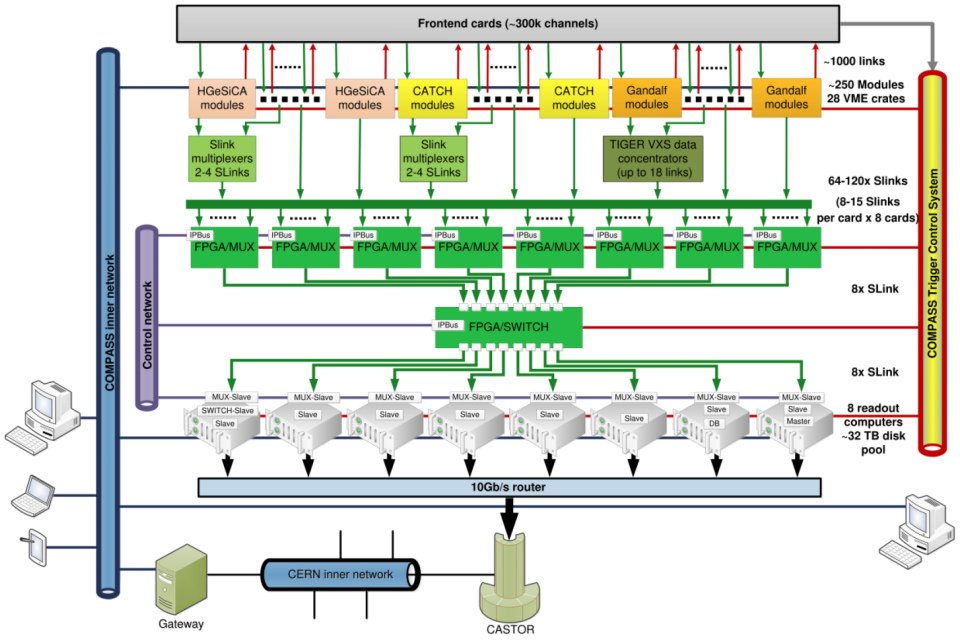

Fig. 2.14: A scheme of the COMPASS DAQ framework [96].

The reconstruction of CAMERA data is not performed by CORAL. Two versions of a specific code has been developed by the CEA institute in Saclay (A. Ferrero, A. Vidon, and B. Ventura), and by the Freiburg group (P. Jörg and M. Gorzellik). The two tools showed differences in the recoil proton candidates reconstruction up to 3%. After internal discussions, the Saclay code was chosen. Except of the recoiled protons tracks reconstruction, the Saclay code implements CAMERA calibrations [[↪4.]] and corrections for energy losses [20].

3 ECAL Calibrations

This chapter will present the procedure of the calibration of the electromagnetic calorimeters ECAL0, ECAL1, and ECAL2, and the issues that were encountered during the 2016/17 data analysis campaign. The author participated in the investigation of the problem with LED calibration inefficiency, manifesting itself in ECAL2 in particular, and in the deployment of the solution and storing the data in the production database.

3.1 Introduction

The purpose of electromagnetic calorimeters in the exclusive reactions programme was to detect outgoing photons, either a single photon from the DVCS process, or a pair of photons from the exclusive π^0 decay. For the exclusive π^0 production channel, only two of the three COMPASS ECALs were used, ECAL0 and ECAL1. ECAL2 is located in the SAS region of the spectrometer, and records photons from events with a large ν, which are very scarce, as is illustrated in $[\![\hookrightarrow 4.]\!]$. ECAL0 serves to detect low energetic π^0 with photons emitted at large angles, and captures the majority of exclusive π^0 events (about 2/3). ECAL1 detects middle-energetic π^0, however, it encompasses a large part of the experimental acceptance of the spectrometer $[\![\hookrightarrow 5.]\!]$.

In order to ensure the optimal operation of the electromagnetic calorimeters, there are two main types of calibration, the time calibration and the energy calibration. Apart from these, any bad cells (i.e. inactive, or ineffective) are identified and removed during for the reconstruction procedure of the data. The calibrations are obtained from the data from a time range of the data-taking characterised by a particular beam charge (μ^+ or μ^-), called sub-periods, lasting from 3 to 5 days. They are applied during in the next iterations of reconstruction. The sample of events is limited by the requirements of the virtual photon momentum $Q^2 > 0.8$ $(\mathrm{GeV}/c)^2$ and cluster energy lower threshold $E_\gamma > 1$ GeV.

3.2 Time Calibration

In order to detect a noisy or defective channel in the calorimeters and synchronise the cell time with the time information from triggers, a time (T0) calibration is performed, T0 being the difference of the cell time and trigger time. The T0 calibration is performed on the total of 6424 cells of all three calorimeters [20]. The cell time is obtained from analog signals from the PMTs attached to each ECAL cell. The signals are passed through a shaper module to enhance the signal amplitude, and digitally converted in Sampling analog-to-digital converters. 32 samples are then extracted from the wave front of the signal and used to obtain the amplitude and time.

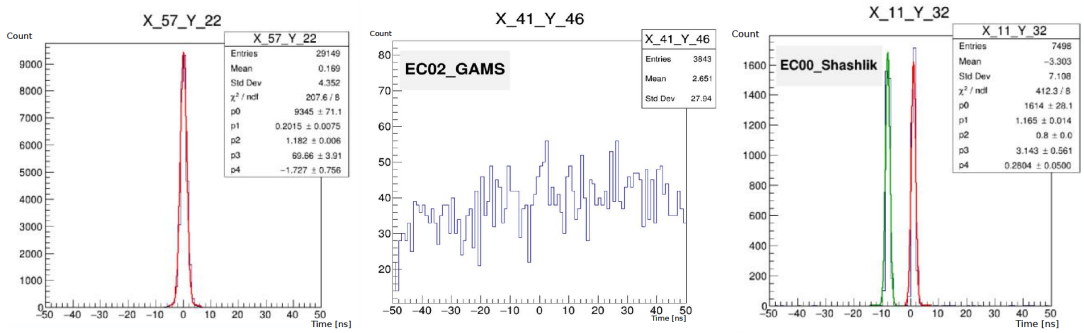

Fig. 3.1: Example of different responses of the ECAL cells during the time calibration of ECALs. On the leftmost, a good cell response is shown, with a single well-defined peak. In the middle, a case of a noisy cell is demonstrated, which contains no peak, such a cell is excluded from the data reconstruction. On the rightmost side, a case of a double peak is presented with the second peak fitted with a green curve. Taken from Ref. [20].

The example plot of the comparison of the trigger time with the cell time is shown in Fig. 3.1. This figure illustrates a clean response from a cell, while a bad behaviour, such as noise (nonexistent peak) or other pathological behaviour (such as a double peak) is demonstrated in Fig. 3.2. When a cell non-responsive (“dead") or noisy cell is detected, it is removed from the next iteration of reconstruction procedure, not to bias the overall signal from other cells, and to improve the efficiency of the clusterisation procedure.

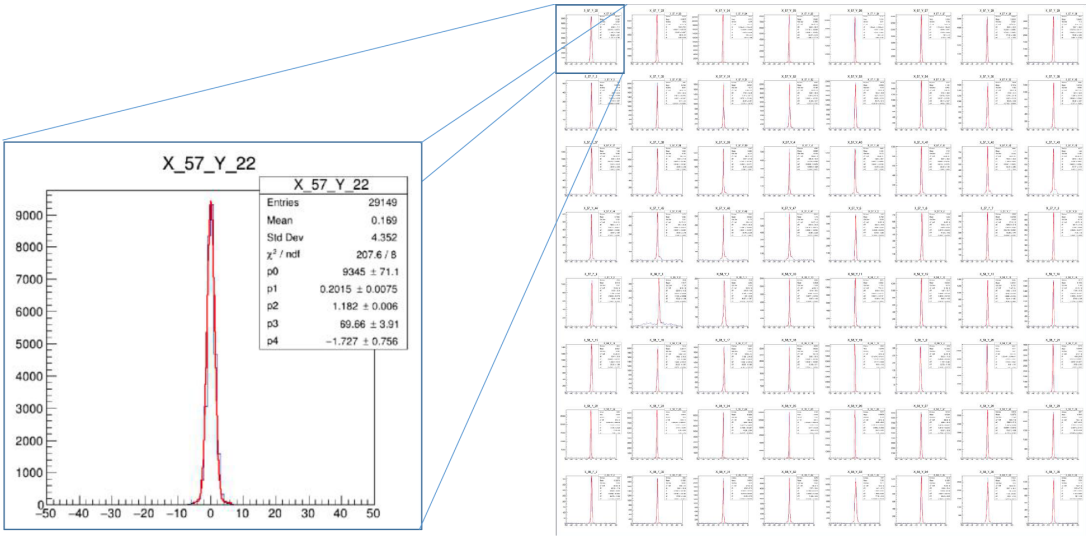

Fig. 3.2: An example of a comparison of the cell time with trigger time from a particular cell. This plot shows a good cell response. The red line indicates a fit with a model function of a Gaussian with a polynomial of the first order [20].

The cells showing other pathological behaviour, such as double peaks, require a more granular analysis, typically leading to discovering an instability in the cell response in a given sub-period. Such a discrepancy is removed in the consequent data reconstruction by introducing a correction factor of the peak position obtained from the time calibration, as illustrated on the right band in Fig. 3.3, which represents the peak positions in time obtained from the same problematic cell as shown in Fig. 3.2.

ECAL Timing Cuts

The output of the time calibrations is used as a basis for the quality cut on a cell timing. The Fig. 3.4 illustrates the cut that is performed on a dependency of difference of the relative cell time and the trigger time T0, with respect to the cluster energy. It can be seen, that the T0 peak width changes with the rising cluster energy. The cut was performed as a $\pm 3\sigma$ around the T0 peak. The figure also illustrates the feature of multiple peaks visible from several calorimeters and different module types. This figure was taken for the data-taking period P07 of an early data production, without any time calibration. In the final production

these problems were resolved by iterative correction from the time calibration. The origin of the time shift resulting to the multiplication of the T0 peaks remains to be unknown, however there was no indication of miscalibration [20].

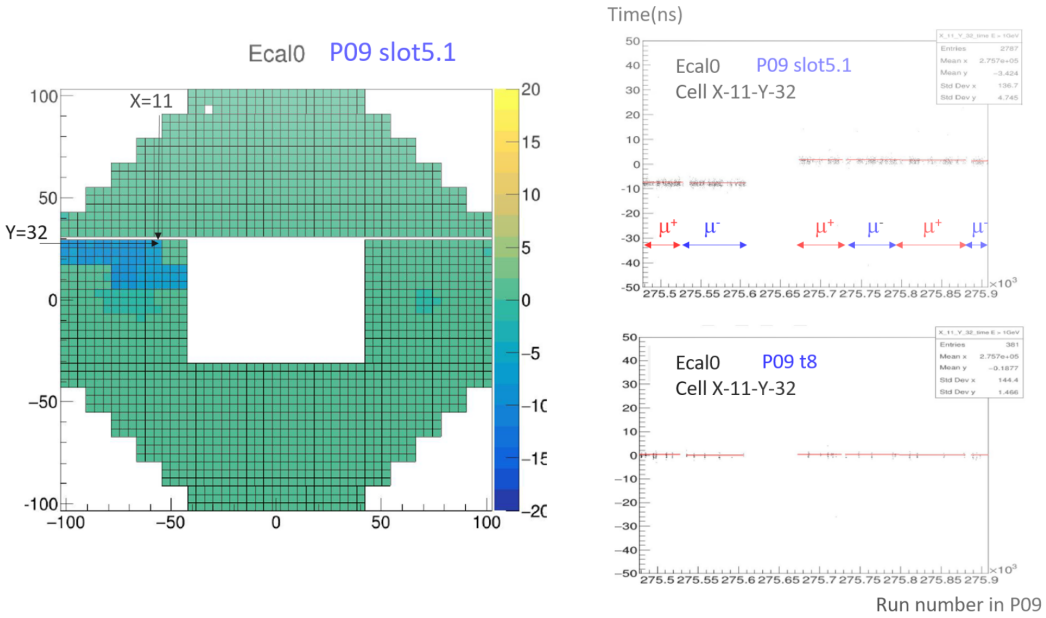

Fig. 3.3: The result of the time calibration of the ECAL0 for a data period (composed of three to four sub-periods with different beam polarisation). The left figure shows the layout of the ECAL0 cells with the mean relative time. One can notice a single dead cell in the right-upper part of the calorimeter, and below the region of cells, where a shift in the mean time occurred within the period. The right band shows one of the affected cells (X11-Y32) before the applied calibration (upper) and after (lower). Taken from Ref. [20].

Bad Cells Removal

Due to the low statistics available for the time calibration over a sub-period of data the algorithm of the identification of bad cells tends to misinterpret noise fluctuations as false peaks. This behaviour needs to be prevented, thus a quality criteria on the fit result is applied based on the minimum signal-over-background ratio. In the case of multiple peaks found, the peak with the best signal-to-background ratio is selected. In the case of a cell with too low statistics accumulated within the

sub-period, a recovery procedure is employed, where the cluster energy threshold is lowered to 300 MeV to gain more statistics. There are cases when this behaviour manifests only during a part of a period. A stability criterion is invoked in such cases, where the number of good spills from each sub-period has to reach at least 70% successfully fitted spills in a period. In the case of a cell fails to reach this criterion, it is marked as bad for a given period.

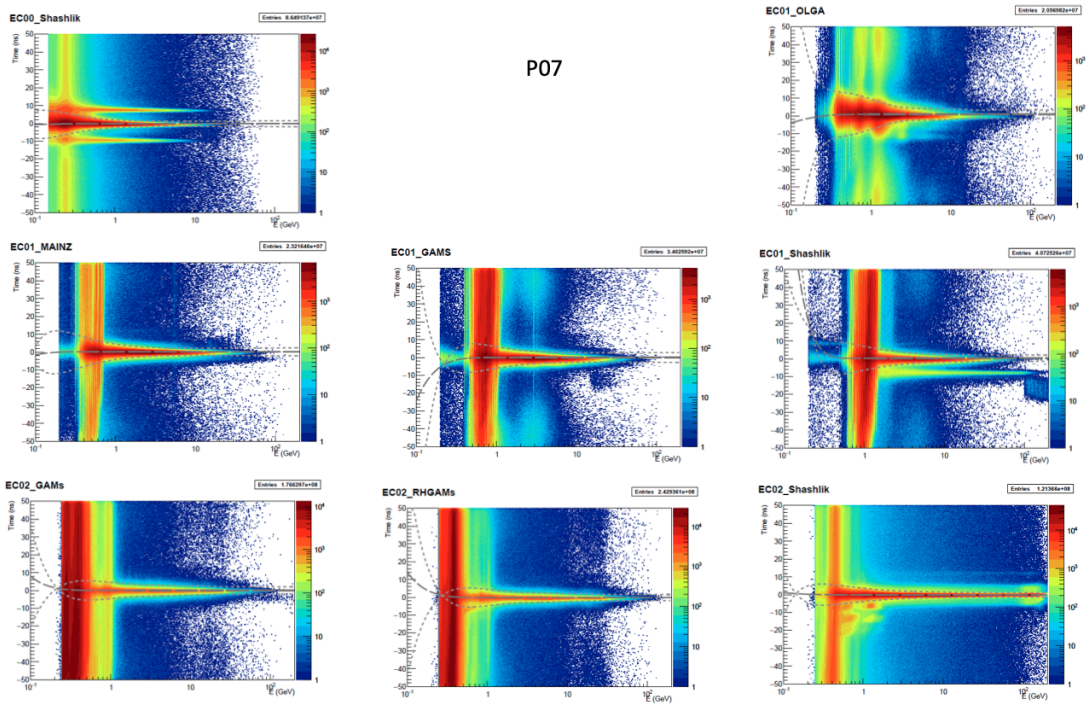

Fig. 3.4: The plots show the relationship between the relative time of the signal from a calorimeter (ECAL0, ECAL1, or ECAL2) for individual cell type with respect to the trigger time (on Y-axis), and the cluster energy (on the X-axis). The dashed lines indicate the timing cut applied at $\pm 3\sigma$ from the signal peak. Taken from Ref. [100].

3.3 Energy Calibration

The energy calibration of the ECALs has three main steps. As will be shown in the following section, some additional post-production calibrations were performed to improve the results further.

Electron Calibration

First step of the ECAL calibration is electron calibration. It is used in the case of ECAL1 and ECAL2. The calibration procedure is automated, i.e. the calorimeter is automatically moved horizontally and vertically between two consecutive spills to expose an individual cell to a 40 GeV electron beam. The total cluster charge, i.e. the sum of the charges of the cell being calibrated and the neighbouring ones collected on the PMTs, is compared to the deposited beam energy. The calibration is performed in several iterations to fine tune the voltage amplifiers used in the ECAL read-out, which allows to keep the ECAL response uniform.

The electron calibration is performed at the beginning of the data-taking each year. ECAL0 cannot be moved with respect to the beam axis, hence the first calibration of ECAL0 is performed with a muon beam of a known energy. Unlike the electron beam the muon beam creates a wide halo, and can illuminate the full calorimeter aperture. The energy deposit in the 25 cm-long shashlik modules then represents the reference for setting of HV of the PMT to give the same response for a given energy.

LED and LASER Calibration

The stability of the electron calibration is monitored periodically during the data-taking by the next step of the energy calibration, the LED and LASER calibrations. This calibration takes into account the stability of the PMT gains of all the 6426 cells. The principle of this calibration is illuminating the cells by a light of a known intensity. The light is generated by LASER diodes in case of ECAL1, and by LED for ECAL0 and ECAL2. The LASER diodes emit a light pulse with a variable amplitude, while the LED diode uses a light of a stable amplitude. The light is delivered to the calorimeter cells by light-guides. The LED and LASER monitoring signals are recorded on a run-to-run basis and applied in the data reconstruction. The correction of the measured PMT amplitude from a cell i and a run j is derived as follows

$$A^{i,j}_{[\mathrm{GeV}]} = A^{i,j}_{[\mathrm{ADC}]} \times C^{i,j_0} \times \frac{L^{i,j_0}}{L^{i,j}}, \tag{3.1}$$

where $A^{i,j}_{[\mathrm{GeV}]}$ denotes the energy deposited in the cell i during a run j, $A^{i,j}_{[\mathrm{ADC}]}$ is the ADC amplitude in the cell i for the run j, C^{i,j_0} represents the conversion coefficient from ADC amplitude to energy in GeV for the cell i provided from the electron

beam calibration during the run j_0, $L^{i,j}$ is the ADC amplitude of the i^{th} cell for the run j, and L^{i,j_0} is the ADC amplitude of the cell i taken during the run j_0 within the electron calibration. It was mentioned above, that the LED amplitude should be stable, ergo the relation $L^{i,j_0}/L^{i,j}$ should be 1. In reality the LED generators have a tendency to fluctuate in time, as will be shown in Section ⟦↪3.4.⟧.

π^0 Calibration

The last step of the standard ECAL calibration procedure is the π^0 calibration. This calibration uses the peak of the π^0 in the invariant mass of photon pairs. It is performed in three phases [101]:

1. The first is a "1D" π^0 calibration, where the π^0 reconstructed mass is used for each calorimeter module, assuming that the π^0 originated from the primary vertex. A 1D histogram with the π^0 mass shift with respect to the PDG value is filled for each of the probed module. The energy correction coefficient for each module (for each data period) is calculated out of the mean of the π^0 peak fitted by a Gaussian+1^{st} order polynomial. The resulting corrections are applied and the procedure is repeated several times. The Fig. 3.5 shows the effect of the 1D π^0 calibration on the π^0 mass shift.

2. The second phase is the time-dependent calibration. It uses 2D histograms with π^0 mass shift as a function of event time in spill. The energy correction factors are calculated from π^0 peak position fitted by a Gaussian $+1^{\text{st}}$ order polynomial in bins on time. These corrections are applied only once. The first row of the Fig. 3.6 shows the effect of the time-dependent π^0 calibrations.

3. The last phase of the π^0 calibrations is performed in several iterations like the first one. The E-dependent calibration is done analogically as the time-dependent calibration, a 2D histogram with π^0 mass shift as a function of cluster energy is filled for each module and fitted with a Gaussian and 1^{st} order polynomial in each cluster energy bin. The effect of this calibration is depicted in the lower row of Fig. 3.6.

In addition to the π^0 calibration applied during the reconstruction, there is post-production run-by-run calibration to take into account the full calorimeter,

instead of individual cells. In total, the full calibration procedure is summarised by the following relation, extended from the Eq. 3.1

$$A^{i,j}_{[\mathrm{GeV}]} = A^{i,j}_{[\mathrm{ADC}]} \times C^{i,j_0} \times \frac{L^{i,j_0}}{L^{i,j}} \times S^{i,p} \times S^{j}, \tag{3.2}$$

where $S^{i,p}$ is the final online π^0 calibration per period p and for calorimeter cell i, and S^j denotes the offline run-by-run correction. To tune the ECAL performance, it was not sufficient to mechanically apply all described calibration steps, but thorough investigation and manual interventions were needed ⟦↪3.4.⟧.

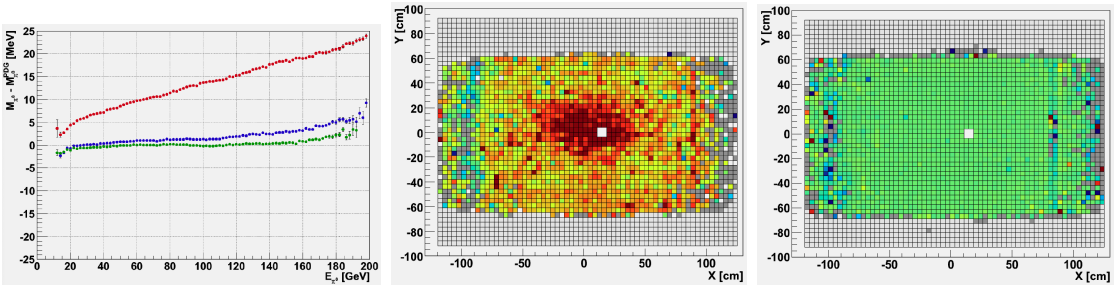

Fig. 3.5: The leftmost part of figure shows the initial mass shift depending on the π^0 energy (in red) the effect of the LED calibrations (in blue, LED calibrations are described in the previous subsection), and the effect of the LED and of several iterations of the 1D calibration on an example of the analysis of COMPASS data from 2010. The middle and rightmost parts demonstrate the π^0 mass shift depending on the cell position in the ECAL2 [101].

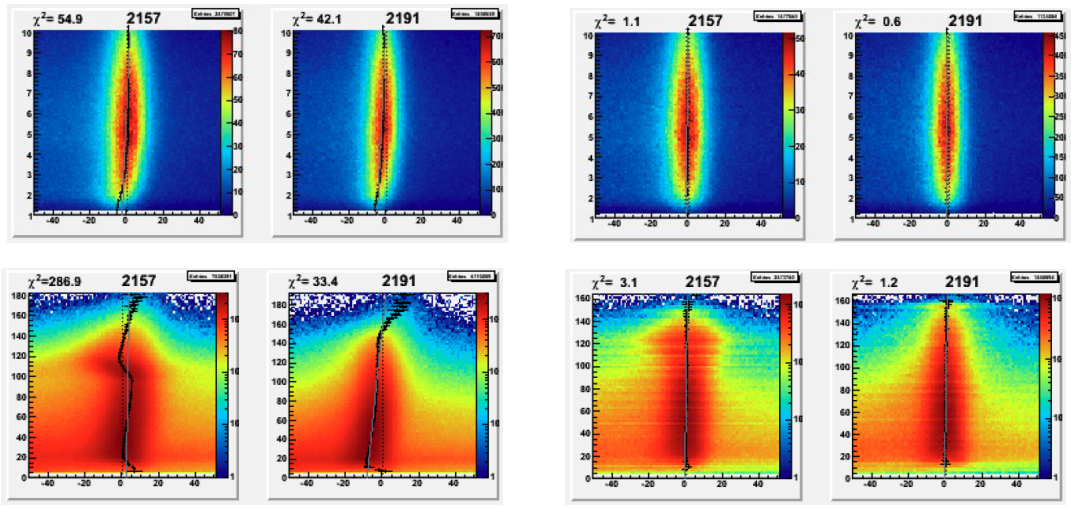

Fig. 3.6: An example of two central cells from ECAL2 (2010 COMPASS data). The upper row shows the effect of the time-dependent π^0 calibration before (left side) and after the application of the calibration. The lower row shows the application of the E-dependent calibration on the same two cells. From [101].

3.4 2016 ECAL Calibrations Challenges

In the 2016 data preparation campaign there were several problems arising during the ECAL calibration. In addition to the complication with the time calibration described above, several problems appeared after application of the LED correction of the energy calibration as described by Eq. 3.1 (in the so-called t2 data production). The Fig. 3.7 illustrates the effect seen in the ECAL2[1]. An inefficiency in the reconstruction of the $\gamma\gamma$ invariant mass began to show in the ECAL2, a double-peak structure appeared in the position of π^0 peak. This naturally decreased the signal-to-background ratio. It was discovered that the problem arose in the central part of the calorimeter, where the correction factors were consistently higher than elsewhere, see the left part of Fig. 3.9. The right part of Fig. 3.9 illustrates the issue. The LED generators began to exhibit instabilities in gain and caused

[1]ECAL2 was not used for the analysis presented in this thesis, however it was essential for the other exclusive reaction channels (DVCS, in particular) and the author participated in investigation of the issue and deployment of the corrections.

jumps in the HV amplitude of the affected ECAL2 central modules. As the LED calibration relies on a stable LED gain, a bias was then introduced in the LED calibration data. There were two possible solutions:

1. Correction factor calculated for each ECAL2 cell and averaged over a group of affected cells $\frac{\sum_{i=1}^{N} \frac{L^{i,j}}{L^{i,j_0}}}{N}$, where the N represents the number of ECAL2 affected cells (in this case shashlik type cells). The purpose of this treatment was to equalize the response of the affected shashlik region with the rest of the calorimeter, where the instabilities did not occur. The Fig. 3.8 shows the ratio of LED amplitudes from two runs, which differ by the HV jump occurring in the shashlik part of ECAL2. It can be seen that the whole inner part of ECAL2 gives higher values.

2. Using backup FEM diodes with a stable intensity and gain, which measure the intensity of the LED pulses, and serve to correct potential instabilities. The correction factor would take a form of $\frac{F^{m,j}}{F^{m,j_0}}$, where $F^{m,j}$ is the amplitude of the signal of a FEM diode dedicated to a particular group of cells m (there are 28 FEM groups for ECAL2) and a run j, and F^{m,j_0} is the FEM amplitude for the same group of modules from the electron calibration run.

The original plan was to employ the first solution as a temporary fix and when the extraction of FEM correction coefficients is finished, use the FEMs. The Fig. 3.10 shows an example of a ECAL2 central cell (X14-Y24) and the ratio of distribution of cluster energy E over a distribution of momenta of charged tracks p_{track} plotted before (left) and after (right) the application of LED calibration. The calculated correction coefficients for several parts of ECAL2 are illustrated in Fig. 3.11.

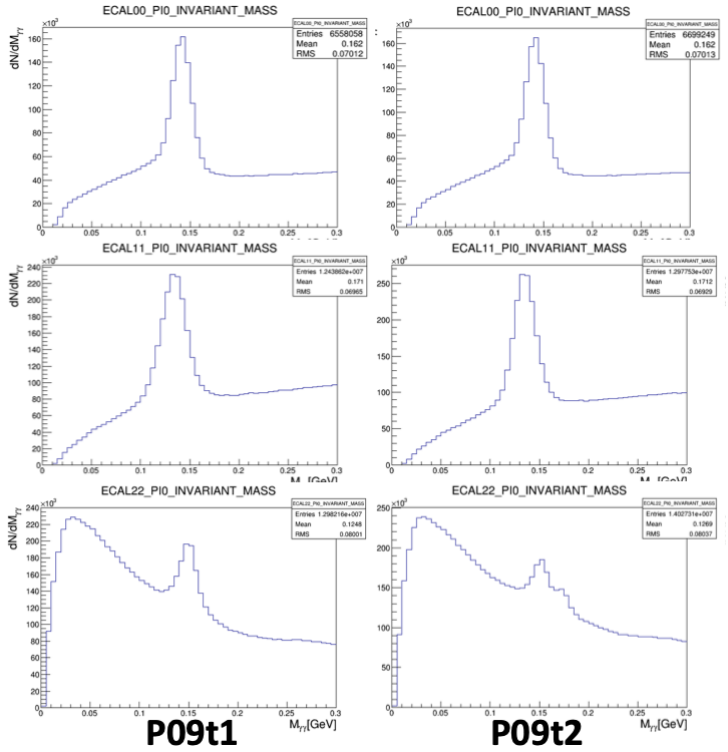

Fig. 3.7: The illustration of the problem with ECAL calibrations. The figures show the invariant $\gamma\gamma$ mass from ECAL0 (top), ECAL1 (middle), and ECAL2 (bottom). The P09t1 marks the first test production of the data, without any LED corrections. After the application of the LED calibration, however, a double-peak structure appeared in the data from ECAL2. From Ref. [102].

The effect of the application of the corrections is illustrated in Fig. 3.12. One can notice that the situation improved. There was hope that the updated version with the FEM corrections would lead to even further improvement. The example of extracted FEM corrections for the same cell as in Fig. 3.10 in ECAL2 is depicted in left part of Fig. 3.13. The red distribution represents the situation with the LED calibration without correction, while the green shows the effect of FEM correction, which was apparently too large.

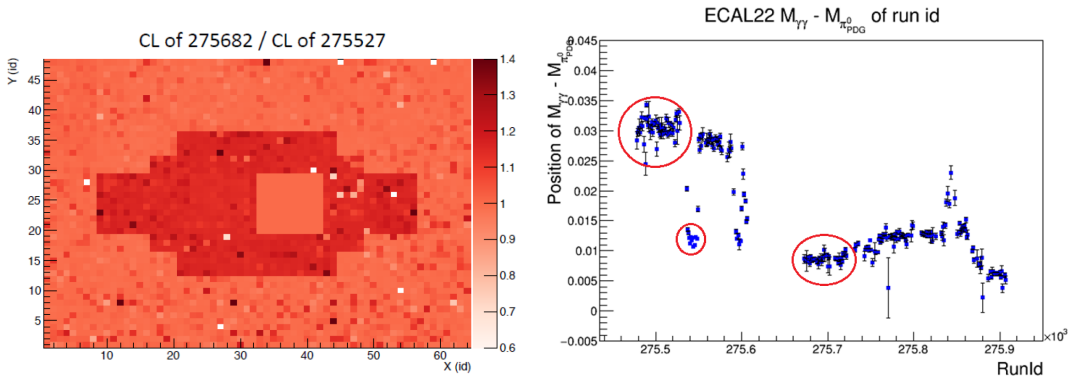

Fig. 3.8: The illustration of the problem with ECAL2 LED amplitude instabilities of the shashlik modules. The left figure shows the ratio of LED amplitudes from two runs, where the jump in the gain occurred. The inner part of the calorimeter shows higher values than the rest. The right figure shows the ratio of distribution of cluster energy E over a distribution of momenta of charged tracks p_{track} per runs. The bands highlighted by the red circles indicate the runs, where the jump occurred. From Ref. [100, 102].

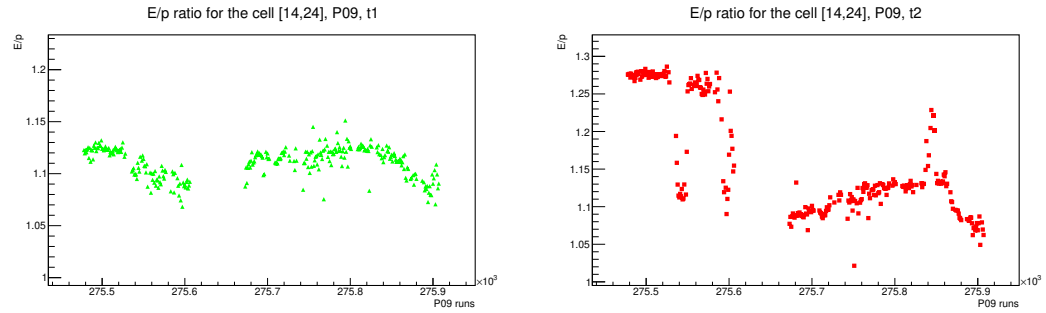

Fig. 3.10: An example of a central ECAL2 cell of shashlik type with the problematic response after application of the LED calibration. On the left there is the ratio of a distribution of cluster energy E over a distribution of momenta of charged tracks p_{track} plotted before the calibration, and on the right the same distribution after the calibration and the evolution in one data period.

The Fig. 3.14 shows the effect of the FEM corrections on the reconstructed π^0 mass (left panel) and the combination of the FEMs and the temporary coef-

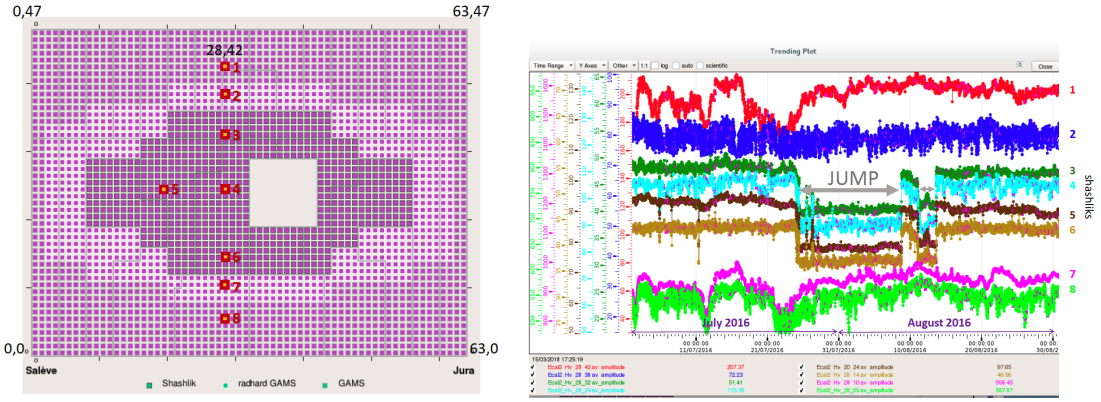

Fig. 3.9: The figure shows a study performed on eight different cells of ECAL2 to investigate the LED response. The choice of cells can be seen on the left of the figure. The response from the LEDs associated to the probed cells is shown on the right. One can notice the apparent abrupt change in the amplitude in four cells, which all belong to the centre part of the ECAL2 (shaslik modules). From Ref. [103].

ficients (middle). For comparison, also the original situation with the temporary coefficients is shown in the right panel.

As the temporary solution already brought performance similar to the past experience, it was decided not to investigate the FEM corrections further and make the temporary correction permanent. The final form of the full ECAL calibration procedure then takes the following shape

$$A^{i,j}_{[\mathrm{GeV}]} = A^{i,j}_{[\mathrm{ADC}]} \times C^{i,j_0} \times \frac{L^{i,j_0}}{L^{i,j}} \times \left(\frac{\sum_{i=1}^{N} \frac{L^{i,j}}{L^{i,j_0}}}{N} \right) \times S^{i,p} \times S^{j}. \tag{3.3}$$

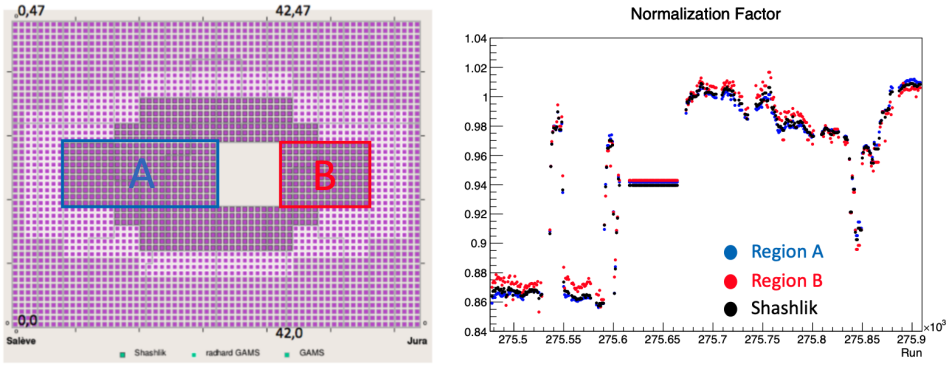

Fig. 3.11: The left panel shows the regions of the centre part of ECAL2 used for various tests of the corrections. The right panel depicts the correction coefficients, which were obtained on the run-by-run basis for the particular regions indicated by the same colours. From [100].

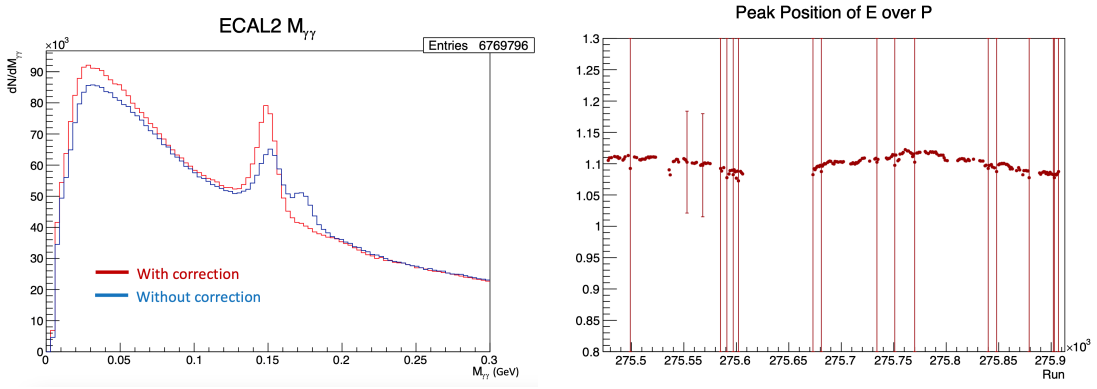

Fig. 3.12: The plots show the effect of the correction coefficients used on affected modules of ECAL2 in distribtution of π^0 (on the left) and cluster E/p_{track} (on the right). On the left plot, the blue curve depicts the situation before the correction and the red one shows the status after the correction. From Ref. [100].

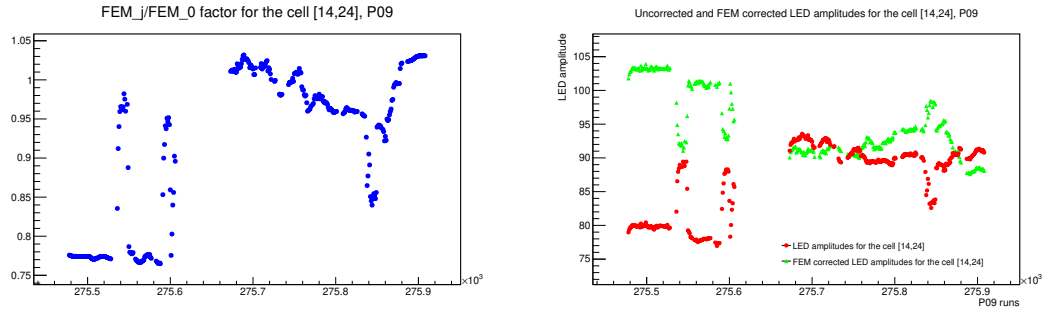

Fig. 3.13: The extracted FEM corrections for the cell X14-Y24 in ECAL2 (left). On the right plot, the effect of the FEM corrections is presented. The red distribution shows the situation with the LED calibration only, while the green shows the effect of FEM re-calibration. One can notice that the FEMs strongly over-corrected the amplitudes.

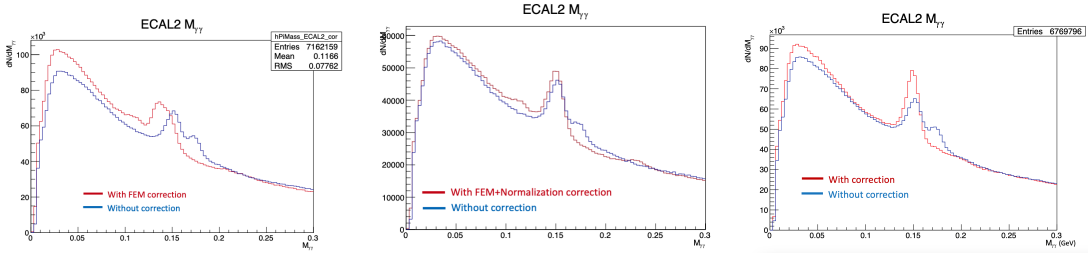

Fig. 3.14: The plots show the effect of the FEM correction coefficients on affected modules of ECAL2 in distribution of π^0 (on the left), the combination of the first correction method and FEMs (middle) and the first correction method alone, for comparison (right). The blue curve represents the situation before the correction and the red one shows the status after the correction on each plot. One can notice that the first, temporary correction method shows the best improvement. From Ref. [100].

Problems with the π^0 Calibration

The LED calibrations were not the only problematic step during the tuning of the ECAL performance. First problem that arose during the 2016 analysis campaign was simple to correct, yet took the longest time to discover. The Fig. 3.15 illustrates the issue on one data period, it concerned a discrepancy discovered between μ^+ and μ^- data, which manifested itself in one of the exclusivity variables, $\Delta\varphi$ (top row), which denotes the difference of the recoiled proton azimuthal angle measured from the CAMERA time-of-flight detector with respect to the indirect determination of the same variable from the spectrometer based on momentum conservation. The bottom row of the figure shows a different exclusivity variable, Δp_{T}, which represents the difference between the directly and indirectly measured values of the recoiled proton transverse momentum. One can notice from the distributions that there is an excess of background in the $\Delta\varphi$, not visible in Δp_{T}, where only a decrease of signal is indicated.

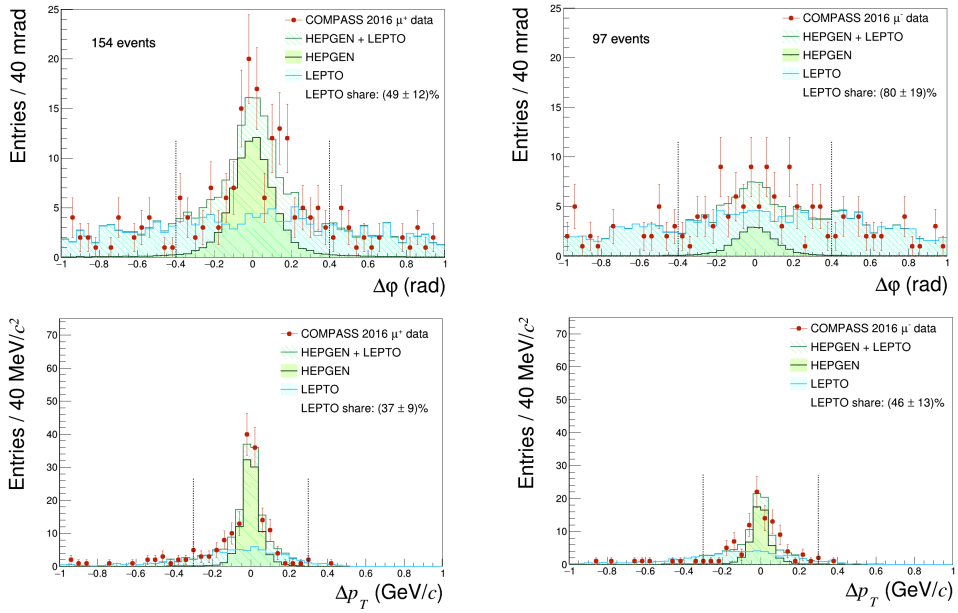

Fig. 3.15: The distributions of the exclusivity variable $\Delta\varphi$ for the period P05, μ^+ data (left), compared to the μ^- data (right), which manifested the problem with much higher background. This problem appeared for the periods P04, P05, and P06 of the 2016 statistics.

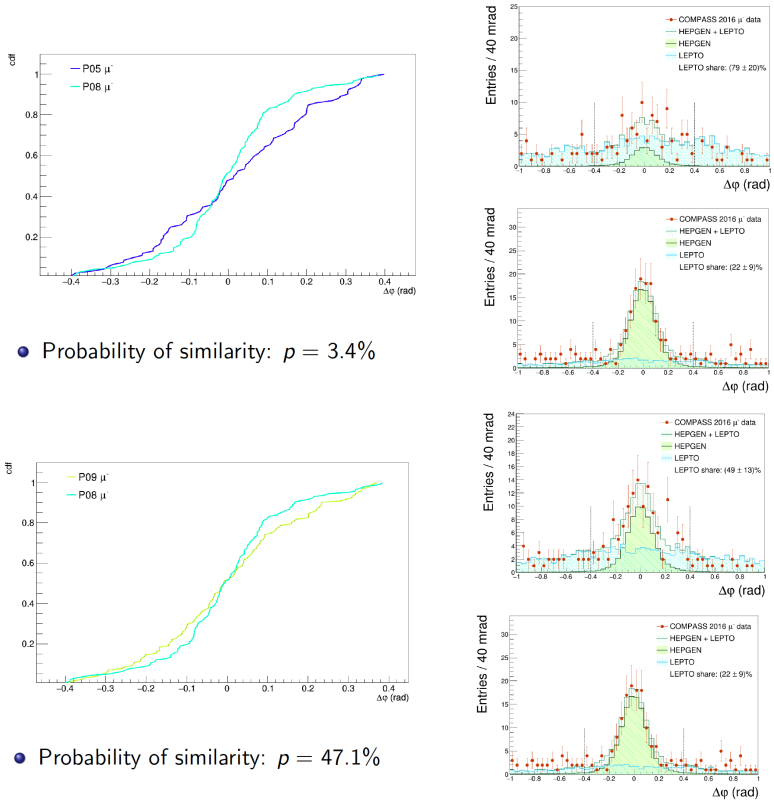

Fig. 3.16: An example of the result of the Kolmogorov-Smirnoff test performed on 5 data periods (for the list of periods and their details [[↪4.]]). A comparison of one period with the best resolution of the signal and lowest level of background (P08) has been made with the rest of the periods. The figures show one period from the first part of data-taking (P05), which was affected by the problem with high background in the μ^- data (top band), and a later period (P09), where this issue did not appear. The Kolmogorov-Smirnoff test was performed on the distribution of $\Delta\varphi$. One can see, that the compatibility of the periods P05-P08 is much lower that the one of P09-P08. This test however did not reveal any indications on the root of the problem.

Several methods were tested to tackle this issue and find the cause of this behaviour, which occurred only in μ^- data for the first half of the 2016 data sample. The excess of the background had not been explained for several months. A Kolmogorov-Smirnoff test was performed to quantify the difference of the "bad"

data periods to those, where the problem did not manifest, proving that the difference was statistically significant and could not occur by chance. The Fig. 3.16 demonstrates the results of the Kolmogorov-Smirnoff test when comparing the "bad" period P05 with the "good" P08 for μ^-. This test however did not provide any indication for the origin of the problem.

The solution of this issue has been discovered a few months later. Due to an error in database synchronisation, a wrong π^0 ECAL calibration had been used during the data reconstruction, and surprisingly, the $\Delta\varphi$ distribution was the only indication of the problem. No clear difference between the μ^+ and μ^- was seen in the exclusive π^0 distribution. The Fig. 3.17 shows the effect of correctly applied π^0 calibration in the case of P05 period. One can see the apparent improvement in the background level and equalising of the statistics with respect to Fig. 3.15.

However, despite the correct π^0 calibration, the results were still not satisfactory. It was discovered that the π^0 mass remained shifted with respect to the PDG value. A significant shift was observed in case of the period P07, in particular, see the left column of Fig. 3.18. An additional post-reconstruction correction was then introduced for the ECAL cluster energy, which modifies the run-by-run calibration S^j from the Eq. 3.3. This measure improved the situation, as can be seen from the middle column of Fig. 3.18. However, a slight issue remained with the case, where one decay photon of π^0 in ECAL0 and the other in ECAL1. A shift of the z-position of the cluster in ECAL0 by 6 cm was found and corrected. The ECAL post-reconstruction calibration S^j from 3.3 was then further modified to take this shift into account.

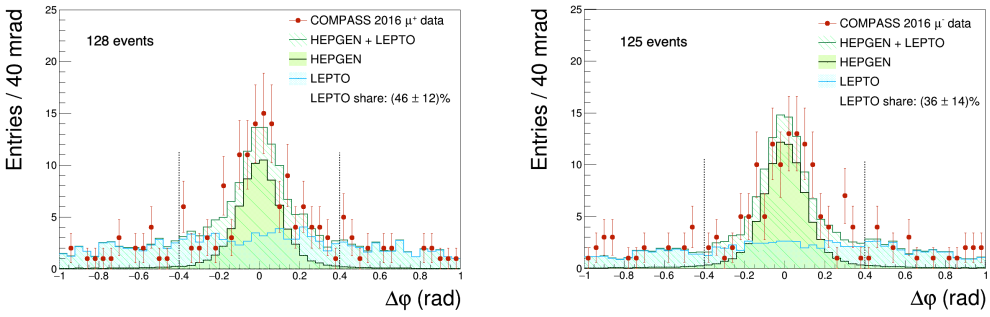

Fig. 3.17: The exclusivity variable $\Delta\varphi$ for the period P05, μ^+ data (left), and μ^- data (right), with correctly applied π^0 calibration to the μ^- data.

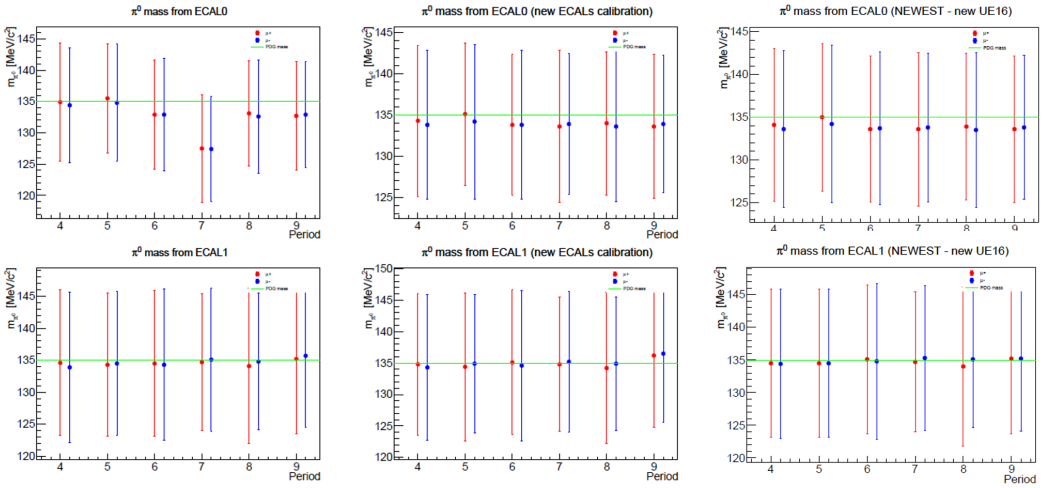

Fig. 3.18: The fitted peak position of the inclusive π^0 mass distribution with both decay photons measured in ECAL0 (top band) and ECAL1 (bottom band) with σ of the Gaussian fit of the peak, per each 2016 period. From Ref. [104].

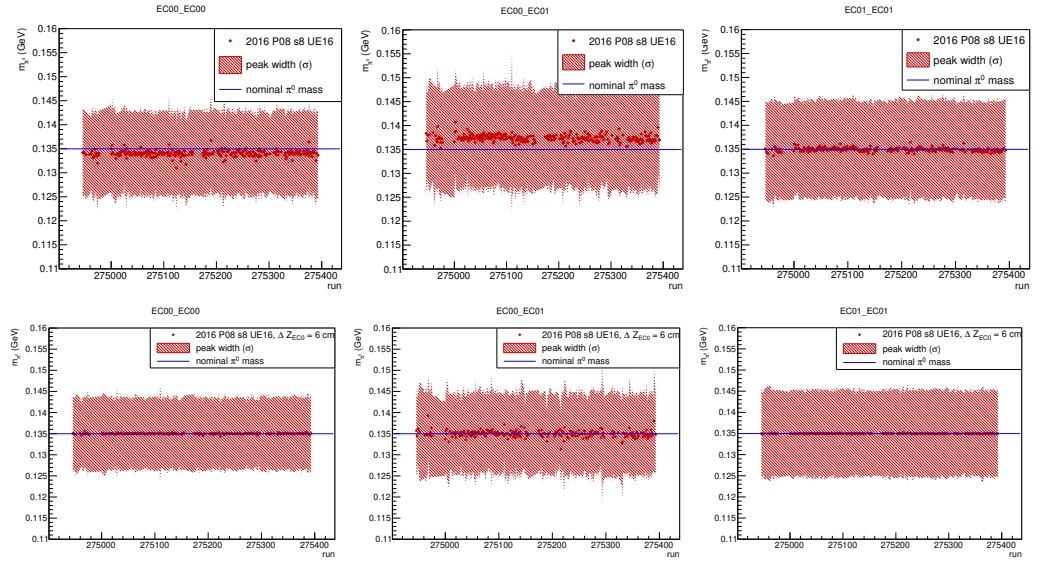

Fig. 3.19: The fitted inclusive π^0 mass peak from configuration of both decay photons in ECAL0-ECAL0 (left column), ECAL0-ECAL1 (middle column), and ECAL1-ECAL1 (right column) from period P08 before the shift of z-position of ECAL0 clusters (top) and after the modification (bottom). From Ref. [105].

3.5 ECAL Calibration in Monte Carlo Data

In COMPASS MC simulations, particles from event generators are propagated through a model of the experimental setup in a software GEANT4 [89] (the information on the used generators can be found in ⟦↪4.⟧). The interaction of the produced MC photons with electromagnetic calorimeters creates a problem due to the complexity of the created particle showers. The simulation of the electromagnetic showers is often the most time consuming part of the simulation. In order to increase the precision and lower the computational demands, an adaptive tool GFlash [106] has been developed by a team from Max Planck Institute of Munich and integrated into the GEANT4 framework. The principle of this method lies in parameterisations of the longitudinal and radial shower profiles in a calorimeter. It replaces the detailed simulation of the incoming particle directly with the energy depositions of all particles from the shower development. The details on the implementation of the algorithm on the COMPASS ECALs can be found in Ref. [89].

The simulated energy deposit is not explicitly determined by the algorithm and an additional calibration is required to ensure a match of the incident particle energy with the simulated energy deposit in an ECAL cluster. This calibration took into account the amount of energy lost in inactive calorimeter materials like space between the cells or absorbers. The calibration was performed on a cell-type basis using a linear parametrisation. It evaluated the difference between the generated cluster energy and the reconstructed one with the fitting parameter b reflecting the deviation. The values of b resulted slightly above 1 as a consequence of the energy-dependent leakage between the calorimeter cells. The last correction c was performed on the relative residual distribution as a function of the reconstructed cluster energy. All three parameter are fitted on a distribution $\frac{\Delta E}{E} = a + \frac{b}{E} + \frac{c}{E^2}$.

4 Data Preparation and Event Selection

During the 2016 data-taking, ten periods were recorded with approximately two-week duration. Each period had between 4 to 7 sub-periods with alternating beam polarity. Prior to the analysis, the data has to undergo a thorough process of preparatory work, such as detector and trigger calibrations, alignment of the spectrometer, the determination of the precise position of the target, and the measurement of the beam flux. The calibration of several equipment vital to the measurement of exclusive processes has been described in Section ⟦↩2.⟧ and ⟦↩3.⟧. This Section will first discuss the procedure to determine the beam flux and luminosity. Then the procedure of the kinematic fit, used to increase the precision and resolution of the measurement, will be elaborated. In the second part of this section, the event selection of the exclusive π^0 candidates will be presented. In the last part, the Monte Carlo (MC) simulations used in this analysis will be described together with the determination of the background.

4.1 Beam Quality and Luminosity

In order to determine a process cross section, one needs a precise knowledge of the target properties, the beam quality examination, and the total beam flux. The beam quality is controlled by initial set of selection criteria:

- **Hits in Sci-Fi, Silicon and BMS stations**:
  - At least 2 hits in Sci-Fis.
  - At least 3 hits in Silicons.
  - At least 3 hits in the BMS.

  The first two conditions provide a sufficiently precise measurement of the muon beam track, while the third gives the measurement of the beam momentum.

- **Beam momentum around 160 GeV**:
  - $140 < |\vec{p}_\mu| < 180$ GeV.

– $\sigma(|\vec{p}_{\mu}|)/|\vec{p}_{\mu}| < 0.025$.

- **Muon beam track fully crossing the target volume**:
  Muon track is required to pass through the full length of the target, as illustrated in the sketch in Fig. 4.1.

- **Time-in-spill $\Delta t_{\mathbf{spill}}$ cut**:
  The beam is required to have a stable intensity. The comprehensive study for the beam spill profile of 2016 data has been performed [108], based on its findings, the cut on the margins of the beam spills have been introduced spill-be-spill. The beam intensity of each spill is reconstructed based on the scaler information from the beam telescope FI02. A profile of a good spill is illustrated in Fig. 4.2 with respect to the time in spill. First, a threshold for sufficiently high intensity, and the time-in-spill cut is performed for each spill to use the data only in the time window with rather constant and high intensity above the threshold.

- **Bad spill cut**:
  As the beam condition may naturally vary a lot, the procedure for the beam stability evaluation has to account for any of such instabilities, and if the case may be, exclude some spills as "bad". The bad spill list is created for each data period, containing not only spill with unstable or too low beam rates, but also additional issues from the side of the detectors, such as unstable rates detected in ECALs, RICH, or in the physics triggers used for the analysis ⟦↪4.3.⟧. In general, the amount of rejected spills per period varies from 6 to 12%, and the majority ($> 50\%$) is represented by empty spills.

When the beam quality is ensured, the flux can be evaluated in order to calculate the luminosity. The integrated luminosity $\mathcal{L}^{\pm}$ for the $\mu^{\pm}$ beams is given

$$\mathcal{L}^{\pm} = \frac{\Phi_{\text{eff}} \cdot l \cdot N_{\text{A}} \cdot \rho_{\ell \text{H}_2}}{M_{\text{p}}} \quad [\text{nb}^{-1}], \tag{4.1}$$

where Φ_{eff} denotes the effective beam flux, l stands for the length of the target $l = 240$ cm, N_A is the Avogadro's constant, $\rho_{\ell \text{H}_2} \sim 0.070146$ g/cm^3 is the density of the liquid hydrogen, and M_{p} is the proton mass.

The method used for the evaluation of the effective beam flux is the random trigger method, based on the random trigger events [108]. The method is based

on counting the number of good tracks passing the beam quality requirements raised above in one spill $N_{\mathrm{RT}}^{\mathrm{tracks}}$ for the events, where the random trigger was fired. These tracks were selected within a time window Δt_{mean} around the random trigger time. Due to the randomness of the event emission from the random trigger, a flat distribution of events is expected around the random trigger time. The time window was selected to be $|\Delta t_{\mathrm{mean}}| = 2$ ns, as both flatness of the plateau and a good statistics are guaranteed.

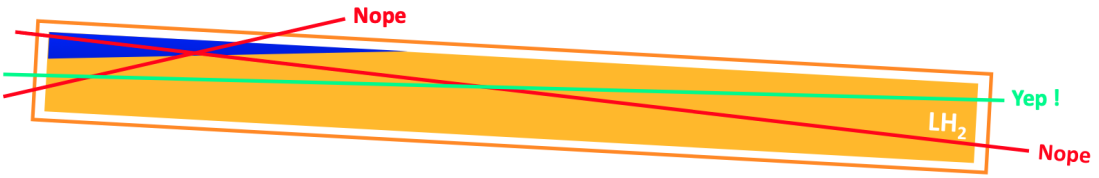

Fig. 4.1: The sketch illustrating the selection criterion for the extrapolated muon beam tracks, which are required to cross the full length of the target. The accepted track is depicted in green, while the rejected ones are in red. The blue area indicates the gaseous region of the target, excluded by the requirement $y_{\mathrm{vtx}} < 1.2$ cm [21].

The effective flux then can be computed as

$$\Phi^{\pm}_{\text{no DAQ corr}} = \frac{N_{\mathrm{RT}}^{\mathrm{tracks}}/\Delta t_{\mathrm{mean}}}{RT_{\mathrm{accepted}}/\Delta t_{\mathrm{spill}}}, \tag{4.2}$$

where the RT_{accepted} is the number of reconstructed random triggers fired in the duration of a spill $\Delta t_{\mathrm{spill}}$. When the DAQ dead time is considered, Eq. 4.2 changes

$$\Phi^{\pm}_{\text{DAQ corr}} = \frac{N_{\mathrm{RT}}^{\mathrm{tracks}}/\Delta t_{\mathrm{mean}}}{RT_{\mathrm{attempted}}/\Delta t_{\mathrm{spill}}}, \tag{4.3}$$

where the number of accepted triggers has to be replaced by the number of attempted triggers $RT_{\mathrm{attempted}}$, accessible from the DAQScaler database. Although the random trigger is an ideal tool for the beam flux determination due to its independence on the muon beam, it has the drawback of being disconnected from the veto system, which prevents distinguishing the beam tracks from the muon halo.

During the dead time of DAQ, good tracks are still counted in the flux, but they are excluded from the physics data, because the physics triggers were not fired.

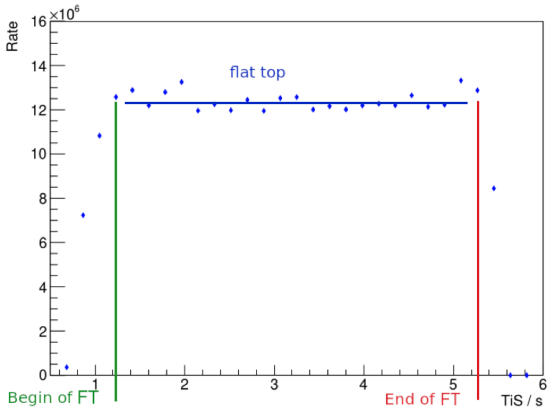

Fig. 4.2: Example of the profile of a good spill with respect to the time in spill. The stable intensity plateau is indicated by a blue line. The green and the red line denote the margins of the flat top region, defining the cut on the time-in-spill. From Ref. [108].

Thus, the veto dead time has to be considered in the effective flux evaluation

$$\Phi^{\pm}_{\text{eff}} = \Phi^{\pm}_{\text{no DAQ corr}} \left(1 - c_{\text{vdt}}\right), \tag{4.4}$$

here the final effective flux calculation is not corrected on DAQ dead time, as the data selection is also affected by the DAQ dead time, and as cross section is the ratio of events to flux (contained in the luminosity), the DAQ correction cancels out. The integrated muon flux for both polarities in 2016 data is shown in Fig. 4.3.

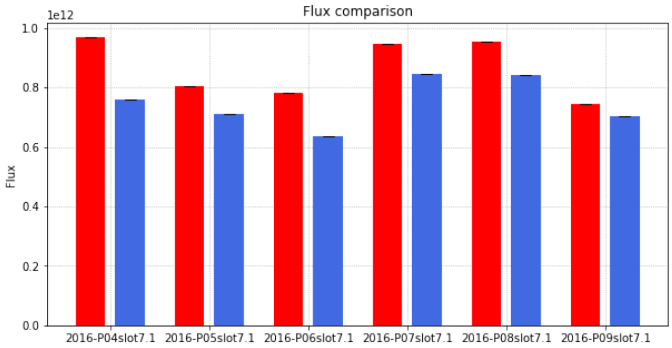

Fig. 4.3: The integrated muon flux for both μ^+ beam (in red) and μ^- (in blue) for the 2016 periods used in this analysis. From Ref. [20].

4.2 Kinematic Fit

The advantage of the COMPASS GPD setup equipped with the CAMERA is the over-constraint of the measurement. This property enables to detect the full topology of the event. The method of kinematic fit can be employed in this instance to improve the precision of measured kinematic quantities within their covariances using conservation of momentum, energy, and mass, and their geometrical constraints, such as a common vertex.

The mathematical framework of the kinematic fit has been developed by P. Jörg [95] for the case of DVCS process, The thorough description of the principles and application for the DVCS process can be found ibid. The modification of the procedure for the exclusive π^0 production, developed later by M. Gorzellik [19], is described in the following subsection.

The main purpose of the kinematic fit is to evaluate how close the event topology is to being an exclusive event. In addition, it provides kinematic quantities optimised, within their covariances, in order to find the best fit to the constraints. It is not necessary to measure all quantities involved in the kinematic fit in order to over-constrain the measurement. Hence, the set of quantities can be divided between the measured quantities $\vec{k}$ and unmeasured ones $\vec{h}$. For the process $\mu p \to \mu' p' \pi^0 \to \mu' p' \gamma_h \gamma_l$, where γ_h and γ_l denote the photon with higher and lower energy, the measured quantities are

$$\vec{k} = \begin{pmatrix} k_1 \\ \cdot \\ \cdot \\ \cdot \\ k_{27} \end{pmatrix} := \begin{pmatrix} \vec{p}_p \\ \vec{p}_\mu \\ \vec{b}_{\perp\mu} \\ \overrightarrow{0}_{18} \end{pmatrix} + \begin{pmatrix} \overrightarrow{0}_{8} \\ \vec{p}_{\mu'} \\ \vec{b}_{\perp\mu'} \\ \overrightarrow{0}_{13} \end{pmatrix} + \begin{pmatrix} \overrightarrow{0}_{13} \\ r_A \\ \varphi_A \\ z_A \\ r_B \\ \varphi_B \\ z_B \\ p_{p'} \\ \overrightarrow{0}_{6} \end{pmatrix} + \begin{pmatrix} \overrightarrow{0}_{20} \\ p_{\gamma_h} \\ \vec{b}_{\perp\gamma_h} \\ p_{\gamma_l} \\ \vec{b}_{\perp\gamma_l} \end{pmatrix}. \tag{4.5}$$

And the vector of unmeasured quantities reads

$$\vec{h} = \begin{pmatrix} h_1 \\ \cdot \\ \cdot \\ \cdot \\ h_9 \end{pmatrix} := \begin{pmatrix} \theta_{p'} \\ \varphi_{p'} \\ \theta_{\gamma_h} \\ \varphi_{\gamma_h} \\ \theta_{\gamma_l} \\ \varphi_{\gamma_l} \\ \vec{r}_{\mathrm{vtx}} \end{pmatrix}, \tag{4.6}$$

in these equations, the $\vec{0}_{\mathrm{N}}$ denote vector of zeros in $\mathbb{R}^{\mathrm{N}}$; the $\vec{p}_{\mu}(\vec{p}_{\mu'})$ are the three-momenta of the beam (scattered) muon; the $\vec{b_{\perp\mu}}(\vec{b_{\perp\mu'}})$ denote their transverse spatial position; $p_{\mathrm{p}'}$ is the magnitude of the recoiled proton momentum; $r_{A(B)}, \varphi_{A(B)}$ and $z_{A(B)}$ represent the radius, azimuthal angle, and the longitudinal position of a hit in the inner (outer) CAMERA ring. The measured quantities are combined with the corresponding unmeasured ones, $\theta_{\mathrm{p}'}$ and $\varphi_{\mathrm{p}'}$ denoting the polar and azimuthal angle of the recoiled proton. The measured p_{γ_h} (p_{γ_l}) and $b_{\perp,\gamma_h}$ $(b_{\perp,\gamma_l})$, representing the magnitudes of the momenta of the higher (lower) energetic photon, and their transverse positions, are also combined with the unmeasured quantities θ_{γ_h} (θ_{γ_l}) and φ_{γ_h} (φ_{γ_l}) denoting the polar and azimuthal angles of the higher (lower) energetic photon; and finally, $\vec{r}_{\mathrm{vtx}}$ is the position of the interaction vertex.

The transverse positions of the photons are taken at the longitudinal positions of the ECAL, where the corresponding clusters were recorded. The optimised kinematic variables are constructed by adding a correction factor $\Delta\vec{k}$ to the measured quantities $\vec{k}$ as

$$\vec{k}_{\mathrm{fit}} = \vec{k} + \Delta\vec{k}, \tag{4.7}$$

which is computed from the minimisation of the least squares function

$$\chi^2(\vec{k}) = \Delta\vec{k}^T \hat{C}^{-1} \Delta\vec{k}, \tag{4.8}$$

here, the $\hat{C}$ denotes the covariance matrix correlating the measured quantities $\vec{k}$. The minimisation procedure of $\chi^2(\vec{k})$ uses the Lagrange multiplier method, satisfying the constraints $g(\vec{k}, \vec{h})$

$$L(\vec{k}, \vec{\lambda}) = \chi^2(\vec{k}) + 2\sum_{i=1}^{N} \lambda_i g_i(\vec{k}, \vec{h}) \tag{4.9}$$

The N constraints are following:

1. **Momentum and energy conservation**:

$$\begin{aligned} g_i &= p^{\text{fit}}_{\mu,i} - p^{\text{fit}}_{\mu',i} - p^{\text{fit}}_{p',i} - p^{\text{fit}}_{\gamma_h,i} - p^{\text{fit}}_{\gamma_l,i} = 0 \\ g_4 &= E^{\text{fit}}_{\mu} + m_p c^2 - E^{\text{fit}}_{\mu'} - E^{\text{fit}}_{p'} - E^{\text{fit}}_{\gamma_h} - E^{\text{fit}}_{\gamma_l} = 0, \end{aligned} \tag{4.10}$$

   for $i \in [1,2,3]$ denoting the components of a three-vector, and the superscript "fit" representing the quantities modified by the kinematic fit

2. **Common vertex for all tracks (except the target and recoiled proton)**:

$$\begin{aligned} g_{5+i} &= p^{\text{fit}}_{j,3}\left(x_{\text{vtx}} - x^{\text{fit}}_j\right) - p^{\text{fit}}_{j,1}\left(z_{\text{vtx}} - z^{\text{fit}}_j\right) = 0, \\ g_{6+i} &= p^{\text{fit}}_{j,3}\left(y_{\text{vtx}} - y^{\text{fit}}_j\right) - p^{\text{fit}}_{j,2}\left(z_{\text{vtx}} - z^{\text{fit}}_j\right) = 0, \end{aligned} \tag{4.11}$$

   for $\forall(i,j) \in \{(0,\mu),(2,\mu'),(4,\gamma_h),(6,\gamma_l)\}$ representing the tracks of the initial and scattered muons and the higher and lower energetic photons, constrained to the common vertex $\vec{r}_{\text{vtx}} = (x_{\text{vtx}}, y_{\text{vtx}}, z_{\text{vtx}})$.

   The form of the constraints is based on the parametrisation of a particle track by a line

$$\vec{r}(\beta) = \vec{r}' + \beta\vec{p}, \tag{4.12}$$

   where the vector $\vec{r}$ denotes the initial point of the track, $\vec{p}$ the momentum of the particle, and β represents a free parameter. The components of the vector can be expressed

$$\begin{aligned} z = z' + \beta p_3 &\Rightarrow \beta p_3 = z - z' \\ x = x' + \beta p_1 &\Rightarrow x p_3 = x' p_3 + \beta p_1 p_3, \\ &\Rightarrow x p_3 = x' p_3 + p_1 (z - z'), \\ &\Rightarrow p_3 (x - x') + p_1 (z - z') = 0 \\ y = y' + \beta p_2 &\Rightarrow (...) \Rightarrow p_3 (y - y') + p_2 (z - z') = 0. \end{aligned} \tag{4.13}$$

3. **Constraints for the recoiled proton**:

$$\begin{aligned} g_{13+i} &= p^{\text{fit}}_{p',3}\left(x^{\text{fit}}_j - x_{\text{vtx}}\right) - p_{p',1}\left(z^{\text{fit}}_j - z_{\text{vtx}}\right) = 0, \\ g_{14+i} &= p^{\text{fit}}_{p',3}\left(y^{\text{fit}}_j - y_{\text{vtx}}\right) - p_{p',2}\left(z^{\text{fit}}_j - z_{\text{vtx}}\right) = 0, \end{aligned} \tag{4.14}$$

   for $\forall(i,j) \in \{(0,A),(2,B)\}$ representing measured points in the inner and outer CAMERA rings. The concept of these extrapolation constraints is similar to the vertex constraints, with the difference that the proton originates

from the vertex r_{vtx} using

$$\vec{r}(\beta) = \vec{r}_{\mathrm{vtx}} + \beta\vec{p}. \tag{4.15}$$

With the similar treatment as in Eq. 4.13 one arrives at the Eq. 4.14.

4. **Mass constraint**:

$$g_{17} = \left(E^{\mathrm{fit}}_{\gamma_h} + E^{\mathrm{fit}}_{\gamma_l}\right)^2 - \left(\vec{p}^{\,\mathrm{fit}}_{\gamma_h} + \vec{p}^{\,\mathrm{fit}}_{\gamma_l}\right)^2 - m^2_{\pi^0} = 0 \tag{4.16}$$

the invariant gamma-gamma system is constrained by the PDG π^0 mass.

The kinematic fit is essential to determine the four-momentum transfer between the target and recoiled proton, t, as it bridges the transition between the low $|t|$, where the CAMERA is more sensitive, $t_{\mathrm{cam}} = (p - p')^2$, and the high $|t|$ region, where the determination of $|t|$ from the spectrometer is more precise.

$$\begin{aligned} k &:= \nu - \sqrt{\nu^2 + Q^2} \cdot \cos\theta_{\gamma^*\pi^0} \\ t_{\mathrm{spec}} &= \frac{-Q^2 - 2\nu k}{1 + k/m_{\mathrm{p}}}, \end{aligned} \tag{4.17}$$

where the $\theta_{\gamma^*\pi^0}$ denotes the polar angle between the virtual photon and the π^0. The illustration of the improvement of the $|t|$ given by the kinematic fit is shown in Fig. 4.4. The kinematic fit also considerably improves the signal-to-background ratio [[↪4.3.]].

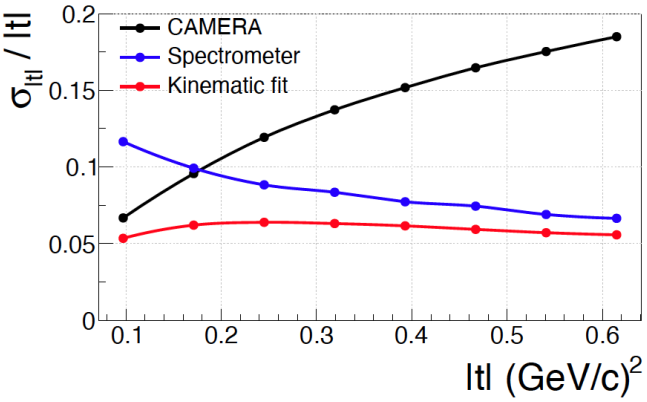

Fig. 4.4: The relative resolution for the four-momentum transfer $|t|$ between the target and recoiled proton, evaluated from the exclusive π^0 MC. The quantity $\sigma_{|t|}$ is evaluated using the data from kinematic fit, $\sigma_{|t|} = t_{\text{fit}} - t_{\text{mc}}$, data from CAMERA, $\sigma_{|t|} = t_{\text{cam}} - t_{\text{mc}}$, and the spectrometer, $\sigma_{|t|} = t_{\text{spec}} - t_{\text{mc}}$ as a function of t_{mc} [95].

4.3 Exclusive π^0 Event Selection

In the following section, the selection of the exclusive π^0 candidates from the process $\mu p \to \mu' p' \pi^0$ will be outlined, with k, k', q, q', p, p' being the four-momenta of the incident muon, the scattered muon, the virtual photon, the exclusive π^0, the target proton and the recoil proton, respectively. Here, the E_{π^0} and E_{p} will represent the energy of the real photon and of the outgoing proton in the laboratory system, $t = (q - q')^2 = (p - p')^2$ the four-momentum transfer to the target proton, and in some instances, we will use $t' = t - t_{\text{min}}$, where $|t_{\text{min}}|$ is the minimum four-momentum transfer.

The event selection can be split into four main steps:

1. Selection of a primary vertex within the proton target, with constraints applied on the incoming and outgoing muons (see subsection 4.3.1).

2. Selection of a pair of neutral ECAL clusters above an energy threshold specific for each calorimeter (see subsection 4.3.2) to construct the π^0 candidate.

3. Selection of a recoiled proton candidate (see subsection 4.3.3) reconstructed

in the CAMERA with securing of the exclusivity of an event candidate[1], using the fact that the measurement of kinematic variables in the COMPASS spectrometer is over-constrained. At the end, the events with more than one combination are excluded (see subsection 4.3.4).

4. Application of the kinematic fit (see subsection 4.3.5) in order to:
   - Improve the resolution of the signal and reduce the background
   - Improve the resolution of the kinematic variables Q^2, ν, t, and ϕ, which are essential to study the dependencies of the π^0 cross section.

4.3.1 Selection of μ Candidates and General Cuts

- General cuts:
  - Physics triggers considered: MT, LT, or OT only
  - Only events inside the stable part of the beam spill are accepted (within the time-in-spill limits, see subsection 4.1)
  - Bad spills rejected
- Vertex selections[2]:
  - A primary vertex within the target volume:
  - $-318.5 < z_{\text{vtx}} < -78.5$ cm
  - $r_{\text{vtx}} < 1.9$ cm
  - $y_{\text{vtx}} < 1.2$ cm
- Incoming muon[2]: The tracks must pass the beam quality requirements defined in Section ⟦↩4.1.⟧.
- Scattered muon:

[1] Made of all possible combinations of a good vertex, a π^0 candidate and a proton candidate in one event

[2] These selection criteria are used for filtering generated MC events for the acceptance calculation ⟦↪4.4.⟧

– A single outgoing charged track with the same charge as the beam muon and traversing at least 15 radiation lengths of material.

– Track of the scattered muon has to point to the active hodoscope areas

– The first measured point of the scattered muon must be upstream of SM1 ($Z_{\text{first}} < 350$ cm), and the last measured point be downstream of SM1 ($Z_{\text{last}} > 350$ cm)

– Kinematic pre-selection of the measured quantities $Q^2 > 0.8$ GeV^2 and $y > 0.01$

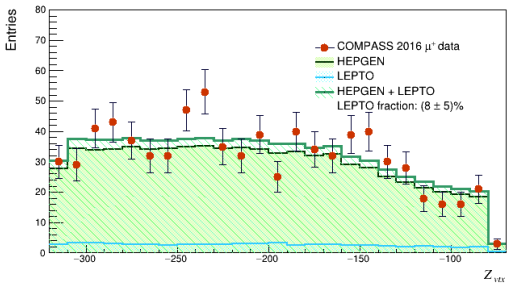

Fig. 4.5: The distribution of longitudinal vertex position z_{vtx}. The data points are represented in red circles with statistical errors displayed. The spring green distribution denotes the HEPGEN++ signal simulation, the light blue area shows the yield of the inclusive background represented by the LEPTO generator, and the dark green curve represents the mixture of both MC samples fitted to the data.

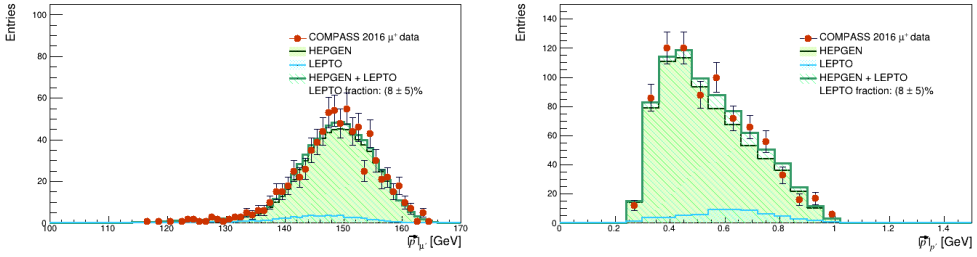

Fig. 4.6: The left plot shows the distribution of the momentum magnitude of the scattered muon. The right plot represents the momentum magnitude of the recoiled proton. Only the μ^+ data are shown as example.

4.3.2 Selection of π^0 Candidate

For the reconstruction of the π^0 candidates, only the neutral clusters (i.e. clusters not associated with a charged track) from ECAL0 and ECAL1 are considered. The kinematic coverage of the ECAL2 is mostly outside the acceptance for the exclusive π^0 events of the COMPASS spectrometer [[↪5.]], thus the signal from this calorimeter is very weak and hidden in the noise.

The selection criteria for finding a π^0 candidate read:

- Selecting a pair of neutral clusters from ECAL0 and ECAL1
- All photon clusters have to meet the condition of timing $|t_{\text{cluster}} - t_{\text{beam}} - \mu_t| < 2.5\sigma_t$, where the variables μ_t and σ_t are determined for every period and cell type based on the time distribution of the clusters as a function of their energy [[↩3.2.]]
- The lower-energetic cluster has to meet the criterion: $E_{\text{cl}_l} > 0.5$ GeV in ECAL0 and $E_{\text{cl}_l} > 0.63$ GeV in ECAL1.
- The higher-energetic cluster has to meet the criterion: $E_{\text{cl}_h} > 2.0$ GeV in ECAL0 and $E_{\text{cl}_h} > 2.5$ GeV in ECAL1.
- The invariant mass of the double-photon system $M_{\pi^0} \in (106.1, 160.5)$ MeV, which corresponds to a 2.5 σ around the Gaussian fit of the peak.

4.3.3 Selection of Recoiled Proton Candidate

The recoiled proton candidates are constructed out of a combination of hits in the inner and outer rings of CAMERA if they fulfill following criteria:

1. The hits belong to mutually correlated azimuthal scintillator sectors.
2. The reconstructed proton velocity is $0.1 < \beta < 0.95$.
3. The longitudinal positions of the hits are contained within the A and B ring aperture $-366.19\text{cm} < z_A < 8.81$ cm and $-338.94\text{cm} < z_B < 71.06$ cm.
4. Only events with $0.06 < |t_{\text{CAMERA}}| < 0.8$ GeV^2 are kept.

4.3.4 Exclusivity Conditions

In COMPASS data one can exploit the fact that the measured kinematics of the exclusive π^0 process are over-constrained, and one can compare the observables related to the proton detected in CAMERA with values predicted by conservation laws from the muon and the photon pair detected in the spectrometer. All the good proton candidates are combined with all the vertices available, and a pair of ECAL clusters that pass the π^0 candidate conditions.

The detection of the proton in the CAMERA allows to perform cuts on the four-momentum balance to remove any background particles:

$$M^2_{\text{undet}} = M^2_{X=0} = (k + p - k' - q' - p')^2, \tag{4.18}$$

where k and k' describe the four-momenta of the initial and final muon; p and p' stand for the four-momenta of target and recoiling proton; and q' the π^0 four-momentum.

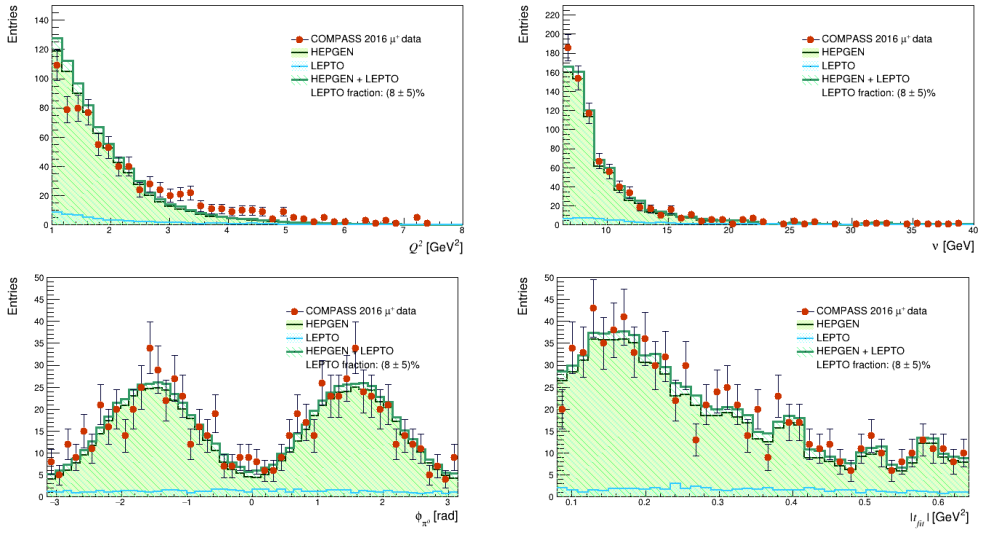

Fig. 4.7: The figure illustrates the four kinematic variables that define the phase space of the differential exclusive π^0 cross section. The left top plot shows the Q^2 distribution refined from the kinematic fit. The right top plot represents the refined ν. The left bottom plot displays the refined azimuthal angle ϕ of the π^0 production plane. And the right bottom plot illustrates the momentum transfer t from the kinematic fit. Only the μ^+ data are shown as example.

Additionally, by matching the predicted four-momentum of the recoiled proton with the one measured in CAMERA, one can also perform a check on the exclusivity of en event on the quantities derived from the four-momentum by the following differences:

- Difference of the measured and predicted azimuthal angle φ:

$$\Delta\varphi = \varphi^{\text{CAMERA}} - \varphi^{\text{pred}} \tag{4.19}$$

- Difference of the measured and predicted value of transverse momentum p_T:

$$\Delta p_{\text{T}} = |p_{\text{T}}^{\text{CAMERA}}| - |p_{\text{T}}^{\text{pred}}| \tag{4.20}$$

- Difference between the longitudinal position of the hit in the inner CAMERA barrel z_A and the interpolated one using the interaction vertex position and the longitudinal position of the hit in the outer barrel z_B:

$$\Delta z_A = z_A - z_{\text{pred}} \tag{4.21}$$

The exclusivity conditions are then defined as follows:

- $|\Delta\varphi| < 0.4$ rad
- $|\Delta p_{\text{T}}| < 0.3$ GeV
- $|\Delta z_A| < 16$ cm
- $|M_X^2| < 0.3$ GeV^2

The exclusivity variable distributions for $\Delta\varphi$, Δp_{T}, Δz_A and M_X^2 are presented in Fig. 4.8, where the comparison between μ^+ (in red) and μ^- (in blue), normalised to the same muon flux, is shown for the full statistics. Note the good agreement between the opposite charge distributions. Such an agreement was not achieved in 2012 due to very different intensities of μ^+ and μ^- beams.

4.3.5 Kinematic Fit and the Last Cuts

The method of kinematic fit adapted for the exclusive π^0 production was introduced in subsection 4.2. The kinematic fit improves the measured and the derived observables and assigns to each event a measure of the fit quality χ^2_{fit} defined in Eq. 4.8. The χ^2_{fit} corresponds to the probability that the event is exclusive. Hence large χ^2_{fit} indicates that the event belong to the background with higher probability. The number of degrees of freedom, defined as the difference of number of constrains and the number of free parameters, for the particular process is $17 - 9 = 8$, hence we can define a reduced $\chi^2_{\text{red}} = \chi^2_{\text{fit}}/8$.

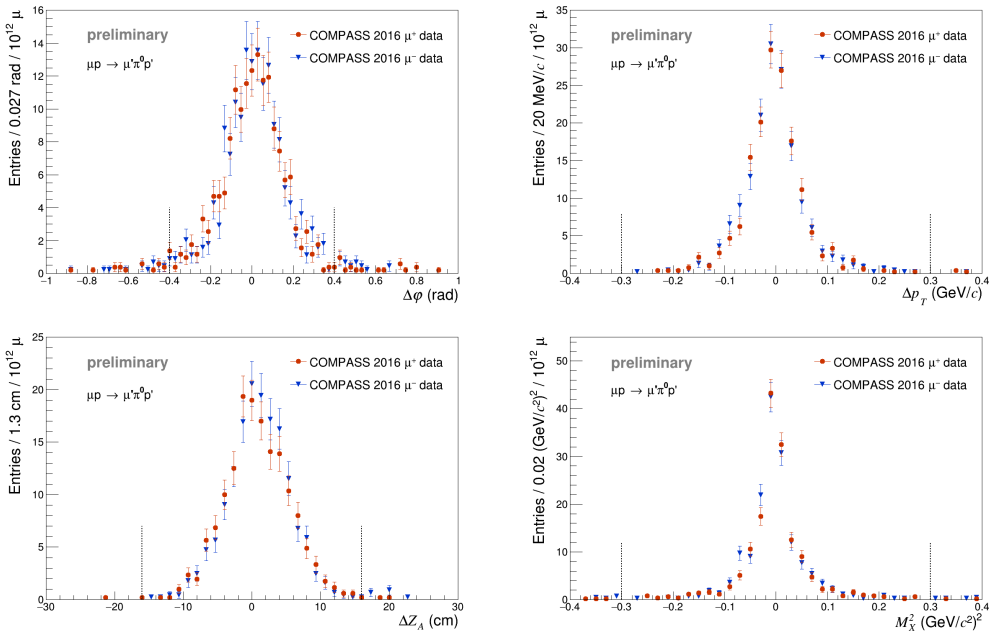

Fig. 4.8: Distributions of the exclusivity variables: $\Delta\varphi$, Δp_{T}, Δz_A and the four-momentum balance M^2_X. Each distribution is plotted after applying all the selection criteria except the cut on the plotted variable itself. The data are represented in red for μ^+ and in blue for μ^- normalised to a muon flux of 10^{12}. The selected range in each variable is indicated by the vertical lines.

Aside from selecting the improved observables arising from the kinematic fit, two cuts have been performed on the data:

- Requirement for the successful convergence of the kinematic fit
- The goodness of the fit has to fulfill $\chi^2_{\text{red}} < 7$

The kinematic fit requirements reduce the data sample to 66%, which implies the insufficiency of the exclusivity conditions and importance of the kinematic fit in filtering the exclusive π^0 events. The Fig. 4.11 shows the agreement of the χ^2_{red} from data with the one obtained from MC, which is satisfactory. Note that at the $\chi^2_{\text{red}} = 7$ the signal, described by the MC simulation HEPGEN++, steeply decreases motivating the choice of this value for the cut. In the 2012 data it was not possible to utilise the χ^2_{red} cut, because the agreement of the data and MC for all the measured observables and their uncertainties was not sufficient and a more conservative method had to be applied.

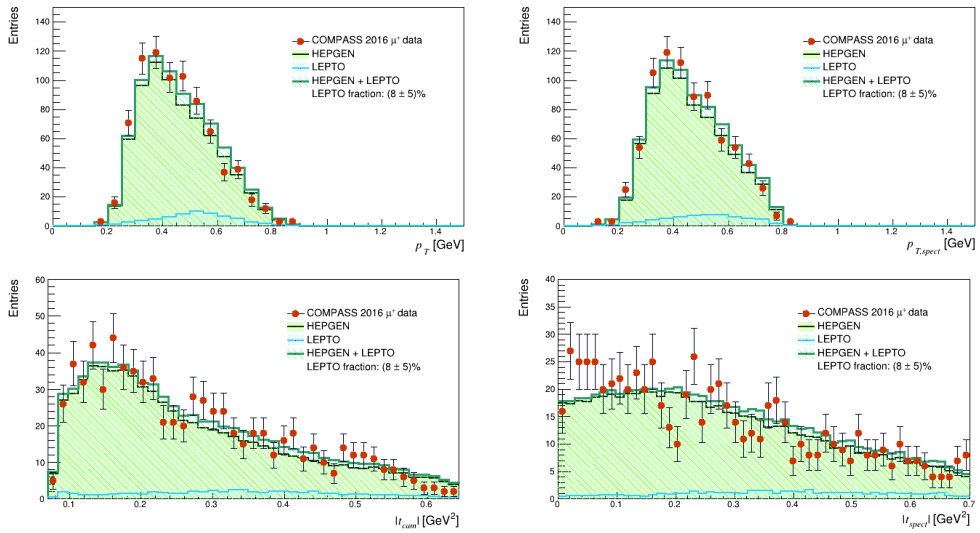

Fig. 4.9: The left top plot shows the p_T distribution of the recoiled proton measured by the CAMERA detector and the right top plot depicts the p_T predicted from the spectrometer information. The bottom plots illustrate the same for the momentum transfer to the proton, t. Only the μ^+ data are shown.

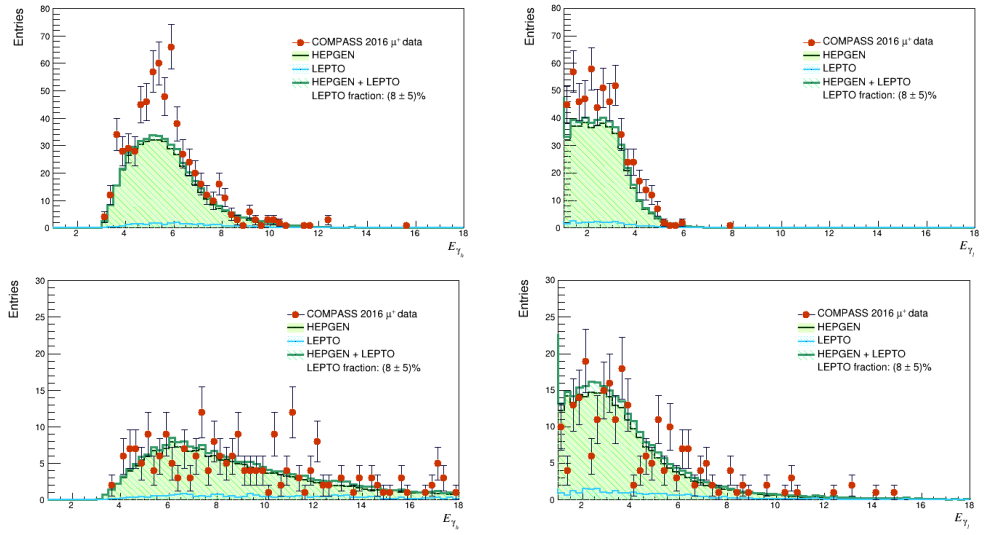

Fig. 4.10: The left top plot shows the energy of the higher-energetic cluster $E_{\mathrm{cl_h}}$ from ECAL0, and the right top represents the energy of the lower-energetic cluster $E_{\mathrm{cl_l}}$ from ECAL0. The bottom pair of plots shows the corresponding distributions for ECAL1. Only the μ^+ data are shown.

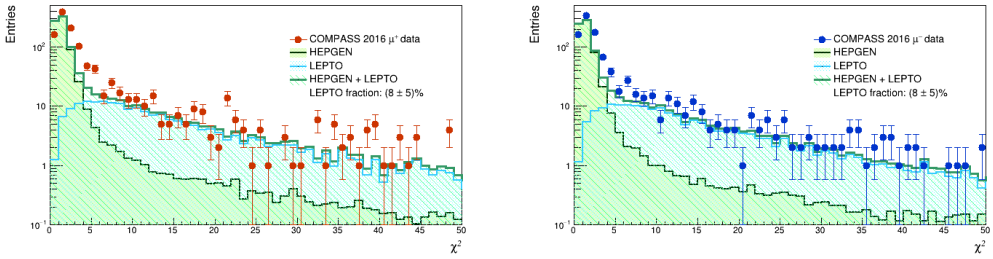

Fig. 4.11: χ^2_{red} distribution of the kinematic fit for μ^+ (left) and μ^- (right) beam. Here, results from both polarities are displayed, the μ^+ data are represented in red and the μ^- data in blue.

The Figs. 4.13, 4.14, and 4.15 show the pull distributions of the difference of the input observables before the kinematic fit with the ones improved by kinematic fit, divided by the difference of their errors (for μ^+ only, for brevity). The

agreement between the data and MC is reasonable, although there are some deviations present, such as in the radial and longitudinal position of recoiled proton hits in the CAMERA rings, or transversal position of the vertex. The quantity σ present in each pull distribution represents the corresponding elements of the covariance matrix $C_{i,j}$ before and after the kinematic fit $\sigma = \sqrt{C_{i,j} - C_{i,j}^{\text{fit}}}$. Most pulls are comparable with the expected normal distribution, which suggests that the kinematic fit provides a reasonable correction to the data.

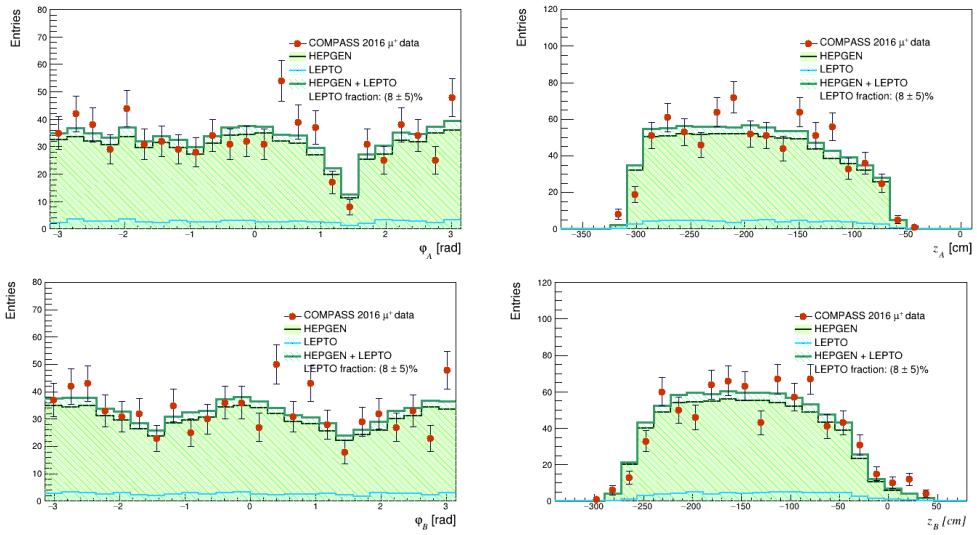

Fig. 4.12: The left top plot shows the azimuthal angle of the hit in CAMERA ring A, ϕ_A, and the right top plot depicts its longitudinal position z_A. The bottom pair of plots shows the same distributions from CAMERA ring B. Only the μ^+ data are shown.

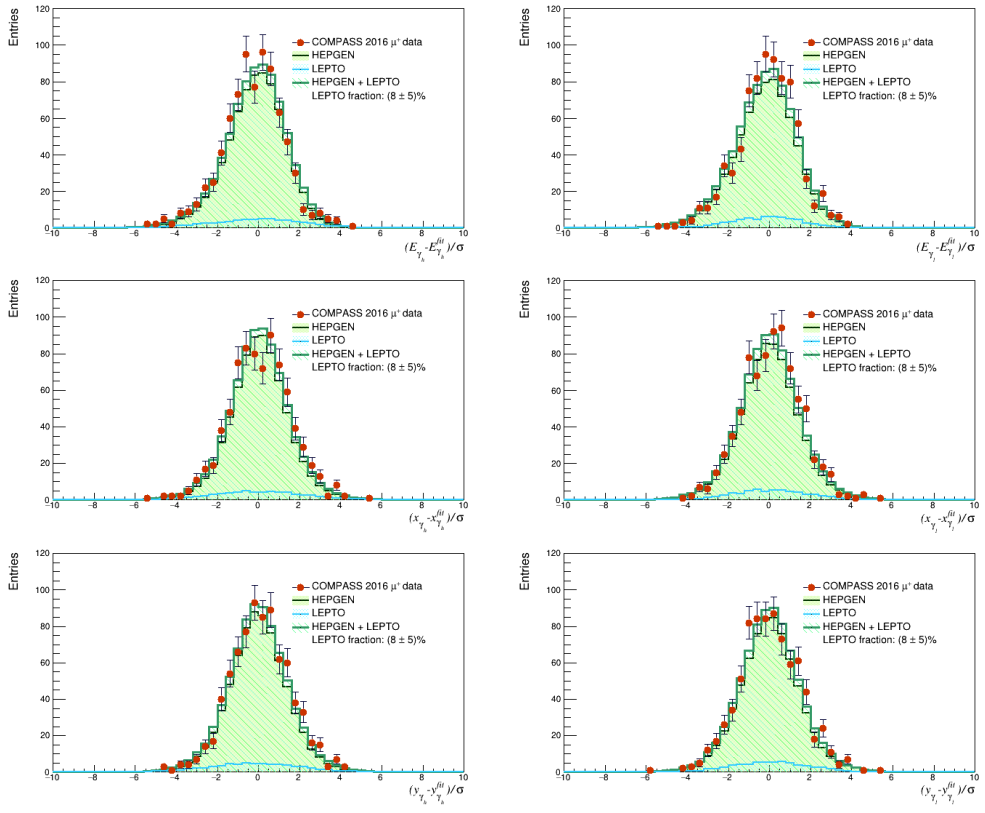

Fig. 4.13: Pull distributions for the higher energetic γ (on the left), and on the lower energetic γ (on the right) of the π^0 decay. E denotes the energy, x and y denote the cluster position at the z-position of the calorimeter, where the cluster has been measured. σ denotes the difference of the error on the quantity before and after the fit. Plots show pulls for μ^+ beam only.

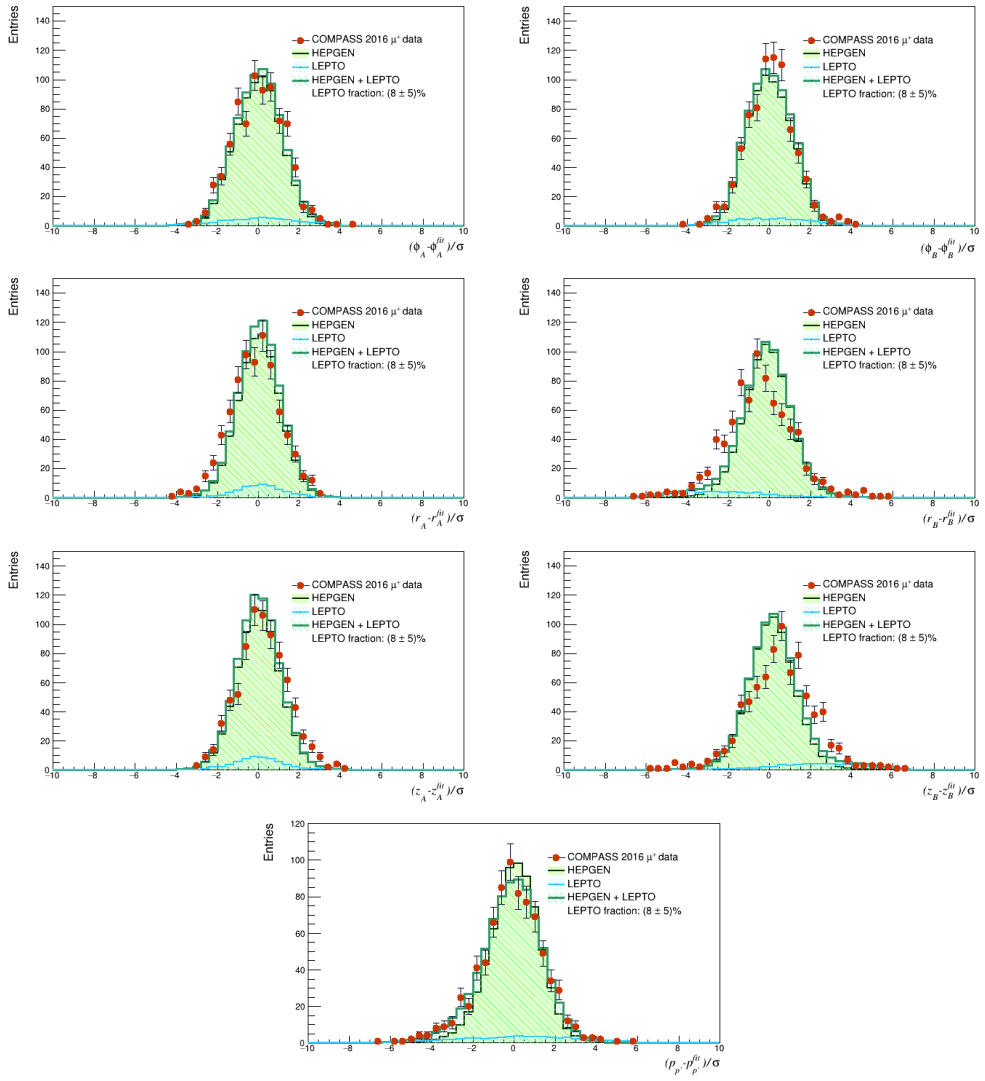

Fig. 4.14: Pull distributions for the position in ring A in CAMERA (left), and in ring B (right). ϕ, r, and z are the polar coordinates of the position where the proton track hits. The bottom plot displays the pull distribution on the momentum of the recoiled proton. σ denotes the difference of the error on the quantity before and after the fit. Plots show pulls for μ^+ beam only.

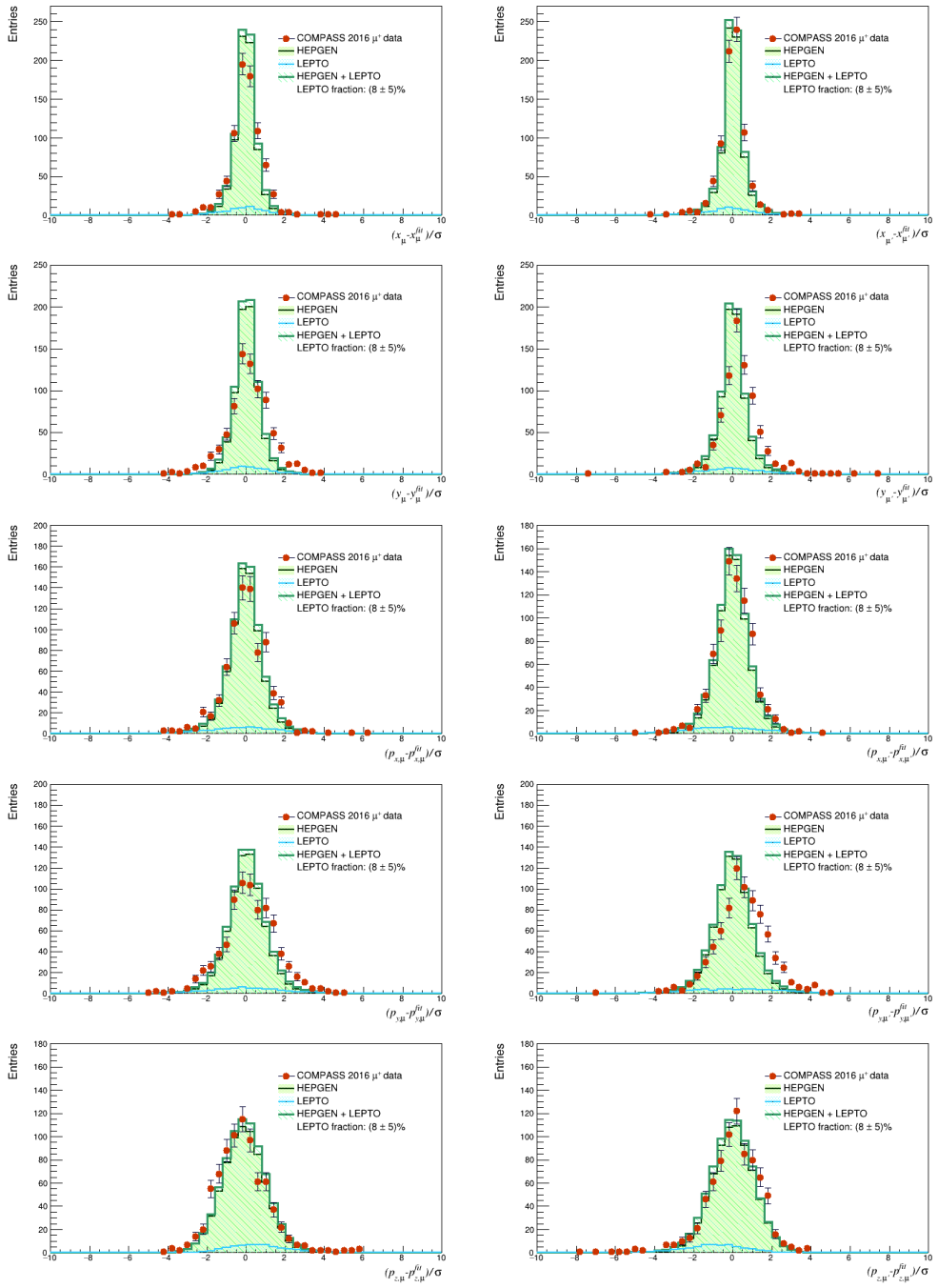

Fig. 4.15: Pull distributions for the incident μ beam (on left) and outgoing μ (on right). x and y denote the track position coordinates at the z-position, and $p_{x,y,z}$ stand for momentum coordinates. σ denotes the difference of the error on the quantity before and after the fit. Plots show pulls for μ^+ beam only.

The last set of cuts is performed on the quantities coming from the kinematic fit, the ambiguity of the event candidates in one event, and the π^0 mass:

- $|t_{\text{fit}}| \in (0.08, 0.64)$ GeV^2, where $|t| = 0.08$ GeV^2 is just above the minimum transfer value for a proton to reach the outer ring of CAMERA and $|t| = 0.64$ GeV^2 is chosen due to the exponential decline of the exclusive π^0 production cross section. Also, for high $|t|$ the separation of proton and other charged particles is less effective.
- $0.04 < y_{\text{fit}} < 0.9$
- 6.4 GeV $< \nu_{\text{fit}} <$ 40 GeV
- 1 GeV$^2 < Q^2_{\text{fit}} <$ 8 GeV^2
- Cut on multiplicity of exclusive π^0 candidates: only one combination of vertex, π^0 candidate, and recoiled proton candidate

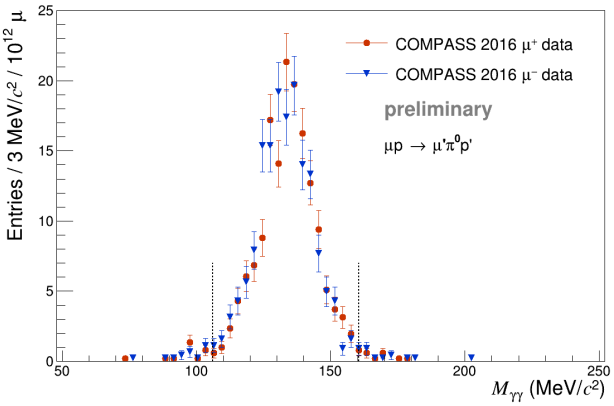

Fig. 4.16: Invariant $\gamma\gamma$ mass for μ^+ (in red) and μ^- (in blue) beam. The margins of the mass cut are indicated by the vertical lines.

The total statistics of all the data periods used from the 2016 data (P04–P09) is listed in Table 4.1. The kinematic coverage has been increased with respect to the published results from 2012 [66]. In 2012, only the inner part of ECAL0 was operational, which reduced the acceptance for the larger azimuthal angles. The

larger acceptance coverage enabled expanding the kinematic domain in ν and Q^2 with respect to 2012 data, which was $8.5 < \nu_{\text{fit}} < 28$ GeV and $1 < Q^2_{\text{fit}} < 5$ GeV^2.

Tab. 4.1: Number of exclusive events after all selection criteria in 2016 periods.

period 2016	μ^+	μ^-
2016-P04	133	117
2016-P05	120	98
2016-P06	127	107
2016-P07	120	141
2016-P08	176	131
2016-P09	116	104
total	792	698

4.4 Monte Carlo Simulations and Background Determination

It is not possible to separate the inclusive inclusive background from the data sample by cuts alone. After applying the full set of the selection criteria to the data, the remaining background has to be evaluated. The description of the background and the determination of its yield in the data sample will be elaborated in this section.

The majority of the background consists of the mentioned DIS events, where the target proton was fragmented and the proton measured in CAMERA and the π^0 can be both coming from fragmentation. Such events can be well simulated by the LEPTO Monte Carlo generator [109], which was chosen as it describes well the DIS at COMPASS. For simulation of the exclusive π^0 signal, the HEPGEN++ generator was selected, which implements the Goloskokov and Kroll model [110, 111].

The simulation of the interaction of the generated particles with the spectrometer is performed by the TGEANT framework [89], which is based on GEANT4 [112]. In TGEANT, all the involved active and inactive materials and detector dimensions are included. It also provides the simulation of a pile-up and beam halo, noise in the calorimeters, and the clusterisation procedure in calorimeters [[↩3.5.]]. The

output of TGEANT is reconstructed in the same fashion as the RD. There are minor modifications to the selection chain, the following cuts are not applied for the MC:

- Rejection of bad spills
- Time-in-spill cut
- Meantime of the beam muon track
- Requirement on the minimum number of hits in BMS.

The list of the used MC samples with their respective number of generated events is given in Table 4.2, where $N^{\Delta\Omega}_{\mu^{+(-)}}$ denote the number of events generated in the whole used phase-space for positive (negative) beam polarity.

Tab. 4.2: MC samples used in 2016 analysis with their respective number of events.

MC	period	$N^{\Delta\Omega}_{\mu^+} \times 10^6$	$N^{\Delta\Omega}_{\mu^-} \times 10^6$
HEPGEN++	2016 P04	1.80	1.79
HEPGEN++	2016 P05	1.84	1.58
HEPGEN++	2016 P06	1.48	1.51
HEPGEN++	2016 P07	1.74	1.85
HEPGEN++	2016 P08	1.80	2.05
HEPGEN++	2016 P09	1.78	1.84
LEPTO	2016 P04	19.97	19.35
LEPTO	2016 P05	19.70	19.12
LEPTO	2016 P06	15.92	16.28
LEPTO	2016 P07	18.49	19.41
LEPTO	2016 P08	19.20	21.82
LEPTO	2016 P09	18.58	18.99

4.4.1 HEPGEN++

The HEPGEN++ is a weighted MC generator. Each point in the phase space of the exclusive cross section $\Delta\Omega_{nijk} = \Delta|t|_n \Delta\phi_i \Delta Q_j^2 \Delta\nu_k$ is weighted by the cross section evaluated at the particular point using the 2016 version of the improved Goloskokov-Kroll model [84], which describes the previous COMPASS results from 2012 data [66]. In order to speed up the weight calculation, a lookup table was first generated using the GK model. Then with the given W, Q^2, and $t' = t - t_{\min}$ of an event, the values of structure functions, σ_{L} and σ_{T}, are deduced by interpolation or extrapolation using the grid points in the lookup table. The kinematic phase space covered by the lookup table is: $5 < W < 15$ GeV, $2 < Q^2 < 16$ GeV^2, $0 < |t'| < 0.75$ GeV^2. The phase space of the generated HEPGEN++ used in this analysis is: $1 < \nu < 40$ GeV, $0.8 < Q^2 < 10$ GeV^2, and $0.001 < |t'| < 0.75$ GeV^2. The distribution of the events within the phase space is not uniform. The events are distributed approximately like the expected number of real data events.

As indicated above, the weight calculated in HEPGEN++ does not involve the ϕ modulation, since it uses only σ_{T} and σ_{L}. To account for the ϕ dependence of the exclusive π^0 cross section (see Eq. 1.65), an additional weight factor was applied using structure function values extracted from the data. Initially, the following set of values for the ϕ-modulation was applied $\epsilon = 0.996$, $\sigma_{\mathrm{T}} + \epsilon\sigma_{\mathrm{L}} = 8.1$ nb, $\sigma_{\mathrm{TT}} = -4.7$ nb, and $\sigma_{\mathrm{LT}} = 1.4$ nb, which was coming from the results of the 2012 data analysis [66]. The corresponding weight factor for a particular event is given as the calculated cross section divided by $\sigma_{\mathrm{T}} + \epsilon\sigma_{\mathrm{L}}$. Note that the σ_{TT} is not exactly the value extracted in [66], as the original value deemed the ϕ-dependent cross section slightly negative in the region where ϕ approaches $\pm\pi$. To prevent this behaviour, a higher value was set. However, in order to further improve the agreement between the data and the simulations, a modification of the ϕ-modulation based on the updated results of 2016 data analysis was introduced: $\sigma_{\mathrm{T}} + \epsilon\sigma_{\mathrm{L}} = 6.49$ nb, $\sigma_{\mathrm{TT}} = -4.53$ nb, and $\sigma_{\mathrm{LT}} = 0.05$ nb, and $\epsilon = 0.997$.

4.4.2 LEPTO

It was observed in the missing energy distribution E_{miss} that LEPTO contains also events with exclusive π^0 topology (i.e. with a scattered muon, scattered proton and two photons in the final state). Such events, with proton either recoiling

from the target, or coming from hadronisation, were rejected. More details on the different event topologies that can be obtained from LEPTO and their features can be found in M. Gorzellik's thesis [19].

After the removal of the mentioned exclusive-like events, LEPTO appears to describe the data background very well, which can be seen in Fig. 4.18, where the exclusive variables are displayed for the data and the respective yields of the signal and background contributions described by HEPGEN++ (in bright green) and LEPTO (in light blue), respectively.

4.4.3 Separation of the SIDIS Background

In order to determine the fraction of HEPGEN++ and LEPTO needed to describe the data, we used the method first established to estimate the visible π^0 leaking into DVCS process [113], and then it was modified for selection of exclusive π^0, see Ref. [19]. The procedure is applied for μ^+ and μ^- separately. The first step is a normalisation of both MC samples to the data using the integral over a 2.5 σ region around the peak of π^0 mass in the $M_{\gamma\gamma}$ spectrum, as is shown in Fig. 4.17, for μ^+ data as an example.

The second step is to scale and sum both MC samples using specific kinematic distributions so that the best possible description of the data is achieved. For this purpose, two exclusivity variables were used: $\Delta\varphi$ (in range from -0.4 up to 0.4 rad) and Δp_T (in range from -0.2 up to 0.2 GeV). Two separate fitting methods were tried in order to estimate the systematic error of the background calculation (see the systematics calculation in Section ⟦↪5.8.⟧).

Both methods use the adapted procedure from the 2012 data analysis [66, 19] to gain the yield of SIDIS background from LEPTO, denoted r_{LEPTO}, from fitting the following relation to a binned distribution from data:

$$f(r_{\text{LEPTO}}; y_{i,L}, y_{i,H}) = r_{\text{LEPTO}} \cdot y_{i,L} + (1 - r_{\text{LEPTO}}) \cdot y_{i,H}, \tag{4.22}$$

where $y_{i,L}$ and $y_{i,H}$ denote the content of i^{th} bin in LEPTO and HEPGEN++ histogram, respectively. The yields of each MC contribution are obtained by performing a fitting procedure, where the combined MC distributions are matched to the corresponding data distribution. Fitting method used in this thesis is the TFractionFitter toolbox [114], which is integrated in the ROOT software. It is

a tool adapted for using more than one MC sample to fit onto the data, using both data and MC statistical uncertainties. It utilises a standard likelihood fit featuring Poisson statistics. In this approach, the statistics of each sample is considered bin-by-bin.

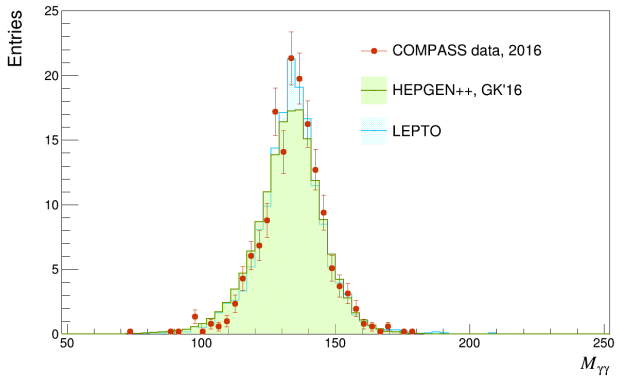

Fig. 4.17: $M_{\gamma\gamma}$ spectrum for data, HEPGEN++ and LEPTO, normalised to the integral of data events inside the $M_{\gamma\gamma}$ cut range (106.1, 160.5) MeV, μ^+ only.

The two histograms used in this procedure are fitted separately and the value of r_{LEPTO} is calculated from their arithmetic average. The fit of MC mixture to the data using TFractionFitter is shown in Fig. 4.19. One can see that the LEPTO events (in blue) are distributed rather flat, while the HEPGEN++ events are concentrated in a narrow peak centred around zero.

The second method [116] uses least squares fit to minimise the sum S running over the bins i of both the chosen histograms $j \in (1, 2)$:

$$S(\vec{r}) = \sum_{j=1}^{2} \sum_{i=1}^{N} (w_i^j r_i^j)^2, \tag{4.23}$$

where r_i are investigated residuals and $w_i = 1/\sigma_i$ are weights of the residuals, σ_i is the statistical error of the respective i^{th} bin. The residual is defined as follows:

$$r_i = y_i - f(r_{\mathrm{LEPTO}}; y_{i,L}, y_{i,H}). \tag{4.24}$$

which is then inserted into the Eq. 4.22 as the fitting parameter r_{LEPTO} for minimisation. The results of the background fitting from both methods are summarised

in Table 4.3 after all the described selection criteria and additional reweighting of HEPGEN++ in ϕ and 2D reweighting procedure as described in the next subsection 4.4.4. One can notice that both methods give very similar results (after averaging the contribution from both histograms in case of the TFractionFitter method). The final value of the background contamination r_{LEPTO} was taken as the arithmetic average of both methods: $r_{\mathrm{LEPTO}} = 8 \pm 5\%$ (considering a larger error as a safe margin).

Another source of background considered in this analysis is exclusive ω contamination. The detailed description of the determination of the level of the contamination is described in the Section of systematics determination ⟦↪5.8.6.⟧. The contamination of exclusive omega misidentified as π^0 was found to be 2.4%, which lead to subtracting 41 events from the final sample of events.

Tab. 4.3: The results of the two background fitting methods: the TFractionFitter method is performed for the two exclusive variables $\Delta\varphi$ and Δp_{T} separately, and resulting r_{LEPTO} is obtained as arithmetic average. the least squares method is done as a simultaneous fit of the two histograms.

Muon beam	Variable	TFractionFitter	Least squares method
μ^+	$\Delta\varphi$	$r_{\mathrm{LEPTO}} = 6\pm7\%$	
	Δp_{T}	$r_{\mathrm{LEPTO}} = 10\pm5\%$	
	average	$r_{\mathrm{LEPTO}} = 8\pm4\%$	$r_{\mathrm{LEPTO}} = 8\pm3\%$
μ^-	$\Delta\varphi$	$r_{\mathrm{LEPTO}} = 4\pm9\%$	
	Δp_{T}	$r_{\mathrm{LEPTO}} = 9\pm4\%$	
	average	$r_{\mathrm{LEPTO}} = 7\pm4\%$	$r_{\mathrm{LEPTO}} = 8\pm3\%$

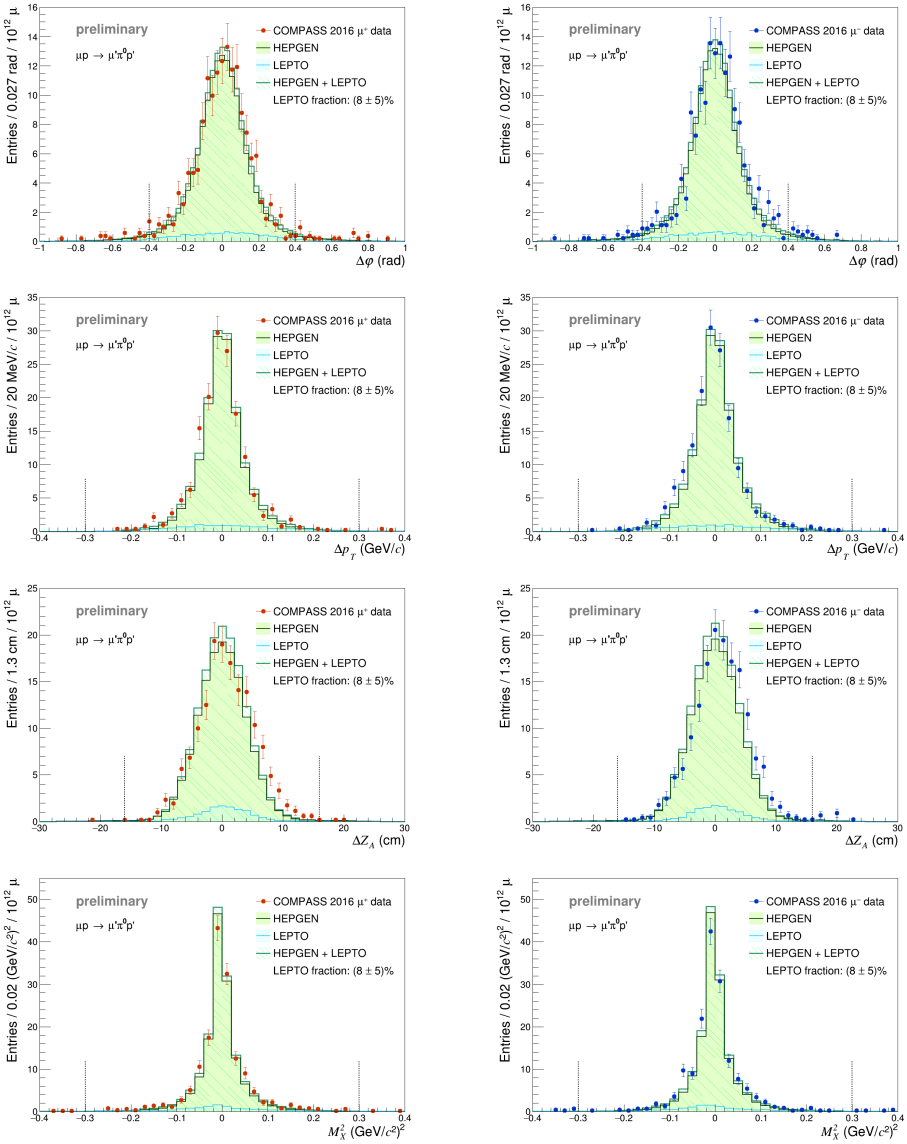

Fig. 4.18: Distributions of the exclusivity variables for μ^+ beam (left) and for μ^+ beam (right): $\Delta\varphi$ is displayed in the top band, followed by the Δp_{T} in the second band, Δz_A in the third band, and the four-momentum balance in the bottom one. The μ^+ data are represented in red and the μ^- data in blue.

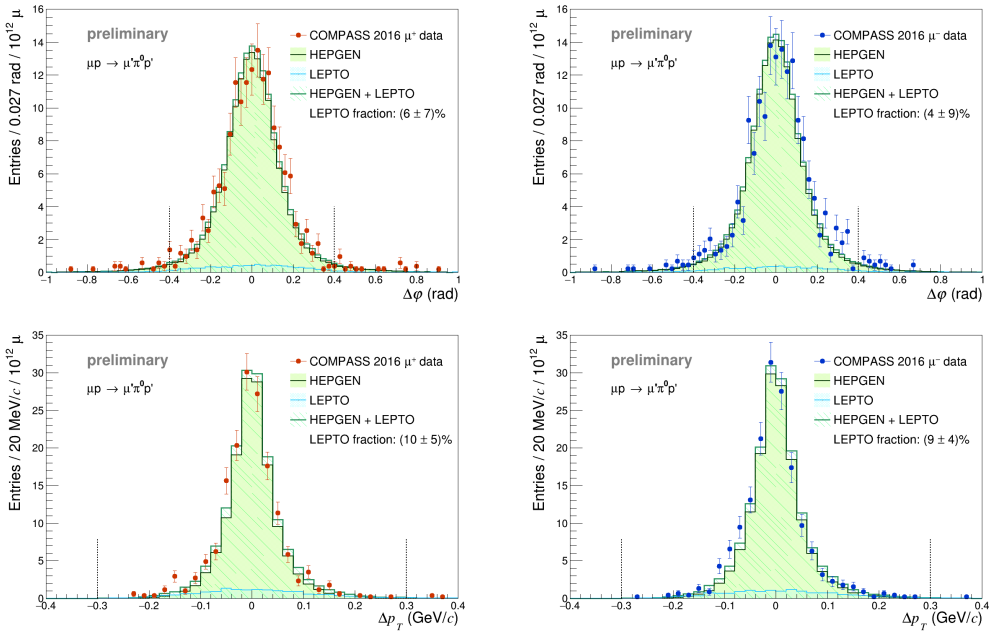

Fig. 4.19: Fitting of the background using the TFractionFitter on exclusivity variables: $\Delta\varphi$ and Δp_{T}.

4.4.4 2D Reweighting of HEPGEN++

After all the steps of the MC treatment described above, the agreement achieved between the data and the MC was satisfactory for most distributions. The only exceptions were the distributions of kinematic variables of ν, Q^2 and $|t|$. The improvement was achieved by performing a 2D reweighting of the HEPGEN++. The illustration of the problem can be seen in Fig. 4.20 in the left-most column, where the three kinematic distributions are shown for the data (in yellow) and the normalised MC mixture (marked by a red line). The HEPGEN++ reweighting method lies in modifying the HEPGEN++ weights by correction coefficients obtained from distribution of ν and $|t|$ from data and both MC simulations as a following combination: "data minus LEPTO divided by HEPGEN++". The obtained coefficients are used to rescale the HEPGEN++ weights of events in the corresponding kinematic domain of ν and $|t|$, and the process of MC normalisation described in the previous Section ⟦↩4.4.3.⟧ is performed.

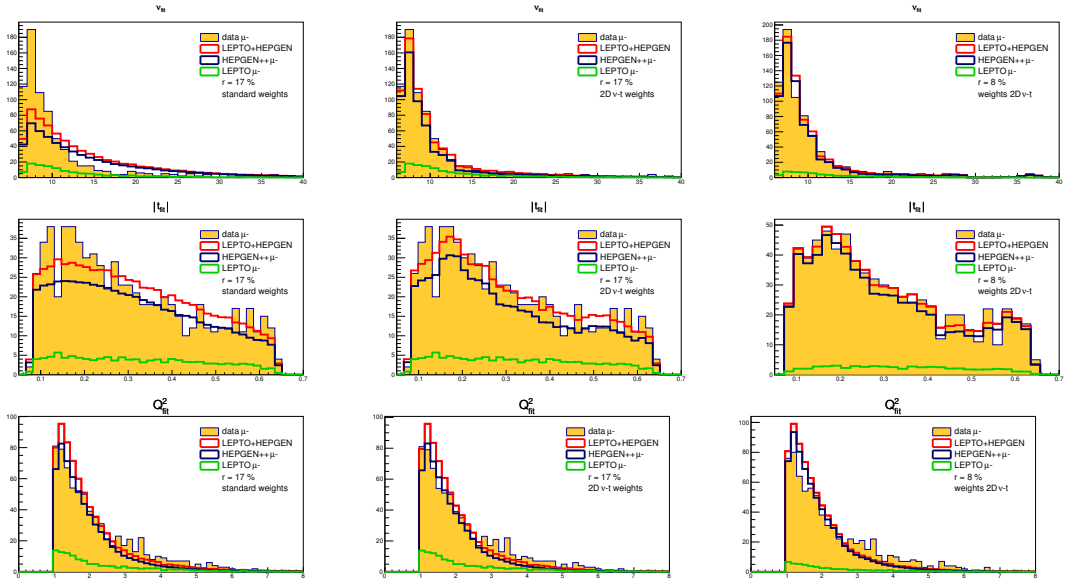

Fig. 4.20: Distributions of ν_{fit} (1^{st} row), $|t_{\text{fit}}|$ (2^{nd} row), and Q^2_{fit} (3^{rd} row), before reweighting HEPGEN++ (1^{st} column), after the first attempt of the 2D reweighting of HEPGEN++ in $(\nu, |t|)$ (2^{nd} column) with $\chi^2_{\text{red}} < 10$, and after the 2D reweighting procedure with included prerequisite reweighting in ϕ in with $\chi^2_{\text{red}} < 7$ (the 3^{rd} column). The background fractions are $r_{\text{LEPTO}} = 17\%$ in the middle column and $r_{\text{LEPTO}} = 8\%$ in right column [116].

Then the reweighting procedure is repeated iteratively until a good agreement of the data and MC mixture in the problematic distributions of ν, Q^2, and $|t|$ is obtained. The reweighting procedure was attempted in two types of tests, using two 1D histograms ν and $|t|$, and 2D histogram ν-$|t|$. The 1D method was unbinned. A smooth function was used to rescale the HEPGEN++ weights, with an exponential function in the case of ν and a polynomial of second order in the case of $|t|$. While the 2D method used coefficients obtained from the histogram bins.

The 1D approach provided similar results as the 2D method in the resulting r_{LEPTO}, however, the agreement of the problematic kinematic distributions was not satisfactorily improved. Thus, the 2D method was chosen at the end. The Fig. 4.21 illustrates the 2D distributions of ν-$|t|$ for the data (left-upper), HEPGEN++ (right-upper), the LEPTO (left bottom), and the "DATA minus LEPTO divided by HEPGEN++" (right bottom), in the binning used the cross

section calculation [[↪5.1.]].

The first attempt for the 2D reweighting for the 2016 analysis was performed before the application of the improved ϕ-modulation of HEPGEN++, and using a looser cut on the reduced χ^2_{red} of the kinematic fit, on a limit of 10. The status of the improvements in this stage is visible in the second column of the Fig. 4.20. At this stage the level of background was not that efficiently suppressed, $r_{\text{LEPTO}} = 17 \pm 5\%$. The second and final 2D reweighting, using an equidistant the cross section binning, included the improved ϕ-modulation of HEPGEN++ and a stricter cut for $\chi^2_{\text{red}} < 7$ and the resulting r_{LEPTO} stabilised at the value $r_{\text{LEPTO}} = 8 \pm 5\%$. Several different types of binning were used for the testing, however, the 2D reweighting method proved to be binning-independent, hence, the cross section binning was kept. The final shape of the MC description of the problematic kinematic distributions is displayed in the right column of Fig. 4.20.

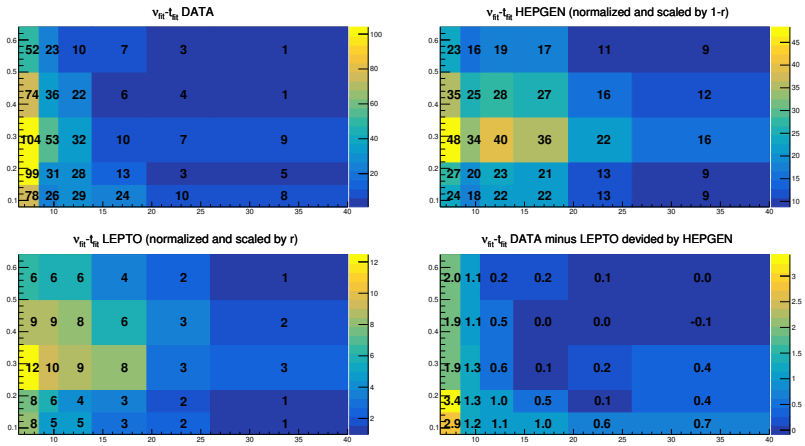

Fig. 4.21: The 2D method of HEPGEN++ reweighting in ν-$|t|$ 2D distributions (ν is displayed on x-axis and $|t|$ on y-axis) with the binning used for the cross section calculation. The last plot shows the multiplicative factors used to modify HEPGEN++ weights in respective bins [116].

5 Exclusive π^0 Production Cross Section

To determine the process of the differential cross section for the hard exclusive muoproduction π^0, $\mu p \to \mu' p' \pi^0$, several steps precede. The luminosity correction [[↩4.1.]], spectrometer acceptance [[↪5.1.]], and bin-by-bin background subtraction ([[↩4.4.3.]] estimating the DIS background, and [[↪5.2.]] for the background subtraction) are needed. The differential exclusive π^0 cross section is evaluated in four-dimensional space $\Delta\Omega = \Delta|t|\Delta\phi\Delta Q^2\Delta\nu$. The dependency of the differential cross section of the exclusive π^0 muoproduction on the four-momentum transfer to the proton, $|t|$, and the azimuthal angle of the produced π^0, ϕ, including the first results on how they evolve with Q^2 and ν, is presented. The systematic studies that have been conducted are detailed in the conclusion part.

5.1 Acceptance Determination

The differential cross section for the hard exclusive muoproduction of π^0 in this analysis is determined in the following kinematic domain

- $6.4 < \nu < 40$ GeV
- $1 < Q^2 < 8$ GeV^2
- $0.08 < |t| < 0.64$ GeV^2

In order to compare the results with the published ones using the 2012 data set [66], the 2016 data were also analysed in the kinematic domain used in the publication

- $8.5 < \nu < 28$ GeV
- $1 < Q^2 < 5$ GeV^2
- $0.08 < |t| < 0.64$ GeV^2

The kinematic domain for this analysis is larger with respect to the 2012 data due to the fully operational ECAL0 in 2016. The element of the phase-space is denoted as $\Delta\Omega_{nijk} = \Delta|t|_n\Delta\phi_i\Delta Q^2_j\Delta\nu_k$.

Tab. 5.1: Four-dimensional grid to evaluate the acceptance in the phase space $\Delta\Omega_{nijk} = \Delta|t|_n \Delta\phi_i \Delta Q^2_j \Delta\nu_k$. The ϕ binning is divided in 8 equidistant bins. The bottom row of the table showcases the full width of the respective dimension.

ϕ /rad	$\lvert t\rvert$ /(GeV^2)	Q^2 /(GeV^2)	ν /(GeV)
$-\pi$ – $\frac{-3\pi}{4}$	0.08 – 0.15	1.0 – 1.5	6.4 – 8.5
$\frac{-3\pi}{4}$ – $\frac{-\pi}{2}$	0.15 – 0.22	1.5 – 2.1	8.5 – 10.5
.	0.22 – 0.36	2.1 – 3.2	10.5 – 13.9
.	0.36 – 0.50	3.2 – 5.0	13.9 – 19.5
.	0.50 – 0.64	5.0 – 8.0	19.5 – 26.0
$\frac{3\pi}{4}$ – π			26.0 – 40.0
$\Delta\phi$/rad	$\Delta\lvert t\rvert$ /(GeV^2)	ΔQ^2 /(GeV^2)	$\Delta\nu$ /(GeV)
2π	0.56	7	33.6

The acceptance a_{nijk} is calculated on a four-dimensional grid as the number of reconstructed events divided by the number of generated events, i.e. events after reconstruction and kinematic fit as

$$a_{\Delta\Omega} = \sum_{i=1}^{N^{\Delta\Omega}_{\text{rec}}} w_i \Big/ \sum_{i=1}^{N^{\Delta\Omega}_{\text{gen}}} w_i, \tag{5.1}$$

where $N^{\Delta\Omega}_{\text{gen}}$ denotes the number of generated events in a phase space element $\Delta\Omega$ and $N^{\Delta\Omega}_{\text{rec}}$ represents the number of HEPGEN++ events reconstructed in the same phase space element. To determine the acceptance, the HEPGEN++ π^0 MC simulation is used [110, 111].

The Tab. 5.1 shows the binning. The range limits of Q^2 and ν were adjusted to take into account the vanishing acceptance in the regions of high Q^2 and high ν. The lower ϕ acceptance in the bin ΔQ^2_5 – $\Delta\nu_1$ corresponds to the finite dimensions of the ECAL0 aperture, while the decrease around $\phi = 0$ in the bin ΔQ^2_1 – $\Delta\nu_6$ is present due to the beam-hole in ECAL2.

The Fig. 5.1 presents the average acceptance computed out of all the six periods. The number of events from data of each beam polarity falling to each kinematic bin is shown in every subplot. To calculate cross-section, the acceptance is determined for each data taking period and beam polarity separately.

The acceptance of the spectrometer has not change notably over time.

In order to compare of the 2016 results with the 2012 ones, the binning used for 2012 analysis was used. The grid of 2012 is defined in Tab. 5.2.

Tab. 5.2: Four-dimensional grid used for the calculation of the acceptance in the phase space $\Delta\Omega_{nijk} = \Delta|t|_n \Delta\phi_i \Delta Q_j^2 \Delta\nu_k$ from the 2016 data with the binning used in 2012 analysis in order to compare results from both years.

ϕ /rad	$\lvert t\rvert$ /(GeV^2)	Q^2 /(GeV^2)	ν /(GeV)
$-\pi$ – $\frac{-3\pi}{4}$	0.08 – 0.15	1.00 – 1.50	8.50 – 11.45
$\frac{-3\pi}{4}$ – $\frac{-\pi}{2}$	0.15 – 0.22	1.50 – 2.24	11.45 – 15.43
.	0.22 – 0.36	2.24 – 3.34	15.43 – 20.78
.	0.36 – 0.50	3.34 – 5.00	20.78 –28.00
.	0.50 – 0.64		
$\frac{3\pi}{4}$ – π			
$\Delta\phi$/rad	$\Delta\lvert t\rvert$ /(GeV^2)	ΔQ^2 /(GeV^2)	$\Delta\nu$ /(GeV)
2π	0.56	4	19.5

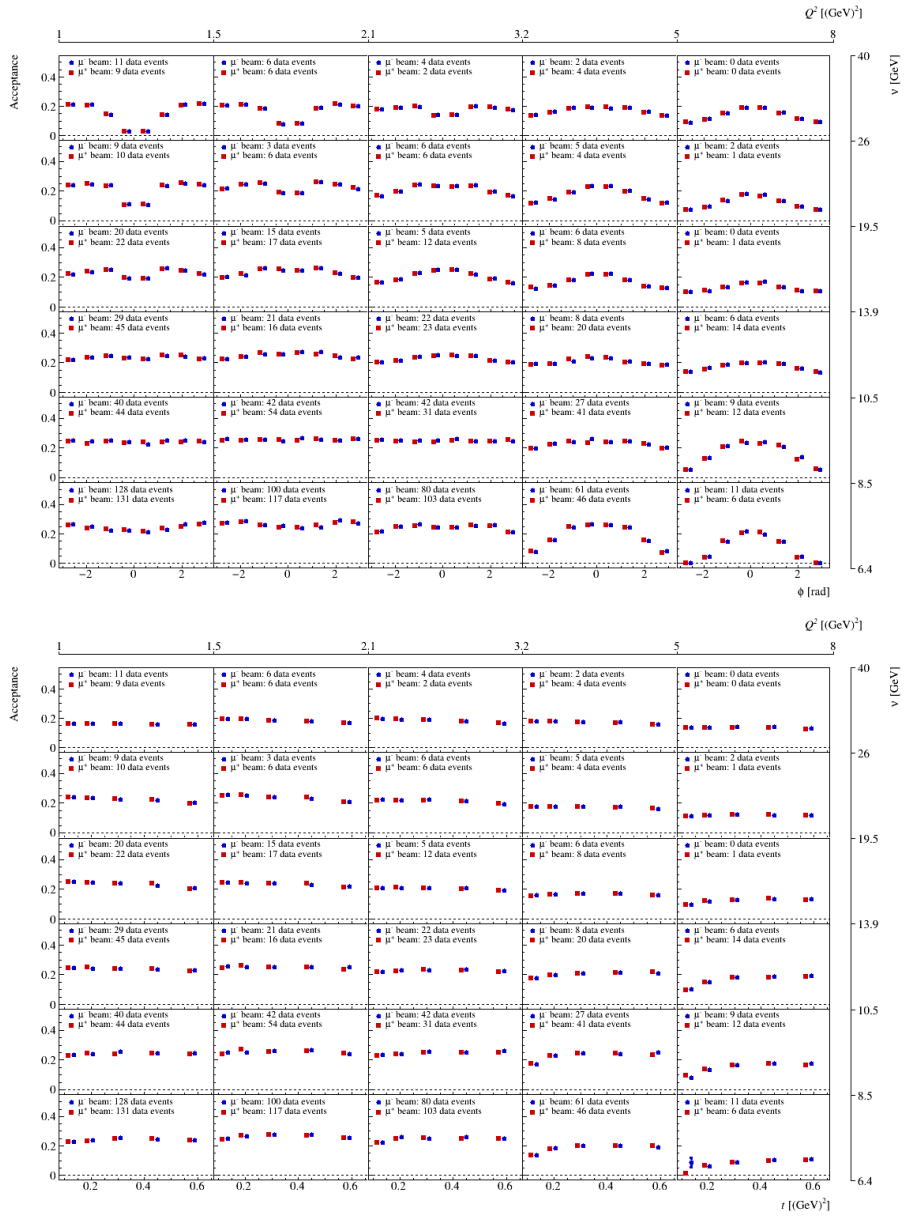

Fig. 5.1: Acceptance for the exclusive π^0 muoproduction. Top panel: The acceptance as a function of Q^2, ν and ϕ for $|t| \in (0.08, 0.64)$ GeV^2 integrated. Each plot in a bin of Q^2 and ν shows the acceptance in 8 equidistant bins of ϕ for μ^+ (in red) and μ^- (in blue) beams. Bottom panel: The acceptance as a function of Q^2, ν and $|t|$ for $\phi \in (-\pi, \pi)$ integrated. Each plot in a bin of Q^2 and ν shows the acceptance in 5 bins of $|t|$ for μ^+ (in red) and μ^- (in blue) beams. The number of RD events of each beam polarity per kinematic bin is presented in each subplot.

5.2 Exclusive π^0 Cross Section Evaluation

The γ^*p cross section of exclusive π^0 production is obtained from the measured μp cross section by applying

$$\frac{\mathrm{d}\sigma^{\gamma^*\mathrm{p}\to\pi^0\mathrm{p}'}}{\mathrm{d}|t|\mathrm{d}\phi} = \frac{1}{\Gamma(Q^2,\nu,E_\mu)}\frac{\mathrm{d}^3\sigma^{\mu\mathrm{p}\to\mu'\pi^0\mathrm{p}'}}{\mathrm{d}Q^2\mathrm{d}\nu\mathrm{d}|t|\mathrm{d}\phi}, \tag{5.2}$$

where the transverse virtual-photon flux $\Gamma(Q^2,\nu,E_\mu)$ is given by

$$\Gamma(Q^2,\nu,E_\mu) = \frac{\alpha_{\mathrm{em}}(1-x_B)}{2\pi Q^2 y E_\mu}\left[y^2\left(1-\frac{2m_\mu^2}{Q^2}\right)+\frac{2}{1+Q^2/\nu^2}\left(1-y-\frac{Q^2}{4E_\mu^2}\right)\right], \tag{5.3}$$

for which the Hand convention [67] is used. Here, m_μ and E_μ denote the mass and energy of the incoming muon, respectively, and α_{em} represents the electromagnetic fine-structure constant.

The cross section can be calculated for each beam charge (noted $\pm$ in the following) in a bin $\Delta\Omega_{nijk}$ by subtracting the inclusive background from the data

$$\left\langle\frac{\mathrm{d}\sigma^{\mu\mathrm{p}\to\mu'\pi^0\mathrm{p}'}}{\mathrm{d}\Omega}\right\rangle^{\pm}_{nijk} = \left\langle\frac{\mathrm{d}\sigma^{\mu\mathrm{p}\to\mu'\pi^0\mathrm{p}'}_{\mathrm{data}}}{\mathrm{d}\Omega}\right\rangle^{\pm}_{nijk} - \left\langle\frac{\mathrm{d}\sigma^{\mu\mathrm{p}\to\mu'\pi^0\mathrm{p}'}_{\mathrm{bg}}}{\mathrm{d}\Omega}\right\rangle^{\pm}_{nijk} \tag{5.4}$$

This relation can be transformed considering the yield of each contribution and taking the acceptance correction into account. Each event is then weighted with the virtual photon flux to obtain the virtual photon yield from the measured yields for muon-proton interactions

$$\begin{aligned}\left\langle\frac{\mathrm{d}\sigma^{\gamma^*\mathrm{p}\to\pi^0\mathrm{p}'}}{\mathrm{d}|t|\mathrm{d}\phi}\right\rangle^{\pm}_{nijk} = \frac{1}{\mathcal{L}^{\pm}\Delta t_n\Delta\phi_i\Delta Q_j^2\Delta\nu_k}\sum_{p\in\mathcal{P}}\left(a^{p,\pm}_{nijk}\right)^{-1}\Bigg(&\sum_{e=1}^{N^{p,\mathrm{data}}_{nijk}\pm}\frac{1}{\Gamma\left(Q_e^2,\nu_e\right)}\\ &- c^{p,\mathrm{LEPTO}\pm}_{\pi^0}\cdot(r_{\mathrm{LEPTO}})\cdot\sum_{e=1}^{N^{p,\pi^0}_{nijk}\pm}\frac{1}{\Gamma\left(Q_e^2,\nu_e\right)}\Bigg)\end{aligned} \tag{5.5}$$

where $\mathcal{L}$ denotes the luminosity, $\mathcal{P}$ the set of data taking periods, and the $c^{p,\mathrm{LEPTO}\pm}_{\pi^0}$ represents the normalisation of LEPTO to data [[↩4.4.3.]].

$$\mathcal{L}^{\pm} = \sum_{p\in\mathcal{P}}\mathcal{L}^{p\pm}$$

$$c^{p,\mathrm{LEPTO}\pm}_{\pi^0} = \frac{N^{p,\mathrm{data}\pm}_{\mathrm{vis.}\pi^0}}{N^{p,\mathrm{LEPTO}\pm}_{\mathrm{vis.}\pi^0}}$$

The mean spin-dependent cross section in each bin of $(|t|, \phi)$ is constructed by integrating over the dimensions of (Q^2, ν) as follows

$$\left\langle \frac{\mathrm{d}\sigma^{\gamma^* \mathrm{p}\to\pi^0\mathrm{p}'}}{\mathrm{d}|t|\mathrm{d}\phi} \right\rangle^{\pm}_{ni} = \frac{\sum_{j,k} \left\langle \frac{\mathrm{d}\sigma^{\gamma^* \mathrm{p}\to\pi^0\mathrm{p}'}}{\mathrm{d}|t|\mathrm{d}\phi} \right\rangle^{\pm}_{nijk} \Delta Q^2_j \Delta\nu_k}{\sum_j \Delta Q^2_j \sum_k \Delta\nu_k} \tag{5.6}$$

The spin-independent virtual photon cross section is obtained as the average of the two muon beam charges

$$\left\langle \frac{\mathrm{d}\sigma^{\gamma^* \mathrm{p}\to\pi^0\mathrm{p}'}}{\mathrm{d}|t|\mathrm{d}\phi} \right\rangle_{ni} = \frac{1}{2}\left(\left\langle \frac{\mathrm{d}\sigma^{\gamma^* \mathrm{p}\to\pi^0\mathrm{p}'}}{\mathrm{d}|t|\mathrm{d}\phi} \right\rangle^{+}_{ni} + \left\langle \frac{\mathrm{d}\sigma^{\gamma^* \mathrm{p}\to\pi^0\mathrm{p}'}}{\mathrm{d}|t|\mathrm{d}\phi} \right\rangle^{-}_{ni} \right) \tag{5.7}$$

The cross section can be integrated over the full 2π-range in ϕ in order to study its $|t|$-dependence

$$\left\langle \frac{\mathrm{d}\sigma^{\gamma^* \mathrm{p}\to\pi^0\mathrm{p}'}}{\mathrm{d}|t|} \right\rangle_{n} = \sum_i \Delta\phi_i \left\langle \frac{\mathrm{d}\sigma^{\gamma^* \mathrm{p}\to\pi^0\mathrm{p}'}}{\mathrm{d}|t|\mathrm{d}\phi} \right\rangle_{ni} \tag{5.8}$$

Similarly to study the ϕ-modulations of the cross section we determine the cross section averaged over $|t|$ as

$$\left\langle \frac{\mathrm{d}\sigma^{\gamma^* \mathrm{p}\to\pi^0\mathrm{p}'}}{\mathrm{d}|t|\mathrm{d}\phi} \right\rangle_{i} = \frac{1}{\sum_n \Delta|t|_n} \sum_n \Delta|t|_n \left\langle \frac{\mathrm{d}\sigma^{\gamma^* \mathrm{p}\to\pi^0\mathrm{p}'}}{\mathrm{d}|t|\mathrm{d}\phi} \right\rangle_{ni} \tag{5.9}$$

Evaluation of the errors

Let the elementary cross section defined in Eq. 5.5 be denoted as

$$Y^{\pm}_{nijk} = \left\langle \frac{\mathrm{d}\sigma^{\gamma^* \mathrm{p}\to\pi^0\mathrm{p}'}}{\mathrm{d}|t|\mathrm{d}\phi} \right\rangle^{\pm}_{nijk} \tag{5.10}$$

Then the statistical errors of the differential cross section, without considering the statistical errors on the acceptance (which are negligible ⟦↩5.1.⟧)

$$\begin{aligned} \Delta(Y^{\pm}_{nijk})^2 = & \frac{1}{\left(\mathcal{L}^{\pm}\Delta t_n \Delta\phi_i \Delta Q^2_j \Delta\nu_k\right)^2} \sum_{p\in\mathcal{P}} \left(a^{p,\pm}_{nijk}\right)^{-2} \left(\sum_{e=1}^{N^{p,\mathrm{data}\,\pm}_{nijk}} \frac{1}{\Gamma^2\left(Q^2_e, \nu_e\right)} \right. \\ & \left. + \left(c^{p\mathrm{LEPTO}\pm}_{\pi^0} \cdot r_{\mathrm{LEPTO}}\right)^2 \sum_{e=1}^{N^{p,\pi^0}_{nijk}\pm} \frac{1}{\Gamma^2\left(Q^2_e, \nu_e\right)} \right) \end{aligned} \tag{5.11}$$

The error of the mean cross section per bin $(|t|, \phi)$ is

$$\Delta\left(\left\langle\frac{\mathrm{d}\sigma^{\gamma^*\mathrm{p}\to\pi^0\mathrm{p}'}}{\mathrm{d}|t|\mathrm{d}\phi}\right\rangle_{ni}^{\pm}\right)^2 = \frac{\sum_{j,k}\Delta(Y^{\pm}_{nijk})^2(\Delta Q_j^2)^2(\Delta\nu_k)^2}{(\sum_j\Delta Q_j^2)^2(\sum_k\Delta\nu_k)^2} \tag{5.12}$$

The error of the spin-independent cross section is

$$\Delta\left(\left\langle\frac{\mathrm{d}\sigma^{\gamma^*\mathrm{p}\to\pi^0\mathrm{p}'}}{\mathrm{d}|t|\mathrm{d}\phi}\right\rangle_{ni}\right)^2 = \frac{1}{4}\left(\Delta\left(\left\langle\frac{\mathrm{d}\sigma^{\gamma^*\mathrm{p}\to\pi^0\mathrm{p}'}}{\mathrm{d}|t|\mathrm{d}\phi}\right\rangle_{ni}^{+}\right)^2 + \Delta\left(\left\langle\frac{\mathrm{d}\sigma^{\gamma^*\mathrm{p}\to\pi^0 p'}}{\mathrm{d}|t|\mathrm{d}\phi}\right\rangle_{ni}^{-}\right)^2\right) \tag{5.13}$$

The error of the $|t|$-dependence of the cross section is

$$\Delta\left(\left\langle\frac{\mathrm{d}\sigma^{\gamma^*\mathrm{p}\to\pi^0\mathrm{p}'}}{\mathrm{d}|t|}\right\rangle_{n}\right)^2 = \sum_i(\Delta\phi_i)^2\Delta\left(\left\langle\frac{\mathrm{d}\sigma^{\gamma^*\mathrm{p}\to\pi^0\mathrm{p}'}}{\mathrm{d}|t|\mathrm{d}\phi}\right\rangle_{ni}\right)^2 \tag{5.14}$$

The error of the ϕ-dependent cross section is obtained in the same fashion.

5.3 The π^0 Cross Section as a Function of ϕ

The results of the differential π^0 cross section as a function of ϕ from Eq. 5.9 averaged over the two beam polarities are depicted in Fig. 5.2. The results separated for μ^+ (red) and μ^- (blue) are shown in Fig. 5.3. The Tab. 5.3 summarises the results.

The data points of the spin-independent distribution are fitted as a ϕ-modulation according to Eq. 1.65, using the mean value $\epsilon = 0.997$. The curve is shown in red in Fig. 5.2 and the 3 structure functions resulting from the fit are listed in Tab. 5.4. The structure functions $p_0 = \langle\frac{\mathrm{d}\sigma_\mathrm{T}}{\mathrm{d}t} + \epsilon\frac{\mathrm{d}\sigma_\mathrm{L}}{\mathrm{d}t}\rangle$ and $p_1 = \langle\frac{\mathrm{d}\sigma_\mathrm{TT}}{\mathrm{d}t}\rangle$ are large and well determined while $p_2 = \langle\frac{\mathrm{d}\sigma_\mathrm{LT}}{\mathrm{d}t}\rangle$ is close to zero within statistical uncertainties. The spin-dependent differential cross section is fitted with the ϕ-modulation from the following equation derived from Eq. 1.64

$$\begin{aligned}\frac{\mathrm{d}\sigma^{\gamma^*\mathrm{p}}}{\mathrm{d}t\mathrm{d}\phi} =& \frac{1}{2\pi}\left[\frac{\mathrm{d}\sigma_\mathrm{T}}{\mathrm{d}t} + \epsilon\frac{\mathrm{d}\sigma_\mathrm{L}}{\mathrm{d}t} + \epsilon\cos(2\phi)\frac{\mathrm{d}\sigma_\mathrm{TT}}{\mathrm{d}t}\right.\\ &\left. + \sqrt{2\epsilon(1+\epsilon)}\cos(\phi)\frac{\mathrm{d}\sigma_\mathrm{LT}}{\mathrm{d}t} + \sqrt{2\epsilon(1-\epsilon)}\sin(\phi)\frac{\mathrm{d}\sigma'_\mathrm{LT}}{\mathrm{d}t}\right].\end{aligned} \tag{5.15}$$

The values from the fit are summarised in Tab. 5.5.

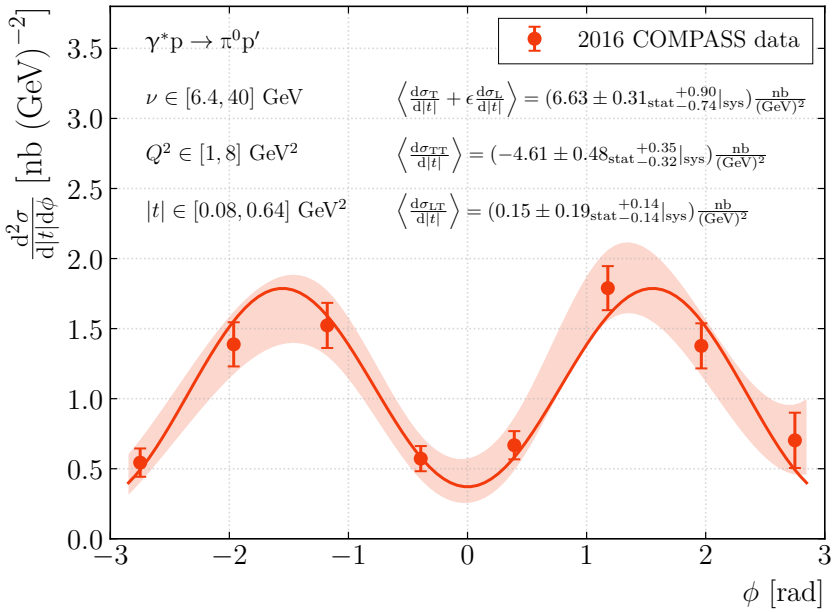

Fig. 5.2: The differential cross section as a function of ϕ, integrated over the full $|t|$ range $\Delta|t| = (0.08, 0.64)$ GeV^2. The red points represent the mean value of the differential cross section per bin. The bars represent the statistical errors and the filled band marks the combined statistical and systematic uncertainties. The average value for μ^+ and μ^-, using the 2016 data in kinematic domain $6.4 < \nu < 40$ GeV, $1 < Q^2 < 8$ GeV^2, $0.08 < |t| < 0.64$ GeV^2, are shown. The data are fitted with 3 structure functions $\sigma_T + \epsilon\sigma_L$, σ_{TT} and σ_{LT}.

Tab. 5.3: Values of the differential π^0 cross section as a function of ϕ in units of $\frac{\text{nb}}{(\text{GeV})^2}$. Only statistical errors are given for the spin-dependent cross section.

ϕ bin	$[-\pi, -\frac{3\pi}{4}]$	$[-\frac{3\pi}{4}, -\frac{\pi}{2}]$	$[-\frac{\pi}{2}, -\frac{\pi}{4}]$	$[-\frac{\pi}{4}, 0]$	$[0, \frac{\pi}{4}]$	$[\frac{\pi}{4}, \frac{\pi}{2}]$	$[\frac{\pi}{2}, \frac{3\pi}{4}]$	$[\frac{3\pi}{4}, \pi]$
$\langle \frac{d\sigma^{\gamma^* p \to \pi^0 p'}}{d\lvert t\rvert d\phi} \rangle$	0.54	1.39	1.52	0.57	0.67	1.79	1.38	0.70
stat. error	0.10	0.16	0.16	0.09	0.10	0.16	0.16	0.20
syst. error ↑	0.13	0.17	0.19	0.14	0.17	0.22	0.17	0.16
syst. error ↓	0.10	0.14	0.15	0.12	0.15	0.17	0.14	0.14
number of events	120	237	264	120	123	297	241	88
$\langle \frac{d\sigma^{\gamma^* p \to \pi^0 p'}}{d\lvert t\rvert d\phi} \rangle^+$	0.64	1.39	1.62	0.73	0.59	1.52	1.40	0.74
stat. error	0.16	0.22	0.23	0.15	0.12	0.21	0.25	0.23
$\langle \frac{d\sigma^{\gamma^* p \to \pi^0 p'}}{d\lvert t\rvert d\phi} \rangle^-$	0.44	1.38	1.42	0.41	0.75	2.06	1.36	0.66
stat. error	0.12	0.23	0.23	0.10	0.16	0.24	0.21	0.32

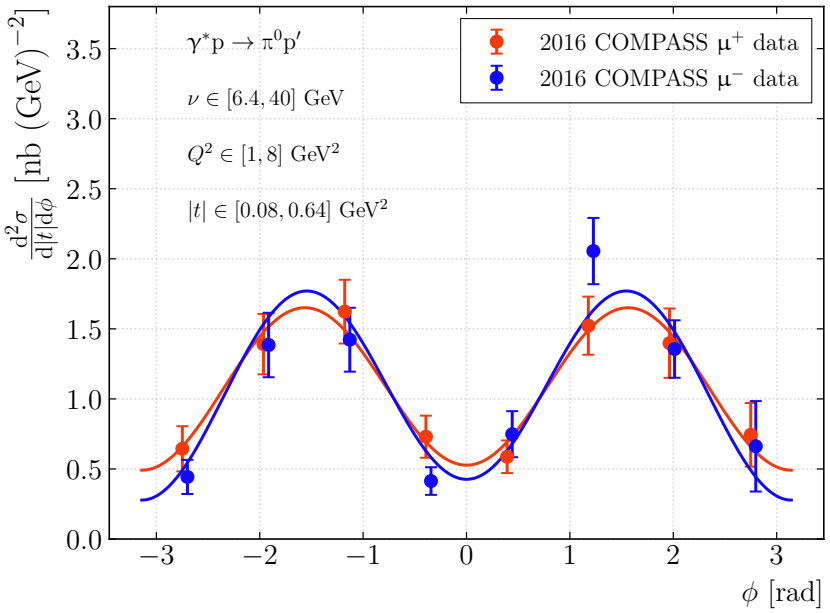

Fig. 5.3: Differential $\gamma^* p$ exclusive π^0 cross section as a function of ϕ for μ^+ and μ^- shown in red and blue separately. Only the statistical errors are evaluated.

Tab. 5.4: The results of the fit of the structure functions in units of $\frac{\mathrm{nb}}{(\mathrm{GeV})^2}$.

	$p_0 = \langle \frac{\mathrm{d}\sigma_\mathrm{T}}{\mathrm{d}t} + \epsilon \frac{\mathrm{d}\sigma_\mathrm{L}}{\mathrm{d}t} \rangle$	$p_1 = \langle \frac{\mathrm{d}\sigma_\mathrm{TT}}{\mathrm{d}t} \rangle$	$p_2 = \langle \frac{\mathrm{d}\sigma_\mathrm{LT}}{\mathrm{d}t} \rangle$	χ^2_red
value	6.63	−4.61	0.15	1.0
stat. error	0.31	0.48	0.19	
syst. error ↑	0.91	0.35	0.14	
syst. error ↓	0.74	0.32	0.14	

Tab. 5.5: Values of spin-dependent the structure functions in units of $\frac{\mathrm{nb}}{(\mathrm{GeV})^2}$.

	$p_0 = \langle \frac{\mathrm{d}\sigma_\mathrm{T}}{\mathrm{d}t} + \epsilon \frac{\mathrm{d}\sigma_\mathrm{L}}{\mathrm{d}t} \rangle$	$p_1 = \langle \frac{\mathrm{d}\sigma_\mathrm{TT}}{\mathrm{d}t} \rangle$	$p_2 = \langle \frac{\mathrm{d}\sigma_\mathrm{LT}}{\mathrm{d}t} \rangle$	$p_3 = \langle \frac{\mathrm{d}\sigma'_\mathrm{LT}}{\mathrm{d}t} \rangle$
$\langle \frac{\mathrm{d}\sigma^{\gamma^* \mathrm{p} \to \pi^0 \mathrm{p}'}}{\mathrm{d}\lvert t\rvert \mathrm{d}\phi} \rangle^+$	6.71	−4.12	0.17	3.9
stat. error	0.43	0.68	0.27	10.9
$\langle \frac{\mathrm{d}\sigma^{\gamma^* \mathrm{p} \to \pi^0 \mathrm{p}'}}{\mathrm{d}\lvert t\rvert \mathrm{d}\phi} \rangle^-$	6.45	−4.97	0.12	20.4
stat. error	0.42	0.67	0.24	11.0

5.4 The π^0 Cross Section as a Function of $|t|$

The results of the differential π^0 cross section as a function of $|t|$ from Eq. 5.8 are represented in Fig. 5.4 The results separated for μ^+ (red) and μ^- (blue) are shown in Fig. 5.5. The numerical values are shown in Tab. 5.6.

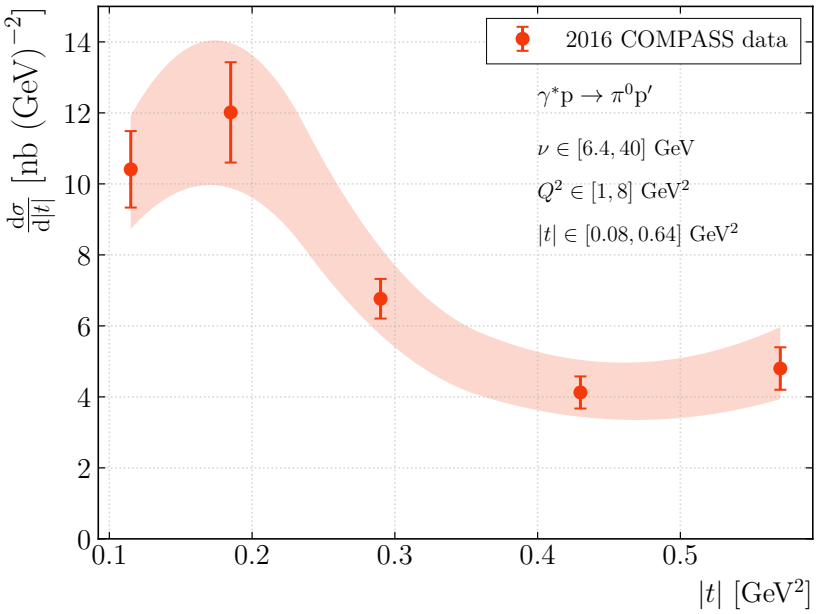

Fig. 5.4: The differential cross section as a function of $|t|$, integrated over the full 2π range of ϕ. The points represent the mean value in a particular bin. The bars represent the statistical errors and the filled band marks the combined statistical and systematic uncertainties. The average value for μ^+ and μ^-, using the 2016 data in kinematic domain $\nu \in (6.4, 40)$ GeV, $Q^2 \in (1, 8)$ GeV^2, $|t| \in (0.08, 0.64)$ GeV^2, is shown.

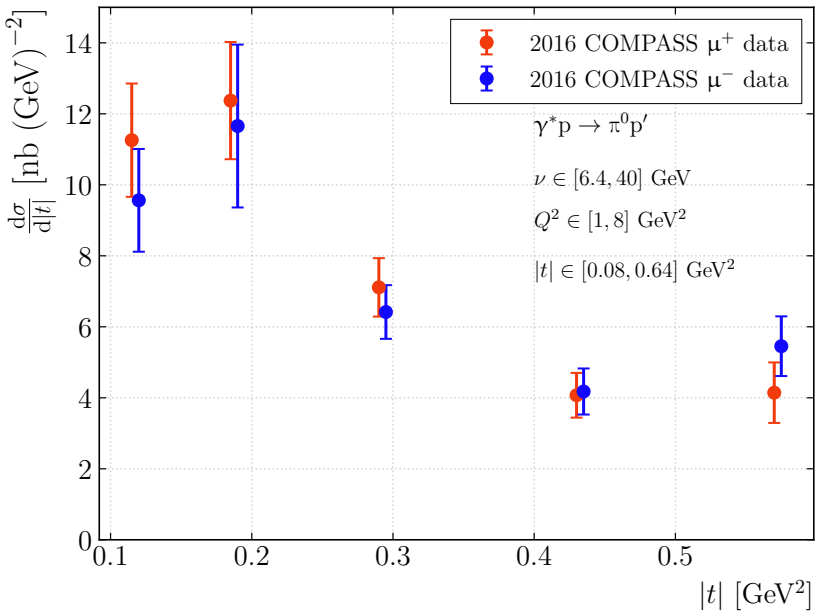

Fig. 5.5: The differential cross section as a function of $|t|$ as in Fig. 5.4 for μ^+ and μ^- separately.

Tab. 5.6: Values of the differential π^0 cross section as a function of $|t|$ in units of $\frac{\text{nb}}{(\text{GeV})^2}$. For the spin-dependent results, only statistical uncertainties are shown.

$\lvert t\rvert$ bin	$[0.08, 0.15]$	$[0.15, 0.22]$	$[0.22, 0.36]$	$[0.36, 0.5]$	$[0.5, 0.64]$
$\langle \frac{d\sigma^{\gamma^* p \to \pi^0 p'}}{d\lvert t\rvert} \rangle$	10.41	12.01	6.76	4.12	4.80
stat. error	1.08	1.41	0.56	0.45	0.60
syst. error ↑	1.06	1.36	1.32	0.80	1.00
syst. error ↓	1.29	1.60	0.85	0.52	0.62
number of events	288	324	419	251	208
$\langle \frac{d\sigma^{\gamma^* p \to \pi^0 p'}}{d\lvert t\rvert} \rangle^+$	11.26	12.37	7.11	4.07	4.14
stat. error	1.60	1.65	0.82	0.63	0.85
$\langle \frac{d\sigma^{\gamma^* p \to \pi^0 p'}}{d\lvert t\rvert} \rangle^-$	9.56	11.66	6.42	4.18	5.45
stat. error	1.45	2.29	0.76	0.65	0.84

5.5 Extraction of the Total Cross Section

The mean value of the total cross section is derived from integrating over ϕ and t,

$$\left\langle \sigma^{\gamma^* \mathrm{p} \to \pi^0 \mathrm{p}'} \right\rangle = \frac{1}{\sum_n \Delta|t|_n} \sum_n \Delta|t|_n \sum_i \Delta\phi_i \left\langle \frac{\mathrm{d}\sigma^{\gamma^* \mathrm{p} \to \pi^0 \mathrm{p}'}}{\mathrm{d}|t|\mathrm{d}\phi} \right\rangle_{ni}. \tag{5.16}$$

The error is determined in analogy to Eq. 5.14.

The result of the total cross section in the range measured in the 2016 data is

$$\left\langle \sigma^{\gamma^* \mathrm{p} \to \pi^0 \mathrm{p}'} \right\rangle = 6.72 \pm 0.32_{\mathrm{stat}}{}^{+\ 0.99}_{-\ 0.79}\Big|_{\mathrm{sys}} \text{ nb}$$

with the mean vales of the kinematics:

$$\begin{aligned} \langle Q^2_{\mathrm{fit}} \rangle &= 2.266 \text{ GeV}^2, \\ \langle \nu_{\mathrm{fit}} \rangle &= 10.160 \text{ GeV}, \\ \langle |t_{\mathrm{fit}}| \rangle &= 0.293 \text{ GeV}^2, \\ \langle x_B \rangle &= 0.134, \\ \langle W \rangle &= 4.100 \text{ GeV}, \\ \langle |t_{\mathrm{CAMERA}}| \rangle &= 0.297 \text{ GeV}^2. \end{aligned}$$

5.6 Comparison of the π^0 Cross Section with the 2012 results

The results of the differential exclusive π^0 cross section averaged over spin-dependent contributions in the reduced kinematic domain:

$$8.5 < \nu < 28 \text{ GeV}, \ 1 < Q^2 < 5 \text{ GeV}^2, \text{ and } 0.08 < |t| < 0.64 \text{ GeV}^2,$$

are shown in Fig. 5.6 as a function of ϕ and in Fig. 5.7 as a function of $|t|$, compared to the 2012 results [66] and the phenomenological GK model [84]. Results from both experimental sets are in reasonable agreement within the statistical uncertainties, however, the theoretical prediction for $|t|$ deviates slightly both for the new and old results. Numerical values are given in Tab. 5.7 and 5.8.

Tab. 5.7: Values of the differential π^0 cross section as a function of ϕ in units of $\frac{\text{nb}}{(\text{GeV})^2}$ in the reduced kinematic domain.

ϕ bin	$[-\pi, -\frac{3\pi}{4}]$	$[-\frac{3\pi}{4}, -\frac{\pi}{2}]$	$[-\frac{\pi}{2}, -\frac{\pi}{4}]$	$[-\frac{\pi}{4}, 0]$	$[0, \frac{\pi}{4}]$	$[\frac{\pi}{4}, \frac{\pi}{2}]$	$[\frac{\pi}{2}, \frac{3\pi}{4}]$	$[\frac{3\pi}{4}, \pi]$
$\langle \frac{d\sigma^{\gamma^* p \to \pi^0 p'}}{d\lvert t\rvert d\phi} \rangle$	0.59	1.91	1.76	0.76	1.13	2.90	1.86	0.59
stat. error	0.13	0.26	0.25	0.15	0.20	0.32	0.27	0.16
syst. error ↑	0.10	0.16	0.13	0.17	0.13	0.21	0.19	0.10
syst. error ↓	0.16	0.16	0.13	0.17	0.23	0.18	0.12	0.10
number of events	47	107	101	49	65	145	99	34

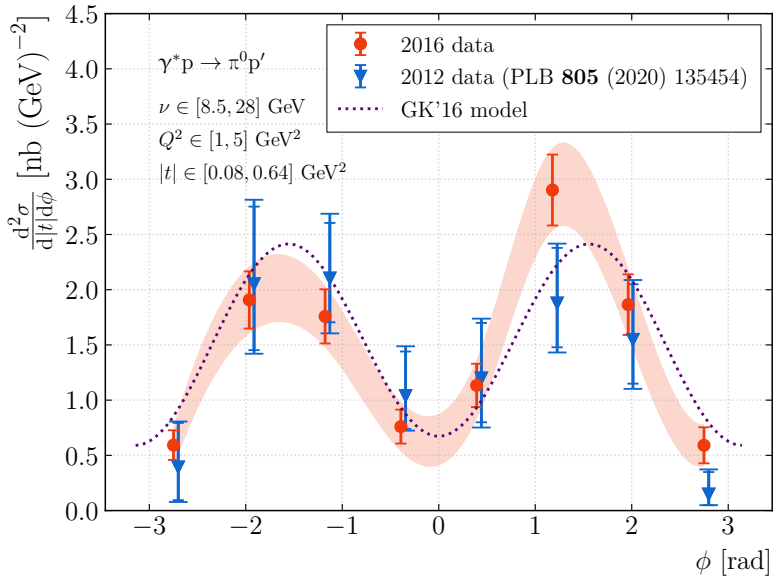

Fig. 5.6: Differential γ^*p exclusive π^0 cross section as a function of ϕ averaged over μ^+ and μ^-. The results of 2016 are represented by the red points. The bars represent the statistical errors and the filled bands mark the combined statistical and systematic uncertainties. They are compared with the results from 2012 data [66] (in blue), with the inner bars representing the statistical errors and the outer the combined errors, for better readability. The GK model [84] is represented by the violet dashed line. The reduced kinematic domain is $8.5 < \nu < 28$ GeV, $1 < Q^2 < 5$ GeV^2, $0.08 < |t| < 0.64$ GeV^2.

Tab. 5.8: Values of the differential π^0 cross section as a function of $|t|$ in units of $\frac{\text{nb}}{(\text{GeV})^2}$ in the reduced kinematic domain.

$\|t\|$ bin	$[0.08, 0.15]$	$[0.15, 0.22]$	$[0.22, 0.36]$	$[0.36, 0.5]$	$[0.5, 0.64]$
$\langle \frac{d\sigma^{\gamma^* p \to \pi^0 p'}}{d\|t\|} \rangle$	16.87	16.79	10.32	4.91	4.11
stat. error	1.86	1.98	1.07	0.74	0.74
syst. error ↑	1.41	1.21	1.56	0.83	0.55
syst. error ↓	2.03	1.83	1.24	0.70	0.39
number of events	142	148	181	99	77

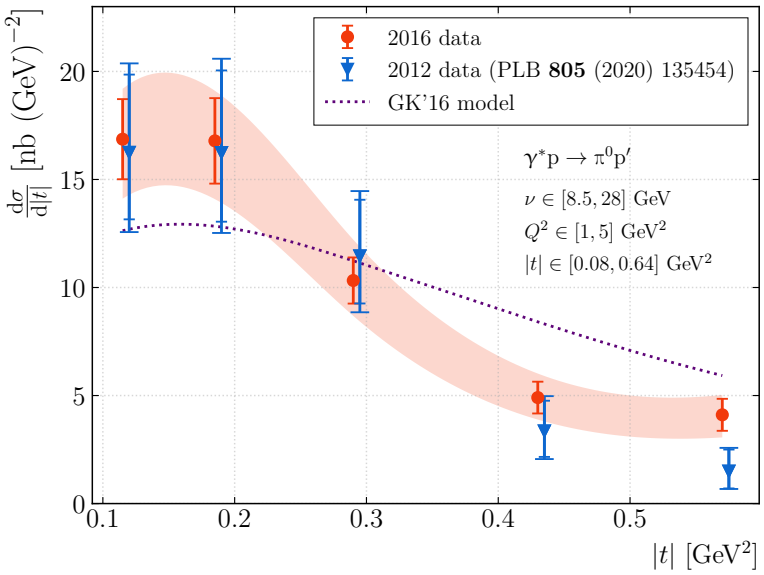

Fig. 5.7: Differential $\gamma^* p$ exclusive π^0 cross section as a function of $|t|$ averaged over μ^+ and μ^-. The results of 2016 are represented by the red points. The bars represent the statistical errors and the filled bands mark the combined statistical and systematic uncertainties. They are compared with the results from 2012 data [66] (in blue), with the inner bars representing the statistical errors and the outer the combined errors, for better readability. The GK model [84] is represented by the violet dashed line. The reduced kinematic domain is $8.5 < \nu < 28$ GeV, $1 < Q^2 < 5$ GeV^2, $0.08 < |t| < 0.64$ GeV^2.

5.7 Evolution in Q^2 and ν

The gain of the 2016 statistics with respect to the 2012 statistics is about 2.3 times larger. The improved statistics allows to study the ν evolution as well as the Q^2 evolution. After the pilot 2012 run the aperture of the ECAL0 calorimeter had been enlarged to allow reaching smaller ν or x_B, providing additional motivation to probe different ν and Q^2 regions. The evolution of the cross section was studied in three bins in ν:

$$(6.4, 8.5)\ \text{GeV}, \quad (8.5, 13.9)\ \text{GeV}, \quad (13.9, 40.0)\ \text{GeV}.$$

To study the evolution of the cross section with Q^2, four bins were chosen:

$$(1.0, 1.5)\ \text{GeV}^2, \quad (1.5, 2.1)\ \text{GeV}^2, \quad (2.1, 5.0)\ \text{GeV}^2, \quad (5.0, 8.0)\ \text{GeV}^2.$$

The Figs. 5.8, 5.9 show the evolution in the three bins of ν as a function of $|t|$ and ϕ. The Figs. 5.10, and 5.11 depict the evolution in four Q^2 bins as a function of $|t|$ and Q^2. The amplitude of the cross section in both variables is decreasing, as can be expected from the shape of ν and Q^2 distributions ⟦↩4.3.3.⟧.

Tab. 5.9: Differential cross section as a function of $|t|$ in 3 ν bins (units $\frac{\text{nb}}{(\text{GeV}/c)^2}$).

$\|t\|$ bin	$[0.08, 0.15]$	$[0.15, 0.22]$	$[0.22, 0.36]$	$[0.36, 0.5]$	$[0.5, 0.64]$	$[0.08, 0.64]$
Complete ν domain		$6.4 < \nu < 40$ GeV		$\langle\nu\rangle = 10.16$ GeV		
$\langle \frac{d\sigma^{\gamma^* p \to \pi^0 p'}}{d\|t\|} \rangle$	10.41	12.01	6.76	4.12	4.80	6.72
stat. error	1.08	1.41	0.56	0.45	0.60	
syst. error ↑	1.06	1.36	1.32	0.80	1.00	
syst. error ↓	1.29	1.60	0.85	0.52	0.62	
1^{st} ν bin		$6.4 < \nu < 8.5$ GeV		$\langle\nu\rangle = 7.35$ GeV		
$\langle \frac{d\sigma^{\gamma^* p \to \pi^0 p'}}{d\|t\|} \rangle$	34.53	55.36	40.11	34.67	39.28	39.75
stat. error	4.21	6.83	3.84	4.82	6.73	2.49
2^{nd} ν bin		$8.5 < \nu < 13.9$ GeV		$\langle\nu\rangle = 10.32$ GeV		
$\langle \frac{d\sigma^{\gamma^* p \to \pi^0 p'}}{d\|t\|} \rangle$	20.73	31.13	19.62	10.29	12.41	17.10
stat. error	3.00	4.47	2.43	1.62	2.40	1.16
3^{rd} ν bin		$13.9 < \nu < 40$ GeV		$\langle\nu\rangle = 21.08$ GeV		
$\langle \frac{d\sigma^{\gamma^* p \to \pi^0 p'}}{d\|t\|} \rangle$	6.46	3.98	1.98	0.80	0.84	2.21
stat. error	1.26	0.93	0.44	0.31	0.29	0.25

Tab. 5.10: Differential cross section as a function of ϕ in 3 ν bins (units $\frac{\text{nb}}{(\text{GeV}/c)^2}$).

ϕ bin	$[-\pi, -\frac{3\pi}{4}]$	$[-\frac{3\pi}{4}, -\frac{\pi}{2}]$	$[-\frac{\pi}{2}, -\frac{\pi}{4}]$	$[-\frac{\pi}{4}, 0]$	$[0, \frac{\pi}{4}]$	$[\frac{\pi}{4}, \frac{\pi}{2}]$	$[\frac{\pi}{2}, \frac{3\pi}{4}]$	$[\frac{3\pi}{4}, \pi]$
	Complete ν domain		$6.4 < \nu < 40$ GeV		$\langle\nu\rangle = 10.24$ GeV			
$\langle \frac{d\sigma^{\gamma^* p \to \pi^0 p'}}{d\lvert t\rvert d\phi} \rangle$	0.54	1.39	1.52	0.57	0.67	1.79	1.38	0.70
stat. error	0.10	0.16	0.16	0.09	0.10	0.16	0.16	0.20
syst. error ↑	0.13	0.17	0.19	0.14	0.17	0.22	0.17	0.16
syst. error ↓	0.10	0.14	0.15	0.12	0.15	0.17	0.14	0.14
	1^{st} ν domain		$6.4 < \nu < 8.5$ GeV		$\langle\nu\rangle = 7.35$ GeV			
$\langle \frac{d\sigma^{\gamma^* p \to \pi^0 p'}}{d\lvert t\rvert d\phi} \rangle$	3.84	7.57	9.39	3.98	4.16	9.55	9.40	2.73
stat. error	0.99	1.22	1.14	0.68	0.91	1.18	1.79	0.64
	2^{nd} ν domain		$8.5 < \nu < 13.9$ GeV		$\langle\nu\rangle = 10.32$ GeV			
$\langle \frac{d\sigma^{\gamma^* p \to \pi^0 p'}}{d\lvert t\rvert d\phi} \rangle$	1.76	3.93	3.76	1.49	1.82	3.97	3.12	1.88
stat. error	0.49	0.62	0.60	0.39	0.37	0.51	0.51	0.62
	3^{rd} ν domain		$13.9 < \nu < 40$ GeV		$\langle\nu\rangle = 21.08$ GeV			
$\langle \frac{d\sigma^{\gamma^* p \to \pi^0 p'}}{d\lvert t\rvert d\phi} \rangle$	0.11	0.42	0.53	0.16	0.23	0.73	0.41	0.23
stat. error	0.05	0.12	0.15	0.06	0.08	0.14	0.11	0.13

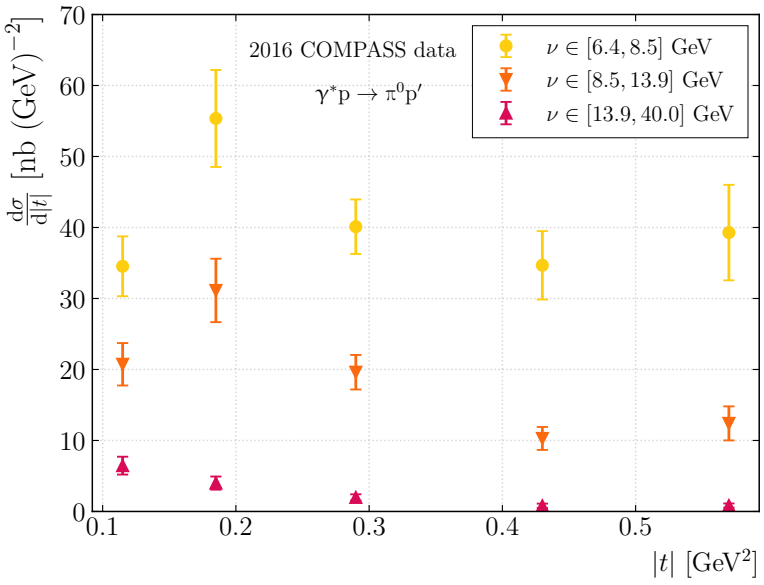

Fig. 5.8: The evolution of the differential exclusive π^0 cross section in three bins of ν as a function of $|t|$. Only the statistical errors are shown.

Tab. 5.11: Determination of the structure functions in 3 ν bins (units $\frac{\text{nb}}{(\text{GeV}/c)^2}$).

	$p_0 = \langle \frac{d\sigma_T}{dt} + \epsilon \frac{d\sigma_L}{dt} \rangle$	$p_1 = \langle \frac{d\sigma_{TT}}{dt} \rangle$	$p_2 = \langle \frac{d\sigma_{LT}}{dt} \rangle$	χ^2_{red}
Complete ν domain	$6.4 < \nu < 40$ GeV	$\langle \nu \rangle = 10.16$ GeV		
value	6.63	−4.61	0.15	1.0
stat. error	0.31	0.48	0.19	
syst. error ↑	0.91	0.35	0.14	
syst. error ↓	0.74	0.32	0.14	
1^{st} ν domain	$6.4 < \nu < 8.5$ GeV	$\langle \nu \rangle = 7.35$ GeV		
value ± stat. err.	39.10 ± 2.33	-26.40 ± 3.67	1.93 ± 1.30	0.4
2^{nd} ν domain	$8.5 < \nu < 13.9$ GeV	$\langle \nu \rangle = 10.32$ GeV		
value ± stat. err.	16.89 ± 1.13	-9.96 ± 1.79	-0.04 ± 0.77	0.4
3^{rd} ν domain	$13.9 < \nu < 40$ GeV	$\langle \nu \rangle = 21.08$ GeV		
value ± stat. err.	2.06 ± 0.23	-1.74 ± 0.36	0.14 ± 0.12	0.9

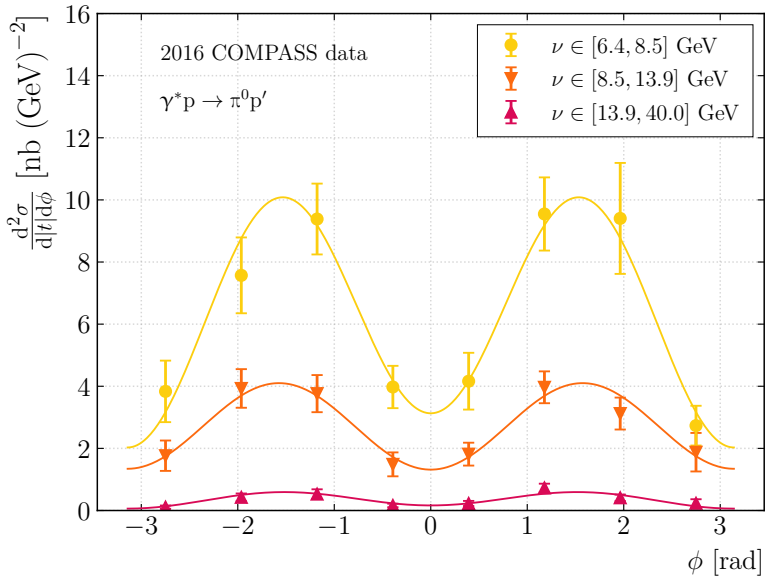

Fig. 5.9: The evolution of the differential exclusive π^0 cross section in three bins of ν as a function of ϕ. Only the statistical errors are shown.

Tab. 5.12: Differential cross section as a function of $|t|$ in 4 Q^2 bins (units $\frac{\text{nb}}{(\text{GeV}/c)^2}$).

$\|t\|$ bin	$[0.08, 0.15]$	$[0.15, 0.22]$	$[0.22, 0.36]$	$[0.36, 0.5]$	$[0.5, 0.64]$	$[0.08, 0.64]$
	1^{st} Q^2 bin	$1. < Q^2 < 1.5$ GeV^2		$\langle Q^2 \rangle = 1.22$ GeV^2		
$\langle \frac{d\sigma^{\gamma^* p \to \pi^0 p'}}{d\|t\|} \rangle$	33.00	29.17	13.40	6.29	4.87	13.91
stat. error	4.36	3.51	1.68	1.04	0.92	0.89
	2^{nd} Q^2 bin	$1.5 < Q^2 < 2.1$ GeV^2		$\langle Q^2 \rangle = 1.77$ GeV^2		
$\langle \frac{d\sigma^{\gamma^* p \to \pi^0 p'}}{d\|t\|} \rangle$	29.14	20.89	11.35	6.55	3.78	11.67
stat. error	3.98	2.76	1.36	1.17	0.97	0.79
	3^{rd} Q^2 bin	$2.1 < Q^2 < 3.2$ GeV^2		$\langle Q^2 \rangle = 2.58$ GeV^2		
$\langle \frac{d\sigma^{\gamma^* p \to \pi^0 p'}}{d\|t\|} \rangle$	12.53	16.22	10.09	5.59	6.74	9.20
stat. error	2.21	2.41	1.30	1.05	1.25	0.66
	4^{th} Q^2 bin	$3.2 < Q^2 < 8.0$ GeV^2		$\langle Q^2 \rangle = 4.33$ GeV^2		
$\langle \frac{d\sigma^{\gamma^* p \to \pi^0 p'}}{d\|t\|} \rangle$	5.48	6.84	4.98	3.42	4.02	4.65
stat. error	1.29	1.31	0.70	0.58	0.64	0.36

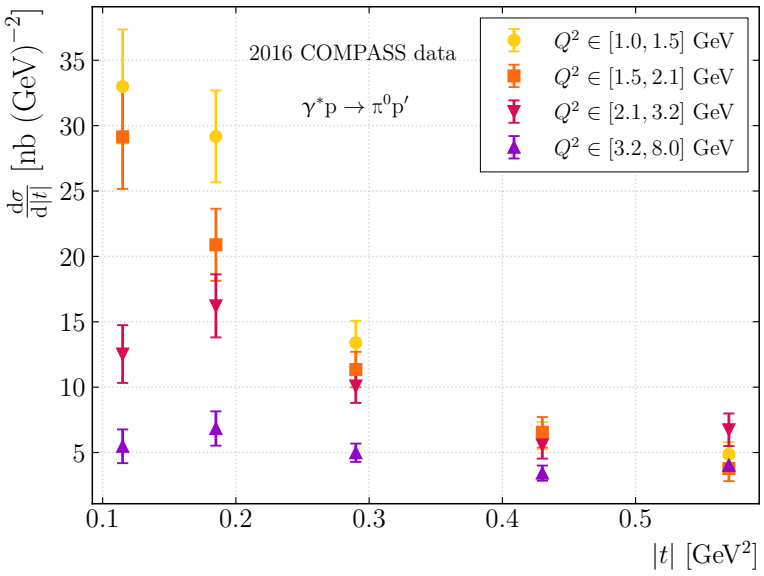

Fig. 5.10: The evolution of the differential exclusive π^0 cross section in three bins of Q^2 as a function of $|t|$. Only the statistical errors are shown.

Tab. 5.13: Differential cross section as a function of ϕ in 4 Q^2 bins (units $\frac{\text{nb}}{(\text{GeV}/c)^2}$).

ϕ bin	$[-\pi, -\frac{3\pi}{4}]$	$[-\frac{3\pi}{4}, -\frac{\pi}{2}]$	$[-\frac{\pi}{2}, -\frac{\pi}{4}]$	$[-\frac{\pi}{4}, 0]$	$[0, \frac{\pi}{4}]$	$[\frac{\pi}{4}, \frac{\pi}{2}]$	$[\frac{\pi}{2}, \frac{3\pi}{4}]$	$[\frac{3\pi}{4}, \pi]$
	1^{st} Q^2 domain		$1 < Q^2 < 1.5$ GeV^2		$\langle Q^2 \rangle = 1.22$ GeV^2			
$\langle \frac{d\sigma^{\gamma^* p \to \pi^0 p'}}{d\lvert t\rvert d\phi} \rangle$	1.61	2.53	2.99	1.22	1.12	4.30	3.00	0.96
stat. error	0.35	0.36	0.43	0.29	0.26	0.64	0.45	0.27
	2^{nd} Q^2 domain		$1.5 < Q^2 < 2.1$ GeV^2		$\langle Q^2 \rangle = 1.77$ GeV^2			
$\langle \frac{d\sigma^{\gamma^* p \to \pi^0 p'}}{d\lvert t\rvert d\phi} \rangle$	1.16	2.68	2.78	0.79	0.91	3.23	2.70	0.63
stat. error	0.31	0.43	0.36	0.23	0.23	0.51	0.44	0.21
	3^{rd} Q^2 domain		$2.1 < Q^2 < 3.2$ GeV^2		$\langle Q^2 \rangle = 2.58$ GeV^2			
$\langle \frac{d\sigma^{\gamma^* p \to \pi^0 p'}}{d\lvert t\rvert d\phi} \rangle$	0.75	1.78	1.56	1.02	0.87	2.61	2.29	0.84
stat. error	0.23	0.31	0.26	0.27	0.24	0.40	0.38	0.25
	4^{th} Q^2 domain		$3.2 < Q^2 < 8.0$ GeV^2		$\langle Q^2 \rangle = 4.33$ GeV^2			
$\langle \frac{d\sigma^{\gamma^* p \to \pi^0 p'}}{d\lvert t\rvert d\phi} \rangle$	0.35	1.00	1.21	0.38	0.53	1.20	0.82	0.43
stat. error	0.13	0.19	0.21	0.10	0.12	0.19	0.17	0.16

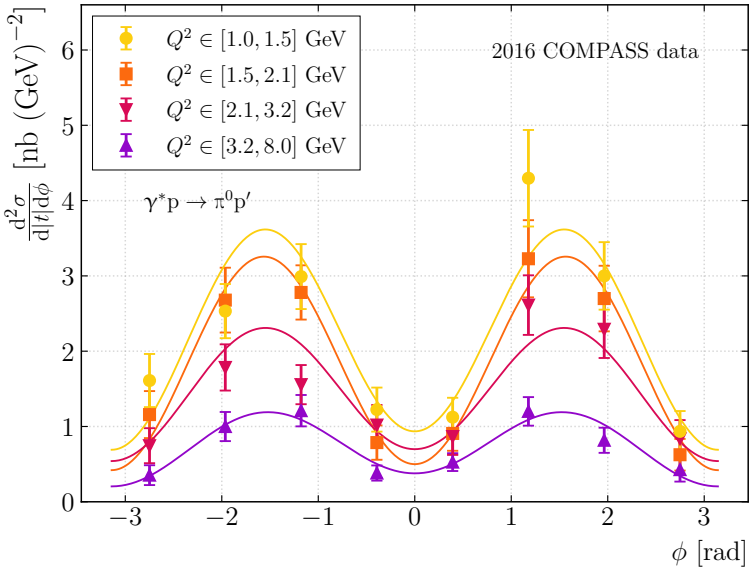

Fig. 5.11: The evolution of the differential exclusive π^0 cross section in three bins of Q^2 as a function of ϕ. Only the statistical errors are shown.

Tab. 5.14: The results of the fit of the structure functions in 4 Q^2 bins (units $\frac{\text{nb}}{(\text{GeV}/c)^2}$).

	$p_0 = \langle \frac{d\sigma_T}{dt} + \epsilon \frac{d\sigma_L}{dt} \rangle$	$p_1 = \langle \frac{d\sigma_{TT}}{dt} \rangle$	$p_2 = \langle \frac{d\sigma_{LT}}{dt} \rangle$	χ^2_{red}
1^{st} Q^2 domain	$1.0 < Q^2 < 1.5$ GeV^2		$\langle Q^2 \rangle = 1.22$ GeV^2	
value	13.04	−8.96	0.16	1.6
stat. error	0.83	1.31	0.49	
2^{nd} Q^2 domain	$1.5 < Q^2 < 2.1$ GeV^2		$\langle Q^2 \rangle = 1.77$ GeV^2	
value	11.40	−9.87	0.14	0.6
stat. error	0.77	1.21	0.41	
3^{rd} Q^2 domain	$2.1 < Q^2 < 3.2$ GeV^2		$\langle Q^2 \rangle = 2.58$ GeV^2	
value	8.74	−5.25	0.19	1.3
stat. error	0.64	1.00	0.41	
4^{th} Q^2 domain	$3.2 < Q^2 < 8.0$ GeV^2		$\langle Q^2 \rangle = 4.33$ GeV^2	
value	4.53	−3.12	0.19	0.7
stat. error	0.36	0.56	0.21	

5.8 Systematic uncertainty estimation

In this section, different sources of systematic errors are investigated. The effect of each systematic test is evaluated by comparing modified cross section yields with respect to the default values. The impact of each variation of yields is studied for the individual cross section bin in $|t|$ or ϕ and amplitudes of the azimuthal modulations of the cross section $\frac{\mathrm{d}\sigma_\mathrm{T}}{\mathrm{d}t} + \epsilon\frac{\mathrm{d}\sigma_\mathrm{L}}{\mathrm{d}t}$, $\frac{\mathrm{d}\sigma_\mathrm{TT}}{\mathrm{d}t}$ and $\frac{\mathrm{d}\sigma_\mathrm{LT}}{\mathrm{d}t}$. This Section summarises the process of estimation of systematic uncertainties for the larger kinematic domain.

5.8.1 Variation of the χ^2_red of the Kinematic Fit

The choice of the upper limit on the reduced kinematic fit χ^2 was justified by the steep decrease of the distribution of the χ^2_red in HEPGEN++ describing the signal events, where at the $\chi^2_\mathrm{red} = 7$ the HEPGEN++ vanishes towards zero ⟦↩4.2.⟧. However, as the cut for the efficiency of the kinematic fit impacts most of the inclusive background (around ²⁄₃), it is crucial to test whether choosing this particular offset can introduce any systematic effect in the final selected sample.

A test was performed varying the cut value in the following range: $\chi^2_\mathrm{red} = 7 \pm 3$ in steps of 1. The sensitivity of the cross section yields in bins of $|t|$ and ϕ and the fitting parameters of the ϕ modulation corresponding to the structure functions introduced in the first section were verified. The fitting parameters are:

$$p_0 = \left\langle \frac{\mathrm{d}\sigma_T}{\mathrm{d}t} + \epsilon\frac{\mathrm{d}\sigma_L}{\mathrm{d}t} \right\rangle, \qquad p_1 = \left\langle \frac{\mathrm{d}\sigma_{TT}}{\mathrm{d}t} \right\rangle, \qquad p_2 = \left\langle \frac{\mathrm{d}\sigma_{LT}}{\mathrm{d}t} \right\rangle.$$

The yield of background is extracted from the MC fitting procedure ⟦↩4.4.3.⟧ for each cut value separately.

The Figs. 5.12, 5.14, 5.15 and 5.13 show the effect on averaged cross section in bins. The Tabs. 5.15, and 5.16, and 5.17 summarise the extremities of the effect for each cross section bin. The results for individual points of the cross section proved to be influenced by statistical fluctuations. To suppress their influence, that also introduces differences between cross sections obtained with different cut values, the relative systematic uncertainty from the test has been averaged over bins containing similar statistics.

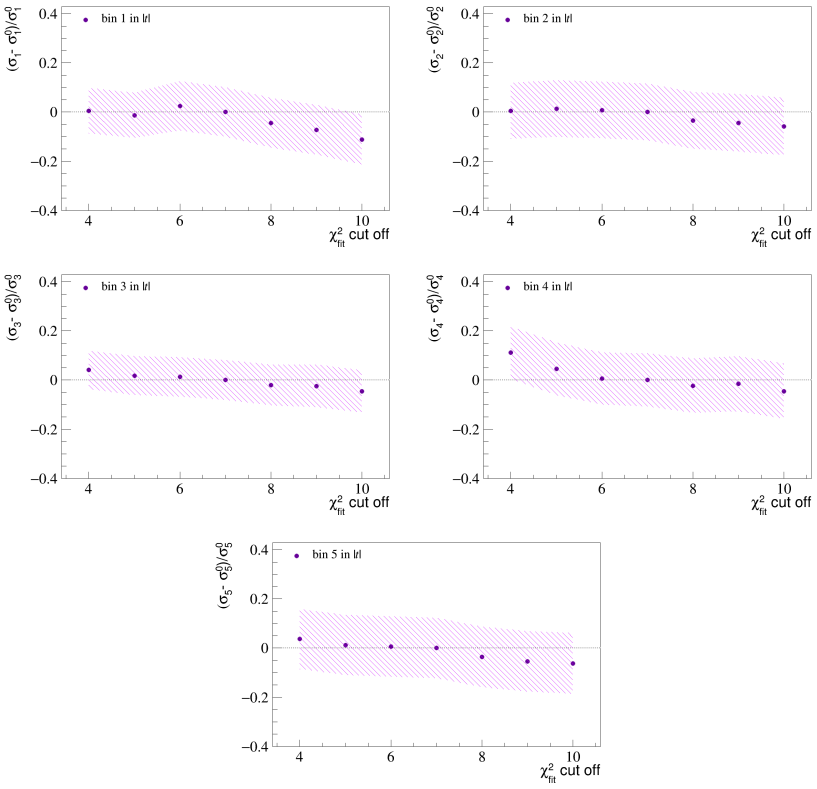

Fig. 5.12: The evolution of the cross section point σ_i, $i \in [1, 2, 3, 4, 5]$ in $|t|$ bins, when the upper limit on χ^2_{red} varies from 4 to 10. The quantity σ_i^4 (in the middle of X-axis) denotes the value of the cross section for $\chi^2_{\text{red}} = 7$. The band corresponds to the relative statistical uncertainty.

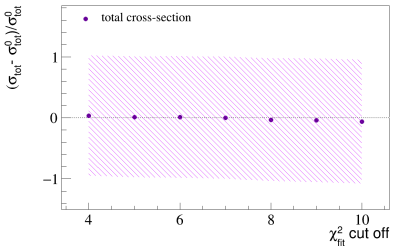

Fig. 5.13: The evolution of the total cross section in case the upper limit on χ^2_{red} varies from 4 to 10. The quantity σ_i^4 denotes the default value for $\chi^2_{\text{red}} = 7$.

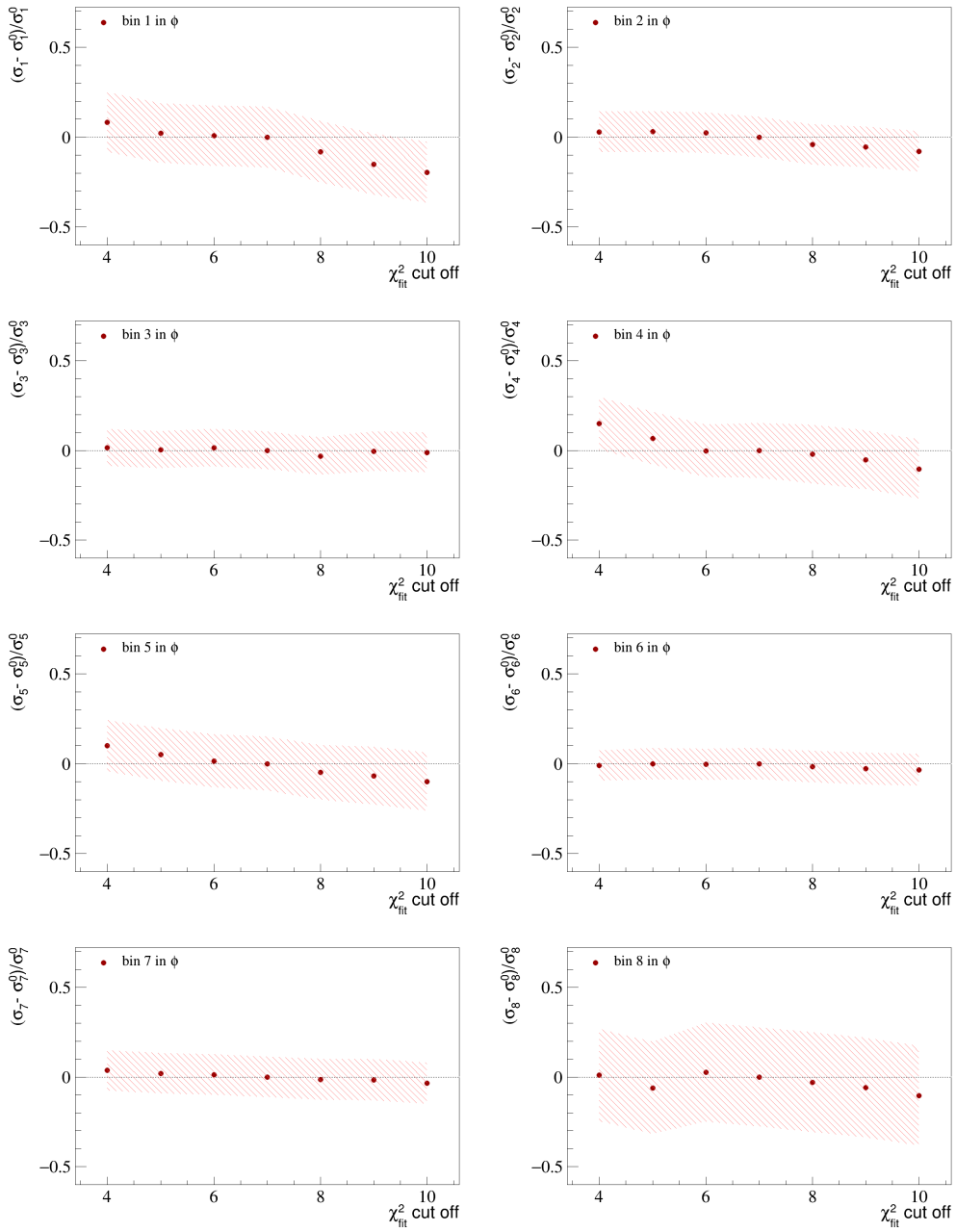

Fig. 5.14: The evolution of the the cross section point σ_i, $i \in [1, 2, 3, 4, 5, 6, 7, 8]$ in ϕ bins, when the upper limit on χ^2_{red} varies from 4 to 10. The quantity σ_i^4 (in the middle of X-axis) denotes the value of the cross section for $\chi^2_{\text{red}} = 7$. The band corresponds to the relative statistical uncertainty.

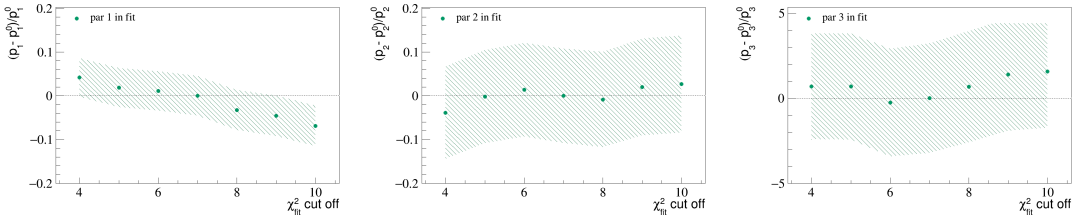

Fig. 5.15: The evolution of the fitted parameters p_i with $i \in [1,2,3]$, in case the upper limit on χ^2_{red} varies from 4 to 10. The quantity p_i^4 denotes the value of the cross section for $\chi^2_{\text{red}} = 7$. The band corresponds to the relative statistical uncertainty.

Tab. 5.15: Relative systematic errors from the variation of the χ^2_{red} cut of the cross section in 5 $|t|$-bins.

$\lvert t\rvert$ bin	$[0.08, 0.15]$	$[0.15, 0.22]$	$[0.22, 0.36]$	$[0.36, 0.5]$	$[0.5, 0.64]$
sys. error $\uparrow$ [%]	1.9	1.9	6.3	6.3	6.3
sys. error $\downarrow$ [%]	8.5	8.5	5.2	5.2	5.2

Tab. 5.16: Relative systematic errors from the variation of the χ^2_{red} cut of the cross section in 8 ϕ-bins.

ϕ bin	$[-\pi, -\frac{3\pi}{4}]$	$[-\frac{3\pi}{4}, -\frac{\pi}{2}]$	$[-\frac{\pi}{2}, -\frac{\pi}{4}]$	$[-\frac{\pi}{4}, 0]$	$[0, \frac{\pi}{4}]$	$[\frac{\pi}{4}, \frac{\pi}{2}]$	$[\frac{\pi}{2}, \frac{3\pi}{4}]$	$[\frac{3\pi}{4}, \pi]$
sys. error $\uparrow$ [%]	9.0	2.1	2.1	9.0	9.0	2.1	2.1	9.0
sys. error $\downarrow$ [%]	12.6	4.5	4.5	12.6	12.6	4.5	4.5	12.6

Tab. 5.17: Relative systematic errors from the variation of the χ^2_{red} cut of the total exclusive π^0 cross section, and 3 fitted parameters of its ϕ modulation.

parameters	σ_{tot}	p_0	p_1	p_2
sys. error $\uparrow$ [%]	3.6	3.0	3.0	25.0
sys. error $\downarrow$ [%]	6.5	5.0	4.0	25.0

5.8.2 Variation of the Energy Thresholds of ECALs

The threshold for the neutral cluster energy deposited in ECALs has a high impact on the extraction of the cross section, as a mismatch of the data and simulations can affect the results. To study the effect of the threshold variation on the results, the energy of lower energetic cluster was stepped from the default value (0.5 GeV for ECAL0, and 0.63 GeV for ECAL1 ⟦↩4.3.2.⟧, up to 1.6 GeV for ECAL0, and 2.2 GeV for ECAL1, in steps of 0.2 GeV. The lowest limit was set on the default values, because they were set as low as possible, just above the region dominated by detector noise, as can be seen in Fig. 3.4 for illustration of the regions of low cluster energy with high occupancy, where the signal is buried in noise and thus not suitable for this systematic study.

Variation of Energy Threshold for ECAL0

The variation of the lower energetic cluster threshold is performed in values: $E_{\mathrm{cl}_\gamma} \in [0.5, 0.6, 0.8, 1.0, 1.2, 1.4, 1.6]$ GeV, for the averaged cross section yields in bins of ϕ and $|t|$ and spin-dependent cross section yields. The Figs. 5.16, 5.17, 5.18, and 5.19 show the effect on cross section yields in bins averaged over beam polarities. The Tabs. 5.18, and 5.19, and 5.20 summarise the estimated uncertainties for each cross section bin. Also it this test the results of the systematic study proved to be influenced by statistical fluctuations, hence the values in ϕ and $|t|$ have been averaged over the high-statistics bins and low statistics bins.

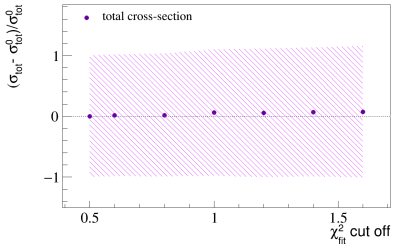

Fig. 5.19: The evolution of the total cross section varying E_{cl_γ} threshold in ECAL0 in values: $E_{\mathrm{cl}_\gamma} \in [0.5, 0.6, 0.8, 1.0, 1.2, 1.4, 1.6]$. The quantity σ^0_i denotes the value of the cross section for $E_{\mathrm{cl}_\gamma} = 0.5$ GeV.

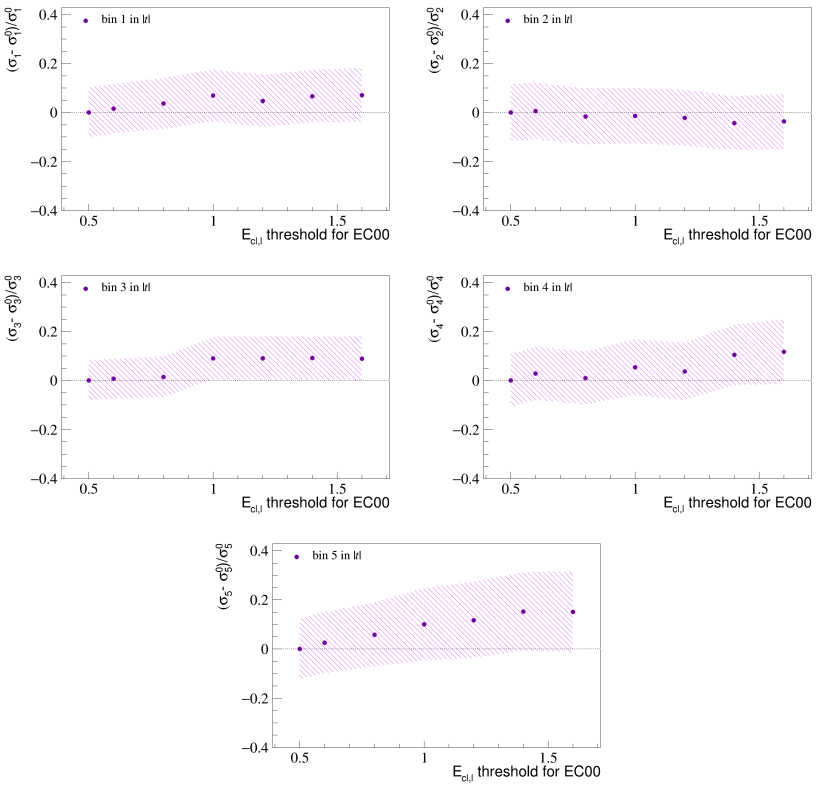

Fig. 5.16: The evolution of the cross section point σ_i, $i \in [1, 2, 3, 4, 5]$ in $|t|$ bins, varying E_{cl_γ} threshold in ECAL0 in values: $E_{\mathrm{cl}_\gamma} \in [0.5, 0.6, 0.8,\ 1.0, 1.2, 1.4, 1.6]$. The quantity σ_i^0 denotes the value of the cross section for $E_{\mathrm{cl}_\gamma} = 0.5$ GeV.

Tab. 5.18: Relative systematic errors from the variation of the energy threshold in ECAL0 of the cross section in 5 $|t|$-bins.

$\lvert t\rvert$ bin	$[0.08, 0.15]$	$[0.15, 0.22]$	$[0.22, 0.36]$	$[0.36, 0.5]$	$[0.5, 0.64]$
sys. error $\uparrow$ [%]	3.9	3.9	12.1	12.1	12.1
sys. error $\downarrow$ [%]	2.2	2.2	0.0	0.0	0.0

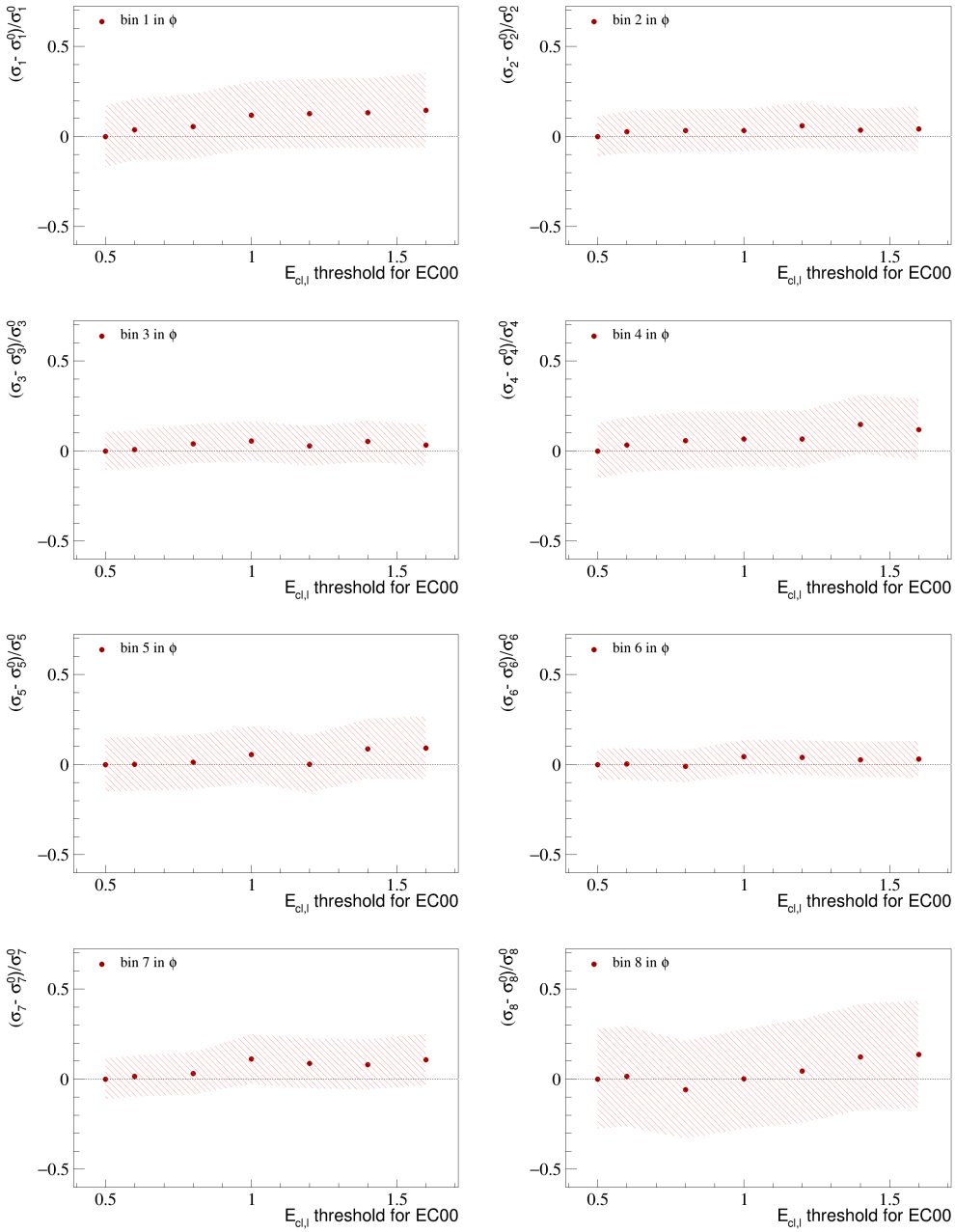

Fig. 5.17: The evolution of the cross section point σ_i, $i \in [1, 2, 3, 4, 5, 6, 7, 8]$ in ϕ bins, varying E_{cl_γ} threshold in ECAL0 in steps: $E_{\mathrm{cl}_\gamma} \in [0.5, 0.6, 0.8, 1.0, 1.2, 1.4, 1.6]$. The quantity σ_i^0 denotes the value of the cross section for $E_{\mathrm{cl}_\gamma} = 0.5$ GeV.

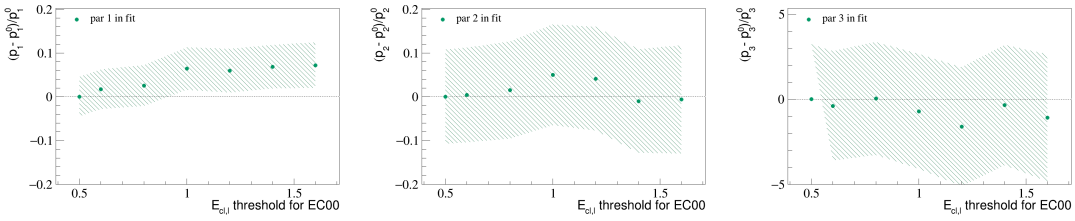

Fig. 5.18: The evolution of the fitted parameters p_i with $i \in [1, 2, 3]$, varying E_{cl_γ} threshold in ECAL0 in values: $E_{\mathrm{cl}_\gamma} \in [0.5, 0.6, 0.8, 1.0, 1.2, 1.4, 1.6]$. The quantity σ_i^0 denotes the value of the cross section for $E_{\mathrm{cl}_\gamma} = 0.5$ GeV.

Tab. 5.19: Relative systematic errors from the variation of the energy threshold in ECAL0 of the cross section in 8 ϕ-bins.

ϕ bin	$[-\pi, -\frac{3\pi}{4}]$	$[-\frac{3\pi}{4}, -\frac{\pi}{2}]$	$[-\frac{\pi}{2}, -\frac{\pi}{4}]$	$[-\frac{\pi}{4}, 0]$	$[0, \frac{\pi}{4}]$	$[\frac{\pi}{4}, \frac{\pi}{2}]$	$[\frac{\pi}{2}, \frac{3\pi}{4}]$	$[\frac{3\pi}{4}, \pi]$
sys. error $\uparrow$ [%]	13.0	6.7	6.7	13.0	13.0	6.7	6.7	13.0
sys. error $\downarrow$ [%]	1.5	0.3	0.3	1.5	1.5	0.3	0.3	1.5

Tab. 5.20: Relative systematic errors from the variation of the energy threshold in ECAL0 of the total cross section and 3 fitted parameters of its ϕ modulation.

parameters	σ_{tot}	p_0	p_1	p_2
sys. error $\uparrow$ [%]	7.3	7.0	5.0	4.0
sys. error $\downarrow$ [%]	0.0	0.0	1.0	4.0

Variation of Energy Threshold for ECAL1

The variation of the lower energetic cluster threshold was performed in values: $E_{\mathrm{cl}_\gamma} \in [0.63, 0.8, 1.0, 1.2, 1.4, 1.6, 1.8, 2.0, 2.2]$ GeV for the averaged cross section yields in bins of ϕ and $|t|$ and spin-dependent cross section yields. The Figs. 5.20, 5.22, 5.23, and 5.21 show the effect on cross section yields in bins averaged over beam polarities The Tabs. 5.21, 5.22, and 5.23 summarise the estimated uncertainties. Also it this test the results of the systematic study proved to be influenced by statistical fluctuations, hence the values in ϕ and $|t|$ have been averaged over the high-statistics bins and low statistics bins.

Tab. 5.21: Relative systematic errors from the variation of the energy threshold in ECAL1 of the cross section in 5 $|t|$-bins.

$\lvert t\rvert$ bin	$[0.08, 0.15]$	$[0.15, 0.22]$	$[0.22, 0.36]$	$[0.36, 0.5]$	$[0.5, 0.64]$
sys. error $\uparrow$ [%]	2.0	2.0	6.0	6.0	6.0
sys. error $\downarrow$ [%]	4.0	4.0	1.7	1.7	1.7

Tab. 5.22: Relative systematic errors from the variation of the energy threshold in ECAL1 of the cross section in 8 ϕ-bins.

ϕ bin	$[-\pi, -\frac{3\pi}{4}]$	$[-\frac{3\pi}{4}, -\frac{\pi}{2}]$	$[-\frac{\pi}{2}, -\frac{\pi}{4}]$	$[-\frac{\pi}{4}, 0]$	$[0, \frac{\pi}{4}]$	$[\frac{\pi}{4}, \frac{\pi}{2}]$	$[\frac{\pi}{2}, \frac{3\pi}{4}]$	$[\frac{3\pi}{4}, \pi]$
sys. error $\uparrow$ [%]	7.7	2.4	2.4	7.7	7.7	2.4	2.4	7.7
sys. error $\downarrow$ [%]	2.9	1.9	1.9	2.9	2.9	1.9	1.9	2.9

Tab. 5.23: Relative systematic errors from the variation of the energy threshold in ECAL1 of the total cross section and 3 fitted parameters of its ϕ modulation.

parameters	σ_{tot}	p_0	p_1	p_2
sys. error $\uparrow$ [%]	3.7	3.0	1.0	30.0
sys. error $\downarrow$ [%]	1.5	2.0	2.0	30.0

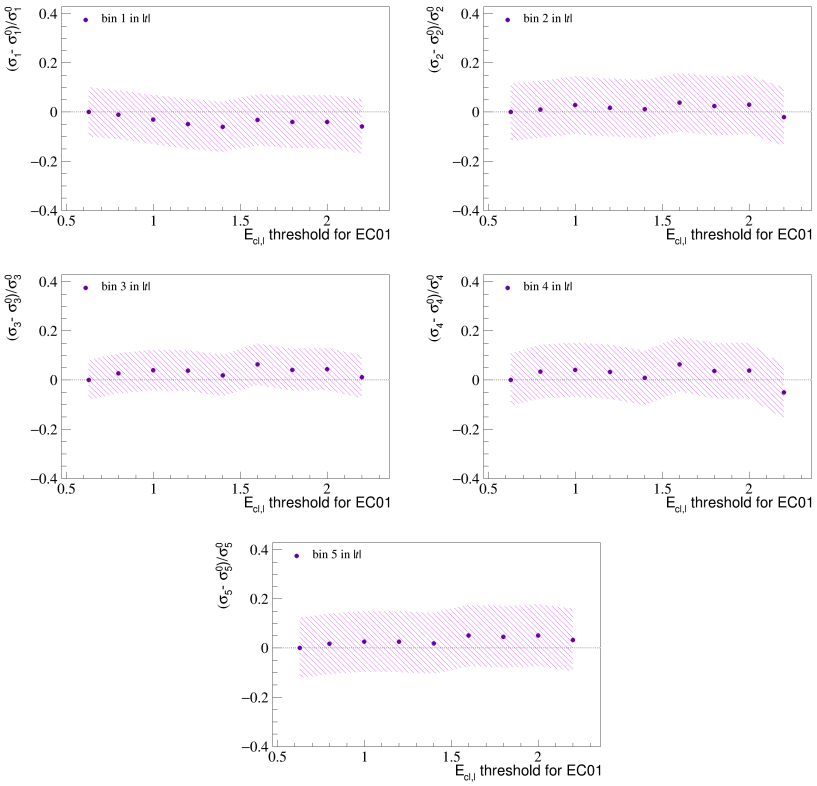

Fig. 5.20: The evolution of the cross section point σ_i, $i \in [1, 2, 3, 4, 5]$ in $|t|$ bins, varying E_{cl_γ} threshold in ECAL1 in values: $E_{\mathrm{cl}_\gamma} \in [0.63, 0.8, 1.0, 1.2, 1.4, 1.6, 1.8, 2.0, 2.2]$. The quantity σ_i^0 denotes the default value.

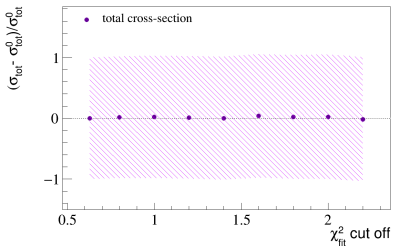

Fig. 5.21: The evolution of the total cross section varying E_{cl_γ} threshold in ECAL1 in values: $E_{\mathrm{cl}_\gamma} \in [0.63, 0.8, 1.0, 1.2, 1.4, 1.6, 1.8, 2.0, 2.2]$. The quantity σ_i^0 denotes the default value.

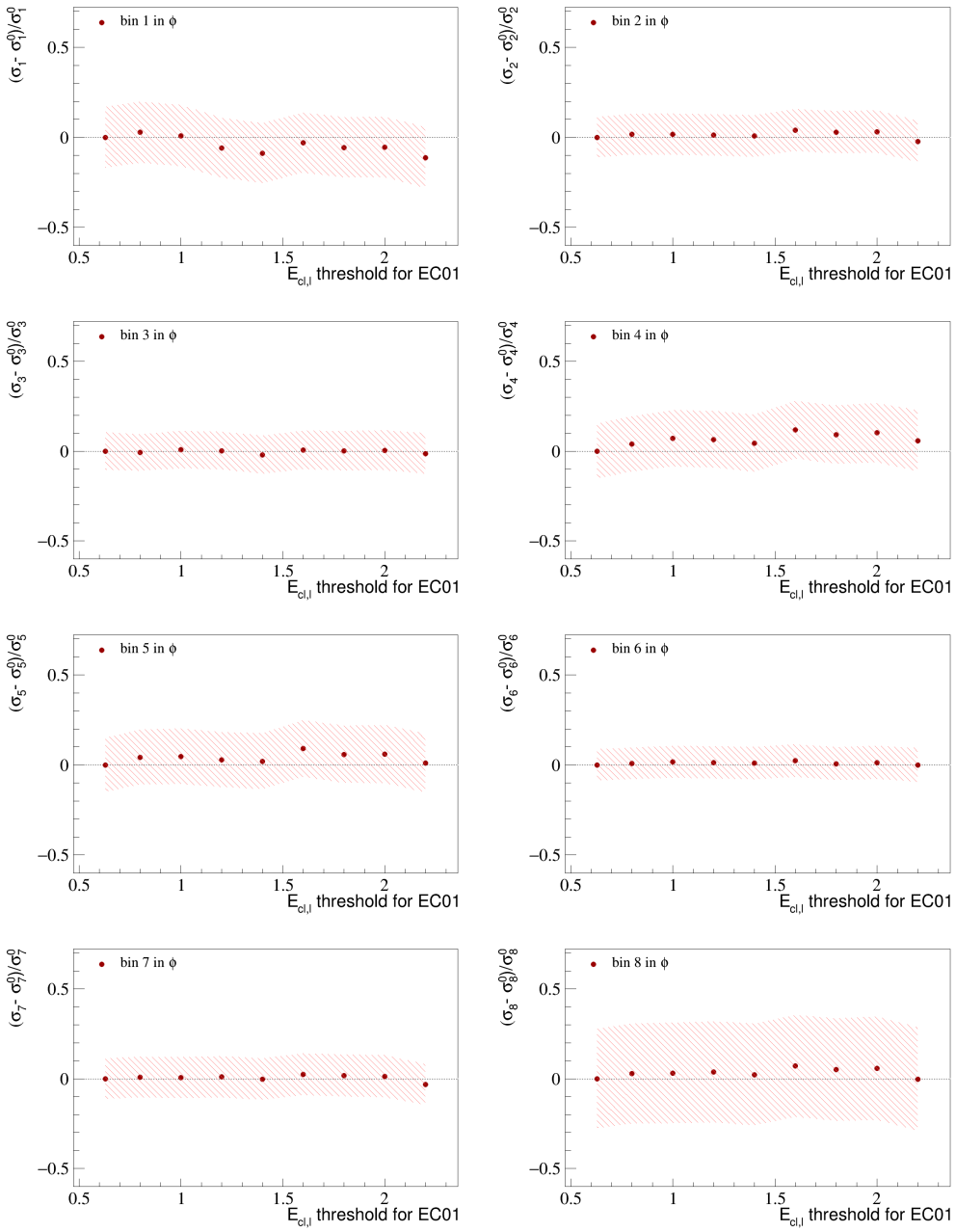

Fig. 5.22: The evolution of the cross section point σ_i, $i \in [1, 2, 3, 4, 5, 6, 7, 8]$ in ϕ bins, varying E_{cl_γ} threshold in ECAL1 in values: $E_{\mathrm{cl}_\gamma} \in [0.63, 0.8, 1.0, 1.2, 1.4, 1.6, 1.8, 2.0, 2.2]$. The quantity σ_i^0 denotes the value of the cross section for $E_{\mathrm{cl}_\gamma} = 0.63$ GeV.

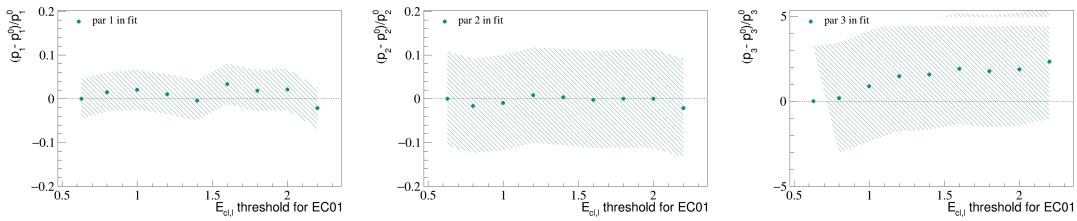

Fig. 5.23: The evolution of the fitted parameters p_i, varying E_{cl_γ} threshold in ECAL1 in values: $E_{\mathrm{cl}_\gamma} \in [0.63, 0.8, 1.0, 1.2, 1.4, 1.6, 1.8, 2.0, 2.2]$. The quantity σ_i^0 denotes the cross section for $E_{\mathrm{cl}_\gamma} = 0.63$ GeV.

5.8.3 Variation of the r_{LEPTO} Normalisation

The determination of the background level has been obtained by two different methods ⟦↤4.4.3.⟧, which may introduce an uncertainty in the background level. The deviation of the two methods, combined with the different results from both beam polarities, is on average 5–10%. This implies a systematic effect on the r_{LEPTO} determination.

The systematic effect on the background level is the variation of the r_{LEPTO} was studied by varying the default value within the range of statistical uncertainties. The impact on the cross section points is shown in Figs. 5.24, 5.25, 5.26, and 5.27 footnoteThe systematic studies were performed as a team effort. Half of the tests were done by the author, the results of tests in Section ⟦↤5.8.3.⟧, ⟦↪5.8.5.⟧, ⟦↪5.8.4.⟧, ⟦↪5.8.7.⟧ come from the collaboration [104]. averaged over both polarities.

Tab. 5.24: Relative systematic errors from the variation of the the LEPTO normalisation of the cross section in 5 $|t|$-bins.

$\lvert t\rvert$ bin	$[0.08, 0.15]$	$[0.15, 0.22]$	$[0.22, 0.36]$	$[0.36, 0.5]$	$[0.5, 0.64]$
sys. error [%]	6.0	6.0	10.0	10.0	10.0

Tab. 5.25: Relative systematic errors from the variation of the the LEPTO normalisation of the cross section in 8 ϕ-bins.

ϕ bin	$[-\pi, -\frac{3\pi}{4}]$	$[-\frac{3\pi}{4}, -\frac{\pi}{2}]$	$[-\frac{\pi}{2}, -\frac{\pi}{4}]$	$[-\frac{\pi}{4}, 0]$	$[0, \frac{\pi}{4}]$	$[\frac{\pi}{4}, \frac{\pi}{2}]$	$[\frac{\pi}{2}, \frac{3\pi}{4}]$	$[\frac{3\pi}{4}, \pi]$
sys. error [%]	12.0	6.0	6.0	16.0	16.0	6.0	6.0	12.0

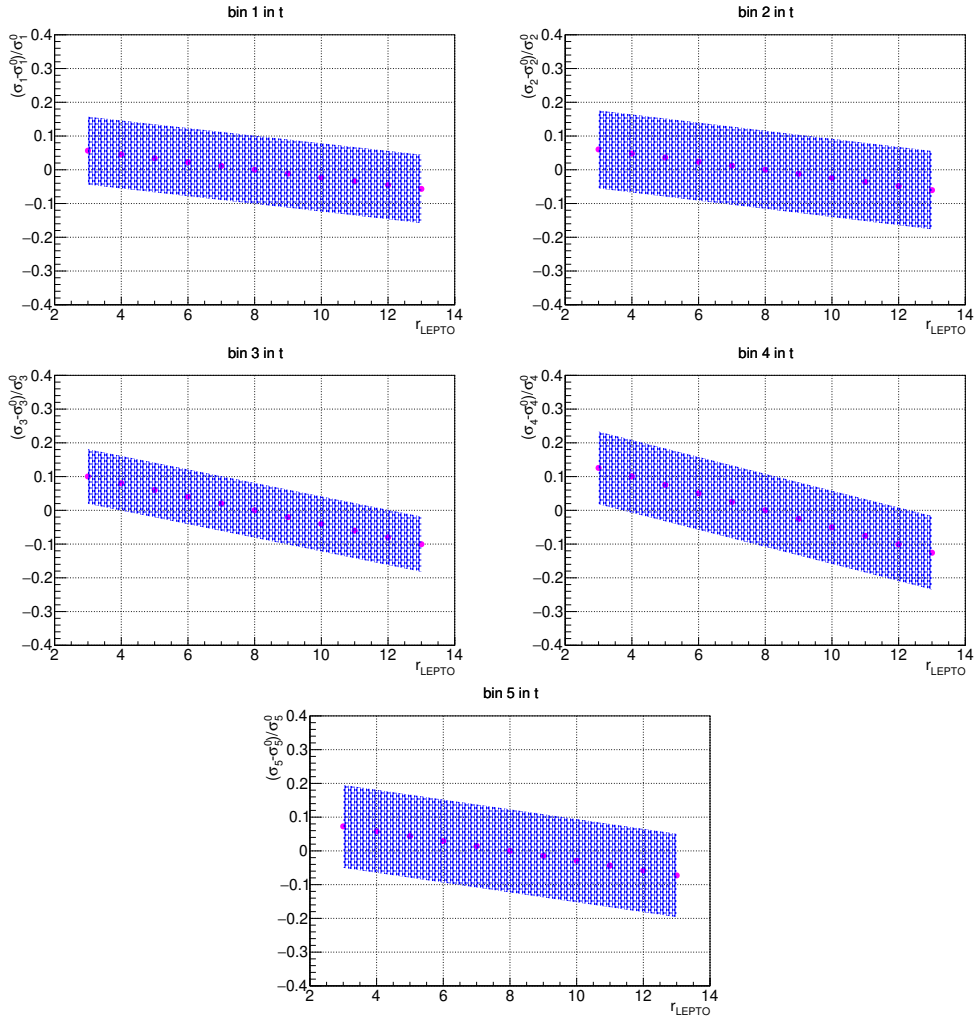

Fig. 5.24: The evolution of the cross-section point $\sigma_{i=1,2,3,4,5}$ in the 5 t bins, when r_{LEPTO} (the SIDIS background) varies from 3% to 13%. The quantity σ_i^0 denotes the value of the cross section for $r_{\mathrm{LEPTO}} = 8\%$. The band corresponds to the relative statistical uncertainty [104].

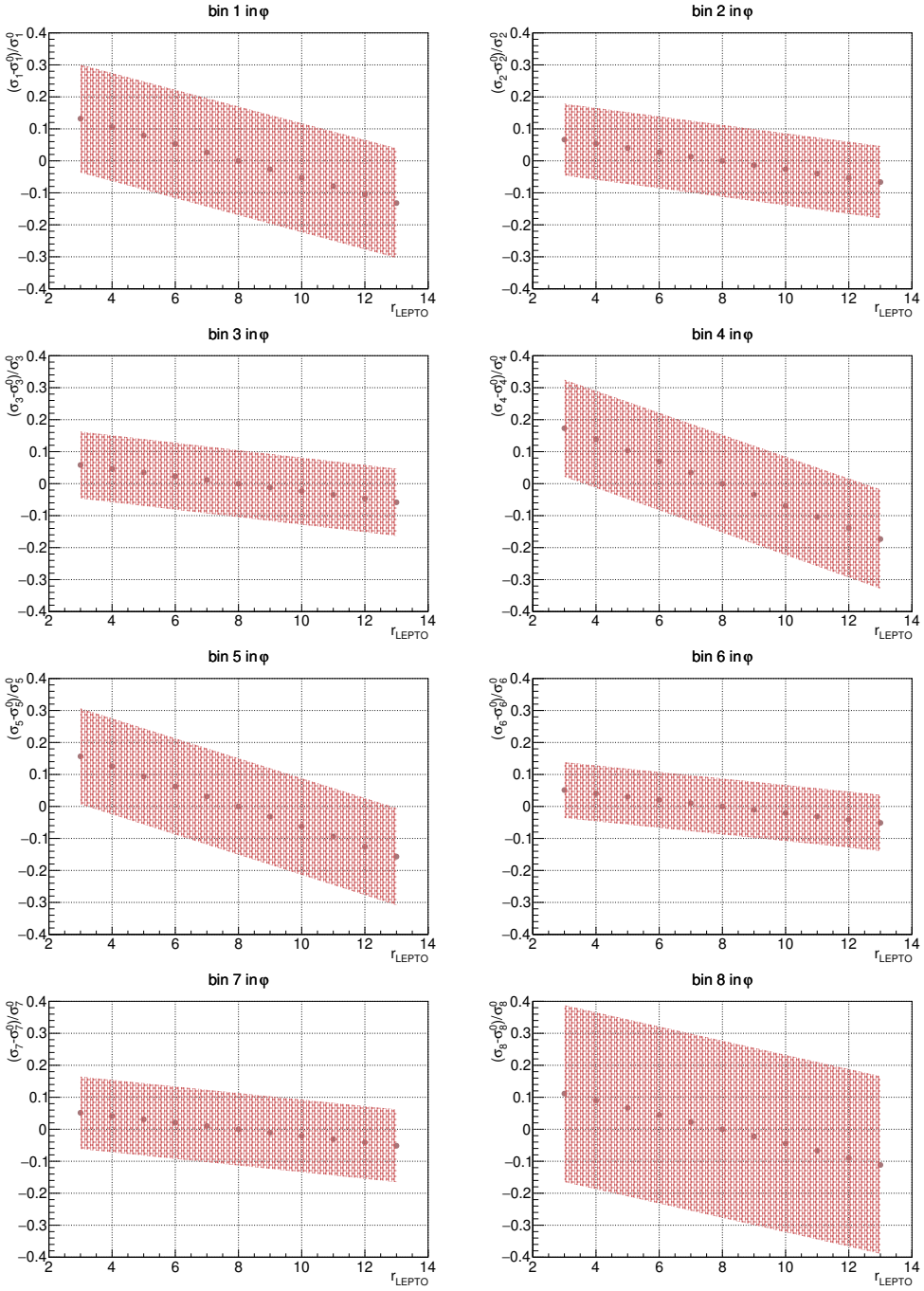

Fig. 5.25: The evolution of the cross-section point $\sigma_{i=1,2,3,4,5,6,7,8}$ in the 8 ϕ bins, when r_{LEPTO} (the SIDIS background) varies from 3% to 13%. The quantity σ_i^0 denotes the value of the cross section for $r_{\mathrm{LEPTO}} = 8\%$ [104].

Tab. 5.26: Relative systematic errors from the variation of the LEPTO normalisation of the total cross section and 3 fitted parameters of its ϕ modulation.

parameters	σ_{tot}	p_0	p_1	p_2
sys. error [%]	8.2	8.3	0.7	62.0

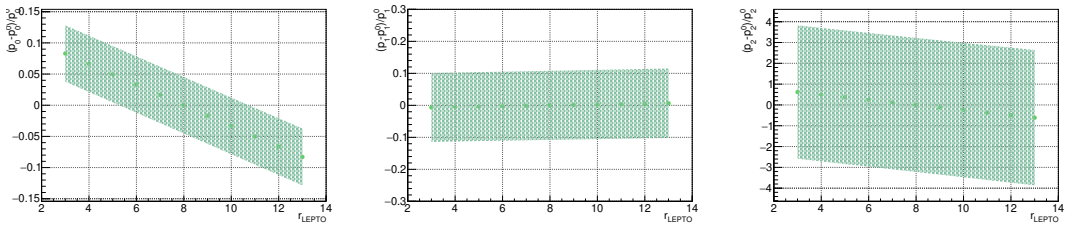

Fig. 5.26: The evolution of the fitted parameters p_i with $i \in [1, 2, 3]$, when r_{LEPTO} varies from 3% to 13%. The quantity p_i^0 denotes the value of the cross section for $r_{\text{LEPTO}} = 8\%$ [104].

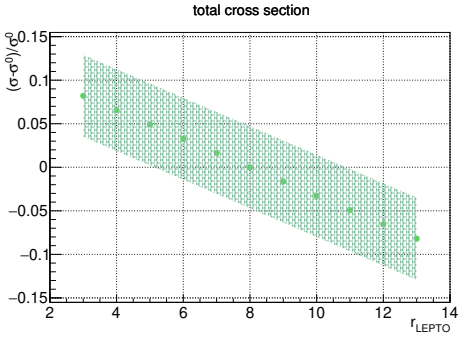

Fig. 5.27: Impact of the variation of r_{LEPTO} on the total exclusive π^0 production cross section. The quantity p_i^0 denotes the cross section point i for $r_{\text{LEPTO}} = 8\%$ [104].

5.8.4 Variation of the Scaling of LEPTO $c_{\pi^0}^{\mathbf{LEPTO}\pm}$

In the cross section extraction, the inclusive background represented by the LEPTO data are normalised by the LEPTO yield r_{LEPTO} and the LEPTO normalisation $c_{\pi^0}^{p\mathrm{LEPTO}\pm}$ [[↩4.4.3.]]. The calculation of the normalisation factor $c_{\pi^0}^{p\mathrm{LEPTO}\pm}$ is straightforward, however, a systematic effect can stem from possible loss of real data due to an inefficiency not contained in other systematic effects. The test is performed by stepping the $c_{\pi^0}^{p\mathrm{LEPTO}\pm}$ by $\pm 20\%$ in steps of ± 4. The influence on the extracted cross section is shown in Figs. 5.29, 5.30, 5.31, and 5.28.

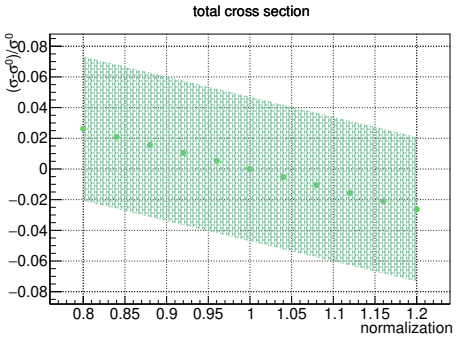

Fig. 5.28: Impact of the variation of $c_{\pi^0}^{p\mathrm{LEPTO}\pm}$ on the total exclusive π^0 production cross section. The quantity σ_i^0 denotes the value of the cross section for $c_{\pi^0}^{p\mathrm{LEPTO}\pm}$ found in our data [104].

Tab. 5.27: Relative systematic errors of the cross section for the 5 $|t|$-bins.

$\lvert t\rvert$ bin	$[0.08, 0.15]$	$[0.15, 0.22]$	$[0.22, 0.36]$	$[0.36, 0.5]$	$[0.5, 0.64]$
sys. error [%]	2.0	2.0	3.0	3.0	3.0

Tab. 5.28: Relative systematic errors of the cross section for the 8 ϕ-bins.

ϕ bin	$[-\pi, -\frac{3\pi}{4}]$	$[-\frac{3\pi}{4}, -\frac{\pi}{2}]$	$[-\frac{\pi}{2}, -\frac{\pi}{4}]$	$[-\frac{\pi}{4}, 0]$	$[0, \frac{\pi}{4}]$	$[\frac{\pi}{4}, \frac{\pi}{2}]$	$[\frac{\pi}{2}, \frac{3\pi}{4}]$	$[\frac{3\pi}{4}, \pi]$
sys. error [%]	4.0	2.0	2.0	5.0	5.0	2.0	2.0	4.0

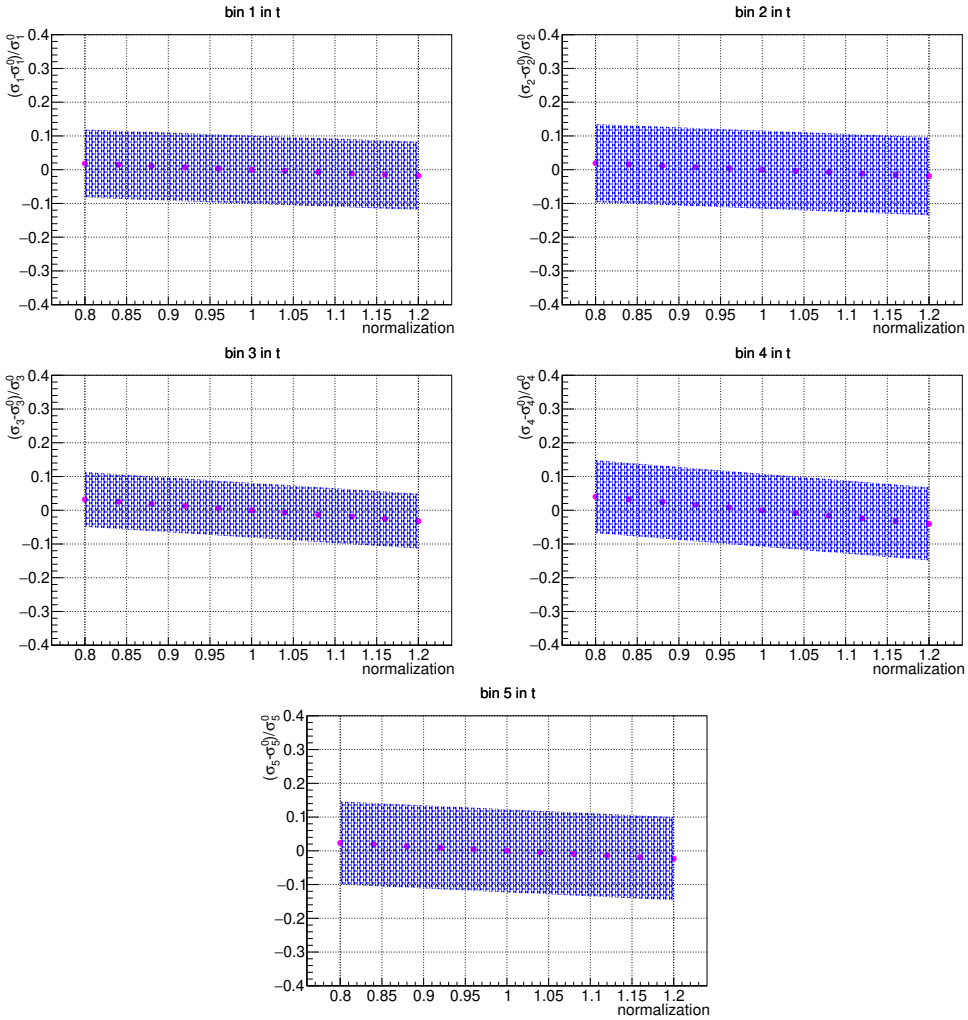

Fig. 5.29: The evolution of the cross-section point $\sigma_{i=1,2,3,4,5}$ in the 5 t bins, when $c_{\pi^0}^{p\mathrm{LEPTO}\pm}$ (the LEPTO normalisation) varies by $\pm 20\%$. The quantity σ_i^0 denotes the value of the cross section for $c_{\pi^0}^{p\mathrm{LEPTO}\pm}$ found in our data [104].

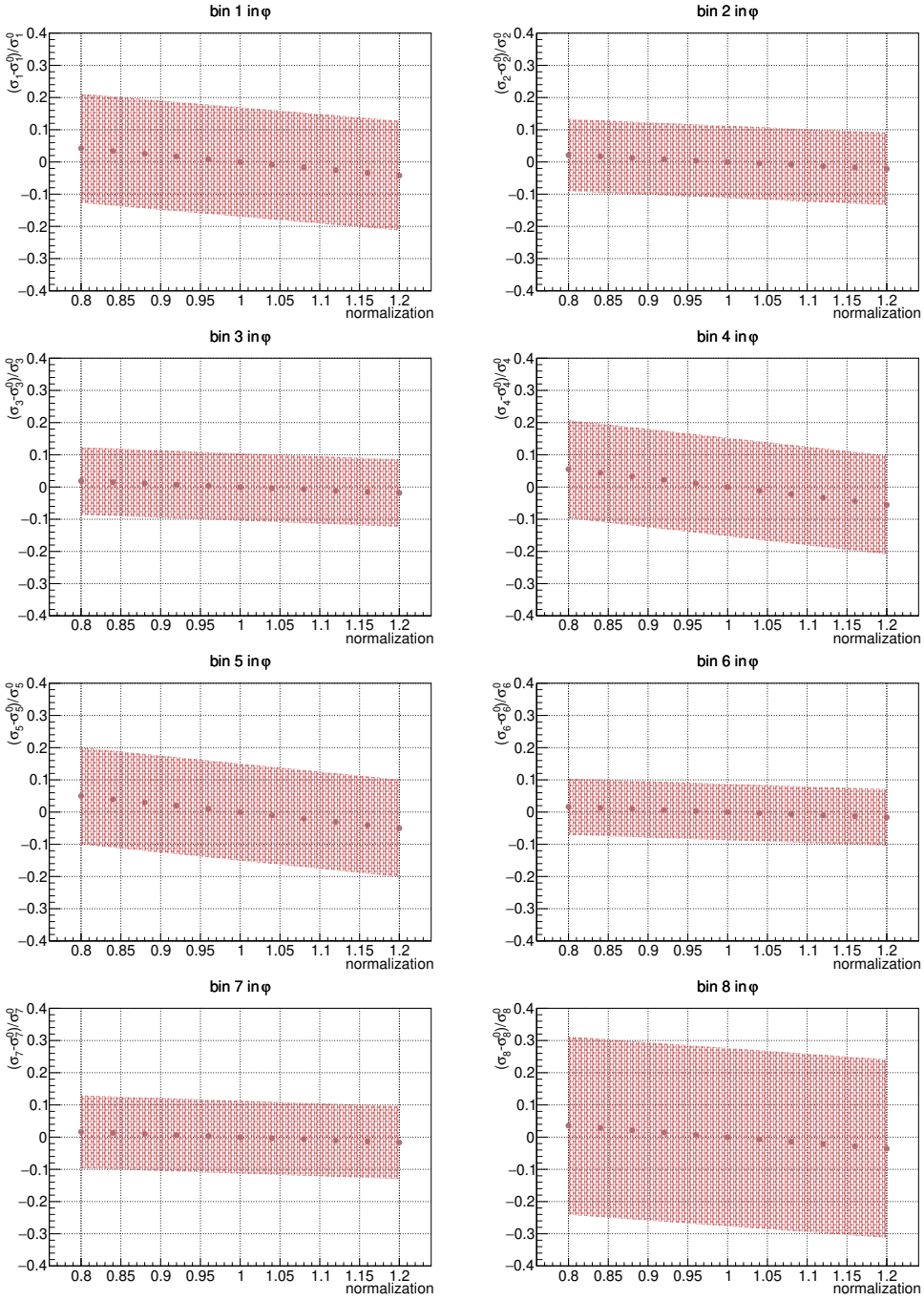

Fig. 5.30: The evolution of the cross-section point $\sigma_{i=1,2,3,4,5,6,7,8}$ in the 8 ϕ bins varying the $c_{\pi^0}^{p\mathrm{LEPTO}\pm}$ by $\pm 20\%$. The quantity σ_i^0 denotes the value of the cross section for $c_{\pi^0}^{p\mathrm{LEPTO}\pm}$ found in our data [104].

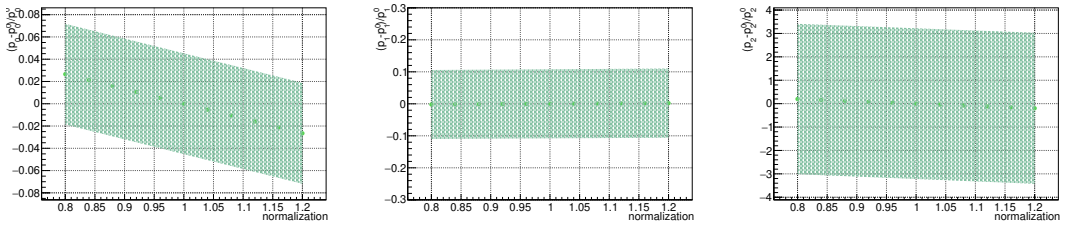

Fig. 5.31: The evolution of the fitted parameters p_i with i $\in$ (1, 2, 3), when $c_{\pi^0}^{p\mathrm{LEPTO}\pm}$ (the LEPTO normalisation) varies by $\pm$ 20%. The quantity σ_i^0 denotes the value of the cross section for $c_{\pi^0}^{p\mathrm{LEPTO}\pm}$ (the LEPTO normalisation) varies by $\pm$ 20%. The quantity p_i^0 denotes the value of the fitted parameter for $c_{\pi^0}^{p\mathrm{LEPTO}\pm}$ found in our data [104].

Tab. 5.29: Relative systematic errors of the total cross section and 3 fitted parameters of its ϕ modulation.

parameters	σ_{tot}	p_0	p_1	p_2
sys. error [%]	2.6	2.6	2.0	20.0

5.8.5 Variation of the Acceptance Binning

The selected binning for the cross section calculation is supposed to maximize the balance of the statistics in bins. The assumption stands that the used binning in variables Q^2 and ν should not have any effect on the final results, as the cross section is integrated over these two variables. To verify this assumption, a stability test was performed varying the binning with respect to the reference in one selected variable, while the other is kept default. The results of the variation in both variables are shown in Figs. 5.33, 5.34, 5.35, and 5.32 where the points $i = (1, 2, 3, 4)$ show the values from varying number of Q^2 bins to $\mathrm{binning}_{Q^2} = (3, 4, 5, 6)$, respectively, while the binning in ν is kept on default, and the points $i = (5, 6, 7, 8, 8)$ represent the variation of $\mathrm{binning}_{\nu} = (3, 4, 5, 6, 7)$, respectively, and Q^2 binning is fixed. The Tabs. 5.32, 5.30, and 5.31 sum up the values of extremities extracted from these plots.

Tab. 5.30: Relative systematic errors of the cross section for the 8 ϕ-bins.

ϕ bin	$[-\pi, -\frac{3\pi}{4}]$	$[-\frac{3\pi}{4}, -\frac{\pi}{2}]$	$[-\frac{\pi}{2}, -\frac{\pi}{4}]$	$[-\frac{\pi}{4}, 0]$	$[0, \frac{\pi}{4}]$	$[\frac{\pi}{4}, \frac{\pi}{2}]$	$[\frac{\pi}{2}, \frac{3\pi}{4}]$	$[\frac{3\pi}{4}, \pi]$
sys.error $\uparrow$ [%]	10.0	4.0	3.0	3.0	3.0	3.0	4.0	0.0
sys.error $\uparrow$ [%]	0.0	4.0	3.0	3.0	3.0	3.0	4.0	6.0

Tab. 5.31: Relative systematic errors of the total cross section and 3 fitted parameters of its ϕ modulation.

parameters	σ_{tot}	p_0	p_1	p_2
sys.error $\uparrow$ [%]	3.0	2.5	3.0	40.0
sys.error $\downarrow$ [%]	1.0	1.0	3.0	40.0

Tab. 5.32: Relative systematic errors of the cross section for the 5 $|t|$-bins.

$\|t\|$ bin	$[0.08, 0.15]$	$[0.15, 0.22]$	$[0.22, 0.36]$	$[0.36, 0.5]$	$[0.5, 0.64]$
sys.error $\uparrow$ [%]	1.0	5.0	3.0	3.0	8.0
sys.error $\downarrow$ [%]	1.0	5.0	0.0	0.0	4.0

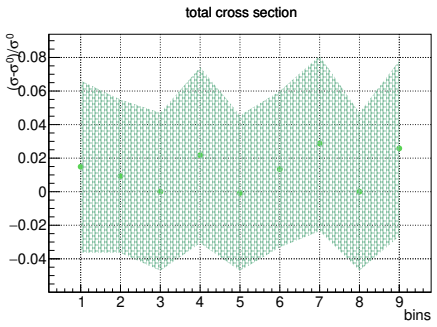

Fig. 5.32: The impact of the variation of the acceptance binning on the total exclusive π^0 cross section [104].

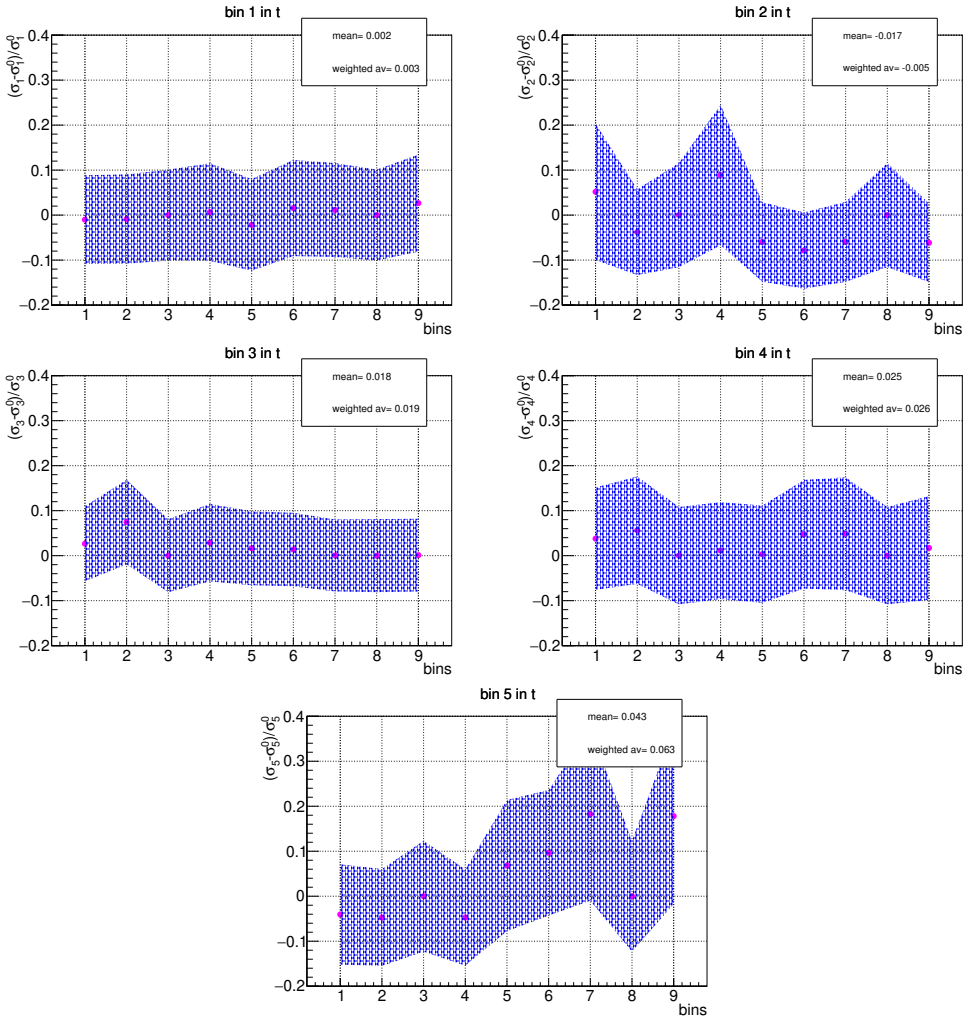

Fig. 5.33: The impact of the variation of the acceptance binning on the $|t|$ cross section $\sigma_{i=1,2,3,4,5}$. The first four points show the results of the variation of the binning in Q^2 in steps $N_{\text{bins}} = (3, 4, 5, 6)$, with the default 6 ν bins, and the consecutive five points show the effect of the variation in bins of νin steps $N_{\text{bins}} = (3, 4, 5, 6, 7)$ with the default 5 Q^2 bins [104].

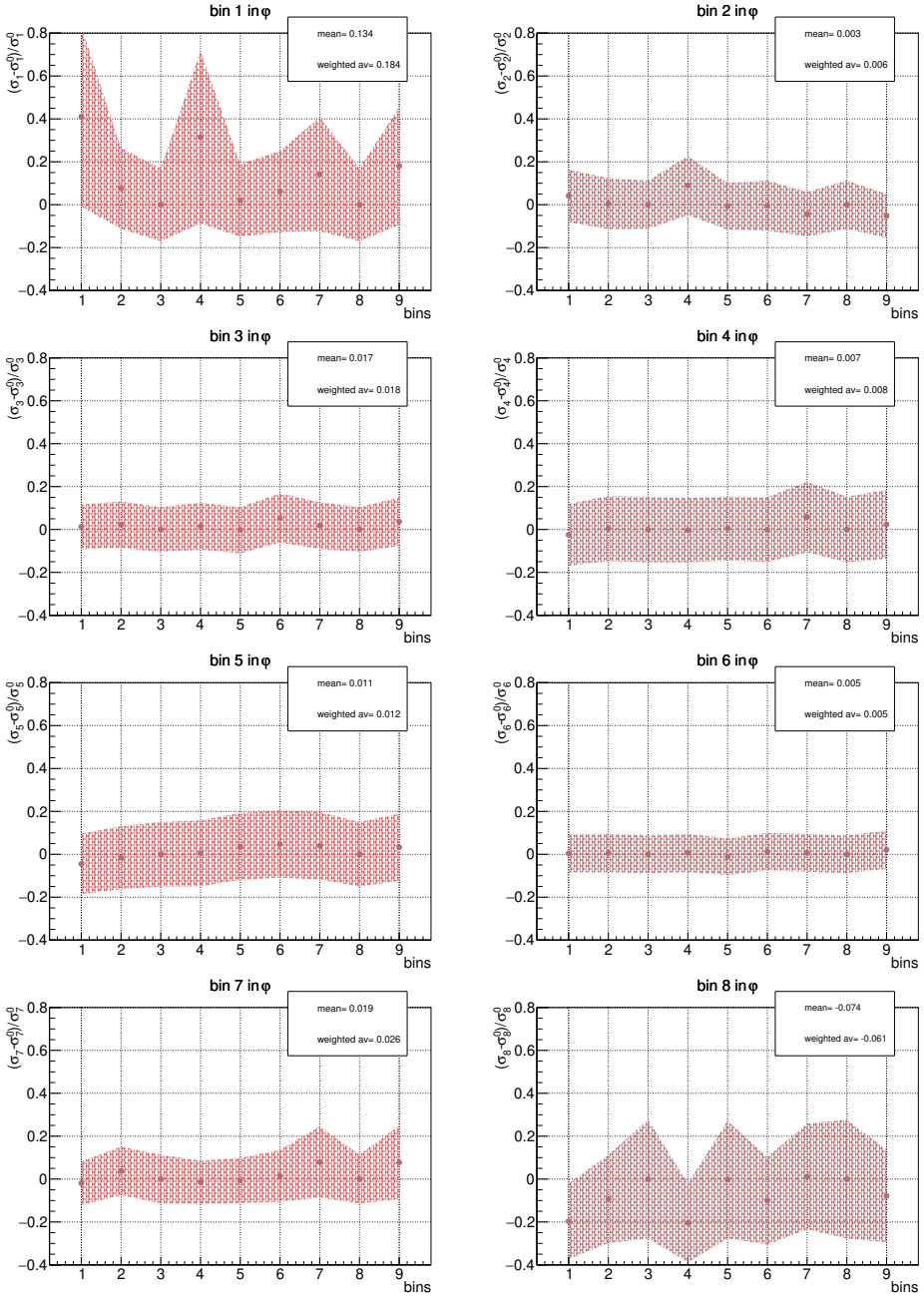

Fig. 5.34: The impact of the variation of the acceptance binning on the ϕ cross-section bins $\sigma_{i=1,2,3,4,5,6,7,8}$. The first four points show the results of the variation of the binning in Q^2 in steps $N_{\text{bins}} = (3, 4, 5, 6)$, with the default 6 ν bins, and the consecutive five points show the effect of the variation in bins of ν in steps $N_{\text{bins}} = (3, 4, 5, 6, 7)$ with the default 5 Q^2 bins [104].

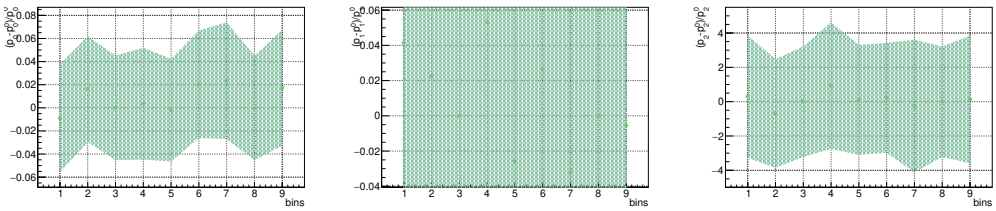

Fig. 5.35: The impact of the variation of the acceptance binning on the fitted parameters p_i with i $\in$ (1, 2, 3). The first four points show the results of the variation of the binning in Q^2 in steps $N_{\text{bins}} = (3, 4, 5, 6)$, with the default 6 ν bins, and the next five points show the variation in bins of ν in steps $N_{\text{bins}} = (3, 4, 5, 6, 7)$, with 5 Q^2 bins [104].

5.8.6 Exclusive ω^0 Contamination

While a majority of background originates from inclusive processes, exclusive processes other than the π^0 production itself contribute as well. The most probable candidate of such a contamination is the exclusive ω^0 meson production, in particular the decay channel into π^0 and γ, which has the branching ratio of 8.28%. Such events, where the photon carries away only a tiny fraction of the total energy, could be misidentified as exclusive π^0 production.

Exclusive ω^0 candidates can be reconstructed in the data combining a π^0 with an additional photon. The Fig. 5.36 shows the invariant mass of $\pi^0\gamma$ system. One can indeed notice a small peak at the nominal ω^0 mass of 782.66 MeV. Out of the full exclusive π^0 sample of 1531 events, in total, 41 exclusive ω^0 candidates were identified. These events represent an additional background of the exclusive π^0 production and need to removed from the original sample. The results from the data were compared with a simulation of the exclusive ω^0 muoproduction (HEPGEN++), applying the exclusive π^0 selection procedure. They were found to be compatible, as can be seen in Fig. 5.36.

Apart from visible ω^0 events, the contribution of the cases where the third photon was not detected (i.e. "invisible" exclusive ω^0) should be accounted for. The same simulation of the exclusive ω^0 production was used for this case with the

event selection identical to the exclusive π^0 one. The number of remaining exclusive π^0 events scaled with the normalisation gives an estimate for the contamination.

The pure exclusive ω^0 events are used for the normalisation of the "visible" ω^0 MC. The normalisation is performed by the integral of the data in range 700–865 MeV. The events are selected analogously to the exclusive π^0 selection. A π^0 candidate is identified, and then combined with an additional neutral cluster to form an ω^0 candidate, which is then subjected to the same selection steps, except of the kinematic fit. The kinematic fit was found to be unstable for constraining three photons and was failing to converge. The distribution of the invariant mass of $\pi^0 - \gamma$ exhibits a high level of background, which has to be removed in order to estimate the number of exclusive ω^0 events. A simple asymmetric constant fit was utilised to estimate the level of the background, which was then subtracted. The normalisation between the exclusive ω^0 MC and the data was then obtained as the ratio of the number of exclusive ω^0 events in the data and MC.

The systematic effect of exclusive ω^0 contamination is summarised in Tables 5.34, 5.35, and 5.36. The resulting contamination by the invisible exclusive ω yields is $s^{\downarrow}_{\omega} = 2.4\%$.

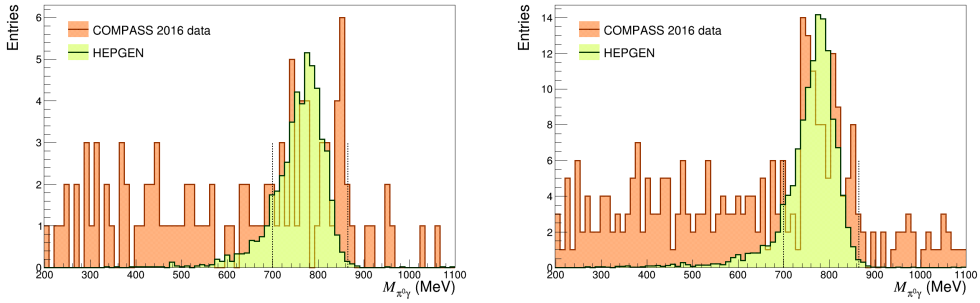

Fig. 5.36: Left: The invariant mass spectrum for exclusive π^0 candidates combined with an additional photon in the event ("visible" ω^0 contamination). The normalisation of the exclusive ω^0 muoproduction HEPGEN++ is obtained from the plot on the right-hand side. Right: The invariant mass spectrum of the $\pi^0\gamma$ system obtained selecting exclusive ω^0 muoproduction, $\mu p \to \mu p \omega^0 \to \mu p \pi^0 \gamma$, for the data and an exclusive ω^0 muoproduction HEPGEN++. The MC is normalised to the integral of the data in the signal region 700–865 MeV.

Tab. 5.33: Event counts in real data and the exclusive ω MC used for estimating the exclusive ω^0 contamination of the exclusive π^0 production: First row contains the number of events under the π^0 peak; the second row represents the integrals of the area of the ω^0 peak (in range 700–865 MeV) from the "visible" ω^0 within the exclusive π^0 sample; and the third row contains the integrals of the area of the ω^0 peak in the exclusive ω^0 selection (after subtracting the background).

Selection	Data peak area [events]	MC peak area [sum of weights]
exclusive π^0	1531	5551.11
visible ω^0 in π^0 sample	41	2244.48
exclusive ω^0	73	6658.02

Tab. 5.34: Relative systematic errors due to ω^0 contamination of the cross section for the 5 $|t|$-bins.

$\lvert t\rvert$ bin [GeV^2]	$[0.08, 0.15]$	$[0.15, 0.22]$	$[0.22, 0.36]$	$[0.36, 0.5]$	$[0.5, 0.64]$
sys. error $\downarrow$ [%]	2.7	2.5	2.5	2.7	1.5

Tab. 5.35: Relative systematic errors due to ω^0 contamination of the cross section for the 8 ϕ-bins.

ϕ bin	$[-\pi, -\frac{3\pi}{4}]$	$[-\frac{3\pi}{4}, -\frac{\pi}{2}]$	$[-\frac{\pi}{2}, -\frac{\pi}{4}]$	$[-\frac{\pi}{4}, 0]$	$[0, \frac{\pi}{4}]$	$[\frac{\pi}{4}, \frac{\pi}{2}]$	$[\frac{\pi}{2}, \frac{3\pi}{4}]$	$[\frac{3\pi}{4}, \pi]$
sys. error $\downarrow$ [%]	4.3	2.0	1.9	3.1	3.1	1.4	2.0	5.7

Tab. 5.36: Relative systematic errors due to ω^0 contamination of the total cross section and 3 fitted parameters of its ϕ modulation.

parameters	σ_{tot}	p_0	p_1	p_2
sys. error $\downarrow$ [%]	2.6	2.6	2.6	20.0

5.8.7 Radiation Corrections

The radiative corrections are assumed to be small for exclusive π^0 muoproduction, not exceeding 10% [117]. The processes with complete detection of all final particles have strongly reduced phase space left for the final radiated photons (compared to inclusive scattering). The size of the radiation corrections was estimated using program EXCLURAD [117], originally developed for the JLab experiments. This program has a limitation, it assumes that only one of the final hadrons is detected (either recoiling proton or π^0), while at COMPASS both hadrons are detected. The processes entering the estimation are Born process, Bremsstrahlung (radiation of a photon), and the vertex correction and vacuum polarisation.

The radiative corrections are very sensitive to the exclusivity cuts, which are represented in EXCLURAD by a cut on inelasticity. The inelasticity considered in the predictions [117] is either the invariant mass v_1, when only the pion is detected, or the invariant mass v_2, when only the recoiling proton is detected:

$$v_1 = (k + p - k' - p_{\pi^0})^2 - m_p^2 \quad \text{or} \quad v_2 = (k + p - k' - p_p)^2 - m_{\pi^0}^2 \tag{5.17}$$

At COMPASS both proton and π^0 are detected and we observe the missing mass $M_X^2 = (k + p - k' - p' - q')^2$ (right bottom plot in Fig. 4.8). One can note a very sharp peak around zero, with the cuts at $|M_X^2| < 0.3$ GeV^2. The cut corresponds to the emission of 4 extra pions at rest, which leads to the inelasticities v_1 and v_2 being very broad. The cut for emission of 4 extra pions is at $v_1^{\text{cut}} = (0.938 + 4 \times 0.135)^2 - 0.938^2) = 1.3$ GeV^2 and $v_2^{\text{cut}} = (5 \times 0.135)^2 - 0.135^2) = 0.44$ GeV^2. Considering these cuts in inelasticities, EXCLURAD results suggest a maximum possible systematic effect up to 6% [103]. The estimated relative uncertainties in all the bins are given in Tabs. 5.37, 5.38, 5.39.

Tab. 5.37: Relative systematic errors due to radiative corrections of the cross section in 5 $|t|$-bins.

$\|t\|$ bin [GeV^2]	$[0.08, 0.15]$	$[0.15, 0.22]$	$[0.22, 0.36]$	$[0.36, 0.5]$	$[0.5, 0.64]$
sys. error $\uparrow$ [%]	6.0	6.0	6.0	6.0	6.0
sys. error $\downarrow$ [%]	3.0	3.0	3.0	3.0	3.0

Tab. 5.38: Relative systematic errors due to radiative corrections of the cross section in 8 ϕ-bins.

ϕ bin	$[-\pi, -\frac{3\pi}{4}]$	$[-\frac{3\pi}{4}, -\frac{\pi}{2}]$	$[-\frac{\pi}{2}, -\frac{\pi}{4}]$	$[-\frac{\pi}{4}, 0]$	$[0, \frac{\pi}{4}]$	$[\frac{\pi}{4}, \frac{\pi}{2}]$	$[\frac{\pi}{2}, \frac{3\pi}{4}]$	$[\frac{3\pi}{4}, \pi]$
sys. error $\uparrow$ [%]	6.3	6.3	6.3	6.3	6.3	6.3	6.3	6.3
sys. error $\downarrow$ [%]	3.6	3.6	3.6	3.6	3.6	3.6	3.6	3.6

Tab. 5.39: Relative systematic errors due to radiative corrections of the total cross section and 3 fitted parameters of its ϕ modulation.

parameters	σ_{tot}	p_0	p_1	p_2
sys. error $\uparrow$ [%]	6.0	6.0	2.0	20.0
sys. error $\downarrow$ [%]	3.0	3.0	2.0	20.0

5.8.8 Systematic effect due to μ^+ and μ^- fluxes

The muon flux is determined with an accuracy better than 2%. On each cross section and parameter a systematic error of 2% is added.

5.8.9 Period Compatibility

The compatibility of 2016 periods was studied for the cross section as a function of ϕ and $|t|$, as shown in Fig. 5.37. Results are compatible within statistical errors.

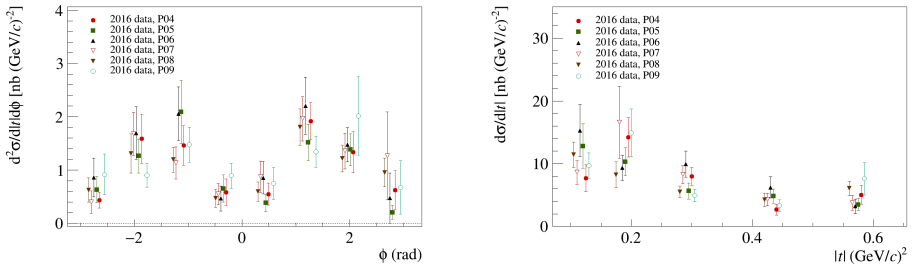

Fig. 5.37: The comparison of the cross section of exclusive π^0 production as a function of ϕ (on the left) and $|t|$ (on the right) averaged over both polarities, for individual 2016 periods.

5.8.10 Summary of Systematic Effects

The summarised results of all the contributions to the systematics are presented in Tables 5.40 for the bins in $|t|$, 5.41 for the bins in ϕ, and 5.42 for the fitted parameters of the cross section ϕ modulation. The individual systematic uncertainties are added in quadrature to obtain the final systematic uncertainties.

Tab. 5.40: Summary of the estimated relative systematic uncertainty of the cross section in the 5 bins of $|t|$. Arrows indicate an increase or decrease of the measured value due to the systematic effect.

section	effect	σ_1	σ_2	σ_3	σ_4	σ_5
5.8.1	χ^2_{fit} cut-off variation $\uparrow$ [%]	1.9	1.9	6.3	6.3	6.3
	χ^2_{fit} cut-off variation $\downarrow$ [%]	8.5	8.5	5.2	5.2	5.2
5.8.2	E_{cl_l} threshold, EC00 $\uparrow$ [%]	3.9	3.9	12.1	12.1	12.1
	E_{cl_l} threshold, EC00 $\downarrow$ [%]	2.2	2.2	0.0	0.0	0.0
5.8.2	E_{cl_l} threshold, EC01 $\uparrow$ [%]	2.0	2.0	6.0	6.0	6.0
	E_{cl_l} threshold, EC01 $\downarrow$ [%]	4.0	4.0	1.7	1.7	1.7
5.8.3	r_{LEPTO} variation [%]	6.0	6.0	10.0	10.0	10.0
5.8.4	$c_{\pi^0}^{p\text{LEPTO}}$ variation [%]	2.0	2.0	3.0	3.0	3.0
5.8.5	acceptance binning $\uparrow$ [%]	1.0	5.0	3.0	3.0	8.0
	acceptance binning $\downarrow$ [%]	1.0	5.0	0.0	0.0	4.0
5.8.6	exclusive ω contamination $\downarrow$ [%]	2.7	2.5	2.5	2.7	1.5
5.8.7	radiation corrections $\uparrow$ [%]	6.0	6.0	6.0	6.0	6.0
	radiation corrections $\downarrow$ [%]	3.0	3.0	3.0	3.0	3.0
5.8.8	μ^+ and μ^- flux [%]	2.0	2.0	2.0	2.0	2.0
	total $\uparrow$ [%]	10.2	11.3	19.5	19.5	20.9
	total $\downarrow$ [%]	12.4	13.3	12.6	12.6	13.0

Tab. 5.41: Summary of the estimated relative systematic uncertainty of the cross section in the 8 bins of ϕ.

section	effect	σ_1	σ_2	σ_3	σ_4	σ_5	σ_6	σ_7	σ_8
5.8.1	χ^2_{fit} cut-off variation ↑ [%]	9.0	2.1	2.1	9.0	9.0	2.1	2.1	9.0
	χ^2_{fit} cut-off variation ↓ [%]	12.6	4.5	4.5	12.6	12.6	4.5	4.5	12.6
5.8.2	E_{cl_l} threshold, EC00 ↑ [%]	13.0	6.7	6.7	13.0	13.0	6.7	6.7	13.0
	E_{cl_l} threshold, EC00 ↓ [%]	1.5	0.3	0.3	1.5	1.5	0.3	0.3	1.5
5.8.2	E_{cl_l} threshold, EC01 ↑ [%]	7.7	2.4	2.4	7.7	7.7	2.4	2.4	7.7
	E_{cl_l} threshold, EC01 ↓ [%]	2.9	1.9	1.9	2.9	2.9	1.9	1.9	2.9
5.8.3	r_{LEPTO} variation [%]	12.0	6.0	6.0	16.0	16.0	6.0	6.0	12.0
5.8.4	$c_{\pi^0}^{p\text{LEPTO}}$ variation [%]	4.0	2.0	2.0	5.0	5.0	2.0	2.0	4.0
5.8.5	acceptance binning ↑ [%]	10.0	4.0	3.0	3.0	3.0	3.0	4.0	0.0
	acceptance binning ↓ [%]	0.0	4.0	3.0	3.0	3.0	3.0	4.0	6.0
5.8.6	exclusive ω contamination ↓ [%]	4.3	2.0	1.9	3.1	3.1	1.4	2.0	5.7
5.8.7	radiation corrections ↑ [%]	6.3	6.3	6.3	6.3	6.3	6.3	6.3	6.3
	radiation corrections ↓ [%]	3.6	3.6	3.6	3.6	3.6	3.6	3.6	3.6
5.8.8	μ^+ and μ^- flux [%]	2.0	2.0	2.0	2.0	2.0	2.0	2.0	2.0
	total ↑ [%]	24.8	12.4	12.2	25.4	25.4	12.2	12.4	22.6
	total ↓ [%]	19.1	10.0	9.7	21.8	21.8	9.6	10.0	20.4

Tab. 5.42: Summary of the estimated relative systematic uncertainty of the total cross section and 3 fitted parameters of its ϕ modulation.

section	effect	σ_{tot}	$\langle \frac{d\sigma_U}{dt} \rangle$	$\langle \frac{d\sigma_{TT}}{dt} \rangle$	$\langle \frac{d\sigma_{LT}}{dt} \rangle$
5.8.1	χ^2_{fit} cut-off variation ↑ [%]	3.6	3.0	3.0	25.0
5.8.1	χ^2_{fit} cut-off variation ↓ [%]	6.5	5.0	4.0	25.0
5.8.2	E_{cl_l} threshold, EC00 ↑ [%]	7.3	7.0	5.0	4.0
	E_{cl_l} threshold, EC00 ↓ [%]	0.0	0.0	1.0	4.0
5.8.2	E_{cl_l} threshold, EC01 ↑ [%]	3.7	3.0	1.0	30.0
	E_{cl_l} threshold, EC01 ↓ [%]	1.5	2.0	2.0	30.0
5.8.3	r_{LEPTO} variation [%]	8.2	8.3	0.7	62.0
5.8.4	$c_{\pi^0}^{p\text{LEPTO}}$ variation [%]	2.6	2.6	2.0	20.0
5.8.5	acceptance binning ↑ [%]	3.0	2.5	3.0	40.0
	acceptance binning ↓ [%]	1.0	1.0	3.0	40.0
5.8.6	exclusive ω contamination ↓ [%]	2.6	2.6	2.6	20.0
5.8.7	radiation corrections ↑ [%]	6.0	6.0	2.0	20.0
	radiation corrections ↓ [%]	3.0	3.0	2.0	20.0
5.8.8	μ^+ and μ^- flux [%]	2.0	2.0	2.0	10.0
	total ↑ [%]	14.8	13.7	7.5	91.0
	total ↓ [%]	11.8	11.2	7.0	91.0

Conclusion

The GPD represent one of the approaches to describe the nucleon 3D structure. GPDs can be parametrised through evaluating the differential cross section of exclusive processes, such as HEMP, or DVCS. The differential cross section provides access to structure functions corresponding to bi-linear combinations of helicity amplitudes. Assuming factorisation, the helicity amplitude is a convolution of the hard scattering kernel with a soft term containing the GPDs. The GPDs can be thus extracted from the scattering amplitudes. While DVCS provides access to the chiral-even GPDs, HEMP enables to determine complementary GPDs, in particular, the chiral-odd ones. In addition, examining different meson species provides information on flavour dependency of GPDs.

The COMPASS experiment dedicated two years for measurement of exclusive processes in 2016–17 using 160 GeV muon beam of both polarities and an unpolarised hydrogen target. The subject of this thesis is the hard exclusive π^0 production process $\mu p \to \mu' p' \pi^0$ in the kinematic domain of average $x_B \sim 0.134$. The main feature of the experimental setup was the over-constraintment of the measurement employing the recoiled proton time-of-flight detector CAMERA combined with the rest of the spectrometer, which detected the scattered muon and the π^0 decaying into two photons. This provided higher precision in the determination of the exclusivity of events, which together with utilising the kinematic fit procedure ensured the reduction of the background. The CAMERA allowed to access the region of low four-momentum transfer t of the recoiled proton, where the spectrometer resolution is limited.

A high resolution measurement of exclusive processes requires a precise calibration of the apparatus, particularly of the CAMERA, and the electromagnetic calorimeters. The preparation of the ECALs encompasses several methods of timing and energy calibration applied in several iterations of the data reconstruction. During the analysis of the 2016 data, the calibrations were tested and tuned, ensuring the reliable performance of the calorimeters.

The collected data has been processed to select the exclusive π^0 production events, identifying a scattered muon, a recoiled proton, and a π^0 candidate. The exclusivity of the event was ensured by requirements matching the measured proton momentum with its prediction based on the measurement of the remaining

particles and conservation laws. To improve precision and reduce the background, the kinematically constrained fit has been deployed. The dominant contribution to the background comes from inclusive π^0 production. The estimation of the background is performed using Monte Carlo simulations based on event generators HEPGEN++ for modelling the exclusive π^0 signal and LEPTO for describing the inclusive background. Two different methods were employed to fit both simulation samples to the data, obtaining the background level of $8 \pm 5\%$. Another source of background is the 2.4% exclusive ω^0 production yield. Both background sources were subtracted from the selected event sample.

The differential cross section of exclusive π^0 production as a function of the four-momentum transfer t and the azimuthal angle of the π^0 ϕ was determined in the kinematic domain:

$$\begin{aligned} 6.4 < \nu < 40 \text{ GeV}, \\ 1 < Q^2 < 8 \text{ GeV}^2, \\ 0.08 < |t| < 0.64 \text{ GeV}^2, \end{aligned}$$

characterised by average values of kinematic variables:

$$\begin{aligned} \langle Q^2_{\text{fit}} \rangle &= 2.266 \text{ GeV}^2, \\ \langle \nu_{\text{fit}} \rangle &= 10.160 \text{ GeV}, \\ \langle |t_{\text{fit}}| \rangle &= 0.293 \text{ GeV}^2, \\ \langle x_B \rangle &= 0.134, \\ \langle W \rangle &= 4.100 \text{ GeV}, \\ \langle |t_{\text{CAMERA}}| \rangle &= 0.297 \text{ GeV}^2. \end{aligned}$$

The ϕ-modulation of the exclusive π^0 production cross section was fitted to determine the contributions of the particular amplitudes with the following results:

$$\begin{aligned} \left\langle \frac{\mathrm{d}\sigma_{\mathrm{T}}}{\mathrm{d}|t|} + \epsilon \frac{\mathrm{d}\sigma_{\mathrm{L}}}{\mathrm{d}|t|} \right\rangle &= (6.63 \pm 0.31_{\text{stat}}{}^{+\ 0.90}_{-\ 0.74}\Big|_{\text{sys}}) \frac{\text{nb}}{(\text{GeV})^2} \\ \left\langle \frac{\mathrm{d}\sigma_{\mathrm{TT}}}{\mathrm{d}|t|} \right\rangle &= (-4.61 \pm 0.48_{\text{stat}}{}^{+\ 0.35}_{-\ 0.32}\Big|_{\text{sys}}) \frac{\text{nb}}{(\text{GeV})^2} \\ \left\langle \frac{\mathrm{d}\sigma_{\mathrm{LT}}}{\mathrm{d}|t|} \right\rangle &= (0.15 \pm 0.19_{\text{stat}}{}^{+\ 0.14}_{-\ 0.14}\Big|_{\text{sys}}) \frac{\text{nb}}{(\text{GeV})^2}. \end{aligned}$$

The strong contribution of the transverse cross section amplitude σ_{TT}, observed at COMPASS in the 2012 pilot run was confirmed. The total cross section integrated over ϕ and over the accessed range in t obtained from the 2016 COMPASS data analysis is $6.72 \pm 0.32_{\mathrm{stat}} {}^{+\ 0.99}_{-\ 0.79}\big|_{\mathrm{sys}}$ nb. The obtained results will serve as input for further constraining phenomenological models, such as Goloskokov–Kroll or Liuti–Goldstein. In addition, the evolution of the differential cross section as a function of t and ϕ was studied in three bins of ν and four bins of Q^2.

The 2016 data sample is 2.3× larger as compared to the 2012 pilot measurement. Moreover, the background suppression has been improved, leading to a reduction of the measured uncertainties almost 3×. They could be further improved by expanding the analysis to the 2017 data, enlarging the complete statistics to 9× the amount of 2012. This would not only reduce statistical uncertainties, but enable extraction of spin-dependent cross sections for μ^+ and μ^- as well, allowing to determine the polarisation-dependent interference term $\sigma_{\mathrm{LT}'}$.

Bibliography

[1] Ellis, J., Jaffe, R. *Sum rule for deep-inelastic electroproduction from polarized protons.* Phys. Rev. D, 9:1444–1446, Mar 1974. DOI: 10.1103/PhysRevD.9.1444. URL: https://link.aps.org/doi/10.1103/PhysRevD.9.1444.

[2] Ashman, et al. (**EMC** Collaboration) *A Measurement of the Spin Assymetry and Determination of the Structure Function g(1) in Deep Inelastic Muon-Proton Scattering.* Phys. Lett. B **753** 18-28 (2016), DOI: 10.1016/0370-2693(88)91523-7.

[3] Florian, D. et al. *Evidence for Polarization of Gluons in the Proton* Phys. Rev. Lett. **113** 012001 (2014), DOI: 10.1103/PhysRevLett.113.012001. https://doi.org/10.1103/PhysRevLett.113.012001.

[4] Ji, X. *Gauge-invariant decomposition of nucleon spin*, Physical Review Letters 78, 610–613 (1997) DOI: 10.1103/PhysRevLett.78.610. https://doi.org/10.1103/PhysRevLett.78.610.

[5] Burkardt, M. *Impact parameter dependent parton distributions and off-forward parton distributions for $\xi \to 0$*, Physical Review D 62, 071503 (2000) DOI: 10.1103/PhysRevD.62.071503. URL: https://link.aps.org/doi/10.1103/PhysRevD.62.071503.

[6] Akhunzyanov, R. et al. **COMPASS** Collaboration. *Transverse extension of partons in the proton probed by deeply virtual Compton scattering.* Phys. Lett. B **793** (2019) 188–194. DOI: 10.1016/j.physletb.2019.04.038. https://doi.org/10.1016/j.physletb.2019.04.038.

[7] Masi, R. D. et al. (**CLAS** Collaboration). *Measurement of $ep \to ep\pi^0$ beam spin asymmetries above the resonance region.* Phys. Rev. C **77**, 042201 (2008). DOI: 10.1103/PhysRevC.77.042201. https://doi.org/10.1103/PhysRevC.77.042201.

[8] Bedlinsky, I. et al. (**CLAS** Collaboration). *Measurement of exclusive π^0 electroproduction structure functions and their relationship to transverse generalized parton distributions.* Phys. Rev. Lett. **109**, 112001 (2012).

DOI: 10.1103/PhysRevLett.109.112001. https://doi.org/10.1103/PhysRevLett.109.112001.

[9] Kim, A. et al. (**CLAS** Collaboration). *Beam Spin Asymmetry Measurements of Deeply Virtual* π^0 *Production with CLAS12*. Submitted to print (2023). DOI: 10.48550/arXiv.2307.07874. https://doi.org/10.48550/arXiv.2307.07874.

[10] Mazouz, M. et al. (JLab Collaboration). *Deeply Virtual Compton Scattering off the Neutron*. Phys. Rev. Lett. **99**, 242501 (2007). DOI: 10.1103/PhysRevLett.99.242501. https://doi.org/10.1103/PhysRevLett.99.242501.

[11] Rostomyan, A. et al. (HERMES Collaboration). *Transverse Target-Spin Asymmetry of Exclusive* ρ^0 *Meson Production on Proton at HERMES*. DIS2007 proceedings. DOI: 10.48550/arXiv.0707.2486. https://doi.org/10.48550/arXiv.0707.2486.

[12] Airapetian, A. et al (HERMES Collaboration). *Measurement of azimuthal asymmetries with respect to both beam charge and transverse target polarization in exclusive electroproduction of real photons*. Journal of High Energy Physics, Volume 2008, JHEP06(2008). DOI: 10.1088/1126-6708/2008/06/066. https://doi.org/10.1088/1126-6708/2008/06/066.

[13] Adolph, C. et al (COMPASS Collaboration). *Transverse target spin asymmetries in exclusive* ρ^0 *muoproduction*. Phys. Lett. B **731**, 19-26 (2014). DOI: 10.1016/j.physletb.2014.02.005. https://doi.org/10.1016/j.physletb.2014.02.005.

[14] Diehl, M. *Generalized parton distributions.* Deutsches Elektronen-Synchroton DESY, DESY-THESIS-2003-018 (2003). DOI: 10.1016/j.physrep.2003.08.002. https://arxiv.org/abs/hep-ph/0307382.

[15] Diehl, M. *Introduction to GPDs and TMDs.* Eur. Phys. J. A52.6 (2016), p. 149. DOI: 10.1140/epja/i2016-16149-3. http://arxiv.org/abs/1512.01328.

[16] Diehl, M. *Generalized Parton Distributions with Helicity Flip.* Eur. Phys. J. C **19** (2001) 485-492. DOI: 10.1007/s100520100635. https://doi.org/10.1007/s100520100635.

[17] Diehl, M. and Sapeta, S. *On the analysis of lepton scattering on longitudinally or transversely polarized protons.* Eur. Phys. J. C 41, 515–533 (2005). DOI: 10.1140/epjc/s2005-02242-9. https://doi.org/10.1140/epjc/s2005-02242-9.

[18] Mezrag, C. An introductory lecture on Generalised Parton Distributions. Few-Body Syst. **63**, 62 (2022). DOI: 10.1007/s00601-022-01765-x. https://doi.org/10.1007/s00601-022-01765-x.

[19] Gorzellik, M. *Cross-section measurement of exclusive π^0 muoproduction and firmware design for an FPGA-based detector readout.* PhD thesis. Physikalisches Institut Albert-Ludwigs-Universität Freiburg (2018). http://wwwcompass.cern.ch/compass/publications/theses/2018_phd_gorzellik.pdf.

[20] Ventura, B. *Study of Deeply Virtual Compton Scattering at COMPASS at CERN.* PhD thesis. Johannes Gutenberg-Universiät Mainz and Université Paris-Saclay (2019). https://tel.archives-ouvertes.fr/tel-02283265/document.

[21] Vidon, A. *Probing the proton structure thorugh deep virtual Compton scattering at COMPASS, CERN.* PhD thesis. Université Paris-Saclay (2019). http://wwwcompass.cern.ch/compass/publications/theses/2019_phd_vidon.pdf.

[22] Stern, O. *Über die magnetische Ablenkung von Wasserstoff-molekülen und das magnetische Moment des Protons. I.* Zeitschrift fur Physik **85** 4–16 (1933). DOI: 10.1007/BF01330773. https://doi.org/10.1007/BF01330773.

[23] Rosenbluth, M. N. *High Energy Elastic Scattering of Electrons on Protons.* Phys. Rev. **79** 615–619 (1950). DOI: 10.1103/PhysRev.79.615. https://doi.org/10.1103/PhysRev.79.615.

[24] McAllister, R. W. and Hofstadter, R. *Elastic Scattering of 188 Mev Electrons from the Proton and the Alpha Particle.* Phys. Rev. **102** 851–856 (1956). DOI: 10.1103/physrev.102.851. https://doi.org/10.1103/physrev.102.851.

[25] Hofstadter, R. *Electron Scattering and Nuclear Structure.* Rev. Mod. Phys. **28** 214–254 (1956). DOI: 10.1103/RevModPhys.28.214. https://doi.org/10.1103/RevModPhys.28.214.

[26] Foldy, L. L. *The Electromagnetic Properties of Dirac Particles.* Phys. Rev. **87** 688–693 (1952). DOI: 10.1103/PhysRev.87.688. https://doi.org/10.1103/PhysRev.87.688.

[27] Perdrisat, C. F., Punjabi, V and Vanderhaeghen, M. *Nucleon electromagnetic form factors.* Prog. Part. Nucl. Phys. **59** 694 – 764 (2007). DOI: 10.1016/j.ppnp.2007.05.001. https://doi.org/10.1016/j.ppnp.2007.05.001.

[28] Barone, V., Drago, A., and Ratcliffe, P. G. *Transverse polarisation of quarks in hadrons.* Phys. Rept., 359, 1–168, 2002. DOI: 10.1016/S0370-1573(01)00051-5. https://arxiv.org/abs/hep-ph/0104283.

[29] Workman, R.L. et al. *Review of Particle Physics*, PTEP 2022, 083C01 (2022). DOI: 10.1093/ptep/ptac097. https://pdg.lbl.gov/2023/reviews/contents_sports.html

[30] Feynman, R. P. *The behavior of hadron collisions at extreme energies.* Conf.Proc. C690905 (1969) 237-258.

[31] Gell-Mann, M. *A Schematic Model of Baryons and Mesons.* M. Phys. Lett. B8 (1964), 214-215.

[32] Zweig, G. *An SU(3) model for strong interaction symmetry and its breaking* CERN-TH-412, NP-14146, PRINT-64-170.

[33] Callan, C. G., Gross, D. J., *High-Energy Electroproduction and the Constitution of the Electric Current.* Phys. Rev. Lett. 22 (1969) 156–159. http://link.aps.org/doi/10.1103/PhysRevLett.22.156.

[34] Lampe, B., Reya, E. *Spin physics and polarized structure functions.* Phys. Rept. 332 1-163 (2000), DOI:10.1016/S0370-1573(99)00100-3.

[35] Larin, S. A. *The next-to-leading QCD approximation to the Ellis-Jaffe sum rule.* Phys. Lett. B 334 192-198 (1994), DOI:10.1016/0370-2693(94)90610-6.

[36] Kodaira, J. *QCD Higher Order Effects in Polarized Electroproduction: Flavor Singlet Coefficient Functions.* Nucl. Phys. B 165 129-140 (1980), DOI:10.1016/0550-3213(80)90310-7.

[37] Levorato, S. *Measurement of transverse spin effects in COMPASS on a polarised proton target.* PhD thesis, Trieste (2008), http://wwwcompass.cern.ch/compass/publications/theses/2009_phd_levorato.pdf.

[38] Adolph, C. et al. (**COMPASS** Collaboration) *The spin structure function g_1^p of the proton and a test of the Bjorken sum rule.* Phys. Lett. B **753** (2016) 18-28. DOI: 10.1016/j.physletb.2015.11.064. http://dx.doi.org/10.1016/j.physletb.2015.11.064

[39] Jaffe, R. L., Manohar, A. *The g_1 problem: Deep inelastic electron scattering and the spin of the proton.* Nucl. Phys. B **337** (1990), 509.

[40] Ralston, J. P., Soper, D. E. *Production of dimuons from high-energy polarized proton-proton collisions.* Nuclear Physics B152 (1979) 109-124.

[41] Anselmino, M. et al. *Simultaneous extraction of transversity and Collins functions from new SIDIS and e^+e^- data.* Phys. Rev., D87, 094019, 2013. doi: 10.1103/PhysRevD.87.094019. http://arxiv.org/abs/1303.3822.

[42] Lorcé, C. and Pasquini, B. *Quark Wigner distributions and orbital angular momentum.* Phys. Rev. D 84 (2011), p. 014015. DOI: 10.1103/PhysRevD.84.014015. https://link.aps.org/doi/10.1103/PhysRevD.84.014015.

[43] Burkardt, M. and Pasquini, B. *Modelling the nucleon structure.* Eur. Phys. J. A (2016) **52**: 161. DOI: 10.1140/epja/i2016-16161-7. https://doi.org/10.1140/epja/i2016-16161-7.

[44] Wigner, E. *On the Quantum Correction For Thermodynamic Equilibrium.* Phys. Rev. **40** (1932), pp. 749–759. DOI: 10.1103/PhysRev.40.749. https://link.aps.org/doi/10.1103/PhysRev.40.749.

[45] Müller, D., Robaschik, D., Geyer, B., Dittes, F.-M. and Hořejší, J. *Wave Functions, Evolution Equations and Evolution Kernels*

from Light-Ray Operators of QCD. Fortsh. Phys. 42 (1994) 101. DOI: 10.1002/prop.2190420202. https://doi.org/10.1002/prop.2190420202.

[46] Ji, X.-D. *Gauge-Invariant Decomposition of Nucleon Spin* Phys. Rev. Lett. **78**, 610 (1997). DOI: 10.1103/PhysRevLett.78.610. https://doi.org/10.1103/PhysRevLett.78.610.

[47] Radyushkin, A. *Nonforward parton distributions.* Phys. Rev. D **56** (1997) 5524-5557. DOI: 10.1103/PhysRevD.56.5524. https://doi.org/10.1103/PhysRevD.56.5524.

[48] Jaffe, R. L. *Spin, Twist and Hadron Structure in Deep Inelastic Processes.* Lect. Notes Phys. **496** (1997) 178. DOI: 10.48550/arXiv.hep-ph/9602236. https://doi.org/10.48550/arXiv.hep-ph/9602236.

[49] Vanderhaeghen, M., Guichon, P. A., and Guidal, M. *Hard Electroproduction of Photons and Mesons on the Nucleon.* Phys. Rev. Lett. **80** (1998) 5064-5067. DOI: 10.1103/PhysRevLett.80.5064. https://doi.org/10.1103/PhysRevLett.80.5064.

[50] Wolbeek, J. ter *Azimuthal asymmetries in hard exclusive meson muoproduction off transversely polarized protons.* PhD thesis, Albert-Ludwig-Universität Freiburg (2015). http://wwwcompass.cern.ch/compass/publications/theses/2015_phd_ter_wolbeek.pdf.

[51] Radyushkin, A. V. *Asymmetric gluon distributions and hard diffractive electroproduction.* Phys. Lett. B **385**, 333–342 (1996). DOI: 10.1016/0370-2693(96)00844-1. https://doi.org/10.1016/0370-2693(96)00844-1.

[52] Collins J. C. et al. *Factorization for hard exclusive electroproduction of mesons in QCD.* Phys. Rev. D **56**, 2982–3006 (1997). DOI: 10.1103/PhysRevD.56.2982. https://doi.org/10.1103/PhysRevD.56.2982.

[53] Mankiewicz, L. and Piller, G. *Remarks on exclusive electroproduction of transversely polarized vector mesons.* Phys. Rev. D **61** (2000) 074013. DOI: 10.1103/PhysRevD.61.074013. https://doi.org/10.1103/PhysRevD.61.074013.

[54] Goloskokov, S. V. and Kroll, P. *Transversity in hard exclusive electroproduction of pseudoscalar mesons.* Eur. Phys. J. A **47** 112 (2011). DOI: 10.1140/epja/i2011-11112-6. https://doi.org/10.1140/epja/i2011-11112-6.

[55] Saeed, A., Goldstein, G. R., and Liuti, S. *Nucleon tensor charge from exclusive π^0 electroproduction.* Phys. Rev. D **79**, 054014 (2009). DOI: 10.1103/PhysRevD.79.054014, https://doi.org/10.1103/PhysRevD.79.054014.

[56] Ji, X. *Gauge-invariant decomposition of nucleon spin.* Phys. Rev. Lett. **78**, 610-613 (1997). DOI: 10.1103/PhysRevLett.78.610. https://doi.org/10.1103/PhysRevD.78.610.

[57] Kumerički, K., Liuti, S., Moutarde, H. *GPD phenomenology and DVCS fitting - Entering the high-precision era.* Eur. Phys. J. A (2016). DOI: 10.1140/epja/i2016-16157-3. https://doi.org/10.1140/epja/i2016-16157-3.

[58] Pire, B., Soffer, J. and Teryaev, O. *Positivity constraints for off-forward parton distributions.* Eur. Phys. J. C **8** (1990) 103. DOI: 10.1007/s100529901063. https://doi.org/10.1007/s100529901063.

[59] Boffi, S. and Pasquini, B. *Generalized parton distributions and the structure of the nucleon.* Riv. Nuovo Cim. 30:387 (2007). DOI: 10.1393/ncr/i2007-10025-7. https://doi.org/10.1393/ncr/i2007-10025-7.

[60] Burkardt, M. *Impact parameter space interpretation for generalized parton distributions.* Int. J. Mod. Phys. A **18** 173–208 (2003). DOI:10.1142/S0217751X03012370. https://doi.org/10.1142/S0217751X03012370.

[61] (**COMPASS** Collaboration) *COMPASS-II, proposal.* CERN, Geneva, SPS and PS Experiments Committee (2010). CERN-SPSC-2010-014/SPSC-P-340. http://wwwcompass.cern.ch/compass/proposal/compass-II_proposal/compass-II_proposal.pdf.

[62] Burkardt, M. *Transversity decomposition of quark angular momentum.* Phys. Lett. B **639**, 462 (2006). DOI: 10.1016/j.physletb.2006.01.076. https://doi.org/10.1016/j.physletb.2006.01.076.

[63] Goldstein, G. R., Hernandez, J. O. G, and Liuti, S. *Flexible parametrization of generalized parton distributions: The chiral-odd sector.* Phys. Rev. D **91**, 114013 (2015). DOI: 10.1103/PhysRevD.91.114013. https://doi.org/10.1103/PhysRevD.91.114013.

[64] Goloskokov, S. V. and Kroll, P. *Vector-meson electroproduction at small Bjorken-x and generalized parton distributions.* Eur. Phys. J. C 42, 281–301 (2005). DOI: 0.1140/epjc/s2005-02298-5. https://doi.org/0.1140/epjc/s2005-02298-5.

[65] Arens, T., Nachtmann, O., Diehl, M. and Landshoff, P. V. *Some tests for the helicity structure of the pomeron in ep collisions.* Z. Phys. C **74**, 651 (1997). DOI: 10.48550/arXiv.hep-ph/9605376. https://doi.org/10.48550/arXiv.hep-ph/9605376.

[66] Alexeev, M. G. et al (**COMPASS** Collaboration). *Measurement of the cross section for hard exclusive π^0 muoproduction on the proton.* Physics Letters B 805 (2020) 135454. DOI: 10.1016/j.physletb.2020.135454. https://doi.org/10.1016/j.physletb.2020.135454.

[67] Hand, L. N. et al. *Experimental investigation of pion electroproduction.* Phys. Rev. **129**, 1834–1846 (1963) DOI: 10.1103/PhysRev.129.1834. https://doi.org/10.1103/PhysRev.129.1834.

[68] Goloskokov, S. V. and Kroll, P. *An attempt to understand exclusive π^+ electroproduction.* Eur. Phys. J. C (2010) 65: 137–151. DOI: 10.1140/epjc/s10052-009-1178-9. https://doi.org/10.1140/epjc/s10052-009-1178-9.

[69] Bedlinsky, I. et al. (**CLAS** Collaboration). *Exclusive π^0 electroproduction at $W > 2$ GeV with CLAS.* Phys. Rev. C **90**, 025205 (2014). DOI: 10.1103/PhysRevC.90.025205. https://doi.org/10.1103/PhysRevC.90.025205.

[70] Airapetian A. et al. (**HERMES** Collaboration). *Single-spin azimuthal asymmetry in exclusive electroproduction of π^+ mesons*. Phys. Lett. B **535**, 85–92 (2002). DOI: 10.1016/S0370-2693(02)01780-X. https://doi.org/10.1016/S0370-2693(02)01780-X.

[71] Airapetian A. et al. (**HERMES** Collaboration). *Single-spin azimuthal asymmetry in exclusive electroproduction of π^+ mesons on transversely polarized protons*. Phys. Lett. B **682**, 345–350 (2010). DOI: 10.1016/j.physletb.2009.11.039. https://doi.org/10.1016/j.physletb.2009.11.039.

[72] Airapetian A. et al. (**HERMES** Collaboration). *Cross sections for hard exclusive electroproduction of π^+ mesons on a hydrogen target*. Phys. Lett. B **659**, 486–492 (2008). DOI: 10.1016/j.physletb.2007.11.079. https://doi.org/10.1016/j.physletb.2007.11.079.

[73] Goldstein, G. R. et al. *Flexible parametrization of generalized parton distributions from deeply virtual Compton scattering observables*. Phys. Rev. D **84**, 034007 (2011. DOI: 10.1103/PhysRevD.84.034007. https://doi.org/10.1103/PhysRevD.84.034007.

[74] Goldstein, G. R. et al. *Easy as π^0: on the interpretation of recent electroproduction results*. Journal of Physics G: Nuclear and Particle Physics **39**, 115001 (2012). DOI: 10.1088/0954-3899/39/11/115001. https://doi.org/10.1088/0954-3899/39/11/115001.

[75] Fuchey, E. et al. (**JLab Hall A Collaboration**). *Exclusive neutral pion electroproduction in the deeply virtual regime*. Phys. Rev. C **83**, 025201 (2011). DOI: 10.1103/PhysRevC.83.025201. https://doi.org/10.1103/PhysRevC.83.025201.

[76] Defurne, M. et al. (**JLab Hall A Collaboration**). *Rosenbluth separation of the π^0 electroproduction cross section*. Phys. Rev. Lett. **117** (2016). DOI: 10.1103/PhysRevLett.117.262001. https://doi.org/10.1103/PhysRevLett.117.262001.

[77] Vanderhaeghen, M. et al. *Deeply virtual electroproduction of photons and mesons on the nucleon: Leading order amplitudes and power corrections*. Phys. Rev. D **60**, 094017 (1999). DOI: 10.1103/PhysRevD.60.094017. https://doi.org/10.1103/PhysRevD.60.094017.

[78] Villano, A. N. et al. (**JLab Hall C Collaboration**). *Neutral pion electroproduction in the resonance region at high Q^2*. Phys. Rev. C **80**, 035203 (2009). DOI: 10.1103/PhysRevC.80.035203. https://doi.org/10.1103/PhysRevC.80.035203.

[79] Horn, T. et al. (**JLab Hall C Collaboration**). *Scaling study of the pion electroproduction cross sections*. Phys. Rev. C **78**, 058201 (2008). DOI: 10.1103/PhysRevC.78.058201. https://doi.org/10.1103/PhysRevC.78.058201.

[80] Adolph, C. et al. (**COMPASS** Collaboration) *Transverse target spin asymmetries in exclusive ρ^0 muoproduction*. Phys. Lett. B **731**, 19–26 (2014). DOI: 10.1016/j.physletb.2014.02.005. https://doi.org/10.1016/j.physletb.2014.02.005.

[81] Adolph, C. et al. (**COMPASS** Collaboration) *Exclusive ω meson muoproduction on transversely polarised protons*. Nucl. Phys. **915**, 454–475 (2017). DOI: 10.1016/j.nuclphysb.2016.12.015. https://doi.org/10.1016/j.nuclphysb.2016.12.015.

[82] **COMPASS** Collaboration. *Spin density matrix elements in exclusive ω meson muoproduction*. Eur. Phys. J. C (2021) 81:126. DOI: 10.1140/epjc/s10052-020-08740-y. https://doi.org/10.1140/epjc/s10052-020-08740-y.

[83] **COMPASS** Collaboration. *Spin density matrix elements in exclusive ρ^0 meson muoproduction*. Eur. Phys. J. C (2023) 83:924. DOI: 10.1140/epjc/s10052-023-11359-4. https://doi.org/10.1140/epjc/s10052-023-11359-4.

[84] Goloskokov, S. V. and Kroll, P. Private communications (2016).

[85] Abbon, P. et al. (**COMPASS** Collaboration). *The COMPASS experiment at CERN*. NIMA 577, 455-518, 2007.

[86] Bernhard, J. et al. *Studies for New Experiments at the CERN M2 Beamline within "Physics Beyond Colliders"*, 2019. DOI: 10.1063/5.0008957. https://doi.org/10.1063/5.0008957.

[87] d'Hose, N. https://wwwcompass.cern.ch/compass/gpd/meetings/201606_23juin_CM/dHose_20160623_CM.pdf.

[88] Bielert, E. *A 2.5 m long liquid hydrogen target for COMPASS*. Nuclear Instruments and Methods in Physics Research Section A 746, 20–25 (2014). DOI: 10.1016/j.nima.2014.01.067. https://doi.org/10.1016/j.nima.2014.01.067.

[89] Szameitat, T. *New geant4-based Monte Carlo software for the COMPASS-II experiment at CERN*. Dissertation at Albert Ludwigs Universität Freiburg (2017). DOI: 10.6094/UNIFR/11686. https://freidok.uni-freiburg.de/data/11686.

[90] Pierre, N. *Multiplicities of hadrons in deep-inelastic scattering of muons on nucleons at COMPASS*. PhD thesis. Université Paris-Saclay (2019). http://wwwcompass.cern.ch/compass/publications/theses/2019_phd_pierre.pdf

[91] Herrmann, F. *Development and verification of a high performance electronic readout framework for high energy physics*. MA thesis. Fakultät für Mathematik und Physik Albert-Ludwigs-Universität Freiburg (2011). https://wwwcompass.cern.ch/compass/publications/theses/2011_phd_herrmann.pdf.

[92] Schäfer, R. *Charakterisierung eines Detektors zum Nachweis von Rückstoßprotonen am COMPASS Experiment*. MA thesis. Fakultät für Mathematik und Physik Albert-Ludwigs-Universität Freiburg (2013). https://cds.cern.ch/record/2005748/files/schaefer_diplom_2013.pdf.

[93] Bernet, C. et al. *The COMPASS trigger system for muon scattering*. Nuclear Instruments and Methods in Physics Research, Section A: Accelerators, Spectrometers, Detectors and Associated Equipment 550. 1-2 (2005), pp. 217–240. DOI: 10.1016/j.nima.2005.05.043. https://doi.org/10.1016/j.nima.2005.05.043.

[94] Barth, J. et al. *Trigger configuration summary 2002-2012*. COMPASS note 2016-4 (2016).

[95] Jörg, P. *Deeply virtual compton scattering at CERN - What is the size of the proton?*. PhD thesis. Physikalisches Institut Albert-Ludwigs-Universität Freiburg (2017). http://wwwcompass.cern.ch/compass/publications/theses/2017_phd_joerg.pdf.

[96] Nový, J. *COMPASS DAQ – Basic control system*. Diploma thesis. Czech Technical University, Prague (2012).

[97] Fruhwirth, R. *Application of Kalman filtering to track and vertex fitting*. Nucl. Instrum. Meth. A **262** 444-450 (1987). DOI: 10.1016/0168-9002(87)90887-4. https://doi.org/10.1016/0168-9002(87)90887-4.

[98] Gerassimov, S. *PHysics Analysis Software Tools*. http://ges.home.cern.ch/ges/phast.

[99] Brun, R. and Fons Rademakers. *ROOT - An Object Oriented Data Analysis Framework*. Nucl. Instrum. Meth. A **389** 81-86 (1997).

[100] Lin, Po-Ju. Private communications. 2018.

[101] Gerassimov, Sergei. Private communications. 2024.

[102] Orpel, Piotr. Private communications. 2020.

[103] d'Hose, Nicole. Private communications. 2020.

[104] Lavičková, Karolína. Private communications. 2023.

[105] Matoušek, Jan. Private communications. 2023.

[106] Grindhammer, G., and Peters, S. *The Parameterized Simulation of Electromagnetic Showers in Homogeneous and Sampling Calorimeters.* (2000). arXiv: hep-ex/0001020. https://arxiv.org/abs/hep-ex/0001020.

[107] Scherrers, S. *Extraction of the exclusive* J/Ψ *photoproduction cross section at COMPASS, CERN*. MA thesis. Fakultät für Mathematik und Physik Albert-Ludwigs-Universität Freiburg (2019).

[108] Giarra, J. V. *Analysis of the spill profile and the muon flux in 2016.* COMPASS Note 2021-2 (2021). https://wwwcompass.cern.ch/compass/notes/2021-2/2021-2.pdf.

[109] Ingelman, G. et al. *LEPTO 6.5 - A Monte Carlo generator for deep inelastic lepton-nucleon scattering.* Computer Physics Communications **101**, 108-134 (1997). DOI: 10.1016/S0010-4655(96)00157-9. https://doi.org/10.1016/S0010-4655(96)00157-9.

[110] Sandacz, A., and Sznajder, P. *HEPGEN - generator for hard exclusive leptoproduction* (2012). https://arxiv.org/abs/1207.0333.

[111] Regali, C. *Exclusive event generation for the COMPASS-II experiment at CERN and improvements for the Monte-Carlo chain.* PhD thesis, Albert Ludwigs Universität Freiburg (2016). DOI: 10.6094/UNIFR/11449. https://freidok.uni-freiburg.de/data/11449.

[112] Agostinelli, S. et al. *Geant4 - a simulation toolkit.* Nuclear Instruments and Methods in Physics Research Section A **506**, 250–303 (2003). DOI: 10.1016/S0168-9002(03)01368-8. https://doi.org/10.1016/S0168-9002(03)01368-8.

[113] Ferrero, A. et al. *Extraction of the t-slope of the pure DVCS cross section.* COMPASS Note 2016-5 (2016).

[114] *TFractionFitter.* https://root.cern/doc/master/classTFractionFitter.html.

[115] Barlow, R. and Beeston, C. *Fitting using finite Monte Carlo samples.* Computer Physics Communications 77.2 (1993), pp. 219–228. DOI: 10.1016/0010-4655(93)90005-W. https://doi.org/10.1016/0010-4655(93)90005-W.

[116] Lavičková, K. and Pešková, M. et al. *Update on Exclusive π^0 muoproduction in 2016 data.* COMPASS Note (2023).

[117] Afanasev, A. et al. *QED Radiative Corrections in Processes of Exclusive Pion Electroproduction.* Phys. Rev. D **66** (2002) 074004. DOI: 10.1103/PhysRevD.66.074004. https://doi.org/10.1103/PhysRevD.66.074004.

List of abbreviations

ADC	Analog-to-Digital Converter
BMS	Beam Momentum Station
CAMERA	COMPASS Apparatus for Measurement of Exclusive ReActions
CASTOR	CERN Advanced STORage manager
CATCH	COMPASS Accumulate, Transfer and Control Hardware
CERN	Council Européen pour la Recherche Nucléaire
COMPASS	Common Muon and Proton Apparatus for Structure and Spectroscopy
CORAL	COMPASS Reconstruction AnaLysis software
DAQ	Data AcQuisition
DC	Drift Chamber
DIS	Deep Inelastic Scattering
DOF	Distance Of Flight
DVCS	Deeply Virtual Compton Scattering
ECAL	Electromagnetic CALorimeter
FPGA	Field Programmable Gate Array
GAMS	Russian acronym for hodoscopic multi-gamma Cherenkov spectrometre
GANDALF	Generic Advanced Numerical Device for Analog and Logic Functions
GEM	Gas Electron Multiplier
GeSiCA	GEM and Silicon Control and Acquisition
GK	Goloskokov and Kroll
GL	Goldstein and Liuti
GPD	Generalised Parton Distributions
GTMD	Generalised Transverse Momentum Dependent parton distributions
HEMP	Hard Exclusive Meson Production
LAS	Large Angle Spectrometre
LAST	LAS Trigger
LAT	Large Area Trackers

LT	Ladder Trigger
MPFF	Meson Production Form Factor
MW	Muon Wall
MWPC	Multi-Wire Proportional Chamber
MT	Middle Trigger
OT	Outer Trigger
PDF	Parton Distribution Functions
PHAST	PHysics Analysis Software
Pixel-GEM	Pixel Gas Electron Multiplier
Pixel-MicroMegas	Pixel Micro-Mesh Gaseous Structures
PMT	Photo-Multiplier Tube
RT	Random Trigger
RHGAMS	Radiation Hardened GAMS
RICH	Ring Imaging Cherenkov detector
QCD	Quantum Chromodynamics
SAS	Small Angle Spectrometre
SAT	Small Area Trackers
SIDIS	Semi-Inclusive DIS
SILICON	silicon microstrip trackers
SciFi	Scintilating Fibers
SLAC	Stanford Linear Accelerator Center
SPS	Super Proton Synchrotron
TCS	Trigger Control System
TDC	Time-to-Digital Converter
TIGER	Trigger Implementation for GANDALF Electronic Readout
TOF	Time Of Flight
VSAT	Very Small Area Trackers